CHALMERS
UNIVERSITY OF TECHNOLOGY

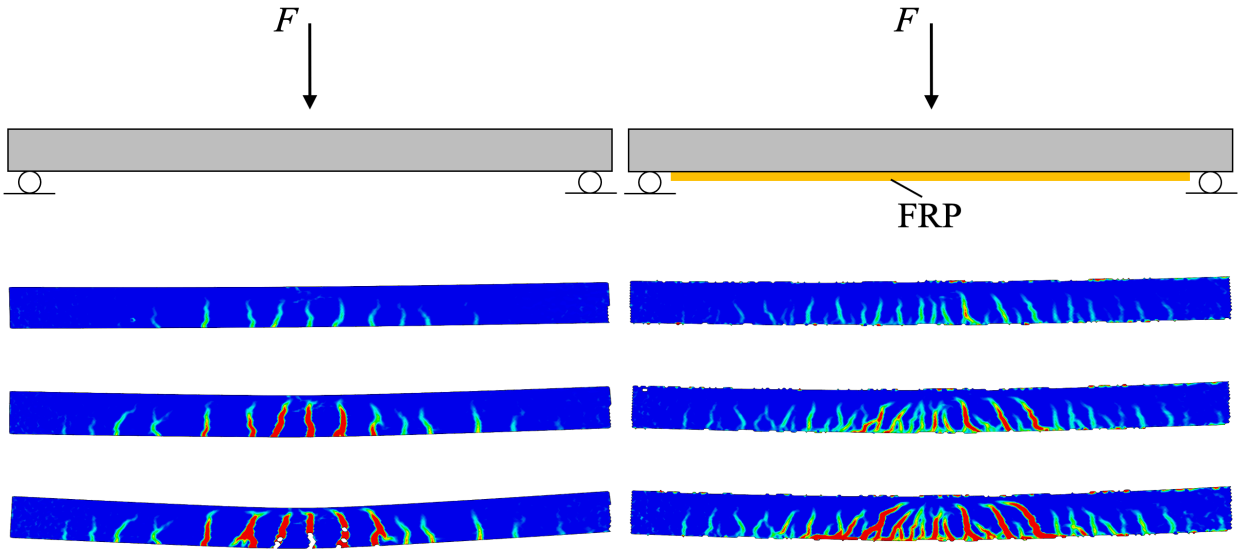

FRP Strengthened Reinforced Concrete Beams Subjected to Drop Weight Impact and Static Loading

Master's Thesis in the Master's Programme Structural Engineering and Building Technology

Edvard Eriksson
Viktor Gustafsson

DEPARTMENT OF ARCHITECTURE AND CIVIL ENGINEERING
DIVISION OF STRUCTURAL ENGINEERING

CHALMERS UNIVERSITY OF TECHNOLOGY
Gothenburg, Sweden 2021
www.chalmers.se

MASTER'S THESIS ACEX30

FRP Strengthened Concrete Beams Subjected to Drop Weight Impact and Static Loading

Master's Thesis in the Master's Programme Structural Engineering and Building Technology

Edvard Eriksson
Viktor Gustafsson

Department of Architecture and Civil Engineering
Division of Structural Engineering
Concrete Structures
CHALMERS UNIVERSITY OF TECHNOLOGY
Göteborg, Sweden 2021

Department of Architecture and Civil Engineering
Division of Structural Engineering
Concrete Structures
CHALMERS UNIVERSITY OF TECHNOLOGY
Gothenburg, Sweden 2021

FRP Strengthened Concrete Beams Subjected to Drop Weight Impact and Static Loading

Master's Thesis in the Master's Programme Structural Engineering and Building Technology

Edvard Eriksson

Viktor Gustafsson

Examensarbete ACEX30
Institutionen för arkitektur och samhällsbyggnadsteknik
Chalmers tekniska högskola, 2021

Department of Architecture and Civil Engineering
Division of Structural Engineering
Concrete Structures
Chalmers University of Technology
SE-412 96 Göteborg
Sweden
Telephone: + 46 (0)31-772 1000

Cover:
Strain fields of unstrengthened and FRP strengthened reinforced concrete beams subjected to static loading

Department of Architecture and Civil Engineering
Göteborg, Sweden, 2021

FRP Strengthened Concrete Beams Subjected to Drop Weight Impact and Static Loading

Master's thesis in the Master's Programme Structural Engineering and Building Technology

EDVARD ERIKSSON

VIKTOR GUSTAFSSON

Department of Architecture and Civil Engineering
Division of Structural Engineering
Concrete Structures
Chalmers University of Technology

ABSTRACT

Concrete is a material that is commonly used in protective structures, e.g. civil defence shelter and fortifying facilities. The structural response in these types of structures when subjected to impulse loading is highly interesting. The aim of this project is to increase the knowledge of the structural response of impulse loaded reinforced concrete (RC) structures strengthened with fibre reinforced polymer (FRP) through an experimental study. Focus on this thesis is on the effect FRP strengthening has on impact loaded structures when it comes to deformation capacity, ultimate load capacity and energy absorption.

A literature study was conducted regarding impulse loaded structures, FRP in general and FRP strengthening of RC structures in particular. Different strengthening methods and how to achieve a good adhesion between concrete and FRP were of interest. The experimental study consisted of drop weight tests from 3.0, 4.0, 5.0 and 5.7 m followed by static loading until failure for unstrengthened and FRP strengthened beams with two types of adhesives. To complement, beams were tested statically only to act as references. High speed cameras were used to capture the response during the tests, one capturing the beam and one capturing the drop weight. The data was later processed using Digital Image Correlation (DIC). Material tests of concrete, reinforcement and the adhesives were also conducted.

FRP proved to give an enhanced structural response compared to unstrengthened beams. The results showed that FRP strengthened beams obtained a higher load carrying capacity, a larger deformation capacity and a good energy absorption. In order to achieve a good adhesion between concrete and FRP, response, a well-treated surface was found to be crucial.

Key words: Reinforced concrete, Fibre reinforced polymer, FRP strengthening, Impulse loading, Drop weight test, FRP debonding, Residual strength, Energy absorption, Plastic rotation capacity.

FRP-förstärkta betongbalkar belastade med fallvikt och statisk belastning

Examensarbete inom mastersprogrammet Konstruktionsteknik och byggnadsteknologi

EDVARD ERIKSSON

VIKTOR GUSTAFSSON

Institutionen för arkitektur och samhällsbyggnadsteknik
Avdelningen för Konstruktionsteknik
Betongbyggnad
Chalmers tekniska högskola

SAMMANFATTNING

Betong är ett material som används i skyddande konstruktioner, till exempel skyddsrum och fortifikatoriska anläggningar. Strukturresponsen i sådana konstruktioner när de utsätts för impulsbelastning är av högsta intresse. Syftet med detta projekt är att öka kunskapen om den strukturella responsen för impulsbelastade armerade betongkonstruktioner förstärka med fiberkompositarmering (FRP) genom ett fallviktsförsök. FRP som användes i detta fall var en samverkande epoxi med aramidfibrer (kevlar). Arbetets fokus är på vilken inverkan FRP har på impulsbelastade konstruktioners deformationskapacitet, lastkapacitet och energiabsorptionsförmåga.

En litteraturstudie gjordes gällande impulsbelastade konstruktioner, FRP generellt och FRP-förstärkta armerade betongkonstrukturer i synnerhet. Olika förstärkningsmetoder och hur en god vidhäftning mellan betong och FRP uppnås var av intresse. Försöksstudien bestod av fallviktsförsök från höjderna 3,0, 4,0, 5,0 och 5,7 m följt av statisk belastning till brott på oförstärkta och FRP-förstärkta balkar där två olika typer av lim användes. Balkar som endast belastades statiskt användes som referens. Under försöken användes två höghastighetskameror för att fånga den erhållna responsen. Den ena kameran fokuserade på balken och den andra fokuserade på fallvikten. Informationen från de två kamerorna sammanställdes och processades sedan med hjälp av så kallad ”Digital Image Correlation” (DIC). Utöver fallvikts- och statiska försök utfördes även tester på materialprover av betong, armeringsstål and lim.

FRP medförde en förbättrad strukturrespons för de förstärkta balkarna jämfört med oförstärkta. Resultaten visade att FRP-förstärkta balkar fick en högre lastkapacitet, en större deformationsförmåga och en god energiabsorptionsförmåga. För att åstadkomma en god vidhäftning mellan betong och FRP, och genom det en förbättrad strukturrespons, var förarbetet av ytan innan applicering av FRP av högsta vikt.

Nyckelord: Armerad betong, FRP-förstärkning, Impulsbelastning, Fallviktsförsök, Vidhäftningsbrott av FRP, Resthållfasthet, Energiabsorption, Plastisk rotationskapacitet.

Contents

Preface

In this study, drop weight tests and static tests of reinforced concrete beams strengthened with fibre reinforced polymers have been done. The work has been performed from January to June 2021. The work is a part of research field treating impulse loaded structures. The project was carried out in a collaboration between the Division of Structural Engineering, Concrete Structures at Chalmers University of Technology and Norconsult and was financed by the Swedish Civil Contingencies Agency (MSB). The experiments carried out were in addition also financially supported by the Swedish Foundation Fortifications Corps (In Swedish: Fortifikationskårens forskningsfond).

First, we would like to thank Morgan Johansson, Norconsult, who has been the supervisor of this work for his never-ending hunger for sharing his knowledge, passion and experiences within impulse loaded structures. We would also like to thank Joosef Leppänen, Chalmers, who has been the examiner of this thesis and has given us great guidance and support with the work. Great thanks to research engineer Anders Karlsson, Chalmers, who has provided great assistance, expertise and creativity, and the experiments would never have worked out so well without his participation. Thanks to Mathias Flansbjer from RISE for his help connected to the dynamic tests and guidance in the postprocessing of the results. Thanks also to Jincheng Yang and Reza Haghani Dogaheh, both Chalmers, for their expertise regarding fibre reinforced polymers.

Finally, we would like to show our deep appreciation for the revered duo referred to as A-vaktis at Chalmers. Thanks for all the coffee breaks and endless anecdotes that has been shared throughout our time as students.

Göteborg June 2021

Edvard Eriksson and Viktor Gustafsson

Notations

Abbreviations

2DOF	Two-degree of freedom
SDOF	Single-degree of freedom
AFRP	Aramid fibre reinforced polymer
BFRP	Basalt fibre reinforced polymer
CFRP	Carbon fibre reinforced polymer
DIC	Digital image correlation
DIF	Dynamic increase factor
EC	Eurocode
FPS	Frame per second
FRP	Fibre reinforced polymer
GFRP	Glass fibre reinforced polymer
RC	Reinforced concrete
ULS	Ultimate limit state
WST	Wedge splitting test

Roman upper case letters

A	Area
E	Young's modulus/modulus of elasticity, Energy
E_k	Kinetic energy
F	Force, Load
G_F	Fracture energy
I	Impulse, Second moment of inertia
L	Length
L_e	Length from support to plastic hinge
M	Moment
R	Internal resistance
R_m	Maximum internal resistance
W	Work

Roman lower case letters

a	Acceleration
b	Width of cross section
c	Damping coefficient, Concrete cover thickness
d	Effective height of cross section
e	Coefficient of restitution
$f_{0.2}$	0.2% proof stress for the reinforcement steel

f_c	Cylinder compression strength of concrete
f_{ck}	Characteristic cylinder compression strength of concrete
f_{cm}	Mean cylinder compression strength of concrete
$f_{cm,cube}$	Mean cube compression strength of concrete
f_{ct}	Tensile strength of concrete
f_{ctm}	Mean tensile strength of concrete
$f_{ct,fl}$	Flexural tensile strength of concrete
$f_{ct.sp}$	Splitting tensile strength of concrete
f_{sc}	Strength of reinforcement in compression
f_{st}	Strength of reinforcement in tension
f_{sv}	Strength of shear reinforcement
g	Gravitational acceleration, Self-weight
h	Height of cross section
k	Stiffness, Hardening ratio
$k´$	Stiffness after cracking
k_λ	Factor considering shear slenderness
l_0	Distance from zero-moment section to a specific plastic hinge
l_{pl}	Length of plastic region
m	Mass
n	Quantity
p	Momentum
r	Radius of curvature
s	Distance between stirrups
s^{-1}	Strain rate
u	Displacement
$\dot{u}$	First derivative of displacement (velocity)
$\ddot{u}$	Second derivative of displacement (acceleration)
u_a	Displacement at the ascending branch for a specific load level
u_b	Displacement at the descending branch for a specific load level
v	Velocity
x	Height of compressive zone

Greek lower case letters

α	Stress block factor in Eurocode 2, Factor in composite cross sections
α_1	Stress block factor in ACI
β	Stress block factor in Eurocode 2
β_1	Stress block factor in ACI
γ	Partial safety factor
δ_G	Stress block factor in fib
ε	Strain
ε_{cy}	Concrete strain when the reinforcement yields
ε_{cu2}	Failure strain for concrete
$\varepsilon_{fd,ic}$	Strain limit in FRP with respect to intermediate crack propagation
η	Stress block factor in Kompositförstärkning betong
θ_{pl}	Plastic rotation capacity
κ	Transformation factor
λ	Stress block factor in Kompositförstärkning betong, Shear slenderness
ρ	Reinforcement amount, Density

σ	Stress
χ	Curvature
ψ	Stress block factor in fib
ω	Mechanical reinforcement ratio

Index

0	Initial
1	Body 1 (the drop weight)
2	Body 2 (the beam)
b	Beam
c	Concrete
cam	Camera
cr	Cracking
crit	Critical
d	Design value
dyn	Dynamic
e	External
el	Elastic
exp	Experimental
F	Force
fe	FRP sheet
i	Internal
imp	Impact
k	characteristic, stiffness
m	Mean value, mass
max	Maximum
pl	Plastic
red	Reduction
s	Steel
sta	Static
tot	Total
u	Ultimate
v	shear reinforcement
y	Yield
I	State I
II	State II
´	Compressive reinforcement

1 Introduction

1.1 Background

Concrete is a material that is commonly used in protective structures, e.g. civil defence shelter and fortifying facilities. The structural response in these types of structures when subjected to impulse loading is highly interesting. The impulse loading, which could be due to a collision or an explosion, might cause failure modes different from the ones expected in a statically loaded structure. A structure subjected to impulse loading will behave in a different way than a statically loaded structure and thus other properties, compared to those wanted in a statically loaded structure, are desirable. In a statically loaded structure, a stiff response and high load resistance is often what is sought but in an impulse loaded structure, this is not necessarily the case. Instead in such structures, a weaker response with lower load resistance but possibility to accept large plastic deformation, in order to have the ability to absorb large amounts of energy, is instead often desired.

A well-used method for strengthening concrete structures is the usage of Fibre Reinforced Polymers, FRP, to strengthen or repair existing structures. FRP strengthening can give an increased load carrying capacity for static loading but its effects on impulse loaded structures are not researched to the same extent. Consequently, the FRP strengthened structure might not be as efficient when it comes to absorption of energy as a normal reinforced concrete structure. There is an uncertainty in the behaviour of the FRP and the adhesive. The important factor for an impulse loaded structure is the absorption of energy and even though the FRP strengthened structure could carry a higher load, this is not necessarily beneficial from a dynamic point of view. The consequence could even be a structure that is less suitable to withstand the effect of impulse loading than the unstrengthened structure. This is because when the FRP fails, the reinforcement may rupture prematurely, thus leading to a smaller total absorption of energy compared to a case without the FRP strengthening. Another important aspect may be the ductility of the glue. To achieve a desirable increase in deformation capacity and prevent early loss of adhesion between the FRP and the structure, the glue needs to have enough ductility. Therefore, it is of great interest to investigate the response of FRP strengthened reinforced concrete subjected to impulse loading.

This master's thesis will contribute to the already ongoing research field about impulse loaded structures between the Swedish Civil Contingencies Agency (MSB) and the Division of Structural Engineering at Chalmers University of Technology. It is a continuation of five previous MSc theses carried out during the years 2016-2020 (Lovén & Svavarsdóttir, 2016; Lozano & Makdesi, 2017; Jönsson & Stenseke, 2018; Andersson & Pettersson, 2019; Nigani & Nordström, 2020). The work is carried out in a collaboration between Norconsult and Chalmers.

1.2 Aim

The aim of this master's thesis is to get a better understanding of the structural response of impulse loaded concrete structures strengthened with FRP, particularly the structural response of reinforced concrete beams subjected to an impulse loading in form of a drop weight. This is done by experimental testing of beams, through drop weight and static test, and to get a better understanding of the structural response, focus will be on

residual strength and plastic deformation capacity. Focus will also be on different types of adhesive and different failure modes for a FRP strengthened reinforced concrete structure.

Another aim is to support the research within this field for the parties mentioned above. The master's thesis from 2020, Nigani and Nordström (2020), will together with this one be part of a new project where the impact of FRP strengthening is studied and experimental test results will be carried out for future comparative non-linear finite element analyses.

1.3 Limitations

In this project there was a desire to investigate two factors and how they influence the behaviour and response of the impulse loaded beams. These were various heights for the drop weight and various types of adhesives. Further, the type of load application varied to beams being subjected to static loading only or impulse loading followed by static loading. The number of beams were limited to 22 and thus were the number of tests per combination of variable limited.

This project is a part of the Swedish Civil Contingencies Agency (MSB) research program where the effects of explosions are investigated but those kinds of tests are both challenging and expensive to conduct, and therefore the experimental testing in this project is limited to drop weight tests. Another limiting aspect is the facilities in which the tests are to be conducted. This limits the drop weight height, drop weight mass and the dimensions of the test specimens.

1.4 Methodology

First of all, a literature study was done to gain needed knowledge within the master's thesis subject. Different publications considering impulse loading and plastic deformation was studied together with the previous master's theses done to get a better understanding about the structural response of impact loaded concrete structures.

Since the response with impact from FRP was of interest a literature study of FRP was also done to get a better understanding about the mechanical properties, normal usage and advantages and disadvantages with the material. Another focus in the literature study was observations and conclusions from other drop weight tests, particularly tests of FRP strengthened structures.

The experimental tests were done by testing of 16 concrete beams loaded in the middle of the span with drop weight impact from various drop heights, followed by statically loading. As reference, 6 concrete beams subjected to static loading only was carried out. Out of 22 beams, 16 beams were strengthened using FRP, which consisted of one layer of kevlar glued to the bottom side. Different configurations for the FRP strengthening were also examined where two different types of glue were used.

During the testing of the beams, two cameras (high-speed cameras for drop weight tests) were used to measure the response of the beam and drop weight with respect to cracks and deformations, and velocity and acceleration respectively. The information gained was then used to calculate strain fields by digital image correlation, DIC, and present them in a way similarly to a finite element analysis.

To get a better understanding of the real behaviour and how to predict it, simplified hand calculations were done and compared with the experimental test results. The simplified hand calculations were done with 2DOF models using central difference method, CDM.

2 Structural Response

The structural behaviour of materials differs a lot depending on which materials that are studied. For example, the response of timber is completely different from the response of steel, but the differences are not only depending on the material but also the load level applied on the structure (Domone & Illston, 2010). The behaviour can be idealized and described in many ways such as linear elastic response, plastic response, elasto-plastic response and tri-linear response.

2.1 Linear Elastic Response

The response of a linear elastic material is characterized by a stress direct proportional to the strain. When the load increases so does the strain and when the load decreases the strain decreases as well meaning that the material is always elastic in its deformations (Domone & Illston, 2010). The linear elastic response is described in Figure 2.1.

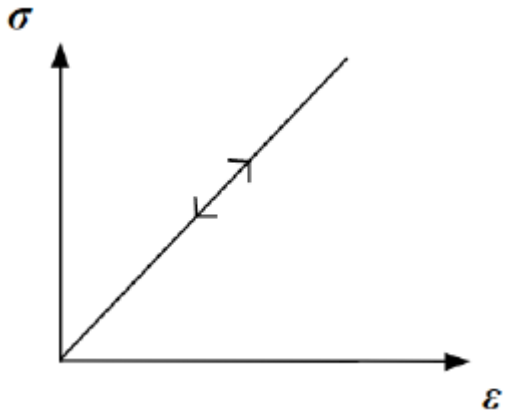

Figure 2.1 Linear elastic response in a stress-strain diagram (Nigani & Nordström, 2020).

The stress-strain response can be described with Hooke's law where the slope of the stress-strain diagram is the Young's modulus, *E*, and is calculated as

$$\sigma = E \cdot \varepsilon \tag{2.1}$$

where σ is stress [Pa]
ε is strain [-]
E is the Young's modulus [Pa]

Another way of describing the linear elastic behaviour is with resistance force *R* versus displacement *u*; i.e. *R(u)* (Johansson & Laine, 2012). The linear elastic structural response can be described with a constant stiffness *k* and in theory no upper limit for the resistance force *R* which is illustrated in Figure 2.2. The deformation is elastic meaning it could become infinitely large but always go back to zero if loading is removed.

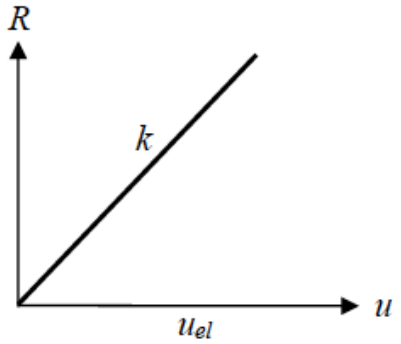

Figure 2.2 Relationship between the internal resistance R and the elastic deformation u_{el} (Jönsson & Stenseke, 2018).

The relation between resistance force and displacement can be described as

$$R = k \cdot u_{el} \tag{2.2}$$

2.2 Plastic Response

Plastic response is characterized by a maximum internal resistance force and irreversible deformations when this force is exceeded (Johansson & Laine, 2012). If an external force *F* is less than the capacity R_m of a structure, then the deformation will be zero. If the external force on the other hand reaches the maximum internal resistance force, R_m, then the deformation becomes larger than zero and is irreversible. The behaviour is described by Equation (2.3) and Figure 2.3.

$$R(u) = \begin{cases} F \; if \; u = 0 \\ R_m \; if \; u > 0 \end{cases} \tag{2.3}$$

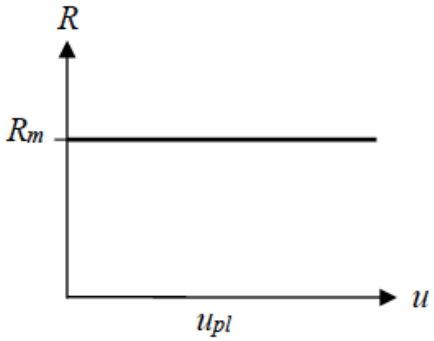

Figure 2.3 Relationship between the internal resistance R and the plastic deformation u_{pl} (Jönsson & Stenseke, 2018).

2.3 Elasto-Plastic Response

The third response described is a combination of the two previous ones. The elasto-plastic response describes the behaviour up to a certain point as elastic, with a stiffness *k*, but when the maximum internal resistance force is exceeded, the response is plastic with irreversible plastic deformations (Johansson & Laine, 2012). When the load is

removed the response is elastic and the total deformation consists of plastic and elastic deformation. This response is illustrated in Figure 2.4.

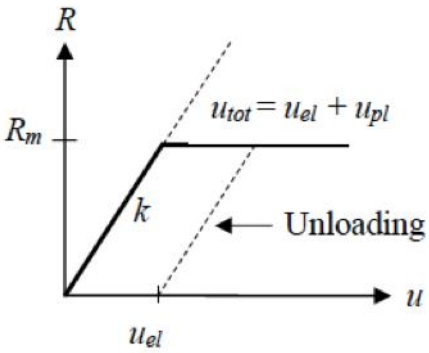

Figure 2.4 Relation between internal resistance R and the deformation (Jönsson & Stenseke, 2018).

For the elasto-plastic response, the relation between internal resistance force and displacement can be described as

$$R(u) = \begin{cases} k \cdot u_{el} & if\ u \leq u_{el} \\ R_m & if\ u > u_{el} \end{cases} \tag{2.4}$$

2.4 Tri-Linear Response

Another way of describing structural response is by tri-linear response, which in case of studying concrete could be more accurate than the linear-elastic, plastic and elasto-plastic models (Jönsson & Stenseke, 2018). The first two parts of the response has different stiffness, which one can relate to the behaviour of concrete with uncracked state and the state when the first crack appears. The relation between internal resistance force and displacement can be described as

$$R(u) = \begin{cases} k \cdot u & if \quad u \leq u_{cr} \\ R_{cr} + k'(u - u_{cr}) & if\ u_{cr} \leq u \leq u_{pl} \\ R_m & if \quad u_{pl} < u \end{cases} \tag{2.5}$$

The tri-linear response is illustrated in Figure 2.5 with the three different stages.

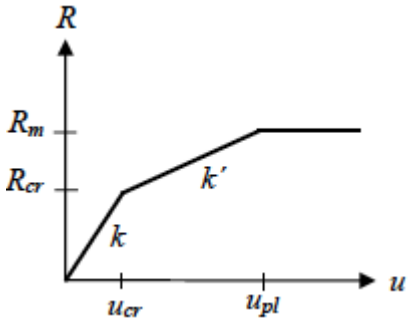

Figure 2.5 Relation between internal resistance R and the deformation for tri-linear response (Jönsson & Stenseke, 2018).

2.5 Ductile and Brittle Response

A common way to describe the response of a material or a structure is to depict is as brittle or ductile, and if the failure of a material or a structure will be a brittle or ductile failure. A brittle failure is characterized by no or small plastic deformations before failure and a sudden collapse (Domone & Illston, 2010). Ductile behaviour is characterized by large plastic deformations before failure. Domone and Illston (2010) state that in very broad terms, strains larger than 1% are common for structures with ductile failure before collapse. But the strain value for ductile response is also depending on the situation so for another situation might not strains larger than 1% be enough to represent a ductile behaviour. In Figure 2.6 is the typical response of ductile and brittle structures illustrated.

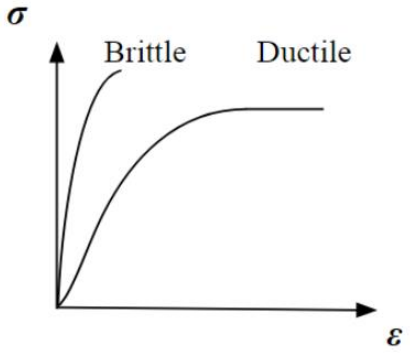

Figure 2.6 Typical stress-strain relation for brittle and ductile response (Nigani & Nordström, 2020).

A ductile response of a structure is often sought, particularly for a construction exposed to an explosion load (Johansson & Laine, 2012). To be able to effectively handle the large amount of energy released in an explosion the structure needs to have the ability to redistribute forces (Johansson & Laine, 2012). One thing that is worth to keep in mind is that the rate of the loading also affects the behaviour of the material. A fast loading could make a material act brittle, although it usually behaves ductile (Domone & Illston, 2010).

3 Materials

The materials used in this work were concrete, reinforcing steel, reinforced concrete and Fibre Reinforced Polymer. Their behaviour and properties are briefly presented in this chapter.

3.1 Concrete

Concrete is a composite material that conventionally consists of cement, sand, aggregate and water (Al-Emrani et al., 2013). It is characterized by its highly different behaviour in compression compared to tension. The compression strength exceeds the tensile strength with normally 10 times higher strength in compression (Al-Emrani et al., 2013).

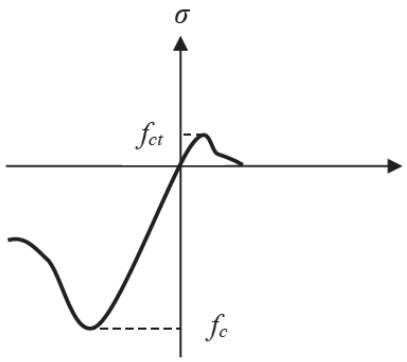

Figure 3.1 Schematic illustration of stress-strain relation for concrete under uniaxial loading where f_c and f_{ct} corresponds to compressive and tensile concrete strength respectively (Jönsson & Stenseke, 2018).

3.1.1 Compressive Strength for Concrete

The compressive strength for concrete is decided by testing of either cylindrical or cube specimen after 28 days according to the standards (CEN, 2005). The test consists of compression being applied in a controlled manner where the stress is registered together with the compressive strain (Al-Emrani et al., 2013). This forms a stress-strain relationship illustrated in Figure 3.2.

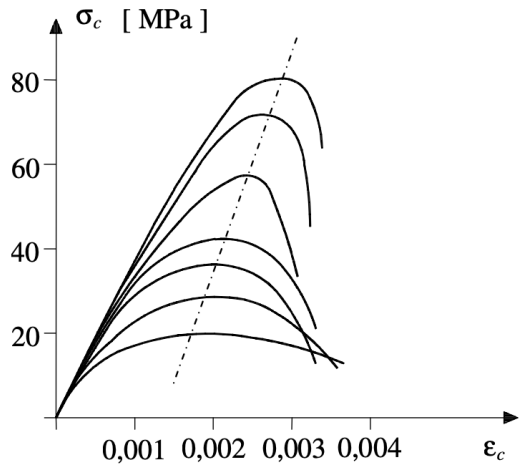

Figure 3.2 Stress-strain relation for concrete with different strengths subjected to compression. From (Al-Emrani et al.,2013).

Figure 3.2 shows that concrete with lower compressive strength experiences a more ductile failure mode compared to concrete with higher compressive strength that behaves more brittle at failure. This is seen as the lower strength concrete can withstand larger deformations after the peak strength is reached. Another aspect that influences the strength and behaviour of concrete is the loading rate. The behaviour of concrete subjected to varying loading rates are illustrated in Figure 3.3. This phenomenon is treated more in Section 3.5.

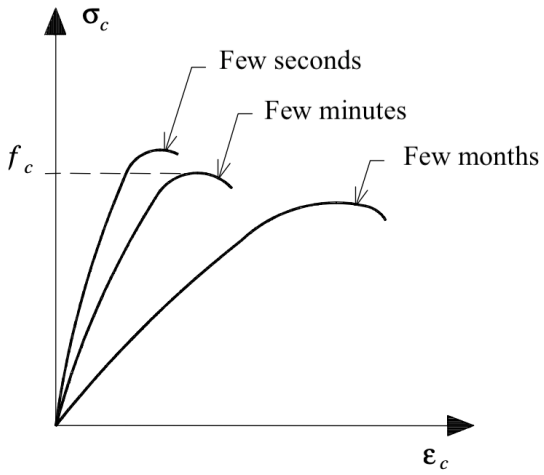

Figure 3.3 Compressive strength of concrete varying with loading rate. From (Al-Emrani et al.,2013).

The testing of concrete in compression are with cylindrical specimen as reference and therefore if cube specimen is used, which is normally used in Sweden, the compressive strength needs to be calculated according to

$$f_{cm} \approx \frac{f_{cm,cube}}{1.2} \tag{3.1}$$

where f_{cm} = mean compressive strength for cylinders
$f_{cm,cube}$ = mean compressive strength for cubes

The reason that the cubic specimen has a higher compressive strength compared to the cylindrical specimen is that when the compression is applied, confinement effects, that are beneficial for the specimen, occur due to friction at the plates where the pressure is applied (Al-Emrani et al., 2013). However, the frictional effect decreases with increasing height and thus the cylindrical specimen has less of this effect in the mid region leading to a lower strength compared to the cubes (Al-Emrani et al., 2013).

3.1.2 Tensile Strength for Concrete

The tensile strength of concrete can be tested in various ways. It can be tested in pure tension, splitting or flexure test, where the test method used has an influence of the tensile strength. Splitting test give a higher strength value than a pure tensile test and the mean tensile strength can according to (CEN, 2005) be calculated with mean tensile strength from a splitting test as

$$f_{ctm} = 0.9 f_{ct,sp} \tag{3.2}$$

where f_{ctm} = mean tensile strength
$f_{ct,sp}$ = mean tensile strength from a splitting test

If a flexure test is used, then the flexural tensile strength can be calculated as

$$f_{ctm,fl} = \max\left\{\left(1.6 - \frac{h}{1000}\right) f_{ctm}, f_{ctm}\right\} \tag{3.3}$$

where h = height of the cross section [mm]
f_{ctm} = mean tensile strength

The mean tensile strength at 28 days can be calculated through the compressive strength (CEN, 2005).

$$f_{ctm} = 0.30(f_{ck})^{2/3} \text{ , for concrete class} \leq \text{C50/60} \tag{3.4}$$

$$f_{ctm} = 2.12 \ln\left(1 + \frac{f_{ck}+8}{10}\right) \text{ , for concrete class} > \text{C50/60} \tag{3.5}$$

where f_{ck} = characteristic compressive strength [MPa]

3.1.3 Modulus of Elasticity for Concrete

The modulus of elasticity can be calculated from the stress-strain relationship of concrete. Between σ_c = 0 and σ_c= 0.4f_{cm}, the secant modulus give approximate values of the mean values of the modulus of elasticity, E_{cm} (CEN, 2005). E_{cm} can according to (CEN, 2005) be approximatively calculated as

$$E_{cm} = 22\left(\frac{f_{cm}}{10}\right)^{0.5} \text{ [GPa]} \tag{3.6}$$

where f_{cm} = mean compressive strength [MPa]

The modulus of elasticity is highly dependent on the components used in the concrete and therefore it could be necessary to reduce or increase the value depending on what type of materials is used in the concrete mix.

3.2 Reinforcing Steel

Steel has similar behaviour both in tension and compression, but the interesting aspect is the tensile behaviour when combining it with concrete. Since concrete has very good properties in compression but very poor properties in tension, the reinforcement in form of reinforcing steel creates a great complement to the concrete to be able to handle tensile forces due to its great properties in tension.

The reinforcing steel can be created in different ways, either plain, intended or ribbed bars (Al-Emrani et al., 2013). The main difference between these sorts of bars is the bonding between the reinforcing steel and the concrete which becomes larger due to the friction. Another aspect of the reinforcing steel that can differ is the production method. According to Al-Emrani et al. (2013) there are three different kinds of reinforcing steel: hot rolled, heat treated and cold worked where, hot rolled and cold worked steel will be described further. In Figure 3.4 the typical behaviour of hot rolled and cold worked steel is described.

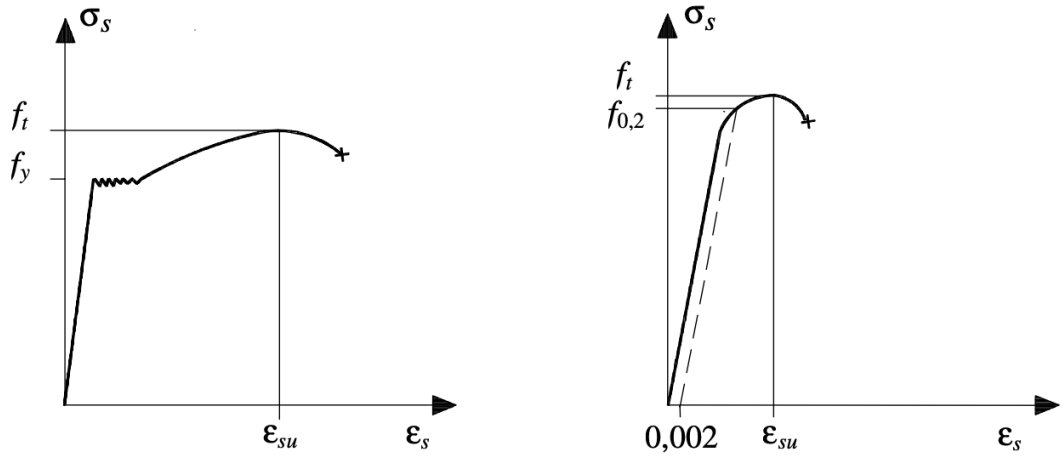

Figure 3.4 Stress-strain diagram for hot rolled or heat treated (left) and cold worked steel (right). From (Al-Emrani et al., 2013).

For hot rolled steel, four different stages can be recognized. The first stage is the linear elastic behaviour described with a line with constant slope. The steel act elastic up to the yield strength of the material where next part starts, the yield plateau. The plastic plateau is followed by a part with strain hardening where the stress increases until the last part where it decreases a bit before rupture. When studying cold worked steel, three different stages can be recognized. One elastic part, like the hot rolled steel followed by a stage with strain hardening up to maximum load and then the last stage with decreased load until failure when the bar ruptures (Al-Emrani et al., 2013). As seen in Figure 3.4 the strain at failure of the bar is much larger for hot rolled steel compared to cold worked steel, which can be described with ductile and brittle behaviour where ductile behaviour is preferred for an impulse loaded structure in particular (Johansson & Laine, 2012).

Reinforcing steel is sorted into different categories depending on several properties such as e.g. strength, weldability, ductility class and fatigue strength. For impulse loaded structures, the ductile behaviour is of high interest and the hardening ratio could express the ductility properties of the steel. The hardening ratio is a ratio between the tensile strength and the yield strength of the steel and can be calculated as

$$k = \left(\frac{f_t}{f_y}\right) \tag{3.7}$$

The reinforcing steel can be sorted into classes depending on the hardening ratio and the characteristic strain at ultimate stress and these classes are summarized in Table 3.1. For a reinforced concrete structure, the ultimate strain and the hardening ratio is two important parameters.

Table 3.1 Ductility classes for reinforcing steel (Al-Emrani et al., 2013).

Class	**A**	**B**	**C**
$\left(f_t/f_y\right)_k$	≥ 1.05	≥ 1.08	≥ 1.15 < 1.35
ε_{suk}	≥ 0.025	≥ 0.050	≥ 0.075

3.3 Reinforced Concrete

Reinforced concrete is a composite material consisting of concrete and reinforcing steel which utilizes each material's advantage where the concrete works well in compression while the reinforcement is suitable for taking tensile stresses and are therefore placed where tensile stresses are expected. Depending on reinforcement configuration and reinforcement class used, different degree of ductile response may also be obtained.

The response of a reinforced structure can be divided into three stages, denoted as state I, state II and state III. In state I, the structure is uncracked and the response is linear elastic. As a simplification, the reinforcement is often neglected and only the concrete properties are used to determine the stiffness of the structure. However, even though the influence of reinforcement is often seen as small in the uncracked state, reinforcing steel can give an increase to the stiffness of more than 20 % (Engström, 2015).

With increasing load one section will eventually crack which results in a drop in stiffness in that section. In the cracked section, only the concrete in the compressive zone, as well as the reinforcement, contributes in carrying the load. Hence, the reinforcement will have a large influence of the response of a cracked section (Engström, 2015). When cracking has initiated the beam is referred to as state II.

The cracks take place at a certain distance from each other, resulting in uncracked concrete between the cracks that contribute to the load carrying capacity. Therefore, the state II model is an underestimation of the real response (Engström, 2015). This effect is denoted as tensioning stiffening, where high stresses in the reinforcement in the

cracked sections are transferred to nearby concrete. However, the tensioning stiffening effect decrease with increasing load.

If either one, or both, of the materials experience a non-linear response then the reinforced concrete is regarded to be state III (Al-Emrani et al., 2013). From this point the load can be increased even further until the ultimate capacity is reached and from here the structure can either experience a brittle or ductile behaviour. The response of a reinforced concrete member in its different stages is illustrated in Figure 3.5.

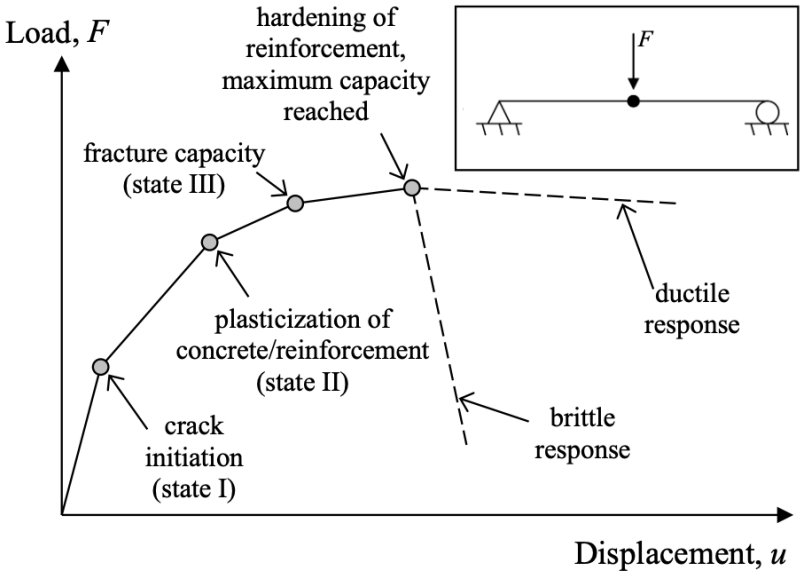

Figure 3.5 *Schematic illustration showing the response of reinforced concrete beam in its different states with either a brittle or a ductile failure. Modified from (Johansson & Laine, 2012).*

As an approximation, the relationship in Figure 3.5 can be simplified to a bi-linear elasto-plastic relationship similar to that shown in Figure 2.4. Here, the stiffness of a fully cracked, state II, member describes the elastic behaviour up to the ultimate capacity in state III, from where it afterwards has an ideally plastic response (Johansson & Laine, 2012). This simplification neglects the influence of the uncracked response in state I; i.e. assumes a fully cracked member from the start of loading, as well as not considering a strain hardening effect in state III. This schematically is illustrated in Figure 3.6.

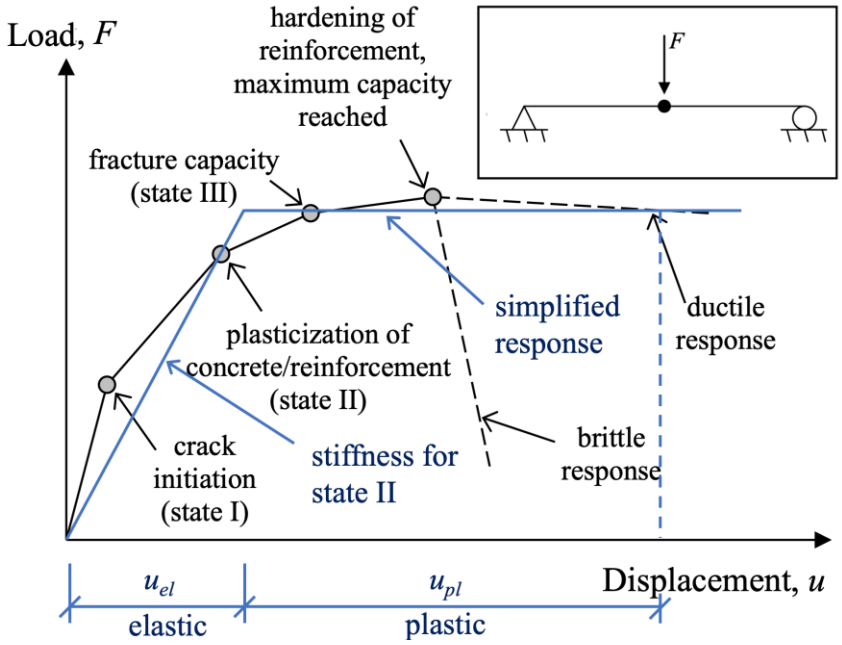

Figure 3.6 *Schematic illustration showing bi-linear elasto-plastic response of a reinforced concrete beam. Modified from (Johansson & Laine, 2012).*

3.4 Fibre reinforced polymer – FRP

Fibre Reinforced Polymer (FRP) is a composite material that consists of fibres and a polymeric matrix (Nordin, 2003). The fibres serve as the load carrying component while the matrix acts as a binder for the fibres as well as giving protection and transferring load between fibres (Wu & Eamon, 2017).

There are different kinds of fibre reinforced polymers where the most common ones used in civil engineering are Carbon Fibre Reinforced Polymer (CFRP), Aramid Fibre Reinforced polymer (AFRP) and Glass Fibre Reinforced Polymer (GFRP) (Nordin, 2003). However, there are also other types of FRP; e.g. Basalt Fibre Reinforced Polymers (BFRP) manufactured from volcanic basalt rocks that also can be used. BFRP has been deemed a potential substitute for CFRP. The matrix consists usually of either polyester, ester, epoxy or vinyl (Wu & Eamon, 2017).

FRP is a material that is anisotropic, meaning it has varying properties in different directions, resulting in that FRP is strong in the fibre direction but weak in the orthogonal directions (Wu & Eamon, 2017). FRP shows good properties in tension but are weak in compression and is therefore well suited for strengthening concrete structures where tensile stresses might occur (Nordin, 2003). The fibres can be modified by making the orientation of the fibres in such a way that the FRP has the desired properties. Fibre orientation, together with fibre amount and constituent materials, are the parameters that decides the mechanical properties of FRP (Nordin, 2003). FRP is explained further and more extensively in Chapter 7.

3.5 Strain Rate Effects

The loading rate of a material has an influence on its mechanical properties. The dynamic increase factor or the DIF is a factor describing how the properties change with varying strain rates. DIF is the ratio between the dynamic strength and the static strength. Increased strain rates can result in increased material strength (Johansson, 2000).

$$DIF = \frac{F_{dyn}}{F_{sta}} \tag{3.8}$$

where F_{dyn} = dynamic strength
F_{sta} = static strength

The strain rates vary with type of loading applied. Figure 3.7 illustrates what loading rates that corresponds with a certain loading condition where hard impact and static with strain rates 10^{-5} and 10^{0}-10^{1} respectively are of interest in this thesis. This chapter will show how the strain rate effect affects concrete, reinforcing steel and FRP.

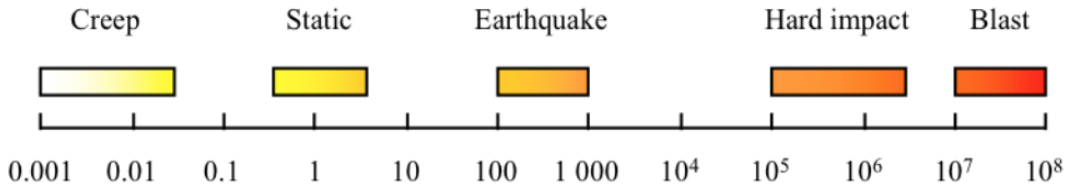

Figure 3.7 Schematic illustration of strain rates in relation to various types of loading (Johansson & Laine, 2012).

3.5.1 Strain Rate for Concrete

The strain rate effect for concrete differs between studies showing data of scatter characteristics. Researchers in these studies has tried to explain how the concrete strength increases with increasing strain rates but they differ both in results in graphs, how the expression is formulated as well as what properties influence the strain rates (Johansson, 2000). What is similar in all these studies however is the fact that the concrete strength increases with increasing strain rate.

Different studies indicate that different properties or parameters affects the expressions on how the concrete strength is influenced by high strain rate. These are for example static compressive strength, if the concrete is wet or dry or fracture toughness among others. Johansson (2000) treats examples of such studies in further detail, but the important aspect is that concrete strength increases with strain rates. How the dynamic increase factor varies with varying strain rates are shown in Figure 3.8 and Figure 3.9 showing concrete in compression and tension respectively.

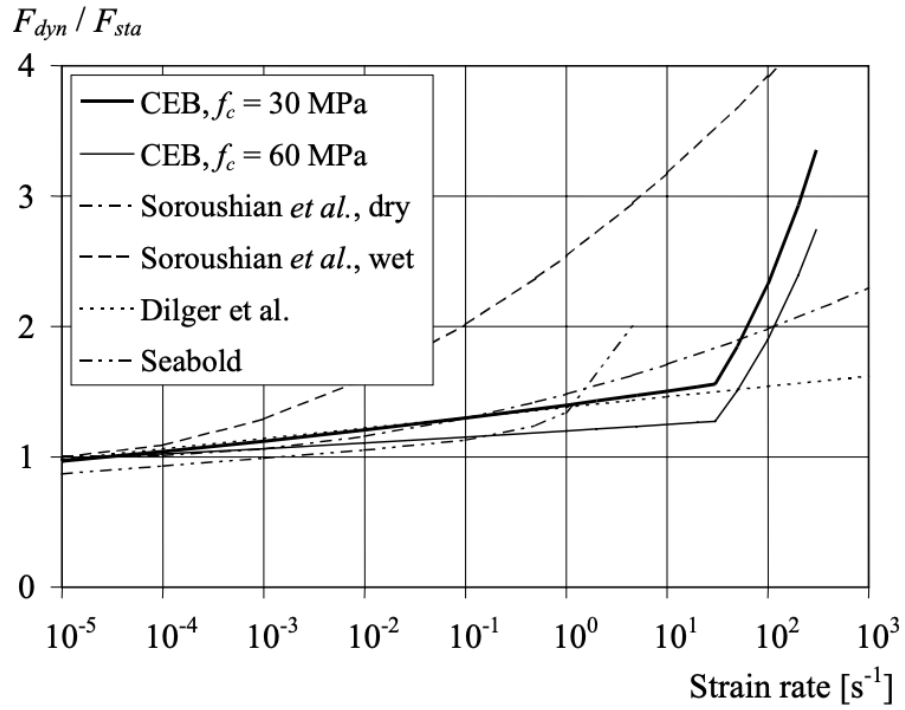

Figure 3.8 *Dynamic increase factor versus strain rate for compressive strength of concrete based on different studies (Johansson, 2000).*

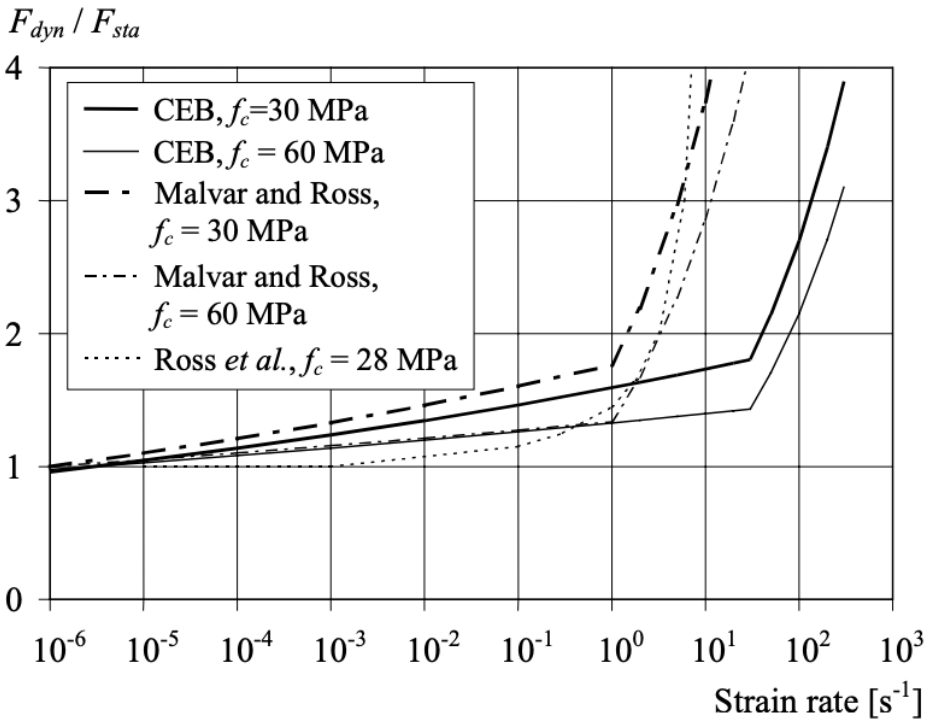

Figure 3.9 *Dynamic increase factor versus strain rate for tensile strength of concrete based on different studies (Johansson, 2000).*

In Figure 3.8 and Figure 3.9 it can be seen that at a certain strain rate the concrete strength increases at a certain rate until a specific point where the strength increases

drastically. This is referred to as the transition zone and these clear distinctions in behaviour is due to viscous and structural effects (Johansson, 2000).

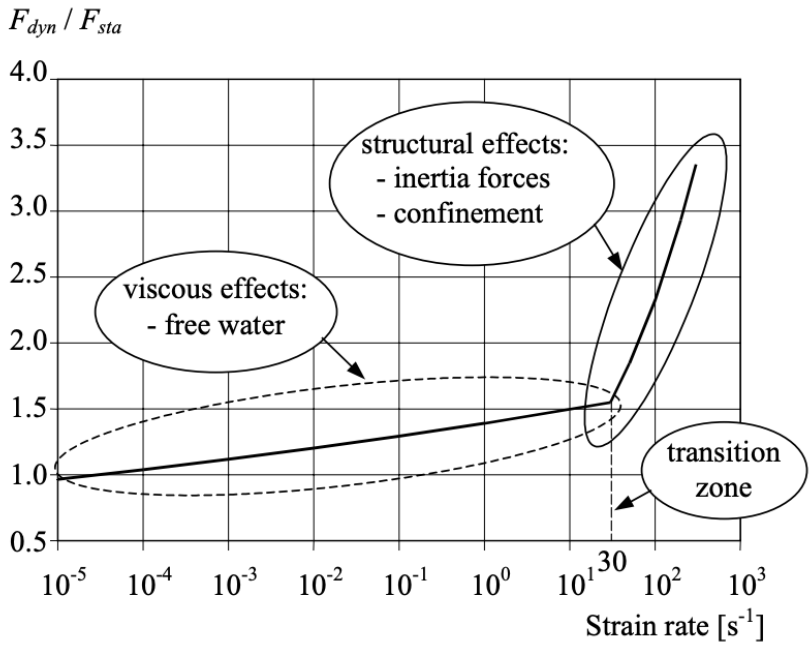

Figure 3.10 Schematic illustration of at which strain rates the viscous and structural effects are occurring (Johansson, 2000).

The viscous effects are because of free water in concrete micropores. Johansson (2000) refers to different studies discussing the viscous effects. Some of the studies name the free water in micropores as what makes the concrete more sensitive to high strain rates than dry concrete resulting in increased strength. What makes the wet concrete more sensitive to high strain rates is the phenomenon of changed crack propagation (Johansson, 2000). The phenomenon can be explained by when a load is applied fast a higher level of energy, compared to a statically loaded structure, needs to be absorbed fast. This results in that cracks that do not have time to develop through the weakest parts of the concrete; instead cracks develop through stronger zones, such as aggregates, instead resulting in a higher concrete strength (Johansson, 2000).

At the transition zone, where the strength starts to increase very rapidly at a critical strain rate, the structural effects are more dominant. The structural effects are inertia effects and inertia confinement. Johansson (2000) refers to two studies where concrete in tension at the transition zone experiences inertia forces a change in stress and energy distribution. The inertia effects are around the corner tips. For concrete in compression the structural effect is inertia confinement. Inertia confinement occurs when concrete is loaded fast enough and the material has not time to react so the structure behaves as if it were restricted to move which results in higher strength (Johansson, 2000).

3.5.2 Strain Rate for Reinforcing Steel

Strain rate is a phenomenon for reinforcing steel as well. There are several properties of reinforcing steel that are affected by an increased strain rate. Both the yield stress and the ultimate stress increase with an increasing strain rate (Johansson, 2000). The

dynamic increase factor-strain rate relationship for reinforcing steel is shown in Figure 3.11.

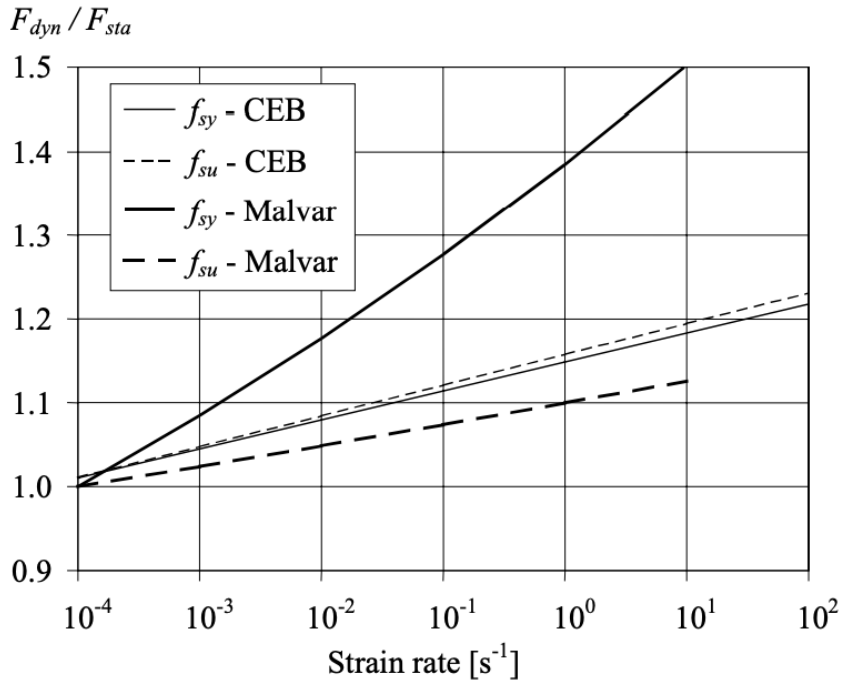

Figure 3.11 Dynamic increase factor versus strain rate for reinforcing steel based on different studies (Johansson, 2000).

The level of increased strength for the reinforcing steel varies both between studies and what material property that is investigated. It is also worth noticing from the studies treated by Johansson (2000) that the ultimate strain is said to be unaffected by strain rate in one study while others claims that the ultimate strain also increases with increasing strain rates.

3.5.3 Strain Rate for FRP

The strain rate effect has an influence on the properties of FRP. The tensile properties of FRP are increased with increasing strain rate (Pham & Hao, 2016a). There are several studies which are presented in (Pham & Hao, 2016a) where a critical strain rate is reached and the dynamic increase factor suddenly increases with increased strain rate; i.e. similar to the behaviour of strain rate effect for concrete described in Section 3.5.1. The critical strain rate varies but the behaviour is the same, which is an increasing strength of tensile properties.

4 Plastic Rotation Capacity

One way to describe the ability of a structure to deform is by plastic rotation capacity (Johansson & Laine, 2012). The plastic rotation capacity could be one way to determine if the structure acts ductile or brittle and to describe its ability to absorb energy. In many cases, a large plastic rotation and a ductile failure is also connected to the amount of energy absorbed by the structure, but this is not always true which is important to emphasize. If a structure is very stiff, it might not experience large deformations although it absorbs a large amount of energy. In such a situation, plastic rotation might not be a suitable method to alone estimate the energy absorption (Johansson, personal communication, 13 April, 2021). Two important aspects affecting the plastic rotation and a ductile failure are the ultimate steel strain and the hardening ratio which are presented in Table 3.1 in Section 3.2.

4.1 Definition of Plastic Rotation

There are two ways to look at plastic rotation in reinforced concrete, one where a certain section is studied and one where a region in a structure is studied. If one certain section is studied, a plastic hinge is assumed to take place in this section. To define the plastic rotation, the need of rotation of a specific hinge is studied (Engström, 2015). When first yielding takes place and load increases, the hinge will continue to rotate until collapse, and the rotation between these two states is the plastic rotation.

If instead a region of a structure is studied, concepts as curvature and plastic region are used. This way is more realistic and corresponds to a region where the steel strain is larger than the yield strain of the steel, not just in a certain section, but over a length l_{pl} (Engström, 2015). The plastic rotation is now obtained by integrating the plastic curvature of all sections over the length of the studied region. Figure 4.1 illustrates the curvature, relation between curvature and moment, relation between rotation and moment and curvature and plastic rotation.

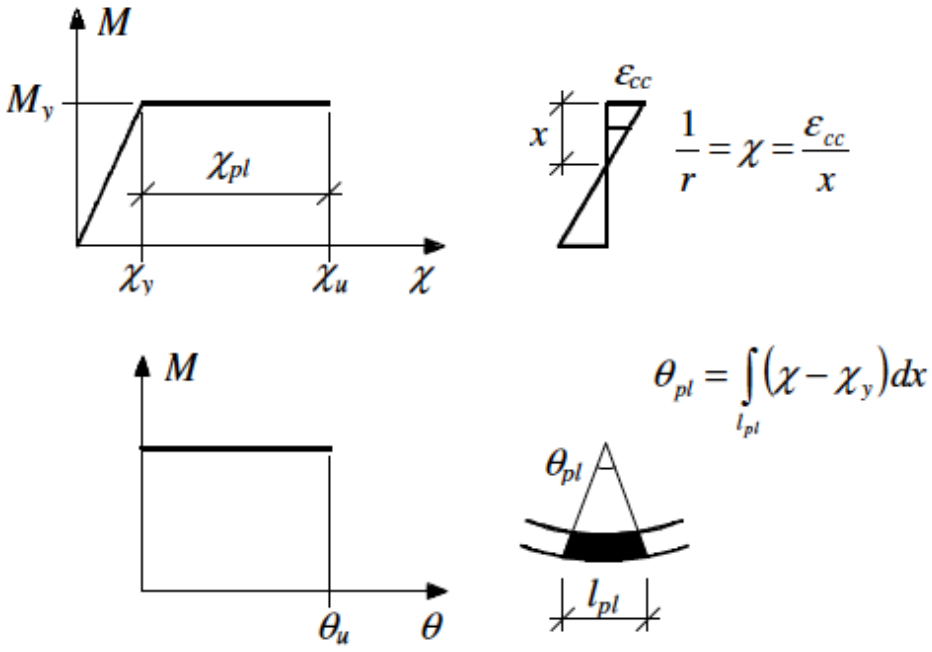

Figure 4.1 *Illustration of relation between curvature and moment, curvature definition, relation between rotation and moment and plastic rotation (Engström, 2015).*

When the plastic rotation is calculated there are different possible cases for the ultimate curvature. Since the ductile behaviour of a structure often is sought the normal case is that the concrete determines the ultimate curvature (Engström, 2015). However, the opposite case cannot be neglected, the structure could be designed with low ductility steel or low steel ratios which leads to an ultimate curvature distinguished by the steel instead. According to Engström (2015), the curvature when yielding starts can be determined as

$$\left(\frac{1}{r}\right)_y = \frac{\varepsilon_{cy}}{x_y} = \frac{\varepsilon_{sy}}{d - x_y} \tag{4.1}$$

where ε_{cy} = concrete strain at the edge of the concrete when the reinforcement steel begins to yield
ε_{sy} = strain of the tensile reinforcement when it begins to yield
x_y = depth of the compressive zone at the time the reinforcement begins to yield

Depending on if the steel or concrete is determining the ultimate curvature it is calculated in two different ways. It is determined with Equation (4.2) or (4.3), depending on the crucial strain capacity, either concrete or steel.

$$\left(\frac{1}{r}\right)_u = \frac{\varepsilon_{cu}}{x_u} = \frac{\varepsilon_s}{d - x_u} \tag{4.2}$$

where ε_{cu} = the ultimate strain in the concrete at the edge on the compression side

ε_s = strain of the steel in the ultimate limit state
x_u = depth of the compressive zone at the time when ultimate limit state is reached

$$\left(\frac{1}{r}\right)_u = \frac{\varepsilon_{cc}}{x_u} = \frac{\varepsilon_{sud}}{d - x_u} \tag{4.3}$$

where ε_{cc} = the ultimate strain in the concrete at the edge on the compression side when the ultimate strain in the reinforcement is reached
ε_{sud} = the design value of the ultimate strain of the reinforcement

With the yielding curvature and the ultimate curvature known the plastic rotation can be determined as

$$\theta_{pl} = \int_{l_{pl}} (\chi_u - \chi_y) dx \tag{4.4}$$

where l_{pl} = length of plastic region
χ_u = ultimate curvature
χ_y = yielding curvature

4.2 Methods to Predict Plastic Rotation Capacity

To be sure that an impulse loaded structure has the ability to withstand large plastic deformations, the plastic rotation capacity could be one way to predict the resistance. If the plastic rotation capacity is large enough, this could be proof of sufficient ductility, at least for regular reinforced concrete structures. One way to predict the plastic rotation capacity of a structure is to follow the procedure proposed in Eurocode 2 (CEN, 2005), another one is the ABC-method in Betonghandbok (1990), a third one is BK25 (Fortifikationsförvaltningen, 1973) and these three are based on static loading (Johansson & Laine, 2012). The different methods described in Section 4.2.1 to 4.2.3 do not use the same definition of rotation angle. The angle illustrated in Figure 4.4 is valid for BK25 and ABC-method but the angle referred to in Eurocode is twice as large which needs to be considered when comparing the different methods.

4.2.1 Eurocode

When Eurocode 2 is considered, a simplified method is presented to predict the plastic rotation capacity in form of a design value from a graph depending on several aspects (CEN, 2005). This method is based on a model with a simply supported beam subjected to a point load in the middle of the span (Johansson et al., 2021).The rotation capacity in Figure 4.2 depends on which steel class that is used in the structure, the strength of the concrete in form of concrete class and the ratio between the height of the compressive zone, *x* in ultimate limit state and the effective depth, *d* of the reinforcement (Engström, 2015).

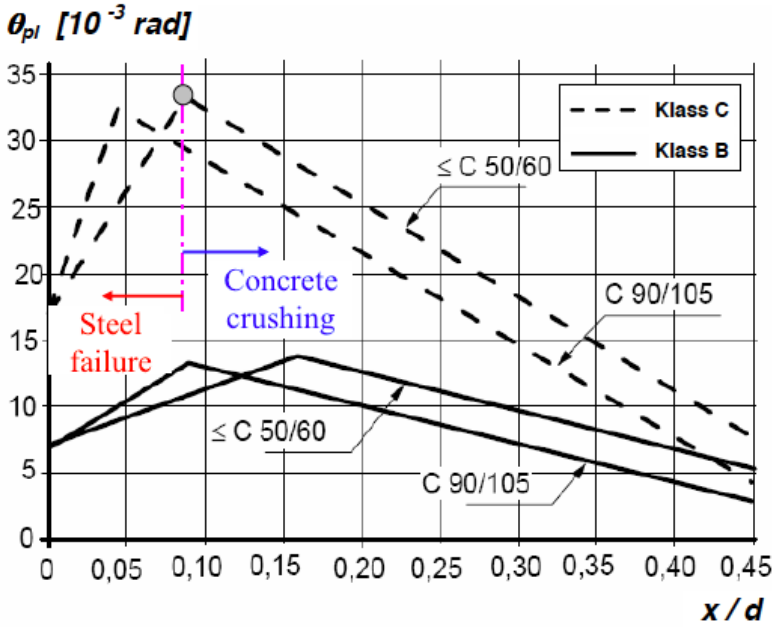

Figure 4.2 *Diagram representing the design value of the plastic rotation capacity (Modified from Johansson & Laine, 2012).*

This diagram provides a simplified method to easy estimate the rotation capacity of a structure and it is conservative since it takes model uncertainties into consideration, but the shear slenderness although needs to be considered by multiplying the rotation capacity with a factor if the shear slenderness is not equal to 3 (Engström, 2015). The factor is calculated as

$$k_\lambda = \sqrt{\frac{\lambda}{3}} \tag{4.5}$$

where $\lambda = \frac{l_0}{d}$ (shear slenderness)

$l_0 =$ distance between the considered maximum moment section and the adjacent zero moment section after plastic redistribution, i.e. the final moment distribution

$d =$ effective depth

4.2.2 ABC-method

ABC-method is a way of predicting the rotation capacity according to Betonghandbok (1990). This method was used in Sweden before Eurocode 2. The principle of the method, here called ABC-method, is that three factors (A, B and C) are taking different aspects into consideration and are then multiplied with each other (Johansson & Laine, 2012).

The plastic rotation capacity is calculated as

$$\theta_{pl} = A \cdot B \cdot C \cdot 10^{-3} \tag{4.6}$$

Factor A is calculated as

$$A = 1 + 0.6 \cdot \omega_v + 1.7 \cdot \omega_s' - 1.4 \cdot \frac{\omega_s}{\omega_{bal}} \tag{4.7}$$

where ω_v, ω_s' and ω_s are calculated with Equations (4.8), (4.9), (4.10) respectively.

$$\omega_v = \frac{A_v}{bs} \cdot \frac{f_{sv}}{f_{ct}} \tag{4.8}$$

$$\omega_s' = \frac{A_s'}{bd} \cdot \frac{f_{sc}}{f_{cc}} \tag{4.9}$$

$$\omega_s = \frac{A_s}{bd} \cdot \frac{f_{st}}{f_{cc}} \tag{4.10}$$

where A_v = area of shear reinforcement
A_s' = area of reinforcement in compression
A_s = area of reinforcement in tension
f_{sv} = strength of shear reinforcement
f_{sc} = strength of reinforcement in compression
f_{st} = strength of reinforcement in tension
f_{ct} = tensile strength of the concrete
f_{cc} = compression strength of the concrete
b = width of the compression zone of the cross-section
d = effective depth of the cross-section
s = distance between each stirrup

$$\omega_{bal} = \frac{0.8 \cdot \varepsilon_{cu}}{\varepsilon_{cu} + \varepsilon_{sy}} \tag{4.11}$$

where ε_{cu} =the ultimate strain in the concrete at the edge on the compression side
ε_{sy} is calculated with Equation (4.12)

$$\varepsilon_{sy} = \frac{f_{st}}{E_s} \tag{4.12}$$

where E_s = Young's modulus of the reinforcement steel

The aspects taken into account by A is the influence of shear reinforcement, tensile reinforcement and compression reinforcement. Factor B considers the mechanical properties of the reinforcement and is taken from Table 4.1.

Table 4.1 Values of factor B (Johansson & Laine, 2012).

Reinforcement type	B	Max A·B
Ks 60, Ks 40, Ss 26, Ss 26S	1.0	1.7
Ks 60S, Ks 40S[1]	0.8	1.1
Cold worked steel with $\varepsilon_{su} \geq 3\%$ and $f_{su}/f_{sy(0.2)} \geq 1.1$	$0.6 \cdot \left(1 - 0.7\frac{\varepsilon_p}{\varepsilon_{su}}\right)$	0.5

The last factor, C, depends on where the yielding strain is exceeded i.e., where the plastic hinge occurs, either in the span or in the support (Johansson & Laine, 2012). Depending on the location of the plastic hinge, factor C is calculated with either Equation (4.13) or (4.14).

$$C_{support} = 10 \cdot \frac{l_{0,support}}{d} \tag{4.13}$$

$$C_{field} = 7 \cdot \frac{l_{0,field}}{d} \tag{4.14}$$

where $l_{0,support}$ = distance from zero-moment section to the plastic hinge at the support
$l_{0,field}$ = distance from zero-moment section to the plastic hinge in the span

Figure 4.3 illustrates the distances together with the plastic hinges.

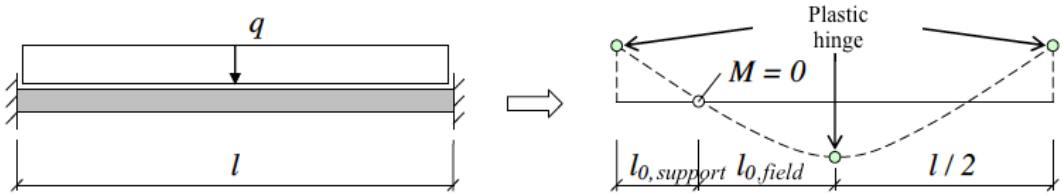

Figure 4.3 Illustration of the distances from zero-moment sections to the plastic hinges (Modified from Johansson & Laine, 2012).

4.2.3 BK25

The method in BK25, Fortifikationsförvaltningen (1973), is suitable for predicting the plastic rotation capacity for a concrete beam or a concrete slab (Johansson & Laine, 2012). BK25 is as a method based on a uniformly distributed load with the corresponding rotation in the middle of the span. The method is here described for a simply supported beam subjected to impact loading with some changes made by Johansson and Laine (2012) but is based on static tests. In Figure 4.4 the model for this method is illustrated.

[1] If $f_{su}/f_{sy} \geq 1.4$ and $\varepsilon_{su} \geq 8\%$ is the values for Ks 60 and Ks 40 used.

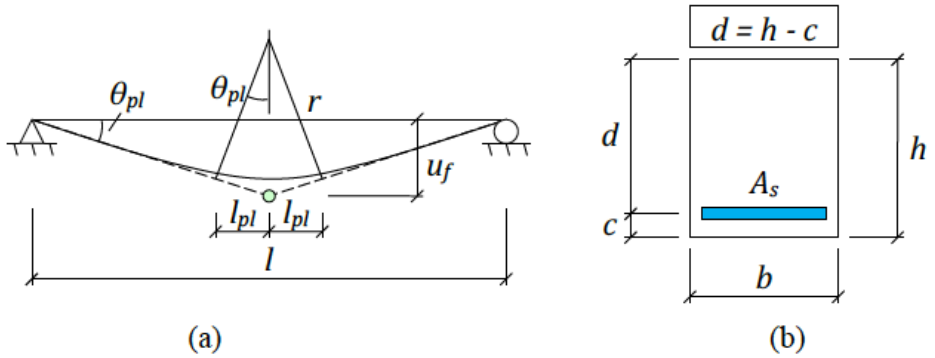

Figure 4.4 *Model for plastic rotation for a simply supported beam (Johansson & Laine, 2012).*

The model clearly illustrates the length of the region where the plastic hinge is supposed to occur and along this length the curvature is assumed to be constant (Johansson & Laine, 2012). With this known the plastic rotation can be described as

$$\theta_{pl} = \frac{l_{pl}}{r} \tag{4.15}$$

where l_{pl} = length of the plastic hinge, calculated with Equation (4.16)
$\frac{1}{r}$ = curvature, calculated with Equation (4.17)

$$l_{pl} = 0.5 \cdot d + 0.15 \cdot l \tag{4.16}$$

$$\frac{1}{r} = \frac{\varepsilon_{cu}}{x} = \frac{\varepsilon_s}{d - x} \tag{4.17}$$

where ε_{cu} = ultimate strain in the concrete at the edge on the compression side
ε_s = mean steel strain over l_{pl}
x = height of the compression zone of the cross-section
d = effective depth

The ultimate capacity is determined either by crushing of the concrete or rupture of the tensile reinforcement. Strain-diagram and the corresponding forces acting on the cross-section is illustrated in Figure 4.5. The mean steel strain, ε_s was calculated as the ultimate steel strain multiplied with a factor 0.4 according to Johansson et al. (2021).

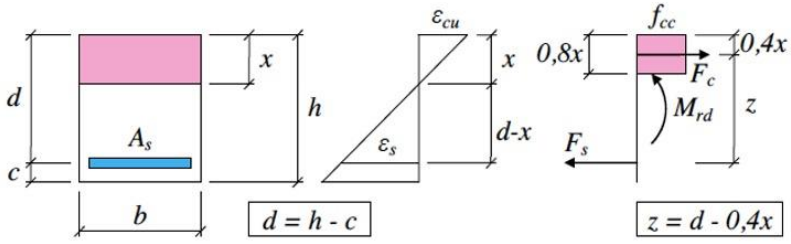

Figure 4.5 Cross-sectional analysis for a section of reinforced concrete subjected to a moment. Modified from (Johansson & Laine, 2012).

If Figure 4.5 is studied and horizontal force equilibrium is established, it results in

$$f_{cc} \cdot b \cdot 0.8x = A_s \cdot f_{st} \tag{4.18}$$

Equation (4.18) together with Equation (4.19), representing the reinforcement amount, and Equation (4.20), representing the mechanical reinforcement ratio gives a new expression for the height of the compression zone presented in Equation (4.21).

$$\rho = \frac{A_s}{bd} \tag{4.19}$$

$$\omega_s = \frac{A_s}{bd} \cdot \frac{f_{st}}{f_{cc}} \tag{4.20}$$

$$\frac{x}{d} = \frac{1}{0.8} \cdot \rho \cdot \frac{f_{st}}{f_{cc}} = \frac{\omega_s}{0.8} \tag{4.21}$$

With this known, the crucial failure mode can now be determined from Equation (4.22) representing the critical mechanical reinforcement ratio. Depending on whether the mechanical reinforcement ratio is greater or less than the critical one, the failure mode is concrete crushing or failure of the reinforcement.

$$\omega_{s,crit} = \frac{0.8 \cdot \varepsilon_{cu}}{\varepsilon_{cu} + \varepsilon_s} \tag{4.22}$$

When concrete crushing is the failure mode, i.e. $\omega_s > \omega_{s,crit}$, the plastic rotation can be calculated as

$$\theta_{pl} = \frac{l_{pl}}{r} = \frac{0.5d + 0.15l}{r} = \frac{0.8 \cdot \varepsilon_{cu}}{\omega_s \cdot d}(0.5d + 0.15l) = \frac{0.4 \cdot \varepsilon_{cu}}{\omega_s}\left(1 + 0.3\frac{l}{d}\right) \tag{4.23}$$

When the steel on the other hand is the crucial part and steel failure determines the failure mode, i.e. $\omega_s < \omega_{s,crit}$ the plastic rotation capacity can be calculated as

$$\theta_{pl} = \frac{l_{pl}}{r} = \frac{0.5d + 0.15l}{r} = \frac{0.8 \cdot \varepsilon_s}{d \cdot (0.8 - \omega_s)}(0.5d + 0.15l) = \frac{0.4 \cdot \varepsilon_s}{0.8 - \omega_s}\left(1 + 0.3\frac{l}{d}\right) \quad (4.24)$$

4.2.4 Plastic Rotation Capacity from experimental results

The actual rotation capacity can be evaluated from experimental results. Lozano and Makdesi (2017) describes a method to calculate the non-elastic rotation, the rotation capacity for a statically loaded structure. The method is based on experimental results from a load versus displacement curve and if a certain percentage of the ultimate load is studied, occurring after maximum load is reached, then the rotation capacity can be calculated with Equation (4.25). Figure 4.6 and Figure 4.7 schematically illustrate an example of such response and the elastic and plastic response for a simply supported beam respectively.

By assuming the angle at the support to be small, the plastic rotation at a certain percentage of the ultimate load can be calculated as

$$\theta_{pl,x\%} = \frac{u_{b,x\%} - u_{a,x\%}}{L_e} = \frac{u_{pl,x\%}}{L_e} \quad (4.25)$$

where L_e = length from support to plastic hinge

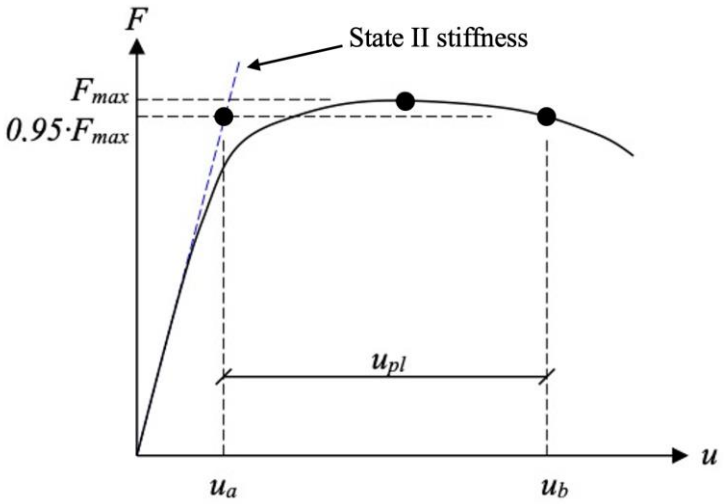

Figure 4.6 Example of load versus displacement curve with definition of rotation capacity at a level of 95% of maximum load. Modified from (Johansson & Laine, 2012).

The elastic displacement at a certain load level in Figure 4.6, in this case 95 %, is represented by u_a. At the same load level after the maximum load, the total displacement corresponding to this load is represented by u_b (Lozano & Makdesi, 2017).

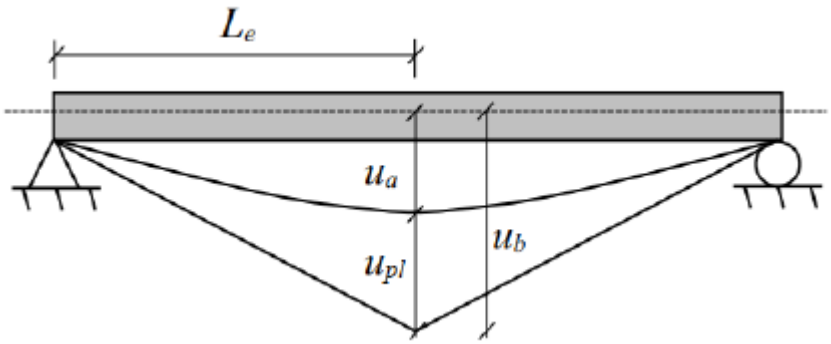

Figure 4.7 *Elastic and plastic response for a simply supported beam with the distance from support to the plastic hinge (Lozano & Makdesi, 2017).*

5 Introduction to Impulse Loading and Dynamics

Dynamic loading may be vastly different from static loading and this may have a large influence of the response of a structure and the behaviour of the load. Dynamic loading can be of different types and the extreme cases are either characteristic impulse loading or characteristic pressure loading. Characteristic impulse loading is best described as an infinitely high pressure during an infinitesimal duration. Characteristic pressure loading is a pressure load acting during an infinitely long duration (Johansson & Laine, 2012). These two extreme cases of dynamic loading are visualized in Figure 5.1.

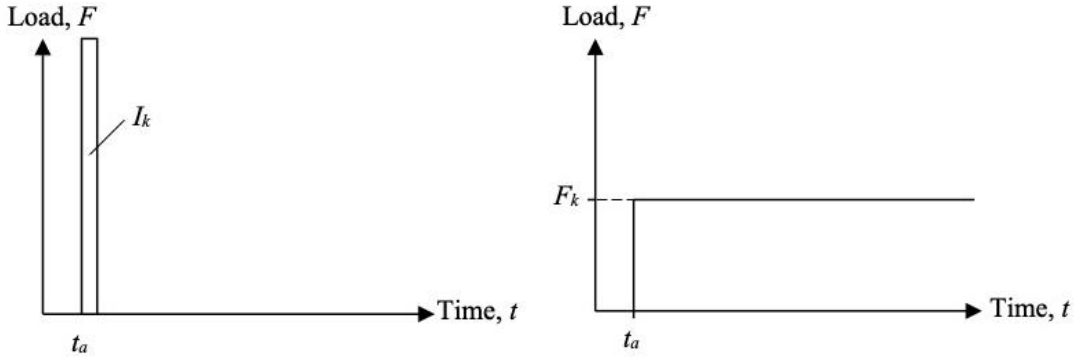

a) b)

Figure 5.1 Illustration of the two extremes of dynamic loading where a) is a characteristic impulse loading and b) is a characteristic pressure loading (Johansson & Laine, 2012)

The impulse load could for example be the blast coming from an explosion or from a collision of objects. In this work the drop weight impact shares most resemblance with a characteristic impulse load case, i.e. case a) in Figure 5.1, and is therefore also the case that is further treated in this report.

5.1 Impulse

The definition of an impulse is the change of momentum due to an external force during a certain time (Johansson & Laine, 2012). Momentum can be expressed as

$$p = m \cdot v \tag{5.1}$$

where m = mass [kg]
v = velocity [m/s]

The change of momentum from time t_0 to t_1 when an object has an initial velocity can be expressed as

$$m \cdot v_1 = m \cdot v_0 + \int_{t_0}^{t_1} F(t)dt \tag{5.2}$$

where $F(t)$ = is the external force [N]
v_0 = initial velocity [m/s]
v_1 = velocity after impulse [m/s]

The second term on the right-hand side is thus the change of momentum due to an external force and the impulse [Ns] is denoted as I.

$$I = \Delta p = \int_{t_0}^{t_1} F(t)dt \tag{5.3}$$

This subject is being treated more extensively by Johansson & Laine (2012) and the reader is directed there for a more detailed explanation.

5.2 Energy Equilibrium

The basis for a structure subjected to an impact load is to be able to withstand the different loadings it is exposed to. This is fulfilled with a capacity of the internal work larger than the external work (Johansson & Laine, 2012). In Figure 5.2, the external and internal work are illustrated as the area under the two graphs $F(u)$ and $R(u)$, respectively. When the area of the external work is equal to the area of the internal work the structure has reached equilibrium. With this known, together with the information gained in Sections 5.3 and 5.4 about external and internal work, the concept about equilibrium for impact loaded structures is established.

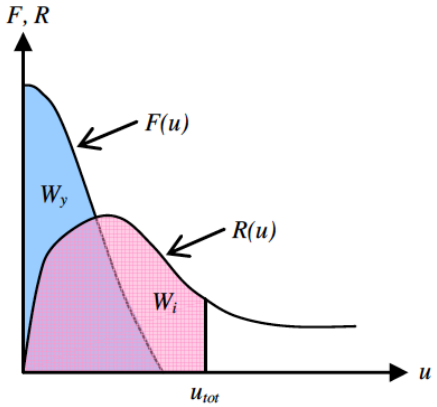

Figure 5.2 Energy equilibrium with the needed total deformation illustrated (Johansson & Laine, 2012).

5.3 External Work

For a structure subjected to a characteristic impulse load, the external work is equal to the structure's resulting kinetic energy, which can be written as

$$E_k = \frac{m \cdot v^2}{2} \tag{5.4}$$

Hence, the external work can accordingly be expressed as the change of kinetic energy according to

$$W_e = \Delta E_k = \frac{m \cdot v_1^2}{2} - \frac{m \cdot v_0^2}{2} \tag{5.5}$$

The kinetic energy can also be expressed as

$$E_k = \frac{I^2}{2m} \tag{5.6}$$

5.4 Internal Work

When a structure is exposed to an external load, the internal resistance is the component which acts as resisting part to be able to reach energy equilibrium and withstand the loading (Johansson & Laine, 2012). Depending on the material properties and the design of the structure, the response could be described by two significantly different cases; one with a stiff response and small deformations and one with a weak response with large deformations. These responses are schematically illustrated in Figure 5.3 where the area under the graph is the interesting part when impulse loaded structures are investigated (Johansson & Laine, 2012). The area under the graph is representing the internal work and the ability of a structure to absorb energy.

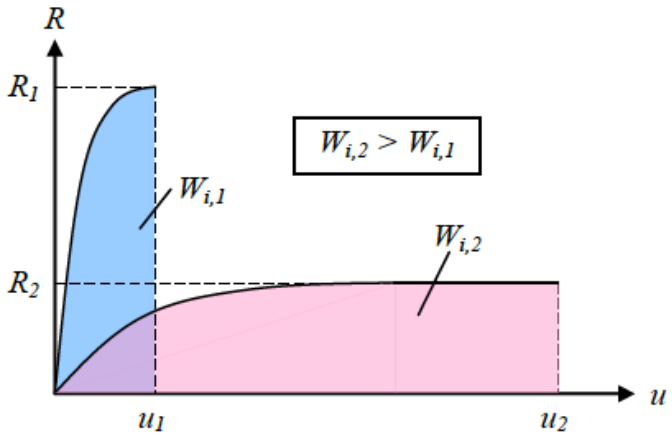

Figure 5.3 *Illustration of a comparison between the energy absorbed by a stiff structure and a ductile structure with lower stiffness (Johansson & Laine, 2012).*

There are different ways of idealizing the response of a structure and the internal work, they are of course theoretical approximations but show reasonable result. Three common ways to describe the response is elastic, plastic and elasto-plastic response which are further described in the following sections together with the description of how the internal work is calculated for the different responses. A fourth one, fitted to the response for FRP strengthened structures subjected to impulse loading based on earlier experiments is also described further in Section 5.4.4 (Nigani & Nordström, 2020; Ye Z, Zhao D, Sui L, Huang Z & Zhou X, 2020; Kishi N, Komuro M, Kawarai M & Mikamo H, 2020).

5.4.1 Elastic Response

Ideal elastic response is characterized by a constant stiffness and a resistance force directly proportional to the displacement and is illustrated in Figure 5.4.

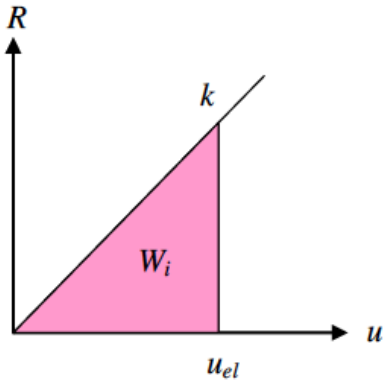

Figure 5.4 *Force versus displacement illustrated together with the internal work for elastic response (Johansson & Laine, 2012).*

The internal work for a structure with elastic response can be calculated with Equation (5.7) (Johansson & Laine, 2012).

$$W_i = \frac{k \cdot u_{el}^2}{2} \tag{5.7}$$

where k = constant stiffness [N/m]
u_{el} = elastic deformation [m]

The needed elastic deformation for a structure to be able to resist the external work can be calculated as

$$u_{el} = \frac{I}{\sqrt{k \cdot m}} \tag{5.8}$$

where I = impulse [Ns]
k = constant stiffness [N/m]
m = mass [kg]

5.4.2 Plastic Response

For plastic response, the internal work depends on a constant resistance force and the plastic deformation. To fulfil equilibrium, the internal work is dependent on the ability to achieve enough plastic deformation (Johansson & Laine, 2012). The response is illustrated in Figure 5.5.

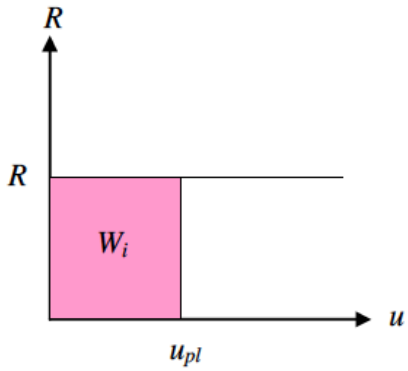

Figure 5.5 *Force versus displacement illustrated together with the internal work for plastic response (Johansson & Laine, 2012).*

The internal work can be calculated as

$$W_i = R \cdot u_{pl} \tag{5.9}$$

where R = resisting force [N]
u_{pl} = plastic deformation [m]

Plastic deformation required to fulfil equilibrium can be calculated as

$$u_{pl} = \frac{I^2}{2 \cdot m \cdot R} \tag{5.10}$$

where I = impulse [Ns]
m = mass [kg]
R = resisting force [N]

5.4.3 Elasto-Plastic Response

To possibly come closer to the real response, the elastic and plastic response can be combined to elasto-plastic response. Elasto-plastic response is characterized by a first part with elastic response followed by a part with plastic response. The response is illustrated in Figure 5.6.

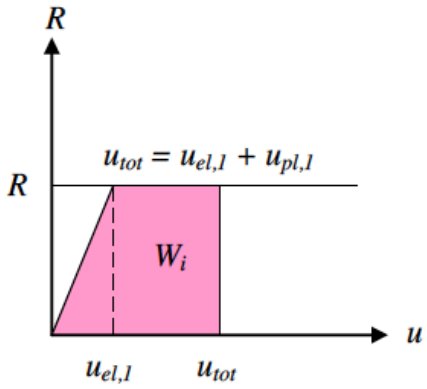

Figure 5.6 *Force versus displacement illustrated together with the internal work for elasto-plastic response (Johansson & Laine, 2012).*

When elasto-plastic response is considered there will be one elastic and one plastic part of the total deformation. The limit for elastic and plastic deformation can be calculated with Equation (5.11) and (5.12) respectively.

$$u_{el,1} = \frac{R}{k} \tag{5.11}$$

where R = resisting force [N]
k = stiffness [N/m]

$$u_{pl,1} = \frac{I^2}{2 \cdot m \cdot R} - \frac{u_{el,1}}{2} \tag{5.12}$$

where I = impulse [Ns]
m = mass [kg]
R = constant capacity [N]
$u_{el,1}$ = limit for the elastic deformation in elasto-plastic response [m]

Finally, the internal work with elasto-plastic response can be calculated as

$$W_i = \frac{R}{2}\left(u_{el,1} - 2u_{pl,1}\right) \tag{5.13}$$

5.4.4 Tri-Linear with Drop-Off

The fourth response is a modified response called tri-linear with drop-off. This response is a theoretical response based on previous experimental tests where results showed an elastic behaviour up to a certain limit where a large drop took place followed by a constant response until failure (Nigani & Nordström, 2020; Camata et al., 2006). Figure 5.7 illustrates the internal work for a structure with this response.

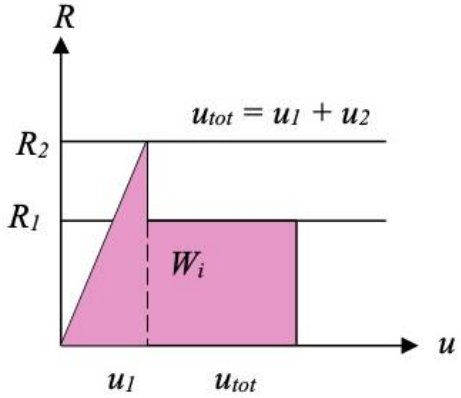

Figure 5.7 Force versus displacement illustrated together with the internal work for tri-linear with drop off response.

Tri-Linear with drop-off is not exactly equal to the real behaviour for FRP strengthened structures subjected to impact loading, it is a simplified response, but it is closer to the response observed in tests than the elastic, plastic or elasto-plastic response. This

response is similar to the one obtained in the experimental tests in this project, see Section 10.3.1.

5.5 Impact Theory

As described in the introduction to Chapter 5, an impulse could for example be a blast from an explosion or an impact, where the basics of the latter can be described using classic impact theory. When one object collide with another the response is most likely between the two extremes, ideally elastic or ideally plastic, but here the theory behind the two extremes are presented. An illustration of the impact between two objects together with the two extremes are presented in Figure 5.8 and Figure 5.9.

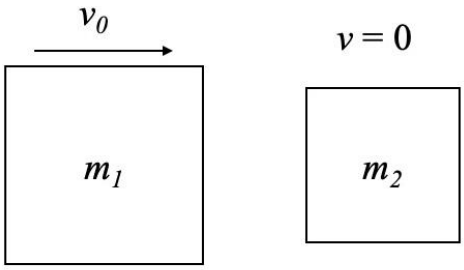

Figure 5.8 Illustration of two objects before impact.

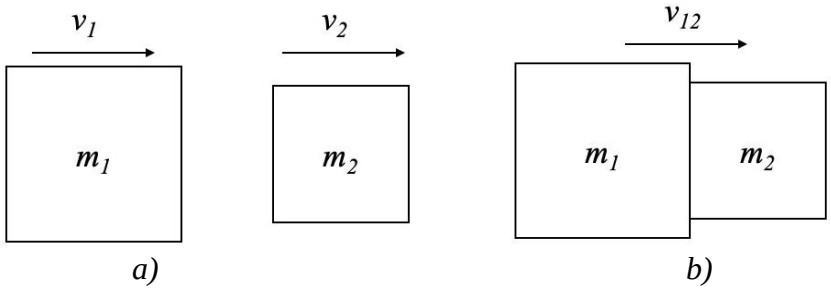

Figure 5.9 Illustration of two objects after impact where a) is with an ideally elastic impact and b) is with an ideally plastic.

In this work the impulse that a structure is subjected to is described using a simplified load pulse based on a drop weight with mass m_1 and initial velocity v_0. The object with mass m_2 and velocity $v = 0$ is then the concrete beam. Classical impact theory uses kinetic energy and momentum, see Section 5.1 and 5.2, respectively. The velocities after the impact can according to Johansson (2014) be expressed as

$$v_1 = \frac{(m_1 - e \cdot m_2)}{m_1 + m_2} \cdot v_0 \tag{5.14}$$

$$v_2 = \frac{(1 + e)m_1}{m_1 + m_2} \cdot v_0 \tag{5.15}$$

where m_1 = mass of object 1 [kg]
m_2 = mass of object 2 [kg]
v_0 = initial velocity of object 1 [m/s]
v_1 = velocity of object 1 after impact [m/s]

v_2 = velocity of object 2 after impact [m/s]
e = coefficient of restitution [-]

The coefficient of restitution is between 0 and 1, where 0 indicates an ideally plastic impact and 1 indicates an ideally elastic impact.

5.5.1 Elastic Impact

For an elastic impact both the kinetic energy and the momentum remains the same after impact (Johansson, 2014). An elastic impact, with a coefficient of restitution equal to 1 gives the following two velocities from Equations (5.14) and (5.15)

$$v_{1,el} = \frac{m_1 - m_2}{m_1 + m_2} \cdot v_0 \tag{5.16}$$

$$v_{2,el} = \frac{2m_1}{m_1 + m_2} \cdot v_0 \tag{5.17}$$

The kinetic energy for the two objects after elastic impact is then

$$E_{k,el,1} = \frac{m_1 \cdot v_{1,el}^2}{2} = \frac{m_1}{2} \cdot \left(\frac{m_1 - m_2}{m_1 + m_2} \cdot v_0\right)^2 = \left(\frac{m_1 - m_2}{m_1 + m_2}\right)^2 \cdot \frac{m_1 \cdot v_0^2}{2} = \left(\frac{m_1 - m_2}{m_1 + m_2}\right)^2 \cdot E_{k,0} \tag{5.18}$$

$$\begin{aligned} E_{k,el,2} &= \frac{m_2 \cdot v_{2,el}^2}{2} = \frac{m_2}{2} \cdot \left(\frac{2m_1}{m_1 + m_2} \cdot v_0\right)^2 = \frac{4m_1^2}{(m_1 + m_2)^2} \cdot \frac{m_2 \cdot v_0^2}{2} \\ &= \frac{4m_1 m_2}{(m_1 + m_2)^2} \cdot \frac{m_1 . v_0^2}{2} = \frac{4m_1 m_2}{(m_1 + m_2)^2} \cdot E_{k,0} \end{aligned} \tag{5.19}$$

where $E_{k,0} = \frac{m_1 \cdot v_0^2}{2}$ = kinetic energy before impact

5.5.2 Plastic Impact

For a plastic impact, only the momentum remains the same while the kinetic energy partly is transformed into potential energy. This is due to when the impact being plastic it results in plastic work when object 1 collides with object 2 (Johansson, 2014). A plastic impact, with a coefficient of restitution equal to 0 gives the following equations for the velocities of the objects

$$v_{pl} = v_{1,pl} = v_{2,pl} = \frac{m_1}{m_1 + m_2} \cdot v_0 \tag{5.20}$$

$$\begin{aligned} E_{k,pl,12} &= \frac{(m_1 + m_2) \cdot v_{pl}^2}{2} = \frac{(m_1 + m_2)}{2} \cdot \left(\frac{m_1}{m_1 + m_2} \cdot v_0\right)^2 \\ &= \frac{m_1}{m_1 + m_2} \cdot \frac{m_1 \cdot v_0^2}{2} = \frac{m_1}{m_1 + m_2} \cdot E_{k,0} \end{aligned} \tag{5.21}$$

6 Discrete Model for Dynamic Analysis

To make a prediction of the dynamic behaviour of the beam, when it is subjected to a drop weight impact, a calculation model is needed. For impulse loaded structures where the characteristics of the load is known, a single-degree-of-freedom system is a suitable model. However, in a drop weight test the characteristics of the load are harder to predict and thus a more developed method is needed. Such a discrete model for analysing the dynamically loaded structure is a two-degree-of-freedom system, here denoted as a 2DOF-system. The 2DOF model develops from two single-degree-of-freedom models, one for the beam and one for the drop weight, which together with the theory behind the equation of motion forms the 2DOF model for the loaded structural system.

6.1 SDOF System

The dynamic single-degree-of-freedom, SDOF system, consists of a mass *m* that is subjected to an external force *F(t)*. The resistance of this force, inhibiting the free movement of the mass, comes from a static and dynamic force $R_{sta}(u)$ and $R_{dyn}(\dot{u})$, respectively (Johansson & Laine, 2012). The viscous damper can be neglected in the model since the load duration for an impulse load is short and only the maximum displacement is of interest. This holds true for a single impact; hence, if repeated impact during a short duration is studied the damper may need to be considered. Here this results in neglecting $R_{dyn}(\dot{u})$ since it depends on the viscous damper. Figure 6.1 illustrates the SDOF system schematically.

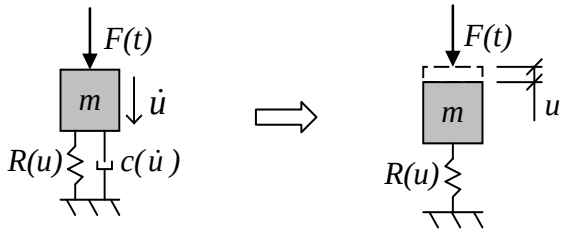

Figure 6.1 Definition of a dynamic SDOF system with the viscous damper neglected (Johansson & Laine, 2012).

6.2 Equation of Motion

As described in Section 6.1 the forces acting on a free body can be described by the external force *F(t)* and the static resistance force $R_{sta}(u)$. From Newton's Second Law it is known that a force could be described by acceleration and mass and with these two parts, the forces acting on a body can be described by equation of motion described in Equation (6.2). With the dynamic resistance neglected, the resistance can be described by the static resistance only. Assuming e.g. a linear-elastic response, the static resistance can be calculated as

$$R_{sta} = k \cdot u \tag{6.1}$$

where k = linear stiffness of a spring

u = displacement of the body

With the expression for the static resistance known, and the knowledge that the second derivative of the displacement is acceleration, finally the equation of motion can be derived as

$$m \cdot \ddot{u} + k \cdot u = F(t) \tag{6.2}$$

where m = mass of the body
$\ddot{u}$ = acceleration of the body

6.3 Transformation of Beam into SDOF

In order to use the SDOF system for an impulse loaded beam the beam has to be converted into a SDOF system. A linearly elastic and statically loaded beam will have a deformed shape, which depends on the load configuration as well as the beam's boundary conditions (Johansson & Laine, 2012). The deformed shape is independent of the load level, and thus the displacement of the beam can be expressed by the displacement of one point only; i.e. the system point. The system point can be chosen arbitrarily but affects the transformation factors. A common choice is to choose the point where the maximum deflection occurs or the middle of the span. The displacement of the system point corresponds to the displacement of the SDOF system meaning

$$u_s = u_{SDOF} \tag{6.3}$$

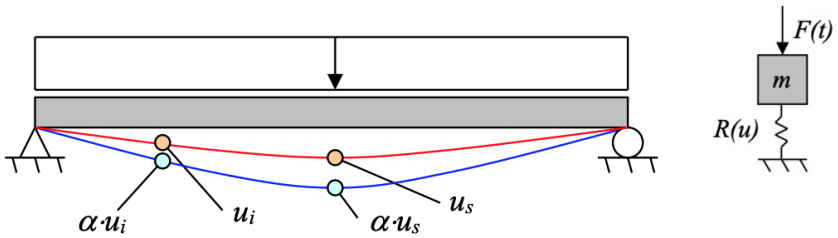

Figure 6.2 *A beam with a deformed shape independent of the magnitude of the load. The displacement along the beam is linearly dependent of a scaling factor α (Johansson & Laine, 2012).*

Figure 6.3 shows the parameters for a beam compared to an equivalent SDOF system. The system point gets a mass *m*, a viscous damper *c*, a resisting force *R(u)* and an external time dependent force *F(t)*.

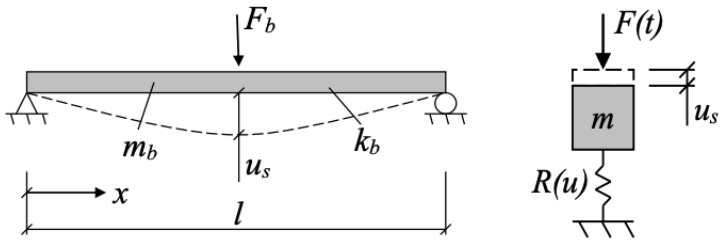

Figure 6.3 Parameters for a beam and parameters for an equivalent SDOF system. Modified from (Johansson & Laine, 2012).

In order to transform the beam into an equivalent SDOF system, so-called transformation factors are needed. The transformation factors κ are such that the kinetic energy or the work performed by the SDOF system should be equal to the kinetic energy and the work performed by the beam (Johansson & Laine, 2012). This means the transformation factors should balance the energy in the beam depending on the mass of the beam m_b, the external load F_b and the internal resistance force R_b by corresponding to the kinetic energy of the mass m in the SDOF system and the work by the external load $F(t)$ and the internal resistance $R(u)$ of the SDOF system.

The equation of motion is defined as Equation (6.4) but since the viscous damping could be neglected due to reasons stated in Section 6.1 resulting in c and the velocity of the mass $\dot{u}$ can be neglected. The modified equation of motion looks according to Equation (6.5).

$$m\ddot{u} + c\dot{u} + ku = F(t) \tag{6.4}$$

$$m\ddot{u} + ku = F(t) \tag{6.5}$$

The parameters connected to the SDOF system can for a beam be expressed as follows

$$m = \kappa_m m_b \tag{6.6}$$

$$k = \kappa_k k_b \tag{6.7}$$

$$F = \kappa_F F_b \tag{6.8}$$

where m_b = mass of the beam
k_b = stiffness of the beam
F_b = external force
κ_m = transformation factor for the mass
κ_k = transformation factor for the stiffness
κ_F = transformation factor for the force

Equation (6.5) then becomes

$$\kappa_m m_b \ddot{u} + \kappa_k k_b u = \kappa_F F_b(t) \tag{6.9}$$

which in turn can be rewritten as

$$\frac{\kappa_m}{\kappa_F} m_b \ddot{u} + \frac{\kappa_k}{\kappa_F} k_b u = F_b(t) \tag{6.10}$$

By utilizing that the factors κ_k and κ_F are equal (Biggs, 1964) together with

$$\kappa_{mF} = \frac{\kappa_m}{\kappa_F} \tag{6.11}$$

Equation (6.10) can finally be written as

$$\kappa_{mF} m_b \ddot{u} + k_b u = F_b(t) \tag{6.12}$$

which for an arbitrary system can be written as

$$\kappa_{mF} m_b \ddot{u} + R_b(u) = F_b(t) \tag{6.13}$$

This means that the transformation factor κ_{mF} is needed in order to transform the beam into a SDOF system. The transformation factors are dependent of the boundary conditions of the beam, the type of loading and if the deformed shape follows an elastic or a plastic case (Johansson & Laine, 2012).

Table 6.1 Transformation factors for a simply supported beam with a point load in the middle of the span (Johansson & Laine, 2012).

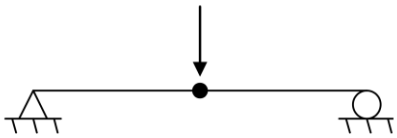	Strain range	Mass factor, κ_m	Load factor, κ_F	Stiffness factor, κ_k	Mass-load factor, κ_{mF}
	Elastic	0.486	1.000	1.000	0.486
	Plastic	0.333	1.000	1.000	0.333

6.4 2DOF

To be able to describe an impact between two bodies with the equation of motion, these two SDOF systems need to be coupled. The coupling of two bodies is illustrated in Figure 6.4. First, an impact between two bodies and the corresponding equation of motions are described for this 2DOF, followed by a description and establishment of equation of motion for the particular case with a drop weight and a beam.

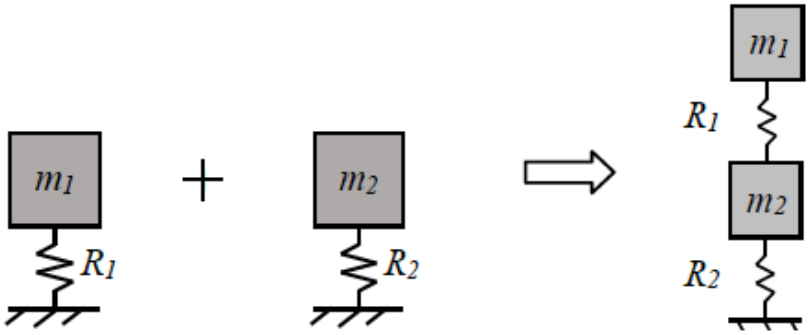

Figure 6.4 *Two SDOF systems coupled into a 2DOF. Modified from (Andersson & Pettersson, 2019).*

6.4.1 Equation of Motion for 2DOF

When the 2DOF-system in Section 6.4 is studied one could illustrate it by looking at the two separate bodies and study the forces acting on each body and this can be seen in Figure 6.5. The spring between the bodies can be described by a force instead, illustrated to the right in Figure 6.5. This free body diagram is the foundation to the equation of motion for a 2DOF system.

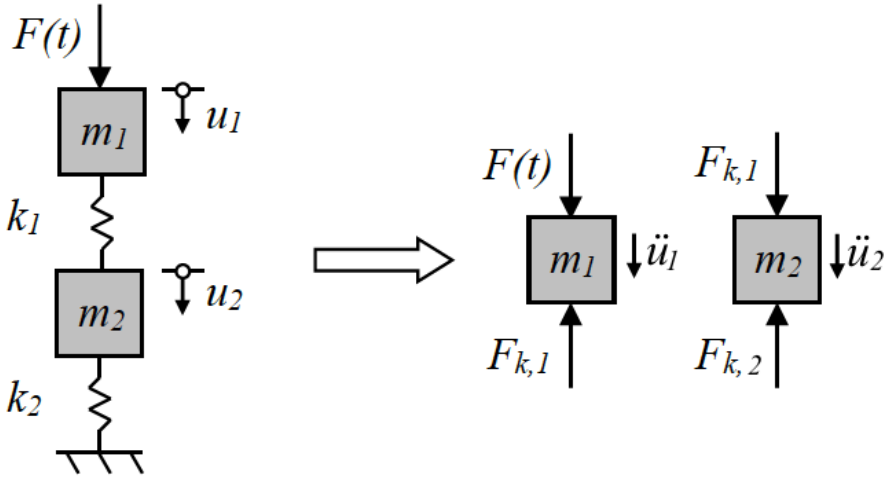

Figure 6.5 *Illustration of a 2DOF-system to describe a collision between two free bodies. Modified from (Jönsson & Stenseke, 2018).*

Force equilibrium combined with Newton's Second Law gives Equation (6.14) and (6.15).

$$F_1(t) - F_{k,1} = m_1\ddot{u}_1 \tag{6.14}$$

$$F_2(t) - F_{k,2} = m_2\ddot{u}_2 \tag{6.15}$$

Which also can be described as in Equation (6.16) and (6.17) where stiffness of the springs and displacement of the bodies also are considered.

$$m_1\ddot{u}_1 + k_1(u_1 - u_2) = m_1\ddot{u}_1 + k_1u_1 - k_1u_2 = F_1(t) \tag{6.16}$$

$$m_2\ddot{u}_2 + k_2u_2 - k_1(u_1 - u_2) = m_2\ddot{u}_2 - k_1u_1 + (k_2 + k_1)u_2 = F_2(t) \tag{6.17}$$

The general form of equation of motion can then be stated on matrix form, see Equation (6.18).

$$\begin{bmatrix} m_1 & 0 \\ 0 & m_2 \end{bmatrix}\begin{bmatrix} \ddot{u}_1 \\ \ddot{u}_2 \end{bmatrix} + \begin{bmatrix} k_1 & -k_1 \\ -k_1 & k_2 + k_1 \end{bmatrix}\begin{bmatrix} u_1 \\ u_2 \end{bmatrix} = \begin{bmatrix} F_1(t) \\ F_2(t) \end{bmatrix} \tag{6.18}$$

or

$$\boldsymbol{M\ddot{u} + Ku = F(t)} \tag{6.19}$$

The last thing to finalize the equation of motion to correspond to the studied cases in this project is to use the transformation factors and transform the general equation of motion in Equation (6.19).

6.4.2 2DOF for a Beam and Drop Weight System

In order to make the 2DOF system that explains the impact between the drop weight and the beam the transformation factors introduced in Section 6.3 needs to be implemented. The transformation factors from Table 6.1 together with a loading condition where no external time dependent force $F_i(t)$ acts on the two bodies are inserted into Equation (6.18). The drop weight impact is described with an initial velocity of the drop weight which is body 1. This results in the following equation if the response is elastic

$$\begin{bmatrix} \kappa_{m,1}m_1 & 0 \\ 0 & \kappa_{m,2}m_2 \end{bmatrix}\begin{bmatrix} \ddot{u}_1 \\ \ddot{u}_2 \end{bmatrix} + \begin{bmatrix} \kappa_{F,1}k_1 & -\kappa_{F,1}k_1 \\ -\kappa_{F,1}k_1 & \kappa_{F,1}k_1 + \kappa_{F,2}k_2 \end{bmatrix}\begin{bmatrix} u_1 \\ u_2 \end{bmatrix} = \begin{bmatrix} 0 \\ 0 \end{bmatrix} \tag{6.20}$$

If the response is instead elasto-plastic, then the equation can be expressed as follows

$$\begin{bmatrix} \kappa_{m,1}m_1 & 0 \\ 0 & \kappa_{m,2}m_2 \end{bmatrix}\begin{bmatrix} \ddot{u}_1 \\ \ddot{u}_2 \end{bmatrix} + \begin{bmatrix} R_1 & -R_1 \\ -R_1 & R_1 + R_2 \end{bmatrix} = \begin{bmatrix} 0 \\ 0 \end{bmatrix} \tag{6.21}$$

The elasto-plastic response for the drop weight to beam case needs some expanding compared to the general description of an elasto-plastic response, which is explained more extensively in Section 2.3. After the drop weight has hit the surface of the beam, body 2, the drop weight, body 1, moves upward creating tension in the spring between the two bodies in the mass-spring system. In theory this would mean there is tension but in reality, there is no connection between the beam and the drop weight moving upwards after collision resulting in the stiffness being equal to zero.

$$R_i = \begin{cases} k_i \cdot u & if\, u \le u_{el,1} \\ R_{m,i} & if\, u > u_{el,1} \\ 0 & if \quad u \le 0 \end{cases} \tag{6.22}$$

To be able to distinguish the internal resistance of the beam and the drop weight different approaches are needed. The internal resistance for the beam can be determined and derived by looking at the expression for ultimate moment for a simply supported beam subjected to a point load in the middle of the span. The expression for internal resistance is presented in Equation (6.23).

$$R_{m,2} = \frac{4M_u}{L} \tag{6.23}$$

where M_u = moment in ultimate limit state
L = span length

Since the beam is not only subjected to the drop weight but also to its own self weight, the internal resistance is reduced. Equation (6.24) presents how the reduced internal resistance can be determined.

$$R_{m,2,red} = R_{m,2} - \frac{g_{beam} \cdot L}{2} \tag{6.24}$$

where g_{beam} = self-weight of the beam

Elasto-plastic response considered leads to a response for the internal resistance as illustrated in Figure 6.6.

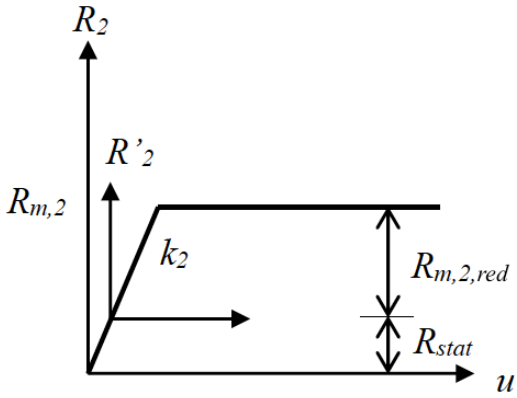

Figure 6.6 *Illustration of the response for the internal resistance reduced due to static load from self-weight. Modified from (Lozano & Makdesi, 2017).*

The internal resistance for the drop weight is determined in another way than the beam and studied in detail by e.g. Lovén and Svavarsdóttir (2016). The internal resistance is dependent on the impact area and the strength of the material considered. Two extreme cases are that either the concrete is crushed, or the yielding strength of the reinforcing steel is exceeded described by Equation (6.25) (Jönsson & Stenseke, 2018).

$$f_{cm} \cdot A_{imp} \leq R_{m,1} \leq f_{ym} \cdot A_{imp} \tag{6.25}$$

The conclusion drawn by Lovén and Svavarsdóttir (2016) was that a reasonable value for the internal resistance of the drop weight would be 50 kN for their experiments. Since the test specimens in this project were different, the internal resistance stated by

Andersson and Pettersson (2019) of 70 kN is more suitable. Another interesting aspect is the stiffness of the beam and the drop weight. The stiffness of the beam could be calculated with Equation (6.26) which is based on elementary cases for a simply supported beam subjected to a point load in the middle of the span. Equation (6.27) presents how to calculate the stiffness of the drop weight.

$$k_2 = \frac{48 \cdot E_{cm} \cdot I_{II}}{L^3} \tag{6.26}$$

where E_{cm} = Young's modulus for the concrete
I_{II} = moment of inertia in state II for the concrete
L = span length

$$k_1 = min\left(\frac{E_{sm} \cdot A}{L}, \frac{E_{cm} \cdot A}{h}\right) \tag{6.27}$$

where E_{sm} = Young's modulus for the steel
A = cross section of the drop weight
L = length of the drop weight
h = height of the beam

The value of k_1 could, as described, be depending on the drop weight properties or the properties of the beam but other alternatives are also possible, further discussed by Andersson and Pettersson (2019). The conclusion drawn by Andersson and Pettersson (2019), though, was that the effect on the results was very small since all presented choice of stiffness was very large and therefore the stiffness obtained using Equation (6.27) is deemed to be a reasonable choice.

7 FRP Strengthened Reinforced Concrete

The strengthening of reinforced concrete structures with FRP is a method that has been used in civil engineering since the late 1980s, early 1990s, and since then the use has been ever increasing (Wu & Eamon, 2017). FRP can be utilized in several forms where some are more common in repairing and strengthening of reinforced concrete structures and some are used in structures that are newly casted (Wu & Eamon, 2017). FRP has many advantages in repairing and strengthening of reinforced concrete structures because of its high stiffness and light weight gives a high strength-to-weight ratio, corrosion resistance and easy to install and transport (Wu & Eamon, 2017; El-Hacha et al., 2001; Huang et al., 2019). Strengthening reinforced concrete structures with FRP results in increased flexural and shear capacity and can with different applications and configurations provide enhanced properties or more desired properties (Wu & Eamon, 2017). Besides increasing flexural and shear capacities, FRP strengthening could also be used to improve the ductility for seismic actions, improve the stiffness as well as improve a structure's durability regarding environmental factors (Pham & Hao, 2016a).

7.1 Properties of Fibre Reinforced Polymers

As briefly mentioned in Section 3.4, there are different types of FRP, which are used in different ways. The following is the most common types used

- Carbon Fibre Reinforced Polymer (CFRP)
- Glass Fibre Reinforced Polymer (GFRP)
- Aramid Fibre Reinforced Polymer (AFRP)
- Basalt Fibre Reinforced Polymer (BFRP)

CFRP has the highest modulus of elasticity and highest strength, and it is very durable and performs very well with respect to fatigue and moisture (Wu & Eamon, 2017). To put the lightweight aspects into perspective it can be said that CFRP can give a mass reduction of 50-60% compared to a corresponding element in steel (Amran et al., 2018) but CFRP has a higher cost than the other FRP options.

GFRP has the lowest modulus of elasticity and is also characterized by high elongation and average strength and weight (Wu & Eamon, 2017). Since the glass fibres are so light it results in a very high strength-to weight ratio. The cost of GFRP is the lowest of the FRP types and has an adequate overall performance, making it the most used FRP type.

AFRP has high modulus of elasticity and strength and it is even lighter than GFRP, approximately 40% lower density than GFRP (Amran et al., 2018). The cost of AFRP is somewhere between CFRP and GFRP. However, the use of Aramid Fibre Reinforced Polymers is somewhat restricted within civil engineering due to its performance in compression being poor (Amran et al., 2018). AFRP has a good tolerance to shock and high strain rates and fulfil its ultimate strength at higher strain rates compared to other FRP materials. This material is the least time dependent material among FRPs and therefore beneficial in this project with impact loading (Haghani Dogaheh personal communication, 1 June,2021).

BFRP is as mentioned briefly in Section 3.4 a new type of FRP which might be able to replace CFRP due to its lower cost and large availability (Wu & Eamon, 2017). BFRP has a good tensile strength as well as a high failure strain compared to some of the other FRP-types. Due to its large availability but not as high strength as CFRP it could be possible to use BFRP instead of GFRP (Amran et al., 2018) but when a high strength FRP is necessary, CFRP is today the most used and best suited alternative (Amran et al., 2018). Table 7.1 presents ranges of properties for different types of FRP.

Table 7.1 Ranges of properties for different types of FRP materials. Based on (Amran et al., 2018).

Fibre type	**Tensile strength [MPa]**	**Modulus of elasticity [GPa]**	**Ultimate strain [%]**
Carbon	1720 - 3690	120 - 580	0.5 - 1.9
Glass	480 - 1600	35 - 51	1.2 - 3.1
Aramid	1720 - 2540	41 - 125	1.9 - 4.4
Basalt	1035 - 1650	45 - 59	1.6 - 3.0

7.2 Failure Modes

Beams that are strengthened with Fibre Reinforced Polymers on the side which is subjected to tension has been studied extensively. Through test observations have different failure modes of flexurally strengthened reinforced concrete beams been identified. Different authors have categorized the failure modes in different ways (Wu & Eamon, 2017; Smith & Teng, 2002; Teng et al., 2003; Zoghi, 2014).

The failure modes could be divided into two categories where the first one consists of failure modes which are not due to failed composite action between the concrete and FRP and the second category is due to failed composite action between the two materials (Wu & Eamon, 2017).

The first category includes failures mode due to concrete crushing, failure of reinforcement before FRP rupture or concrete crushing, rupture of FRP before yielding or concrete at ultimate strain or shear failure. The second category is due to failed composite action which could be debonding of the FRP sheet or peeling of the concrete cover near the cut of zone of the FRP sheet (Wu & Eamon, 2017).

Teng et al. (2003) presents seven failure modes observed in tests for flexural strengthening of reinforced concrete beams. These are presented in Figure 7.1.

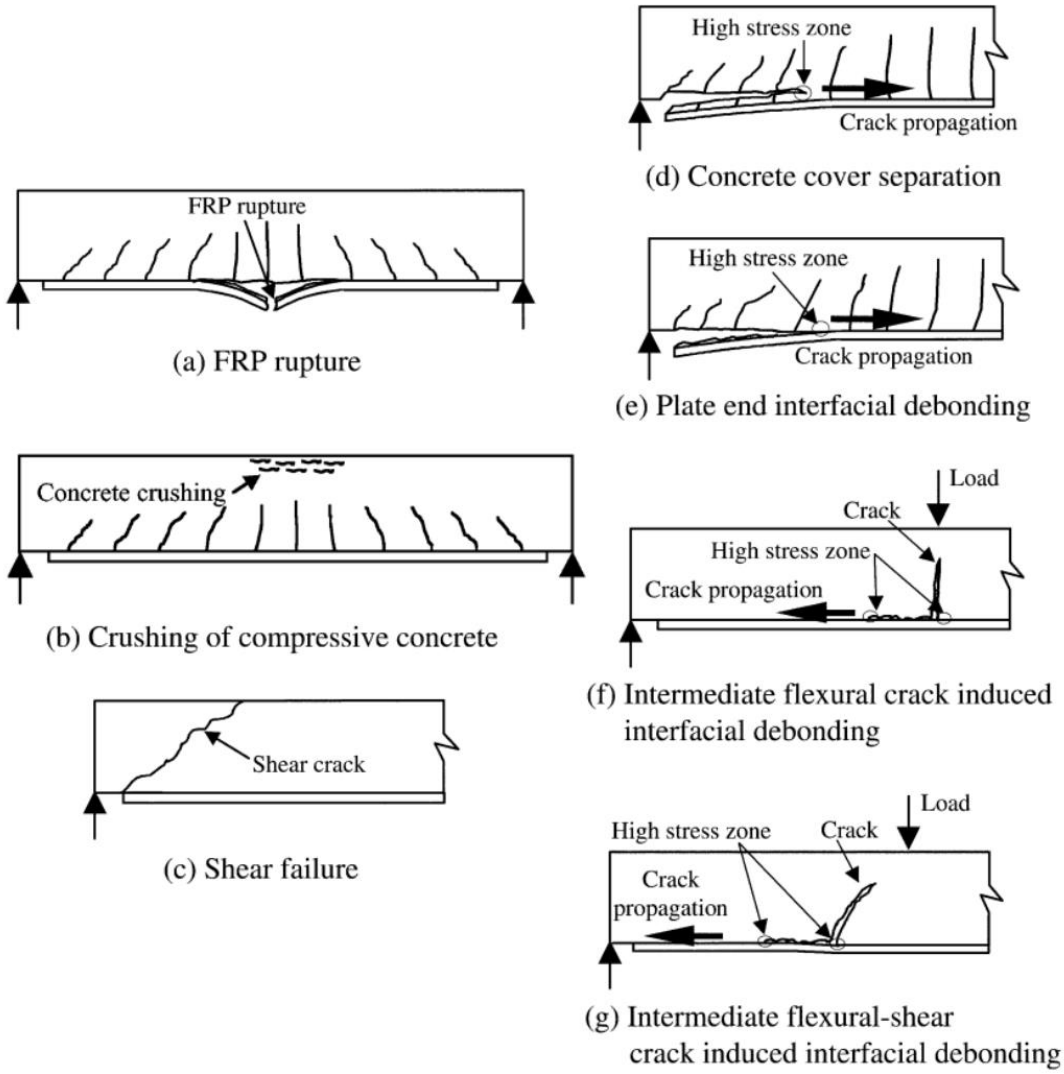

Figure 7.1 Failure modes of flexurally strengthened reinforced concrete beam with FRP-sheet (Teng et al., 2003).

Failure modes (d) to (g) in Figure 7.1 are modes that occur before the flexural capacity of the section has been reached and are commonly referred to as premature debonding type failure modes (Smith & Teng, 2002a). A potential rupture of the FRP sheet is the most brittle failure out of all the failure modes (Wu & Eamon, 2017). The other failure modes are categorised into two groups of debonding failures. The first one is when the debonding starts at the end of the plate or sheet and then moves inwards towards the middle of the beam, modes (d) and (e) in Figure 7.1. The second category is when the debonding starts with an intermediate crack that gives interfacial debonding and moves towards the end of the plate or sheet, modes (f) and (g). The cracks could be either flexural or flexural-shear crack (Smith & Teng, 2002a).

7.2.1 Plate End or Sheet Debonding Failure Modes

Debonding at the plate end are common failure modes (Smith & Teng, 2002a). These failure modes are due to the separation of concrete cover and plate end interfacial debonding, i.e. (d) and (e), respectively, in Figure 7.1. Both of the two end plate debonding failure modes are brittle failures and should be avoided (Teng et al., 2003).

Concrete cover separation is more common among the two end plate debonding failure modes and happens because of high principal stresses at the point where the plate or sheet ends (Smith & Teng, 2002a; Smith & Teng, 2002b). The stresses give rise to a crack at the plate or sheet end where it then grows up towards the reinforcement. At the level of the reinforcement the crack then develops along the level of the reinforcement resulting in a peeling of the concrete cover (Smith & Teng, 2002a). The other failure mode in the category, plate end interfacial debonding, (e) in Figure 7.1, is due to the same factors as for the concrete cover separation which are high stress concentrations at the plate or sheet end (Smith & Teng, 2002a; Pham & Hao, 2016a). This results in that the plate or sheet is delaminated in the concrete directly within the concrete that is connected to the adhesive.

Another type of failure which was observed by Nigani and Nordström (2020) was a failure which is most similar to failure mode (e) in Figure 7.1 but not equal to this failure mode. They experienced a failure where a very small amount of concrete was ripped off from the beam when debonding of FRP occurred, the surface on the FRP was almost clean. The failure took place mostly in the interface between the adhesive and the concrete. This is something that could happen if the preparation of the concrete surface is not done in a proper way and the adhesion between the adhesive and the concrete is insufficient.

7.2.2 Intermediate Crack Debonding Failure Modes

The intermediate crack debonding failure modes are also common debonding type failure modes and important (Smith & Teng, 2002a; Teng et al., 2003). According to Teng et al. (2003) the intermediate flexural or flexural-shear crack interfacial debonding modes are important for slender members or when the externally bonded FRP plate or sheet is thin.

Intermediate crack debonding starts with either a flexural crack or a flexural shear crack. If the crack is a major flexural crack it can lead to an intermediate flexural crack induced interfacial debonding failure, see (f) in Figure 7.1. When the crack occurs the tensile stresses in the concrete at the crack are transferred to the FRP plate or sheet. This gives rise to high stress levels in the interface between the two materials (Teng et al., 2003). When these stresses exceed the capacity due to increased loading debonding starts after the interfacial stresses close to the flexural crack have increased. The debonding increases as the crack moves along the FRP sheet, often in the direction of the closest end of the sheet (Teng et al., 2003).

The other type of failure mode due to intermediate crack debonding is the one due to flexural-shear crack, (g) in Figure 7.1. When this crack occurs the plate on one side of the crack is pushed downwards (Teng et al., 2003). This also leads to high stresses in the interface between concrete and FRP.

7.2.3 Bond-Slip Between Concrete and FRP

As been shown through Section 7.2 in general, and Sections 7.2.1 and 7.2.2 in particular, the debonding of externally bonded FRP to the concrete surface are common and also potentially dangerous failure modes due to being brittle failures (Teng et al., 2002a). The degree of brittleness varies but they are all potentially brittle. The bond-

slip behaviour is not going to be delt with in detail in this work but since it is a key factor regarding debonding failure modes it is still briefly dealt with in this section.

The interfacial crack arises due to the bond-slip relationship between the FRP and concrete (Teng et al., 2002a). The properties of the interface are the governing factor controlling the debonding failure modes. Lu et al. (2005) explains that when the concrete-to-FRP bond fails it is due to cracking of concrete adjacent to the adhesive surface except for two exceptions. These two exceptions are the two extreme cases with either very high strength concrete or very low strength adhesive. There is usually a little concrete layer that is still attached to the adhesive when debonding failure has occurred, so the failure is usually in the concrete adjacent to the concrete-to-adhesive (Teng et al., 2003).

According to Lu et al. (2005), there are six parameters effecting the properties of the interface and thereby the bond strength of the concrete-to-FRP connection:

1. Concrete strength
2. The bond length
3. Axial stiffness of FRP
4. FRP-to-concrete width ratio
5. Stiffness of the adhesive
6. Strength of the adhesive

There is a detail that is of importance for the bond length parameter and that is that the effective bond length is governing. This means a larger bond length will not necessarily increase the capacity (Lu et al, 2005).

7.3 Anchorage and Adhesion

There are further measures that can be made in order to ensure a better bond between concrete and FRP. Different types of anchorages, additional strengthening methods as well as different ways to improve the adhesion. Some of these measures can delay or suppress different failure modes which is desirable, especially if the failure mode is of the brittle nature.

7.3.1 Adhesion

In order to achieve a strong bond between the FRP and the concrete, the concrete surface should be treated in order to achieve a sufficient adhesion of the FRP. Several authors suggest similar procedures to treat the surface of which the FRP sheet is going to be laminated but some minor details or tools might vary (Täljsten et al., 2016; Camata el al., 2006; Pham & Hao, 2016b). The authors all describe the importance of a roughened surface followed by dust, chloride, oil and fat removal. First, the surface should be treated so that the outer layer of concrete is removed making the aggregates appear. This step can be done with e.g. sandblasting, grinding with an angle grinder or pneumatic needle gun. Secondly the surface should be cleaned from any dust with a pressurised air gun. Thirdly the surface should be cleaned with acetone before the bonding between the two materials (Pham & Hao, 2016b; Yang personal communication, 23 February, 2021).

7.3.2 U-jacketing

U-jacketing with FRP is a method to add additional shear capacity, strength and ductility (Teng et al., 2003). The wrapping could also cover the entire cross section and is preferable if it is feasible. The U-jacket could be more beneficial than just increase the shear capacity and thus constrain the shear failure mode. It can also give additional anchorage at the plate ends to avoid plate end debonding failure modes. The U-wrapping can increase the capacity with respect to plate end debonding failure mode but also increase the capacity and ductility of the plate end interfacial debonding failure mode if applied along the length of the beam (Teng et al., 2003).

There are many possible configurations of FRP strengthening of RC beams, with only longitudinal, only transverse or both types (Nigani & Nordström, 2020; Pham & Hao, 2016b; Pham & Hao, 2017). The U-wraps can be fastened vertically to the edges of the beams or it can be fastened with an angle, see Figure 7.2. Inclined FRP U-wraps gives both higher static and impact resistance for a beam (Pham & Hao, 2016a).

Figure 7.2 Vertical and inclined U-jackets on a concrete beam (Yang. J, 2021).

Pham & Hao (2017) also suggested another way where the bottom of a rectangular cross section of a beam is modified into and arc. The purpose with this is to change the behaviour from a resistance of the peeling stress by the adhesive or concrete to a behaviour where the U-jackets can contribute to the resistance. When the cross section is modified confining stresses due to the U-jackets are preventing the FRP from debonding together with the adhesive (Pham & Hao, 2017). U-wrapping is not going to be performed in this work but it can be of interest for future studies within the subject and could enhance the performance of impact loaded beams even further.

7.3.3 Anchors

There are also other methods of anchorage that could improve the capacity and delay potential debonding failure modes. One of these methods is to use anchors with material at the ends that can give additional adhesion and a stronger bond (Teng et al., 2003). The anchors could consist of a bolt which is placed in a predrilled hole in the structural member that needs strengthening and then fibres at the end of the bolt that can give adhesion in a sun fan-like pattern (Teng et al., 2000). The protruding anchors are then distributed on the surface and laminated to the sheet. According to Teng et al. (2000) this method increased the load carrying capacity significantly. The use of fibre anchors has been observed to prevent the debonding failure mode (Lam & Teng, 2001). There are other studies as well that have examined the usage of end anchors. According to El-Hacha et al. (2001) can a more ductile behaviour be achieved for beams with end anchors compared to beams without end anchors. Since the debonding failure modes are the most common failure modes this is of great interest. However, anchors are not going to be covered in this report but, as for the U-wraps discussed in Section 7.3.2, may be of great interest in future studies. A schematic illustration of an anchor and its placement in a FRP strengthened concrete structure is presented in Figure 7.3.

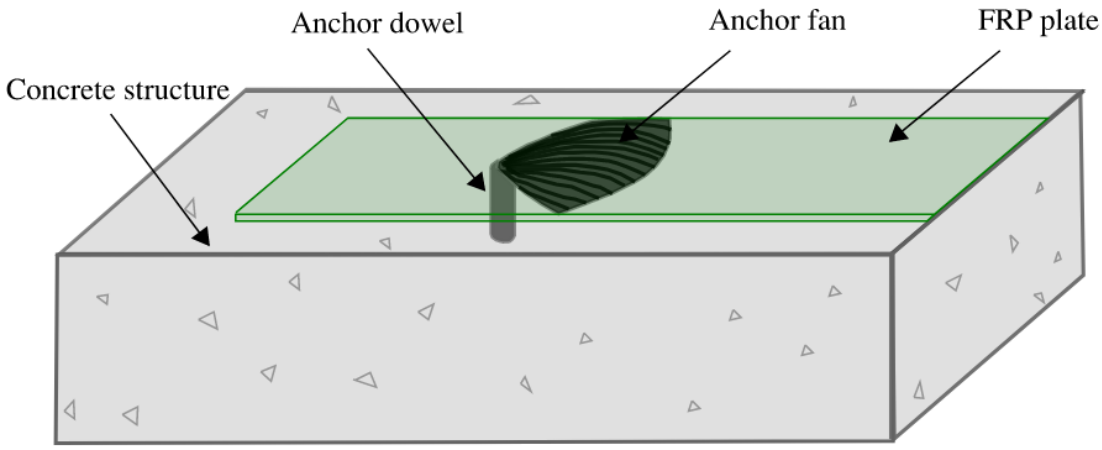

Figure 7.3 Schematic illustration of an anchor used with FRP strengthening.

7.4 Structural Response of Reinforced Concrete Beams Strengthened with FRP

The structural response of reinforced concrete strengthened with FRP is of great interest and has been documented in a fairly extensive way. As far as the authors of this work are aware of, the tests have been performed with beams either subjected to impulse or static loading. However, except for REF (i.e. the MSc thesis on which this work is a continuation of) there have not been tests performed with an impulse loading followed by static loading to capture the behaviour and residual strength. This makes it difficult to predict the structural response for a FRP strengthened beam subjected to a combination of impact and static loading as is of interest in this work. Nevertheless, some general observations and descriptions from previous studies can be made.

Camata et al. (2006) performed static tests of beams and slabs strengthened with FRP. The beams were simply supported, and the load conditions were four point bending test. From this, it was observed that the strengthened beams showed a much higher load carrying capacity, as stated several times in Chapter 7, up to a point where debonding occurred. The debonding occurred at mid span with a registered failure mode as intermediate flexural crack induced interfacial debonding according to Figure 7.1 (f). Camata et al. (2006) also observed that the FRP ripped off some concrete at debonding. After the debonding the strengthened beam returned to the curve of the unstrengthened beam and followed that response. Illustration of the load versus deflection curve for the FRP strengthened reinforced concrete beam compared to an unstrengthened, based on experimental data from Camata et al. (2006), is presented in Figure 7.4. As far as the authors of this project could find, no information about what happened when the experiments ended was presented.

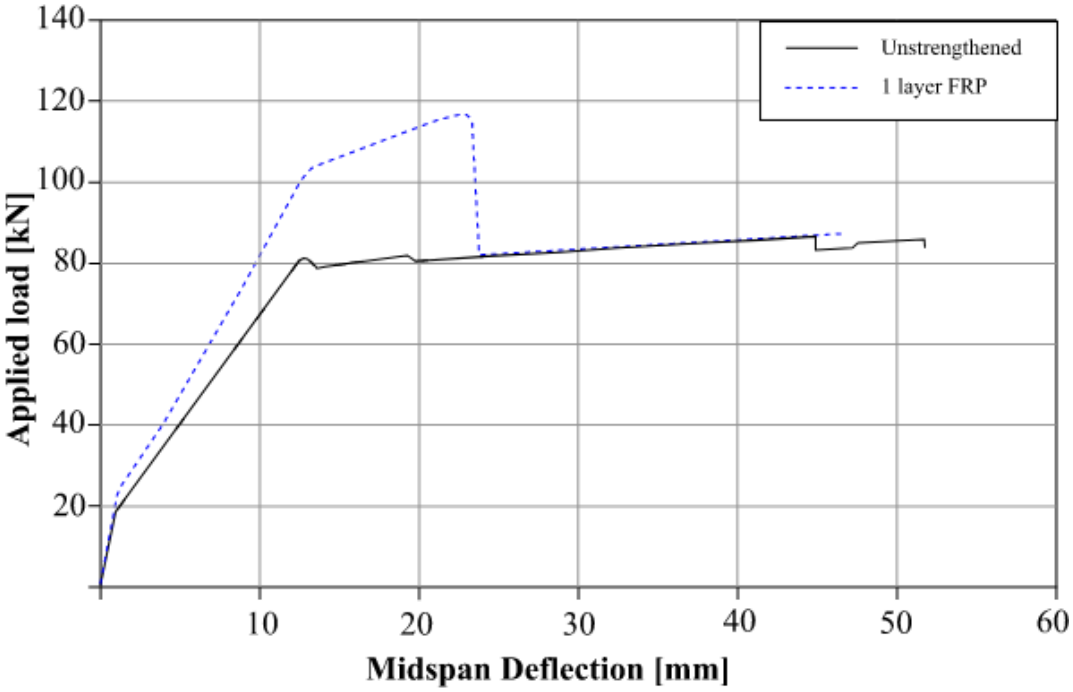

Figure 7.4 *Illustration of load versus deflection for a FRP strengthened and unstrengthened reinforced concrete beam. Based on experimental data presented in (Camata et al., 2006).*

A similar observation was also made in previous year study where before the debonding the capacity was significantly higher for a strengthened beam compared to an unstrengthened (Nigani & Nordström, 2020). The placement of load and the boundary conditions were the same as in this project described in Section 8.8 and 8.9. What could be seen in that study was that after debonding the strengthened beams returned to and followed the response of the unstrengthened for most of the cases. However, some of the beams instead showed a response where they after debonding had lower capacity than the unstrengthened beams. This behaviour is shown in Figure 7.5.

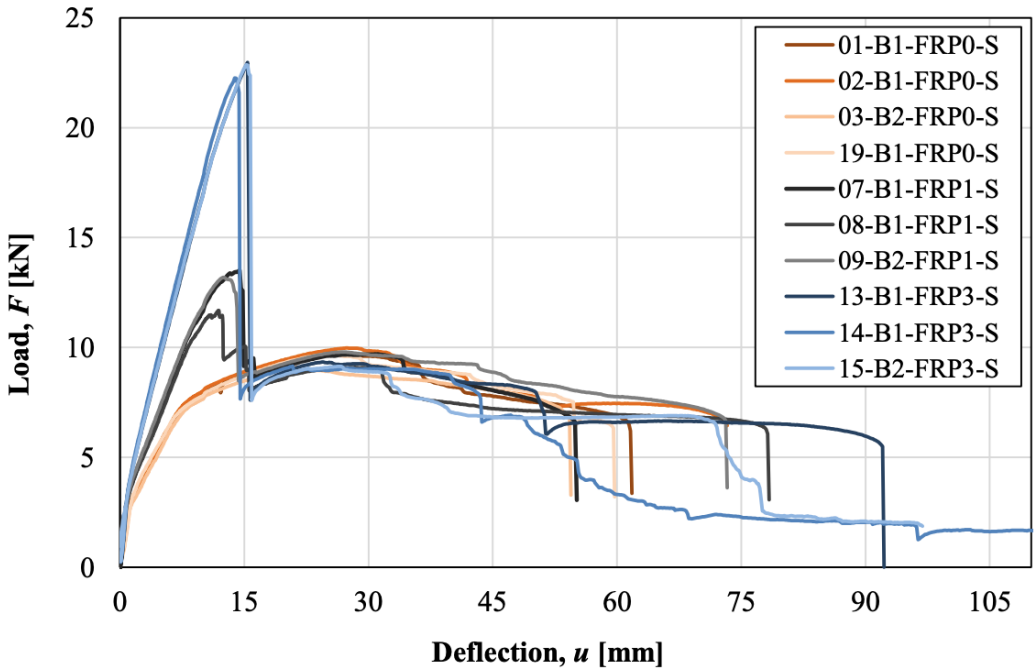

Figure 7.5 Load versus deflection for unstrengthened and strengthened beams (Nigani & Nordström, 2020).

If the response would follow the one of an unstrengthened beam after debonding and reach failure at the same deflection, then there is no doubt that FRP strengthening always is a good option for both static and impulse loading. But if the strengthened beam fails earlier or gets a lower load capacity and/or deformation capacity than an unstrengthened beam after debonding, resulting in a lower absorption of energy than for an unstrengthened beam, then it is not necessarily a good option for impulse loading. This is because the absorption of energy is one of the, perhaps the, most important aspect when it comes to impulse loading and more important than a high load capacity, see Figure 5.3. So, if FRP strengthening gives both a higher ultimate load capacity and a larger area under the load-displacement curve, resulting in a larger energy absorption, it is also a good option. However, it remains to see how the residual response is affected once subjected to an impulse load.

The ductility can increase as mentioned on different occasions, as described in the introduction to Chapter 7 and in Section 7.3.2 but it can depend on design and configuration. In the study performed by Camata et al. (2006) the ductility decreased. In order to calculate the ductility an energy ductility D_E could be used, defined as the ratio between energy at failure in the system and the energy at yielding of reinforcement (Camata et al., 2006).

$$D_E = \frac{E_u}{E_y} \tag{7.1}$$

where E_u = Energy of the system at the time of failure
E_y = Energy of the system at the time of yielding of reinforcement

7.5 Previous Studies of FRP Strengthened RC Structures

Previous experimental studies within the subject of FRP strengthened RC beams subjected to both impact load and static load are limited. However, the number of studies considering FRP strengthened RC beams subjected to either impact load or static load are significant larger. In the following subsections different aspects are presented and comparisons between some different studies made to create a greater knowledge about the subject.

7.5.1 Response from Static or Impact load

If FRP is supposed to be used as a strengthening material for concrete structures subjected to impulse loading, the overall response of the structure needs to be known; i.e. also once potential debonding has occurred. However, this is not always clear when FRP strengthening is used. For impact loaded structures, the energy absorption is of high importance and it is an important part to ensure that the FRP has enough bonding to be able to absorb more energy than the structure would do without the FRP strengthening. The later debonding is not alone the crucial reason to make a FRP strengthened structure to absorb more energy than an unstrengthened one, but could be a large advantage together with good structural response after debonding (Johansson, personal communication, 13 April 2020).

Several experimental studies with respect to load versus deflection are presented in this section. Nigani and Nordström (2020) presented results for beams with one layer of FRP where the response is illustrated in Figure 7.6.

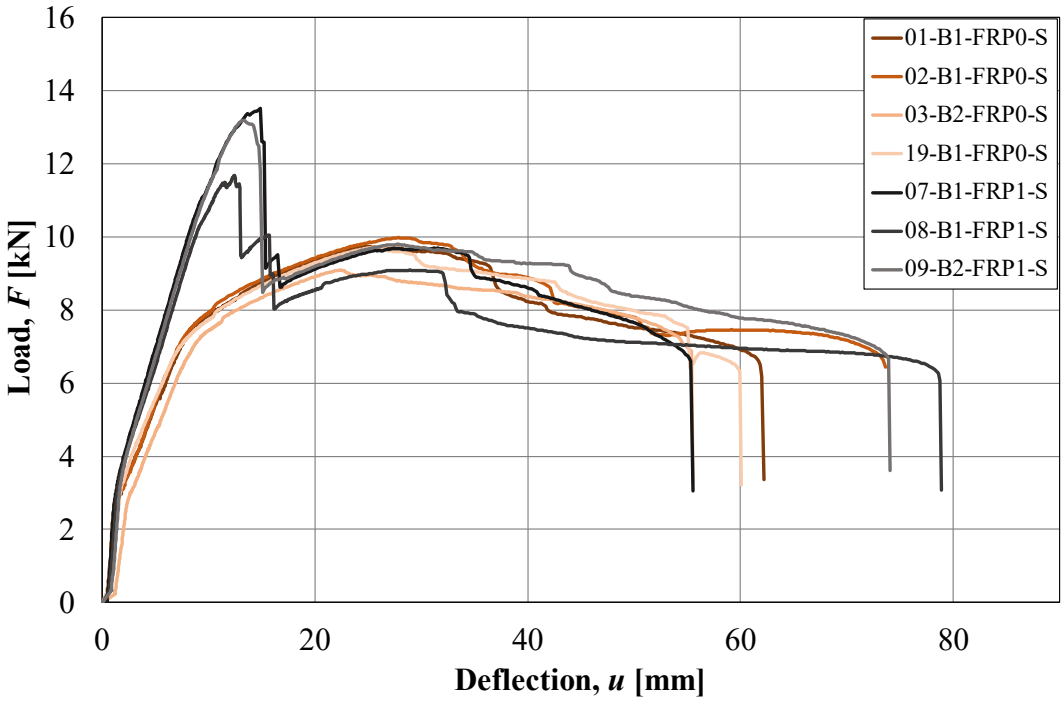

Figure 7.6 Load versus deflection for unstrengthened and FRP strengthened beams from experimental tests (Nigani & Nordström, 2020).

A large drop in the load capacity is noticed in the figure when debonding of the FRP occurs, but before this, the behaviour is almost linear or bi-linear. Once debonding has

occurred, the response is close to the behaviour of an unstrengthened beam with yielding of the reinforcement, which is also illustrated in Figure 7.6. Norimitsu et al. (2020) made another study where they also investigated RC beams strengthened with FRP and the results from their static tests are presented in Figure 7.7.

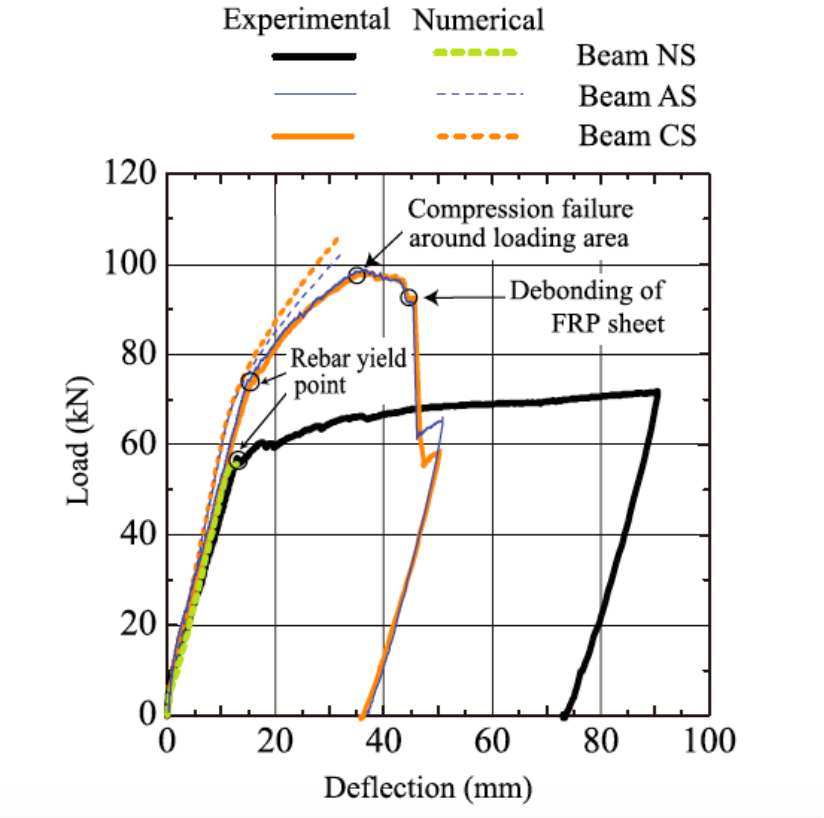

Figure 7.7 "Static load-deflection curves". (Noritmitsu et al., 2020).

Figure 7.7 clearly illustrates the different stages when load was increased with a significant increase in maximum load for strengthened compared to unstrengthened. One important difference between Nigani & Nordström (2020) and Norimitsu et al. (2020) though is the behaviour when debonding of FRP sheet takes place. Nigani & Nordström (2020) presented results showing that the response followed the unstrengthened beam when debonding of FRP took place. Norimitsu et al. (2020) on the other hand showed similar response until debonding and a start of increased load capacity after debonding until the experiment ended as seen in Figure 7.7. The test of the reference beam was ended manually at deflection of 90 mm and the orange and blue curves indicate that the same procedure was done for the strengthened beams but at a deflection of 50 mm. Pham & Hao (2017) made another study of FRP strengthened RC beams and their result for the same case, one layer FRP under static load, is presented together with some other configurations in Figure 7.8.

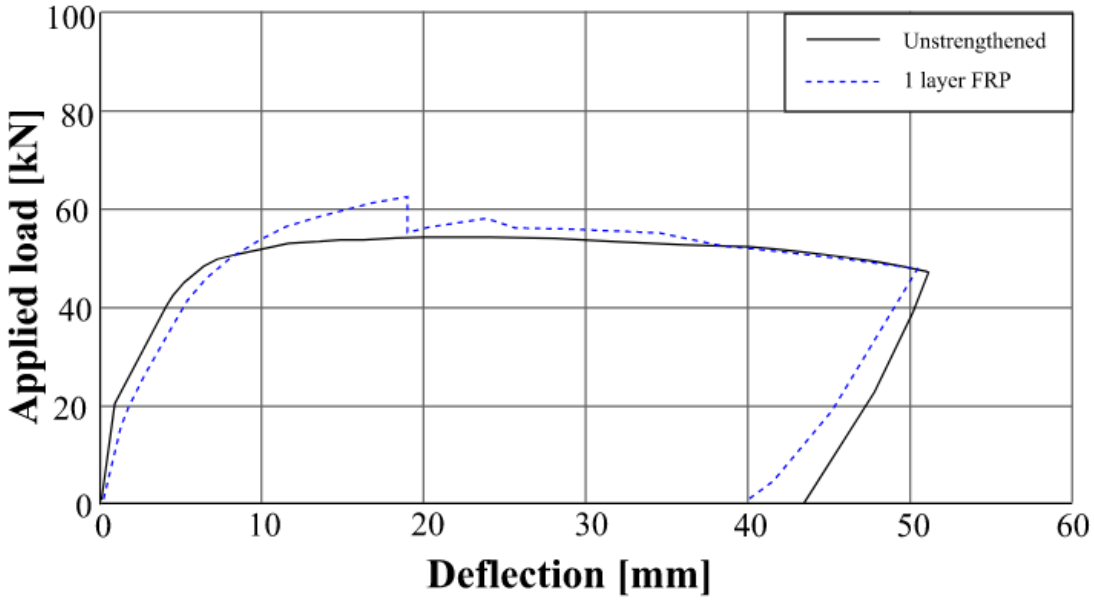

Figure 7.8 *Static response for RC beams unstrengthened or strengthened with FRP. Based on experimental data (Pham & Hao, 2017).*

In Figure 7.8, the blue dotted line is representing the response for a strengthened beam with one layer longitudinal FRP and the black line unstrengthened beam subjected to static load. At around a deflection of 18 mm a small drop in applied load could be recognized for the strengthened beam followed by almost constant load until failure. The beams studied by Pham and Hao (2017) had a width of 150 mm, height of 250 mm, two rebars with diameter of 10 mm in the bottom and two bars with diameter of 12 mm at the top. Stirrups with diameter of 10 mm placed with a centre-to-centre distance of 125 mm were used. In summary, further studies need to be done, but the FRP strengthening is beneficial for statically loaded structures.

When comparing the impact response from Nigani and Nordström (2020) and Pham and Hao (2017) the difference in impact load is significant. Nigani and Nordström (2020) used a drop weight with mass of 20 kg and Pham and Hao (2017) one with a weight of 203.5 kg. The two studies also had different sizes and designs of the beams but when comparing the overall behaviour, it is similar. In Figure 7.9, time versus midpoint deflection is presented from three of Nigani and Nordström's (2020) beams.

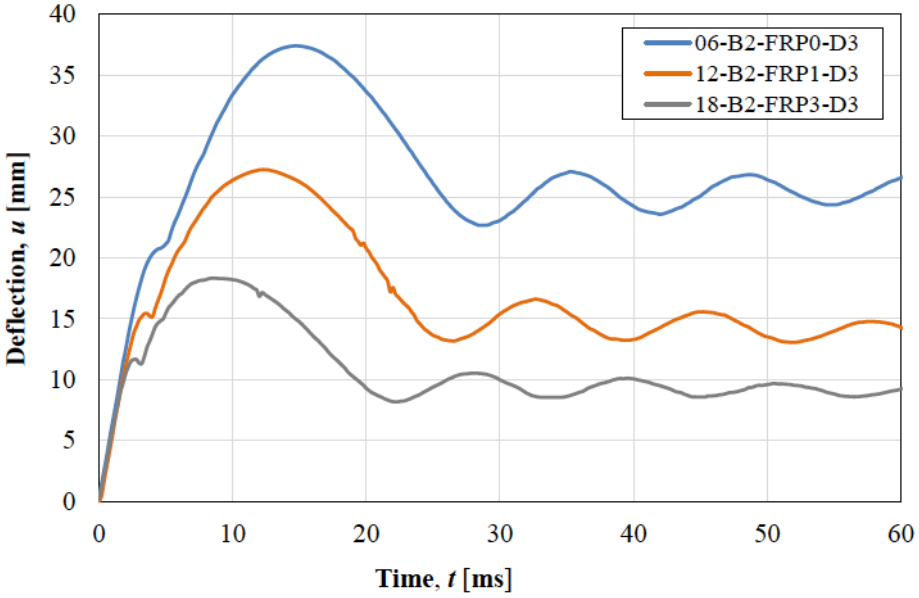

Figure 7.9 *Midpoint deflection versus time for three beams with or without FRP subjected to drop weight from 3 m (Nigani & Nordström, 2020).*

The blue curve is representing an unstrengthened beam, the orange and grey curves represent strengthened beams with one layer and three layers of FRP respectively. The response for a beam with one layer FRP and without from Pham & Hao (2017) is presented in Figure 7.10 where the black curve is unstrengthened and the blue dotted line is a beam with one longitudinal layer of FRP.

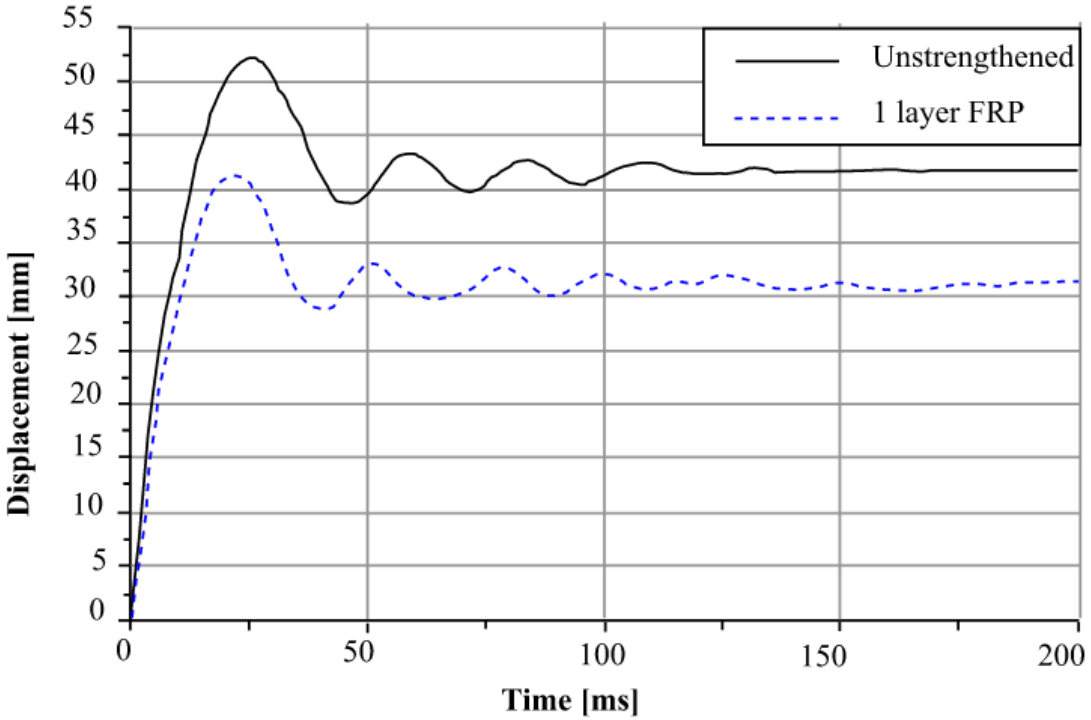

Figure 7.10 *Time versus deflection in midspan for unstrengthened and strengthened beams subjected to drop weight. Based on experimental data (Pham & Hao, 2017).*

Although there are large differences in the drop weight and beam design between Nigani & Nordström (2020) and Pham & Hao (2017) the overall behaviour is similar when comparing unstrengthened and strengthened with one longitudinal wrap. Both show an initial similar linear displacement- time response, independent of the presence of FRP, followed by a certain point where the response for unstrengthened and strengthened beams separate with a following response of a sinus curve with decreasing amplitude which oscillates around the residual deformation until it becomes constant.

Another aspect which could be interesting to investigate further when comparing impact and static loading for FRP strengthened RC beams is the debonding strain. Pham & Hao (2016b, 2017) investigated both static testing and impact testing of beams. The conclusion made from both these cases were that the debonding strain in the impact tests was smaller than the debonding strain in the static tests (Pham & Hao, 2016b; Pham & Hao, 2017).

7.5.2 Large Shear Force due to Impact Load

When a structure is subjected to an impact load in form of a drop weight the failure is not always obvious. Although a beam is designed to fail in bending the shear capacity could still become the limiting capacity (Pham & Hao, 2016a). Due to the fast loading the section subjected to the impact load experience very large shear forces and the support reaction force is zero when the maximum impact force occurs (Saatci & Vecchio, 2009). Pham and Hao (2016b) concluded that the maximum shear force when maximum impact force occurred was larger than at the time for maximum reaction force. With this knowledge, the recommendation was to consider the maximum shear force at time for maximum impact force in design.

7.5.3 Possible Unexpected Behaviour

From a static point of view, an impact load could cause unexpected behaviour in a structure. Pham & Hao (2016a) describes a scenario with structural vibrations where a simply supported beam will experience tensile forces both on the top and bottom. Tang & Saadatmanesh (2003) made experimental testing on several beams exposed to repeated drop weight impact loading and meant that impact loading would result in vibrations causing tensile stresses both on top and bottom. Tang & Saadatmanesh (2003) therefore placed FRP strengthening on both sides of the beams, and the strains were measured both on the top and the bottom of the beam during testing. The results from the tests confirmed their hypothesis, as they found section with higher tensile strains than compressive strains at the top of the beam. This conclusion is something that needs to investigate further but should not be neglected when designing RC structures with FRP strengthening subjected to impact loading.

7.6 Design Methods for Flexural Strengthening

There are several methods for design of flexurally strengthened reinforced concrete beam sections with FRP. The methodology is similar in several of the methods but yet different. The main difference is whether or not the method includes reinforcement in the compression zone or just tensile reinforcement. In this section a couple of chosen design methods are presented together with their assumptions and calculations of different factors in order to calculate the moment capacity of the section.

7.6.1 Design Procedure for Flexural Strengthening, Täljsten et al.

The moment capacity in Stadium III for a composite strengthened cross section can be calculated approximately according to Equation (7.2) and in this case the cross section has just tensile reinforcement according to Figure 7.11 (Täljsten et al., 2016).

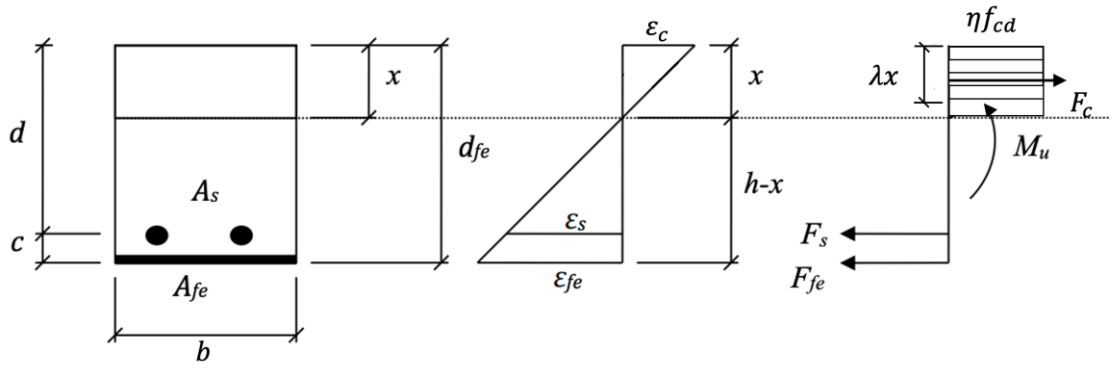

Figure 7.11 Investigate cross section with corresponding stress and strain relations according to the model suggested by Täljsten et al. (2016).

$$M \approx 0.9(A_s f_{yd} d + A_{fe} \varepsilon_{fe} E_{fe} h) \tag{7.2}$$

where M = design moment capacity
A_s = area of reinforcement steel
f_{yd} = design value of the yield strength of reinforcement steel
d = effective height of cross section
A_{fe} = area of composite reinforcement
ε_{fe} = strain of FRP
E_{fe} = modulus of elasticity of FRP
h = height of cross section

To calculate the area of the composite strengthening the following equation could be used

$$A_f \approx \frac{({}^{M_d}/_{0.9} - A_s f_{yd} d)}{\varepsilon_{fe} E_{fe} h} \tag{7.3}$$

The height of the compressive zone, x, and then the moment capacity of the cross section can be calculated as follows

$$x = \frac{A_s f_{yd} + \varepsilon_{fe} E_{fe} A_{fe}}{\lambda \eta f_{cd} b} \tag{7.4}$$

$$M_{Rd} = A_s f_{yd} \left(d - \frac{\lambda}{2} x\right) + \varepsilon_{fe} E_{fe} A_{fe} \left(h - \frac{\lambda}{2} x\right) \tag{7.5}$$

where f_{cd} = design compressive strength
b = width of cross section
η = stress block factor, =1 for $f_{ck} \leq 50MPa$

λ = stress block factor, =0.8 for $f_{ck} \leq 50MPa$

There is a condition that needs to be fulfilled regarding the maximum allowed strain in the FRP. This is due to intermediate crack propagation that moves along the laminate and restricts the FRP from reaching its ultimate strain before debonding is caused.

$$\varepsilon_{fd,ic} = 0.41\sqrt{\frac{f_{cd}}{nE_{fe}t_{fe}}} \leq 0.9\varepsilon_{fu} \tag{7.6}$$

where t_{fe} = is the thickness of the FRP sheet
ε_{fu} = is the ultimate strain of the FRP
n = number of layers of FRP

Similar controls regarding the strains are required as in regular design of moment capacities of cross sections. The reader is referred to (Täljsten et al., 2016) for further information regarding the controls and a more extensive explanation of the design process.

7.6.2 Design Procedure for Flexural Strengthening, fib

The International Federation for Structural Concrete, fib, proposes a similar but yet different method for calculating the moment capacity of a FRP strengthened cross section (Huang et al, 2019). This procedure is based on a cross section and stress-strain relationship as illustrated in Figure 7.12.

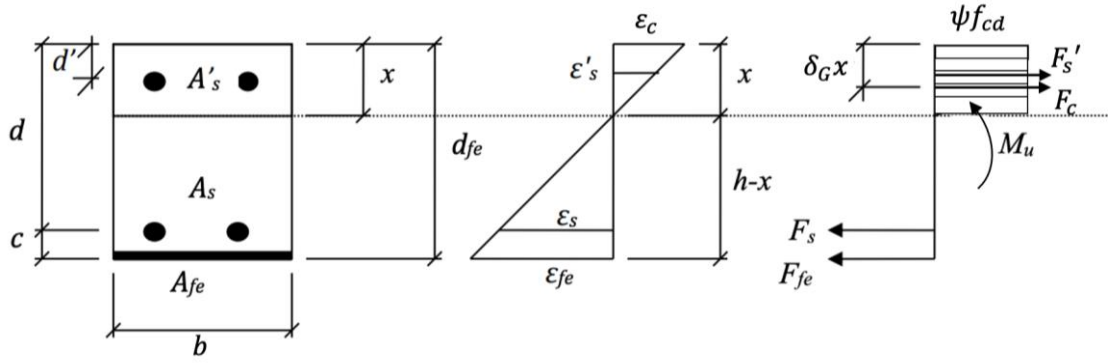

Figure 7.12 Investigated cross section for the fib-model with the corresponding stress and strain relations.

The height of the compressive zone, x, can be calculated from Equation (7.7)[2] and the moment capacity from Equation (7.8) as

$$0.85\psi f_{cd}bx + A_s{}'f_{yd} = A_s f_{yd} + A_{fe}E_{fe}\varepsilon_{fe} \tag{7.7}$$

$$M_{Rd} = A_s f_{yd}(d - \delta_G x) + A_{fe}E_{fe}\varepsilon_{fe}\left(d_{fe} - \delta_G x\right) + A_s{}'E_s\varepsilon_s{}'(\delta_G x - d') \tag{7.8}$$

where ψ = stress block factor

[2] The contribution from the top reinforcement in the horizontal equilibrium for calculating the height of the compressive zone was added since it was absent from the source's equation.

δ_G = stress block factor
d_{fe} = distance from top of cross section to center of fibre reinforcement
A_s' = area of reinforcement steel in the top
ε_s' = strain of top reinforcement
d' = distance from top of cross section to centerline of top reinforcement

The reduction factor in Equation (7.7) of 0.85 is a reduction that considers long term loading and the loss of compressive strength over time. The stress block factors varies with failure modes and are recommended as ψ=0.8 and δ_G=0.4 when the expected failure mode is crushing of concrete (Huang et al, 2019). When instead the expected failure modes are rupture of FRP laminate or a debonding failure mode the stress block factors can be calculated as

$$\psi = \begin{cases} 1000\varepsilon_c(0.5 - 1000\frac{\varepsilon_c}{12}), & \varepsilon_c < 0.002 \\ 1 - 2/(3000\varepsilon_c), & 0.002 \leq \varepsilon_c \leq 0.0035 \end{cases} \quad (7.9)$$

$$\delta_G = \begin{cases} \frac{8-1000\varepsilon_c}{4(6-1000\varepsilon_c)}, & \varepsilon_c < 0.002 \\ \frac{1000\varepsilon_c(3000\varepsilon_c-4)+2}{2000\varepsilon_c(3000\varepsilon_c-2)}, & 0.002 \leq \varepsilon_c \leq 0.0035 \end{cases} \quad (7.10)$$

For end debonding the stress in the FRP can according to Huang et al. (2019) and fib (2001) be calculated as

$$\sigma_{fe} = \frac{c_1}{\gamma_c}\sqrt{\frac{E_f\sqrt{f_{ck}f_{ctm}}}{t_{fe}}} \quad (7.11)$$

where f_{ck} = characteristic compressive strength of concrete
f_{ctm} = mean tensile strength of concrete
γ_c = partial coefficient for concrete, =1.5 normally, =1.2 for accidental loading
c_1 = constant with a value of 0.23

7.6.3 Design Procedure for Flexural Strengthening, ACI

The height of the compressive zone, x, and then the moment capacity of the cross section illustrated in Figure 7.13 can be calculated according to ACI according to (Huang et al, 2019) according to Equations (7.12) and (7.13)[3].

[3] The contribution from the top reinforcement in the horizontal equilibrium for calculating the height of the compressive zone was added since it was absent from the source's equation.

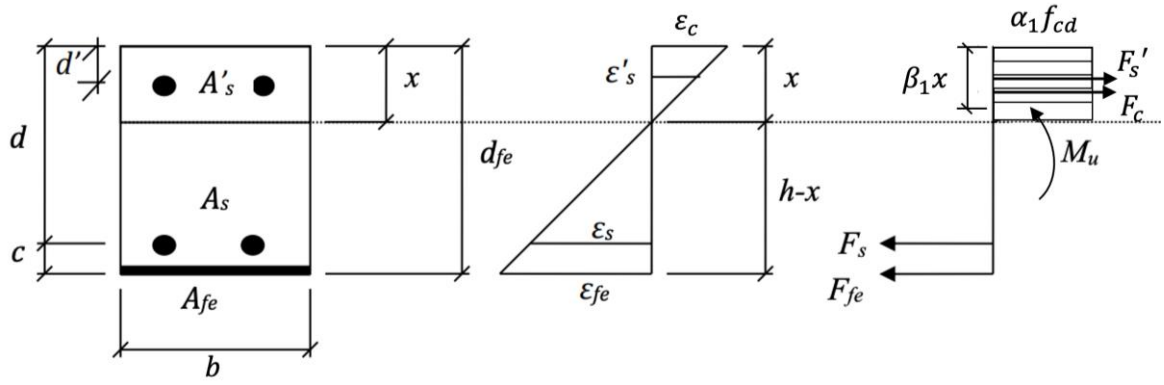

Figure 7.13 Investigated cross section for the ACI-model with the corresponding stress and strain relations.

$$x = \frac{A_s f_{yd} + A_{fe} f_{fe} - A_s' f_{yd}}{\alpha_1 f_{cd} \beta_1 b} \tag{7.12}$$

$$M_{Rd} = A_s f_{yd}\left(d - \frac{\beta_1}{2}x\right) + A_s' f_{yd}\left(\frac{\beta_1}{2}x - d'\right) + \phi_{fe} A_{fe} f_{fe}\left(d_{fe} - \frac{\beta_1}{2}x\right) \tag{7.13}$$

where α_1 = stress block factor, =0.85
β_1 = stress block factor, according to Equation (7.14)
ϕ_{fe} = reduction factor for FRP, recommended value =0.85

$$\beta_1 = \begin{cases} 0.85, & f_{cd} \le 28MPa \\ 0.85 - 0.007(f_{cd} - 28), & f_{cd} > 28MPa \end{cases} \tag{7.14}$$

The strain in the FRP is in the ACI model limited by the same equation as in Täljsten et al. proposed in (Teng et al, 2003) which is Equation (7.6). There is a strength reduction for the materials based on the steel strain (Wu & Eamon, 2017). This reduction factor, ϕ, is explained by the following equation

$$\phi = \begin{cases} 0.90, & \varepsilon_s 0.005 \\ 0.65 + \frac{0.25(\varepsilon_s - \varepsilon_{sy})}{0.005 - \varepsilon_{sy}}, & \varepsilon_{sy} < \varepsilon_s < 0.005 \\ 0.65, & \varepsilon_s < \varepsilon_{sy} \end{cases} \tag{7.15}$$

8 Experimental Procedure

The experimental procedure in this project was static and dynamic loading of 22 beams and corresponding preparations for the test specimens. The testing was divided into either only static loading or dynamic loading followed by static loading to be able to determine the residual strength. The static loading was conducted by three-point bending and the dynamic loading in form of an impact loading from a drop weight of steel from different heights, see Section 8.9 and Section 8.8. In addition to the testing of the beams, testing of several material properties of the concrete and reinforcement steel was also done. The different beams and loading cases and other certain properties connected to the specimens are presented in Table 8.1. Since the beams tested with a drop weight from 3.0 m experienced small deformations a decision was made during the experiments to add a fourth height, 5.7 m. The geometry of the test specimens is described in Section 8.1.

Table 8.1 Summary of the test specimens.

Beam No.	Beam Name	Type of loading	Drop height	Number of FRP layers	Type of Adhesive	Test day
1	01-S-0FRP	Static	-	-	-	March 16
2	02-S-0FRP	Static	-	-	-	March 16
3	03-S-1FRP-S&P	Static	-	1 layer	S&P	March 16
4	04-S-1FRP-S&P	Static	-	1 layer	S&P	March 16
5	05-S-1FRP-NM	Static	-	1 layer	NM	March 16
6	06-S-1FRP-NM	Static	-	1layer	NM	March 16
7	07-IS-3m-0FRP	Impulse + Static	3.0 m	-	-	March 15 + March 18
8	08-IS-3m-1FRP-S&P	Impulse + Static	3.0 m	1 layer	S&P	March 15 + March 17
9	09-IS-5.7m-1FRP-S&P	Impulse + Static	5.7 m	1 layer	S&P	March 15 + March 18
10	10-IS-3m-1FRP-NM	Impulse + Static	3.0 m	1 layer	NM	March 15 + March 17
11	11-IS-5.7m-1FRP-NM	Impulse + Static	5.7 m	1 layer	NM	March 15 + March 18
12	12-IS-4m-0FRP	Impulse + Static	4.0 m	-	-	March 15 + March 18

Beam No.	Beam Name	Type of loading	Drop height	Number of FRP layers	Type of Adhesive	Test day
13	13-IS-4m-1FRP-S&P	Impulse + Static	4.0 m	1 layer	S&P	March 15 + March 17
14	14-IS-4m-1FRP-S&P	Impulse + Static	4.0 m	1 layer	S&P	March 15 + March 17
15	15-IS-4m-1FRP-NM	Impulse + Static	4.0 m	1 layer	NM	March 15 + March 17
16	16-IS-4m-1FRP-NM	Impulse + Static	4.0 m	1 layer	NM	March 15 + March 17
17	17-IS-5m-0FRP	Impulse + Static	5.0 m	-	-	March 15 + March 18
18	18-IS-5.7 m-0FRP	Impulse + Static	5.7 m	-	-	March 15 + March 18
19	19-IS-5m-1FRP-S&P	Impulse + Static	5.0 m	1 layer	S&P	March 15 + March 17
20	20-IS-5m-1FRP-S&P	Impulse + Static	5.0 m	1 layer	S&P	March 15 + March 17
21	21-IS-5m-1FRP-NM	Impulse + Static	5.0 m	1 layer	NM	March 15 + March 18
22	22-IS-5m-1FRP-NM	Impulse + Static	5.0 m	1 layer	NM	March 15 + March 18

8.1 Geometry of Test Specimen

The beams were of equal dimensions with a length of 1400 mm and a cross section of 100x100 mm. The beams were reinforced with four symmetrically placed longitudinal reinforcement bars with a diameter of 6 mm. The concrete cover of the beams was 17 mm which results in 20 mm from edge to centreline of reinforcement. The geometry of the specimens is visualized in Figure 8.1.

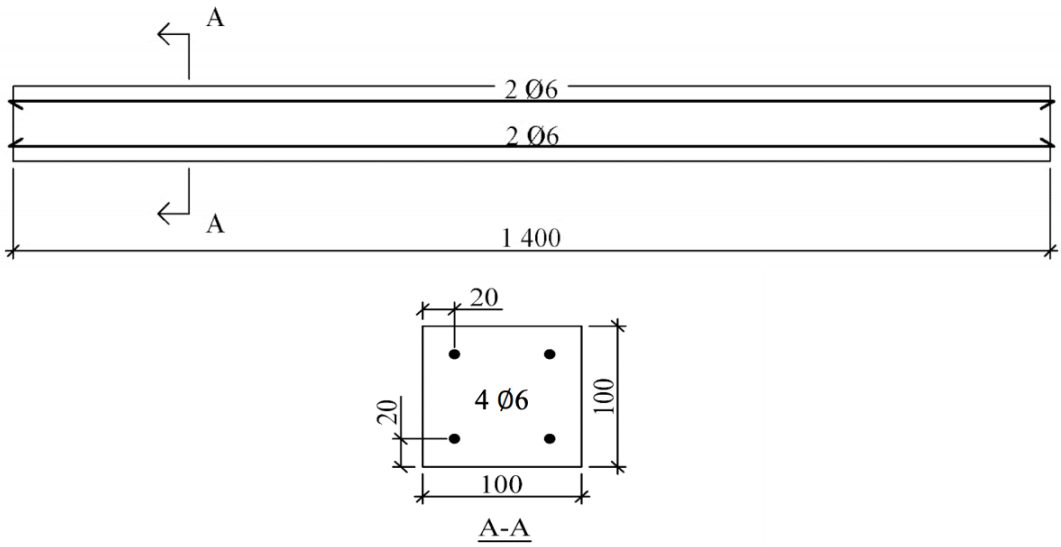

Figure 8.1 Geometry of the specimen (Jönsson & Stenseke, 2018).

8.2 Preparations Before Casting

At first the moulds for the beams were prepared. The moulds were from previous years together with a couple of newly created moulds, but all were of equal dimensions and condition according to Figure 8.1. The moulds were of timber boards that were screwed together. They had four drilled holes, of approximately 5 mm, on either short end at the distance where the reinforcement was to be placed.

Firstly, the moulds were all cleaned and oiled thoroughly. Secondly the reinforcement was cut and placed into the desired locations. In order to make sure the reinforcement kept its desired placement along the whole beam length during the casting steel wires were used to keep the reinforcement bars in its correct place. A short piece of reinforcement was placed transversely across the mould at a distance of approximately L/3. From this transverse bar, the steel wires were attached to the two bars in each layer to ensure correct placement. This is visualized in Figure 8.2.

Figure 8.2 Placement of reinforcement.

In Figure 8.2 wooden blocks in the bottom of the mould can be seen. These were placed to ensure the concrete cover distance during the fastening of the steel wires and later removed before casting. The blocks in the bottom were of 17 mm thickness and the

block in the centre of the cross section between the two layers were 56 mm. Thirdly, all the moulds were marked with a certain number. This was in order to keep track of a specimen if the pulling test of the reinforcement, which was later executed, showed a higher or lower strength than the average strength or another property deviating from the average behaviour of the reinforcement. Since each beam had four bars from one original reinforcement bar, the results from tensile tests and the beams could be connected.

Apart from the beam moulds, moulds for the material tests were also prepared, see Figure 8.3. These were cubes to test the compressive strength and cubes to test the fracture energy with a WST, wedge splitting test.

Figure 8.3 *Moulds for the material tests of concrete. Compressive strength test at 28 days and during the day of testing of the beams as well as cubes for WST.*

8.3 Casting

The concrete recipe was done and ordered from Thomas Betong. A truck with one batch enough for all beams delivered the concrete. The concrete was spread out with a concrete scip to fill up the moulds roughly and finalized with concrete from buckets to get the desired amount. The arrangement of the test specimens is illustrated in Figure 8.4.

Figure 8.4 Arrangement of test specimens.

A concrete class of C40/50, with a water-cement ratio of 0.40, was ordered, see Table 8.2. A retarder was included in the concrete to delay the hydration process and achieve enough workability during the entire casting. The consistency class ordered was S4, corresponding to a slump test result of 160-210 mm (CEN, 2019a). However, when slump tests were done during the casting the consistency class was instead found to correspond to S5. Apart from that, no problems were encountered. The testing of the concrete is further discussed in Section 8.6.

Table 8.2 Concrete properties ordered.

Concrete class	Water cement ratio	Consistency class	Largest aggregate size	Cement type
C40/50	0.40	S4	16 mm	Std. Cem

To get a homogenous concrete a vibrator rod was used to vibrate the concrete and the surface was smoothed; special care was shown to the surface where the drop weight later was supposed to impact the beam. The following step was to cover the test specimens with a plastic sheet, and in case of need put some water on the specimens.

8.4 Preparation and Application of FRP

Before the FRP could be laminated to the tensile face of the beam the face had to be properly prepared. This section deals with the preparations before application as well as the application of the FRP. Mechanical properties of the FRP are presented in Table 8.3.

Table 8.3 Mechanical properties of the Kevlar.

Technical data unidirectional	A-sheet 120 290 g/m
Elastic modulus	≥ 120 GPa
Tensile strength	≥ 2.9 GPa
Fibre weight	0.290 kg/m^2
Weight per unit area of sheet	0.32 kg/m^2
Density	1450 kg/m^3
Elongation at rupture	2.5 %
Design thickness (fibre weight/density), longitudinal	0.20 mm

8.4.1 Preparation of Bottom Surface

In order to get a good adhesion between FRP and concrete the bottom surfaces of the beams were treated according to Section 7.3.1. The surfaces were grinded with an angle grinder with a diamond grinding wheel to remove oil and dust. The aim of this procedure was to remove the top layer of concrete and make the surface rough to enable a better and stronger bond between FRP and the concrete. The angle grinder, the grinding wheel and the working set-up used are presented in Figure 8.5.

Figure 8.5 Tool and set-up for grinding surfaces of specimen.

When the surfaces were grinded it was of importance to remove the entire first layer of concrete and achieve the desired rough surface. This was achieved by going from one edge of the beam towards the other. The surface was grinded in the longitudinal direction and then along the width of the face. It was important to not treat the same place of the surface several times, since this could result in a smoothened surface instead of the rough surface desired.

Figure 8.6 Example of grinded surface compared to ungrinded surface.

After grinding, the surface was cleaned with pressurized air to remove all the dust and excess concrete. And finally, before the lamination of the FRP-sheet the surfaces were cleaned with acetone and dried with pressurized air to ensure a good adhesion.

8.4.2 Preparation of FRP Sheets

The FRP sheets were of the dimensions 1200 mm length and 100 mm width. The width of the entire sheet was 280 mm and therefore two strips from each piece with a length of 1200 mm could be acquired. It was first cut with scissors at 1200 mm and then with a straight cut along the length of the strip.

Figure 8.7 The kevlar used to strengthen the beams.

After the cut along the middle of the width of the strip the sheet was moved to the boards and stacked on top of other sheets with strips of plastic in between. The fibres were then removed from the middle and outwards until a width of 100-105 mm was achieved.

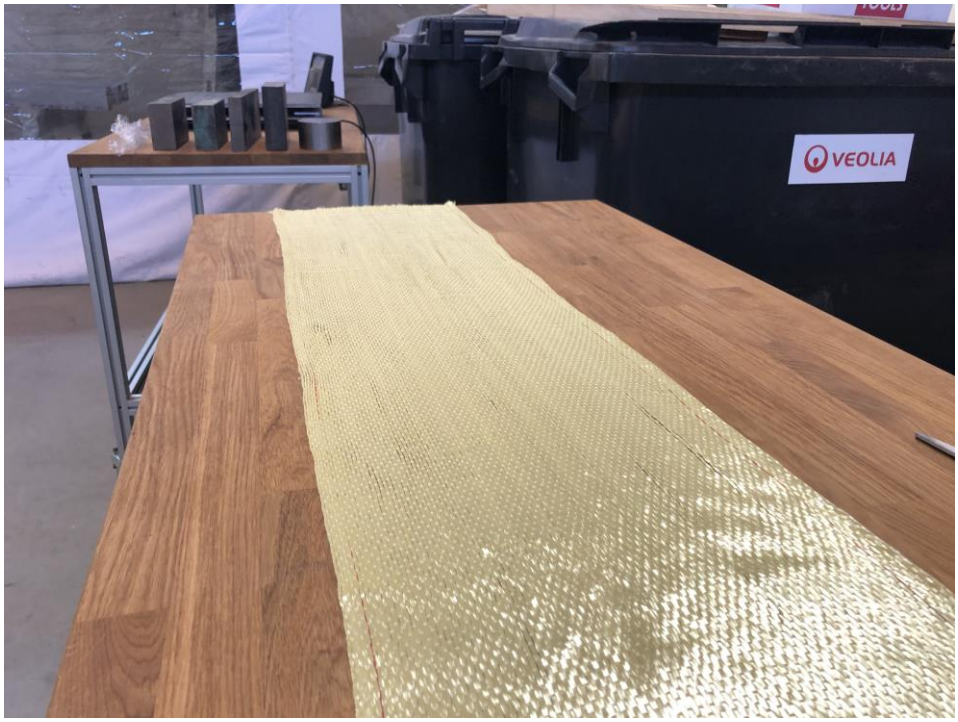

Figure 8.8 A strip of kevlar that later is divided into two strips.

8.4.3 Application of Adhesive and FRP

The adhesives used consisted of two different kinds of epoxies with different configurations in order to achieve different behaviour. The two configurations for the different epoxies came from the companies S&P and Nils Malmgren. The specific adhesives were S&P Resin 55 HP (S&P, n.d.) and NM Laminering 625 (Nils Malmgren, 2011). Different levels of ductility of the adhesives were the desired outcome of the usage of two kinds of adhesive. The mixing and application of epoxy were performed by research engineer Anders Karlsson. One intention during the project was to investigate more types of adhesives with other properties and behaviour but due to different reasons this plan was not realised; however, it could be an interesting topic to investigate in future studies.

Figure 8.9 Application of adhesive and FRP to the bottom surface.

After the epoxies were mixed the bottom surface of the specimen and the kevlar sheet were completely and evenly covered in epoxy. Then the FRP sheet was applied from one of the short ends and then placed accordingly from that first end towards the second edge. The sheets had been placed on a wooden board with alternating strip of plastic and FRP sheet in order to lift the FRP for the adhesion with the epoxy making sure the fibres did not separate. After the FRP sheets had been made the fibre at the cut edge of the strip had a tendency to separate if not treated carefully. Therefore, it was essential to not lift the sheet itself but lift the plastic strip, which the FRP sheet rested on in order to maintain the geometry of the strip as well as ensuring a convenient application of the epoxy and FRP to the bottom surface of the beams. The outmost fibres were also folded inwards using the piece of plastic in order for the sheet to stay together in a desirable way and then the FRP sheet was placed on the surface of the beam. When the sheet was placed the fibres were finely adjusted to make sure that the fibres were completely aligned.

Figure 8.10 Application of adhesive and FRP to the bottom surface.

Figure 8.11 FRP attached to the concrete surface.

8.5 Painting of Specimen

The specimens were first painted in white followed by a black speckly pattern. This was done in order to use Digital Image Correlation, or DIC, to capture the behaviour of the beams under loading, see Section 8.7.

Figure 8.12 Specimen painted with white colour.

The surfaces were cleaned and prepared for the painting and afterwards the surface which was going to be recorded by the cameras was painted white. It was desirable to have a rather thin layer of paint. After the white paint had dried the surface was painted in a black speckly pattern according to Figure 8.13. The distribution between the white and the black paint was approximately even as desirable. If there were any zones with too much white or black markers with the corresponding colour was used to dot the areas with a need of additional paint. If there still were zones which made the DIC not capture the entire area the same procedure was conducted.

Figure 8.13 Specimen painter in a black and white speckly pattern.

To achieve the speckled pattern desired, a certain type of brush was used to apply the black paint, see Figure 8.14. The entire beam length was painted in this pattern. This was because of the camera set up and field of view.

Figure 8.14 The brush used to apply the black paint.

8.6 Material Testing

Several material tests were made to define the properties of the concrete, the reinforcing steel and the adhesive used in the experiments. Tested material properties and their corresponding test procedures are presented in following three sections.

8.6.1 Testing of concrete

Three different aspects were interesting when the concrete was tested: consistency, compressive strength and fracture energy. Consistency was tested with a slump test according to CEN (2019a). Two tests were made, one in the beginning of the casting and one in the end when all moulds were filled. The first slump test gave a result of 250 mm and the second one a result of 240 mm, which results in category S5. The concrete was a bit more volatile than expected but it had no negative consequences on the casting. An illustration of the slump test and results are presented in Figure 8.15.

a) *b)* *c)*

Figure 8.15 Illustration of one slump test made during the casting.

In addition to the testing of the fresh concrete, two different tests were done on the hardened concrete. Six cubes were tested for compressive strength in accordance with CEN (2019b). Half of them were tested at 28 days and the other half at the time for testing of the beams, which was after 40 days. The dynamic tests were performed 38 days after casting and the static tests were performed after 39,40 and 41 days. The cubes were demoulded after 24 hours and then placed in water. Illustration of the test specimens and the testing is presented in Figure 8.16.

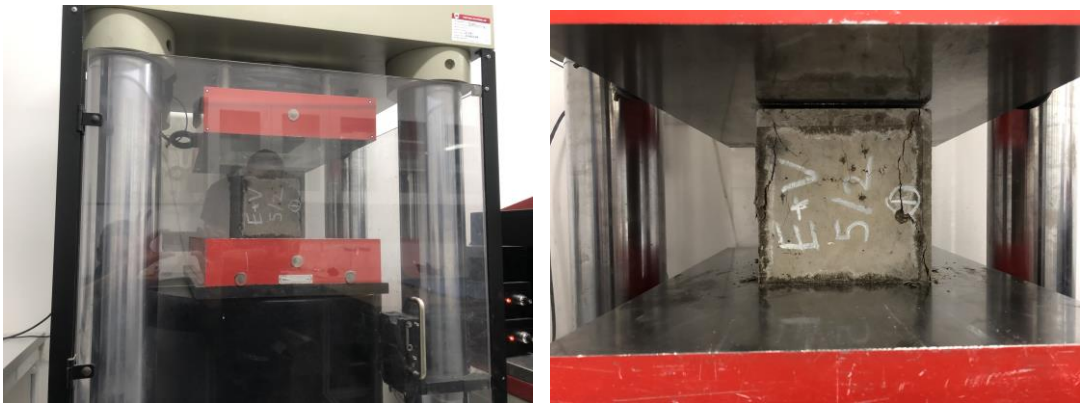

Figure 8.16 Test of cube compressive strength.

The final aspect tested was the concrete fracture energy. Three specimens were prepared for this test and the specimens are illustrated in Figure 8.17 and the test set up in Figure 8.18. They were demoulded after 24 hours and placed in water. The fracture

energy was tested by a Wedge Splitting Test according to Tschegg (1991) and Löfgren et al. (2004).

Figure 8.17 Preparation of the specimen and the sawing of the starting notch.

Figure 8.18 Wedge splitting test set up.

8.6.2 Testing of Reinforcement Steel

Studied parameters when testing of the reinforcement steel was done was proof strength, ultimate strength, ultimate steel strain and modulus of elasticity. To get a trustworthy result from testing samples from six different bars were collected. These bars were also identified and connected to a test beam to be able to examine possible reasons to unexpected behaviour of the beams. Each test specimen was approximately 350 mm long where 50 mm on each side of the specimen was fastened in the test machine, resulting in approximately 250 mm left for testing. The test configuration is presented in Figure 8.19.

Figure 8.19 Tensile test of reinforcement bars.

The machine used for the tensile test was the same as was used for the wedge splitting test. The test was performed in two stages, with different deformation rates. The first one was until the bars reached yielding and then at a higher deformation rate until failure of the bar. The deformation rates were 5 mm/min and 120 mm/min where an extensometer was used during the first stage to measure the strains in a more precise way. After the first stage the machine paused and the extensometer was removed and then the second stage with a much faster loading rate initiated and the bars were pulled until failure.

8.6.3 Testing of Epoxy Adhesive

The two different types of adhesive used was tested in the same manner as the reinforcement bars in form of tensile tests. Since this has not been done in the previous thesis in 2020 it resulted in many challenges, both with the creation of the test specimens and the tensile testing.

Six test specimens were casted from each adhesive type to a form of a dogbone. The mould used were sawn out from a fibre board. To be able to create the specimens a vacuum pump was used to try to soak up the epoxy into the forms, which was concluded as a good process. One problem though was that air leaked through the fibre boards and to get rid of this problem, a plastic bag was used around the moulds to prevent the provision of air. This measure was enough to create good specimens for one of the adhesives (Nils Malmgren) but the other one (S&P) got some air bubbles although measures were done. The casted specimens are shown in Figure 8.20 a) and b).

a) b)

Figure 8.20 Dogbones for test of adhesives.

To provide good attachment in the test machine, small aluminium plates were glued on the top and bottom on both sides of the test specimens, see Figure 8.21. Testing of the specimens were then done in the same machine as the reinforcement bars. The speed used was 1 mm/min. An extensometer was attached at the specimens, placed in an area with as few defects as possible (defects were most often in the form of air bubbles) and later removed at a certain load value with the purpose to make sure it was not attached when failure was assumed to take place. Since the test specimens were of varying quality and the presence of air bubbles had a large effect of the final load capacity, a considerable scatter in the load capacity was obtained in the tests. Due to this, it was decided to only study the elastic modulus of the two adhesives.

Figure 8.21 Test specimen with aluminium plates attached.

Since the hardening time of the two adhesives was different, the testing of S&P was done at a time to correspond to the hardening time of the beams with this adhesive and

the testing of NM was done to correspond to the age of the beams with NM but also at an age of seven weeks when the adhesive was supposed to have hardened not completely but much more. Another aspect worth to mention was that the NM adhesive was supposed to be heat cured but it was not possible to accomplish in this project and therefore the hardening time could have been affected. Without heat curing the hardening time would be longer and one part of the experiments was to investigate the effect on the hardening that a longer hardening time had.

8.7 Digital Image Correlation - DIC

Digital Image Correlation or DIC is a method used to analyses strains, deformations, cracks, crack widths, stresses together with other outputs. These outputs come from analysis of a large number of images. The images were taken with two high speed cameras for the dynamic tests. For the static tests a set of two cameras were also used. The software used to analyse the images and calculate the different output results was GOM Correlate 2018 Professional (GOM, 2018). The camera set-ups are discussed more in Sections 8.8 and 8.9 for the dynamic and static tests respectively. Further information about how the settings used for the analysis were produced, for example how the facet size was chosen, see Appendix A .

8.7.1 DIC and Cameras for the Dynamic Tests

The two cameras used to capture the behaviour of the drop weight and the beam had certain specifications and certain settings which were necessary inputs in GOM Correlate when the data were processed. This information is presented in Table 8.4 and Table 8.5 for the two cameras used in the dynamic tests.

Table 8.4 Specifications for camera 1.

High speed camera	Photron SAZ
Distance from camera house to front of the beam	1.87 m
Zoom	Nikon 70-200 mm lens (focal distance 200 mm)
Resolution	1024x400 pixels
Spatial scale	Calibrated with 40 mm measuring scale => 40 mm = 183 pixels => 1 pixel = 0.21858 mm
Approximate measured area	224x87 mm
Frame rate	40000 FPS (every 0.025 ms)
Shutter	1/50000
Trigging	Manual trigging with “centre trigger” capturing approximately 1 s before and after

Table 8.5 Specifications for Camera 2.

High speed camera	Photron SA4
Distance from camera house to front of the beam	2.04 m
Zoom	Nikon 50 mm lens
Resolution	1024x400 pixels
Spatial scale	Calibrated with 40 mm measuring scale => 40 mm = 53 pixels => 1 pixel = 0.75472 mm
Approximate measured area	773x301mm
Frame rate	5000 FPS (every 0.2 ms)
Shutter	1/7000
Trigging	Manual trigging with "centre trigger" capturing approximately 1 s before and after

8.7.2 DIC and Camera for the Static Tests

The cameras used for the static tests were a set of two cameras for the same system. The cameras were mounted on the same rig but with one camera moved slightly towards the left and one towards the right. This set-up works as one camera finds one facet on the beam and the other camera finds the same facet and constantly synchronizes the information between the two cameras. This enables both capturing of the behaviour in the plane as well as out of plane movements. This type of test set-up was less sensitive compared to the cameras used for the dynamic tests because the two cameras synchronize themselves for each facet in the structure it studies. Once it was calibrated it could be moved and re-placed at roughly the same position and still capture the information in a good way. The data from the static tests were processed in GOM Correlate 2018 Professional (GOM, 2018) as for the dynamic tests. The major difference between the static and dynamic DIC were the image frequency, where the frequency for the static tests were 0.5 FPS, i.e. one image every two seconds.

8.8 Dynamic Testing and Set-up

The dynamic testing of the beams was performed as a steel cylindrical rod was dropped from various heights on the top edge and in the centre of the beam. Out of the 22 beams 16 were tested dynamically according to Table 8.1 with drop heights of 3.0, 4.0, 5.0 and 5.7 m. The drop weight tests took place 38 days after casting.

The beams were placed on roller supports that prevented movement downwards but otherwise the movement of the beams were not restricted. The test rig was fixed in the concrete floor which made sure that the beams always were placed symmetrically and in the same spot. Two high speed cameras were used to capture the behaviour of the beams at impact and the data was then analysed using Digital Image Correlation, DIC. Camera 2 had 5 000 FPS and captured slightly more than half of the beam length while Camera 1 with 40 000 FPS focused on the drop weight and the midpoint of the beam where the impact occurred. The test set-up for the dynamic tests is schematically illustrated in Figure 8.22, where the capture zone of the 5 000 FPS camera is illustrated

with black dotted lines and the capture zone of the 40 000 FPS camera is illustrated with red dotted lines.

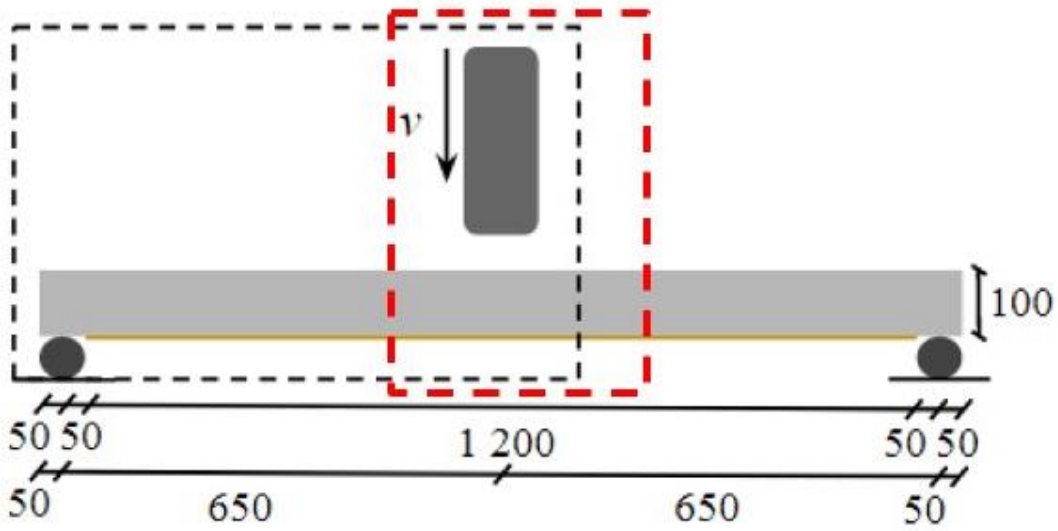

Figure 8.22 Schematic illustration of the test set-up for the dynamic tests where the black and red dotted lines illustrates the capture zone of the 5 000 FPS and 40 000 FPS camera respectively.

The drop weight was raised above the centre of the beam in a steel guiding tube rig by a rope connected to the cylinder. Another rope was connected to a release mechanism which, when pulled, released the drop weight. The drop weight was also painted in the black specky pattern same as the beams in order for the second camera with 40 000 FPS, focusing on the drop weight, to capture the impact. The drop heights were measured prior to the tests and the correct heights were marked on the tube. In order to validate the drop heights web cameras broadcasting live feeds on different heights were used in order to see when the drop weight cylinder was at the correct height. How the test set-up looked in reality can be seen in Figure 8.23 and an example of the web camera set up can be seen in Figure 8.24.

Figure 8.23 Test set-up for dynamical tests.

Figure 8.24 Web camera set-up showing camera placement and height marking on the guiding tube.

8.9 Static Testing and Set-up

The static tests were performed from 38 to 40 days after casting. The tests were performed on undamaged beams, i.e. tested only statically, as well as damaged beams previously subjected to drop weight tests in order to capture their residual strength. The beams were placed on roller supports with a 1300 mm centre-centre distance between the supports. The diameter of the roller supports was 70 mm.

The load was applied as three-point bending where a roller along the entire width of the beam was placed on a steel plate which was placed onto the beams. The dimensions of the plate were 225x70x25 mm, resulting in a contact area with the test beams of 70x100 mm. If the beams were damaged from the drop weight it was made sure that the load was applied in the centre of the span. If a beam was severely damaged from the drop weight, which were the case for some of the beams subjected to a drop from 5.7 m, the steel plate was centralized over the damage instead. This was done so that also the most damaged beams could be statically loaded but made the point load shift a couple of centimetres from the middle of the beam.

Another camera set-up was used for the static tests. How the cameras for the static tests worked is further explained in Section 8.7.2. The static test set-up is illustrated schematically and from the tests in Figure 8.25 and Figure 8.26 respectively.

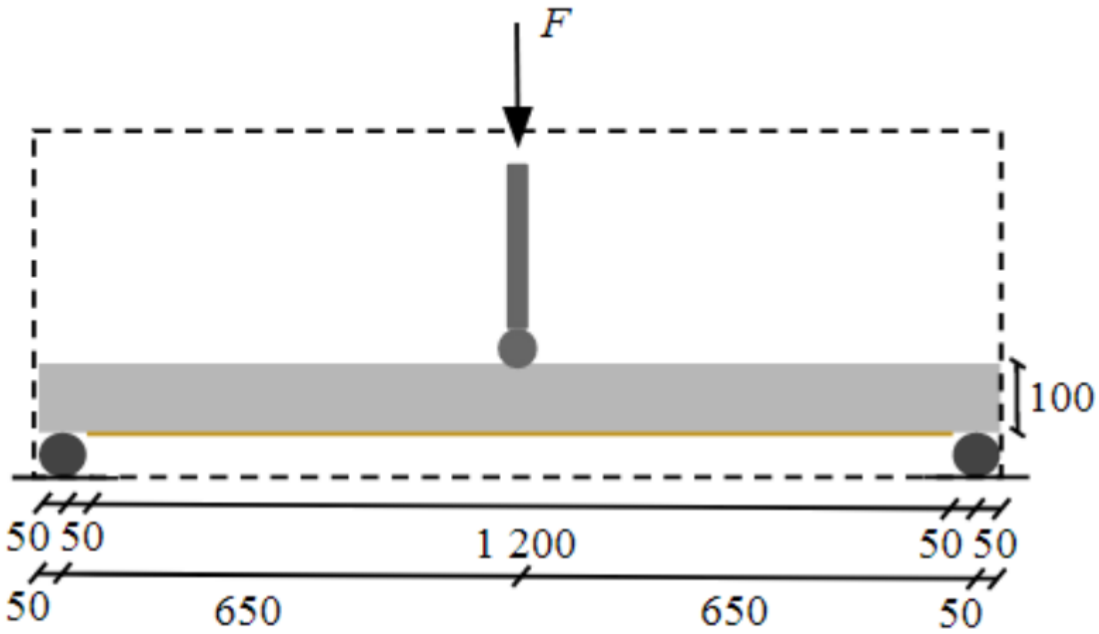

Figure 8.25 *Schematic illustration of the test set-up for the static tests where the black dotted line illustrates the capture zone of the DIC camera used for static tests.*

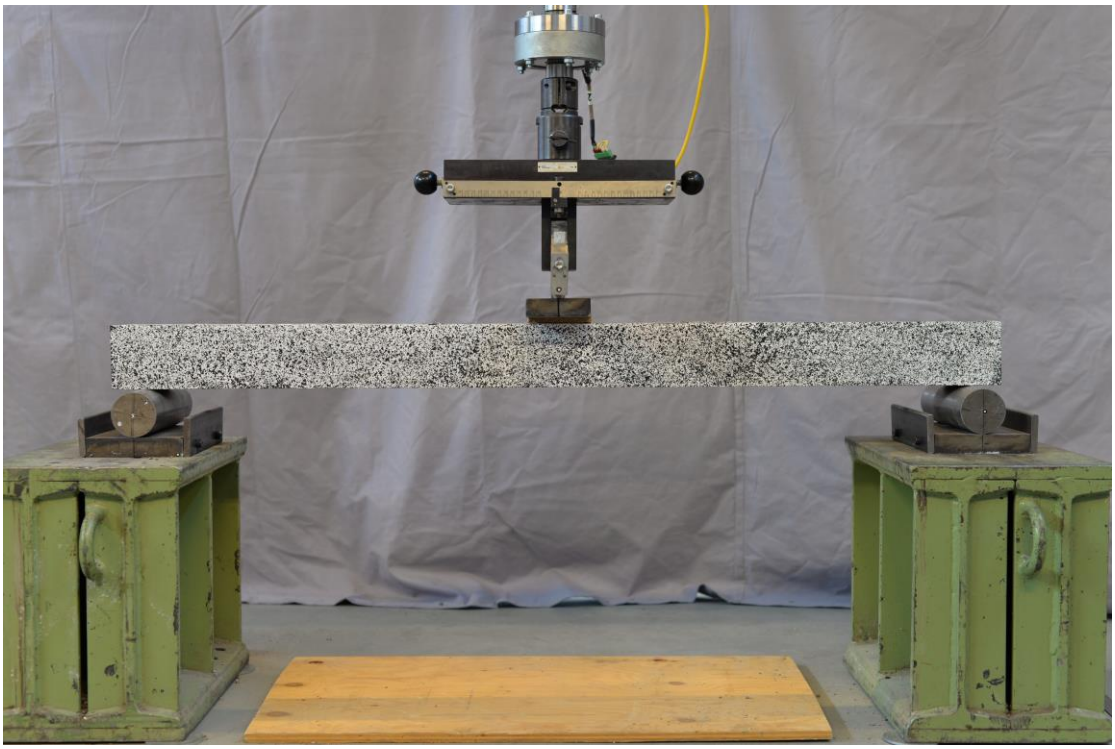

Figure 8.26 Test set-up for static tests.

The load was applied as a deformation-controlled loading where the deformation rate was 2 mm/min the first 30 mm of deformation and after the 30 mm of deformation the deformation rate was increased to 5 mm/min. Load was applied up to 2 kN followed by unloading down to 0.5 kN and then the load was increased until failure according to the deformation rates stated in this section. The tests were usually continued until rupture of a reinforcement bar was obtained. However, in a few cases where damaged beams were tested statically, the residual strength could be low or the plastic deformations from the impulse loading could be large. The load-deflection curve could be protracted with a low load capacity and large deformations. For these cases the tests were not continued until rupture of a reinforcement bar, instead stopped manually at large deformations. This is discussed more under the results of the static tests in Section 10.3.

9 Predictions

Predictions were made in order to compare the real response with an estimated response of the beam. The predictions are treated in this chapter and include both static and dynamic response.

9.1 Static Response

The predictions of the static response include bending stiffness, load and moment capacities in ultimate limit state (ULS), cracking moment and cracking force, load deflection relationships and plastic rotation capacities. The static predictions deal with both unstrengthened and FRP strengthened beams and calculations according to different methods and comparisons between these methods.

9.1.1 Load and Moment Capacity in ULS

For the ULS calculations a linear stress-strain relationship was used together with a criterion that the ultimate concrete strain was reached. The calculation also considered an idealized stress-strain relationship for the concrete in the compressive zone in accordance with Eurocode 2. The model used for the calculations is illustrated in Figure 9.1.

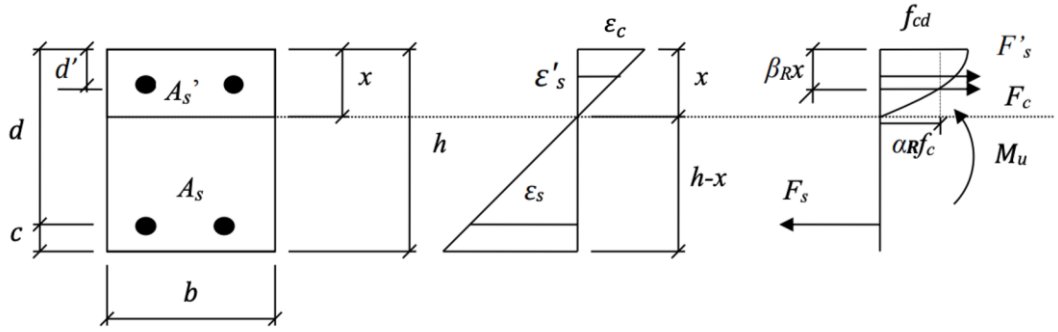

Figure 9.1 Illustration of the assumed response used in the ULS calculations. Modified from (Lozano & Makdesi, 2017).

The concrete and reinforcement properties needed for the calculations came from the material test that were made within the project. The properties are presented in Section 10.1.

The material models used for the concrete and reinforcement is expressed by Equations (9.1) and (9.2), respectively. For concrete, an idealized stress-strain relationship was used in compression. For reinforcement the stress-strain relationship was a simplified idealized relationship with an upper ascending branch from the point of yielding until failure.

$$\sigma_c = \begin{cases} \left[1 - \left(1 - \frac{\varepsilon_c}{\varepsilon_{c2}}\right)^n\right] f_c & 0 \le \varepsilon_c \le \varepsilon_{c2} \\ f_c & \varepsilon_{c2} \le \varepsilon_c \le \varepsilon_{cu2} \end{cases} \quad (9.1)$$

$$\sigma_s = \begin{cases} E_s\varepsilon_s & \varepsilon_s \leq \varepsilon_{sy} \\ f_{yk} + \frac{\varepsilon_s - \varepsilon_{sy}}{\varepsilon_{suk} - \varepsilon_{sy}}(kf_{yk} - f_{yk}) & \varepsilon_{sy} \leq \varepsilon_s \leq \varepsilon_{suk} \end{cases} \quad (9.2)$$

$$k = \left(\frac{f_{tk}}{f_{yk}}\right) \quad (9.3)$$

where ε_c = concrete strain
ε_{c2} = concrete strain when the stress strain relationship gets horizontal branch, = 2 ‰ for ≤C50/60
ε_{cu2} = failure strain, = 3.5 ‰ for ≤C50/60
f_c = concrete strength in compression, here mean values are used
E_s = modulus of elasticity of steel
ε_s = steel strain
ε_{sy} = steel yield strain
ε_{suk} = characteristic steel failure strain
f_{tk} = characteristic ultimate steel strength at tensile failure
f_{yk} = characteristic steel yield strength, here 0.2-limit

Based on Figure 9.1, a horizontal equilibrium was stated and through the calculated height of the compressive zone the ultimate moment capacity could be calculated according to Equation (9.4) and Equation (9.5), respectively. When both layers of reinforcement were considered, the equilibrium was established as shown in Equation (9.4) but when the top reinforcement was neglected its contribution was not considered. It is worth noticing that the compressive zone was above the top reinforcement layer. Therefore, in the calculations for the predictions in this section, the contribution in the horizontal equilibrium, and the moment capacity, was negative when top reinforcement was considered. The calculations treated in this section is presented in its entirety in Appendix M .

$$\alpha_R f_{cd} bx + \sigma_s' A_s' = \sigma_s A_s \quad (9.4)$$

$$M_{Rd} = \alpha_R f_{cd} bx(d - \beta_R x) + A'_s(d - d') \quad (9.5)$$

where α_R = stress block factor, = 0.81 in ULS
β_R = stress block factor, = 0.416 in ULS
f_{cd} = design compressive strength of concrete
b = width of cross section
x = height of compressive zone
d = effective height for bottom reinforcement
d' = effective height for top reinforcement
σ_s = stress in bottom steel
σ'_s = stress in top steel
A_s = area of bottom steel in the cross section
A'_s = area of top steel in the cross section

With the ultimate moment capacity, the ultimate force in a three-point bending was calculated as

$$F_u = \frac{4M_{Rd}}{L} \tag{9.6}$$

and the results are presented in Table 9.1. The self-weight was not considered in this calculation.

Table 9.1 Ultimate moment and load for unstrengthened cross section.

Type of cross section	***Ultimate moment*** M_u **[kNm]**	***Ultimate load*** F_u **[kN]**
Bottom reinforcement only	2.56	7.89
Top and bottom reinforcement	2.75	8.47

When calculating the ultimate moment and force for a FRP strengthened beam the same procedure and assumptions as described earlier in this section was used but with the FRP added in the section and treated as a reinforcement layer but with properties according to FRP. The compressive zone was again above the top layer of reinforcement. Therefore, in the calculations for the predictions in this section, the contribution in the horizontal equilibrium, and the moment capacity, was negative when top reinforcement was considered. The linear stress-strain relationship and the assumed response is illustrated in Figure 9.2.

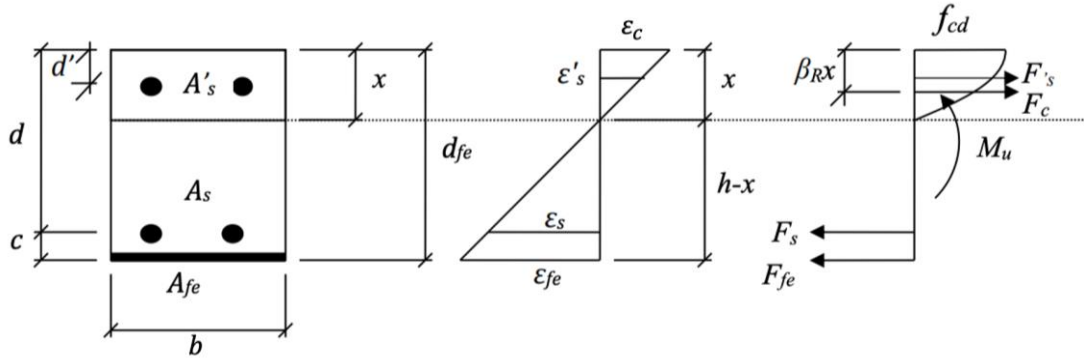

Figure 9.2 Illustration of the assumed response used in the ULS calculations for a FRP strengthened cross section.

$$\alpha_R f_{cd} bx + \sigma_s' A_s' = \sigma_s A_s + \sigma_{fe} A_{fe} \tag{9.7}$$

$$M_{Rd} = \alpha_R f_{cd} bx(d - \beta_R x) + \sigma'_s A'_s (d - d') + \sigma_{fe} A_{fe} (d_{fe} - d) \tag{9.8}$$

where σ_{fe} = stress in the FRP
A_{fe} = area of FRP
d_{fe} = effective height of FRP

The strain in the FRP was also controlled according to Equation (7.6) followed by ultimate force calculation according to Equation (9.6).

The moment and force capacities were also calculated according to the methods described in Täljsten et.al (2016) and fib (2001) as described in Section 7.6.1 and 7.6.2, respectively; the results are presented in Table 9.2.

Table 9.2 Ultimate moment and load for FRP strengthened cross section.

Method	***Ultimate moment*** M_u **[kNm]**	***Ultimate load*** F_u **[kN]**
Eurocode 2 method with FRP included	6.15	18.93
Kompositförstärkning av betong	6.97	21.45
FIB	5.68	17.48

9.1.2 Cracking Moment and Cracking Load

The cracking moment and the corresponding force for both unstrengthened and strengthened beams were calculated with Navier's formula where the stress was the concrete flexural strength and the moment of inertia was the second moment of inertia with reinforcement included for an uncracked concrete member, stadium I, with and without FRP strengthening.

$$M_{cr} = \frac{f_{ct,fl} I_I}{\frac{h}{2}} \tag{9.9}$$

where $f_{ct,fl}$ = flexural concrete strength
I_I = second moment of inertia
h = height of the cross section

The cracking moments for the unstrengthened and the FRP strengthened cross section, where the self-weight was not considered, are presented in Table 9.3. For the calculations the reader is directed to Appendix M .

Table 9.3 Cracking moment and load for unstrengthened and FRP strengthened cross section.

Type of cross section	***Cracking moment*** M_{cr} **[kNm]**	***Cracking load*** F_{cr} **[kN]**
Unstrengthened	1.04	3.20
FRP strengthened	1.06	3.25

9.1.3 Load Deflection Curves

Load deflection curves were done for different cases both for an unstrengthened and a FRP strengthened RC beam. The predicted response for an unstrengthened RC beam was done by calculating the stiffness in stadium I and stadium II for concrete and connect it to the predicted ultimate load. Equations (9.10) and (9.11) show how the stiffness for an unstrengthened beam is calculated.

$$K_I = \frac{48 \cdot E_{cm} \cdot I_I}{L^3} \quad (9.10)$$

$$K_{II} = \frac{48 \cdot E_{cm} \cdot I_{II}}{L^3} \quad (9.11)$$

For the case with stadium I stiffness a tri-linear response was assumed and the stadium I stiffness was used up to a certain value of load and deflection known from Section 9.1.2 when the section cracks. When the cracking load was reached the stiffness was calculated with the knowledge of the ultimate load and the corresponding deflection and then fully plastic response was assumed. For the second case with stadium II stiffness, a bi-linear response was assumed with constant stiffness up to the known value of ultimate load and the corresponding deflection followed by fully plastic response. Figure 9.3 illustrates the predicted response for an unstrengthened beam. The ultimate load predicted in Section 9.1.1 was used as predicted beam resistance R_2 in dynamic predictions.

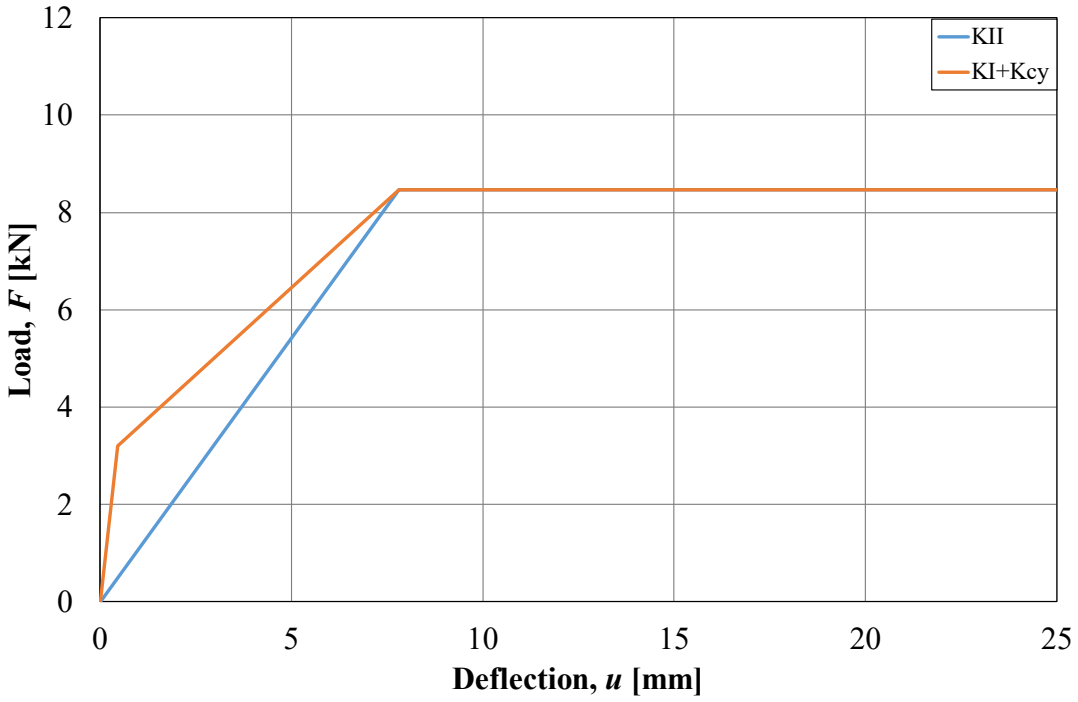

Figure 9.3 Predicted response for an unstrengthened beam.

Predictions for the FRP strengthened RC beam was done in a similar way as for an unstrengthened beam up to ultimate load with one stiffness for stadium I and another for stadium II but now also with FRP included. When the ultimate load was reached, the response was assumed to be fully plastic for an unstrengthened beam at the level of ultimate load for such a beam. The stiffness after cracking was calculated in the same way as described for an unstrengthened beam. Equations (9.14) and (9.15) show how to calculate the stiffness for stadium I and stadium II for FRP strengthened beams. The FRP was treated as the reinforcement by a factor α_{FRP} , depending on the elastic modulus of concrete and FRP and included in the moment of inertia. This factor α_{FRP} and the moment of inertia were calculated using Equations (9.12) and (9.13). Figure 9.4 illustrates the predicted response for a FRP strengthened beam.

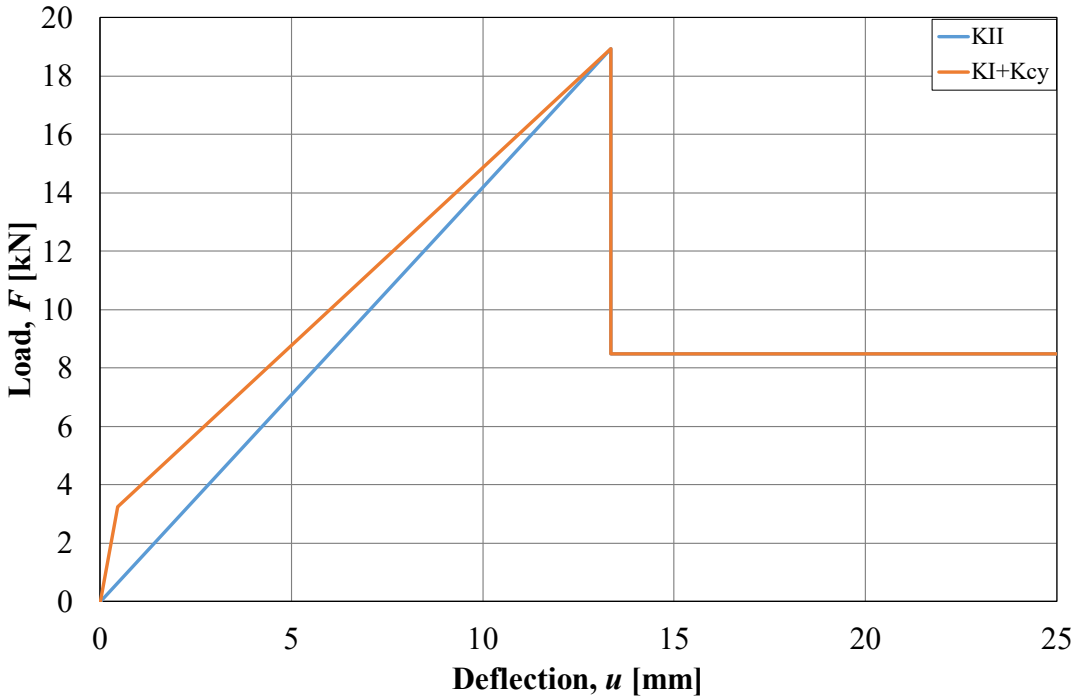

Figure 9.4 Predicted response for an FRP strengthened beam.

$$\alpha_{FRP} = \frac{E_{FRP}}{E_{cm}} \tag{9.12}$$

$$I_{II.FRP} = \frac{b \cdot x_{II}^3}{3} + (\alpha_s - 1) \cdot A'_s \cdot (d' - x_{II})^2 + \alpha_s \cdot A_s \cdot (d - x_{II})^2 + \alpha_{FRP} \cdot A_{FRP} \cdot (d_{FRP} - x_{II})^2 \tag{9.13}$$

$$K_{I.FRP} = \frac{48 \cdot E_{cm} \cdot I_{I.FRP}}{L^3} \tag{9.14}$$

$$K_{II.FRP} = \frac{48 \cdot E_{cm} \cdot I_{II.FRP}}{L^3} \tag{9.15}$$

The stiffnesses for the four different cases are summarized in Table 9.4 and the calculations for the input data for the load deflection curves are presented in Appendix M .

Table 9.4 Predicted stiffness for the load versus deflection curves.

Beam type	k_I [MN/m]	k_{II} [MN/m]	k_{cy} [MN/m]
Unstrengthened	7.06	1.09	0.72
FRP Strengthened	7.19	1.42	1.22

9.1.4 Plastic Rotation Capacity

Plastic rotation capacity was predicted for the studied unstrengthened beams with three methods. The method from Eurocode, ABC-method and BK25 presented in Section 4.2 were used to predict the response. Since the top reinforcement was observed to be in

tension it was neglected in the calculations. Results from the calculations are presented in Table 9.5 and calculations are presented in Appendix N .

Table 9.5 Predictions of rotation capacity.

Method	Plastic rotation θ_{pl} [rad]	Plastic deformation u_{pl} [mm]
Eurocode 2	0.027	17.7
ABC	0.045	29.0
BK25	0.107	69.4

9.2 Dynamic Response

The dynamic response of the beams was also predicted in order to get an understanding of what could be expected from the dynamic test results. For these predictions a 2DOF model in MATLAB describing the problem was used. The model was based on the theory described in Section 6.2 and the MATLAB script in its entirety is presented in Appendix L .

9.2.1 Input Data for 2DOF Model

The 2DOF model needed input data for the different predictions. The prediction that was made were for an unstrengthened beam using the statically predicated resistance of the beam according to Section 9.1.1. The velocity for the prediction was the theoretical velocity for the four different drop heights calculated as

$$v_{0,theoretical} = \sqrt{2 \cdot g \cdot h} \tag{9.16}$$

where $v_{0,theoretical}$ = theoretical initial velocity [m/s]
g = gravitational acceleration [m/s^2]
h = drop weight height [m]

The material input data came from the material tests made described in Section 8.6 and results presented in Section 10.1. The stiffnesses used for the drop weight and the beam was calculated according to Section 6.4.2. The material model used in the model for both bodies were bi-linear elasto-plastic response, described in Section 2.3 and Section 5.4.3. Drop weight resistance was set as R_1 = 70 kN according to Andersson and Pettersson (2019).

9.2.2 2DOF Prediction Results

The results presented in this section are midpoint-time relationship for the four different drop heights together with the velocity-time relationships for the drop weight for the same four drop heights.

Figure 9.5 shows the midpoint deflection over time for the beam subjected to a drop height of 3, 4, 5 and 5.7 m.

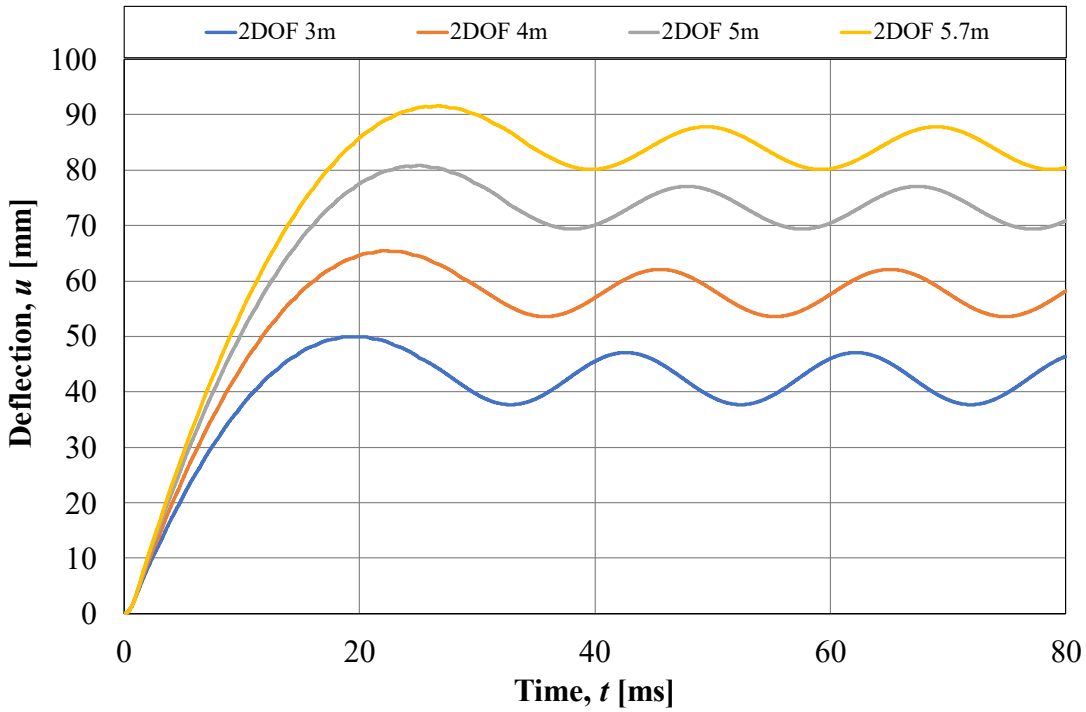

Figure 9.5 *Predicted midpoint deflection versus time relationship different drop heights.*

Figure 9.6 illustrate predicted response for velocity versus time relationship.

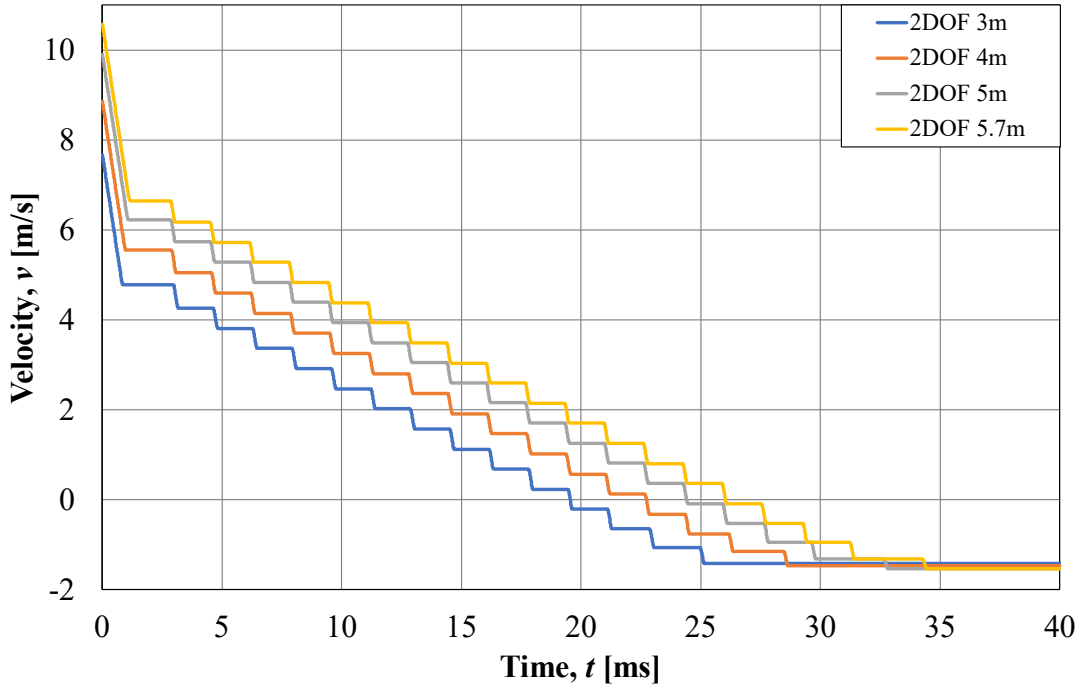

Figure 9.6 *Predicted drop weight velocity versus time relationship from different drop heights.*

10 Experimental Results

In this chapter the experimental results are presented; both results from material testing and from dynamic drop weight and from static tests of the structural response.

10.1 Material Testing

Material properties of several materials used were investigated. Both fresh and hardened concrete, the reinforcement bars and the two types of adhesives were tested to gain knowledge about the materials used in the experiments. The FRP material was not tested, and its properties according to the manufacturer are presented in Table 8.3.

10.1.1 Concrete Properties

The fresh concrete was tested with respect to consistency by a slump test at the beginning and one in the end of the casting. Figure 10.1 illustrates the results of the slump tests and the results from them are also presented in Table 10.1.

a) *b)*

Figure 10.1 Slump test.

Table 10.1 Results from slump test.

Test No.	Result [mm]	Consistency class
1	250	S5
2	250	S5

The hardened concrete was tested in two ways, material properties were defined by cube compression tests at age of 28 and 40 days and a WST test (CEN, 2019b; Tschegg, 1991; Löfgren et.al., 2004). The results of the cube compressive test at an age of 28 days are presented in Table 10.2.

Table 10.2 Concrete properties at age 28 days.

Specimen	Age [days]	Density [kg/m^3]	Compressive Cube Strength [MPa]
No. 1	28	2444	70.3
No. 2	28	2426	69.2
No. 3	28	2332	60.7
Average	**28**	**2401**	**66.8**

Since the drop weight tests and static tests of the beams were done at around 40 days after the casting a second compressive test was done to achieve the concrete properties at that age also. The results are presented in Table 10.3.

Table 10.3 Concrete properties at age 40 days.

Specimen	Age [days]	Bulk Density [kg/m^3]	Compressive Cube Strength [MPa]
No. 1	40	2452	72.1
No. 2	40	2440	70.6
No. 3	40	2444	68.4
Average	**40**	**2445**	**70.4**

Wedge splitting tests were done at an age of 35 days and the results are presented in Table 10.4 and Figure 10.2.

Table 10.4 WST results at age 35 days.

Specimen ID	Accumulated fracture energy G_F [Nm/m^2]	$F_{sp,max}$ [kN]
WST-1	145	5.9
WST-2	134	5.3
WST-3	173	6.2
Average	**151**	**5.8**

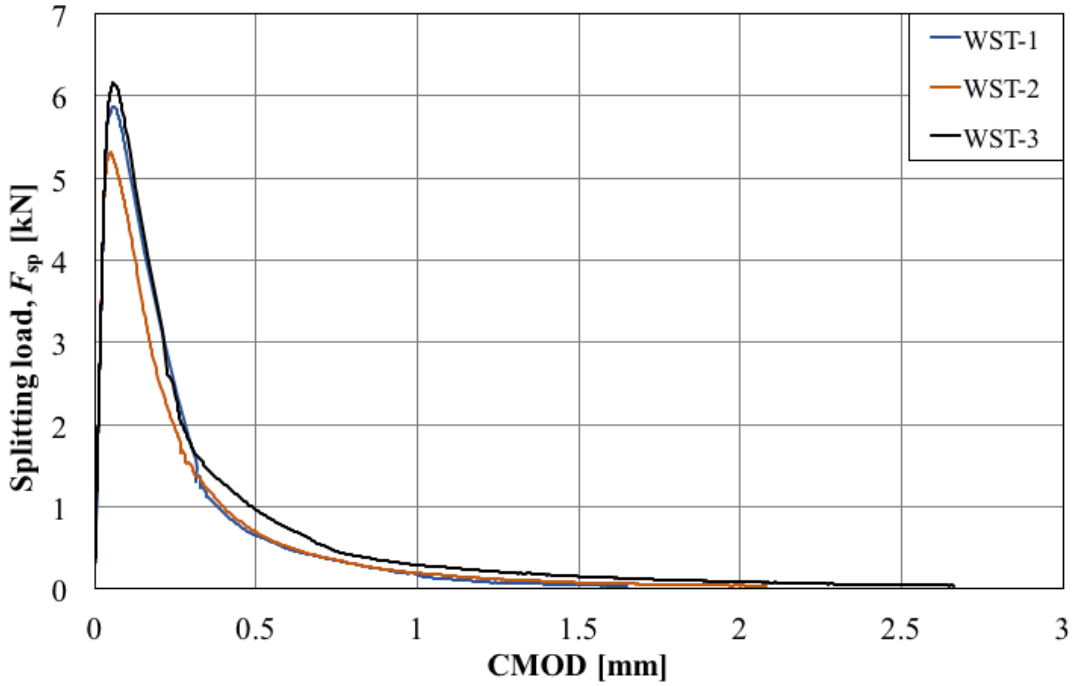

Figure 10.2 Splitting load versus crack mouth opening displacement.

10.1.2 Reinforcement Properties

Steel bars were tested according to Section 8.6.2 and the results are presented in Table 10.5. Stress versus strain relations are presented in Appendix G .

Table 10.5 Results from testing of reinforcement bars.

Specimen	E_s $[GPa]$	ε_{su} [%]	$f_{0.2}$ $[MPa]$	f_u $[MPa]$
1	186	8.4	536	655
2	184	8.1	547	664
3	200	8.6	549	665
4	244[4]	8.6	550	668
5	186	8.3	549	668
6	187	8.0	528	646
Average	**198**	**8.3**	**543**	**661**

10.1.3 Adhesive properties

Tensile tests were done on the test specimens of S&P and NM adhesive (S&P, n.d.; Nils Malmgren, 2011). The specimens, also called dogbones due to their characteristic shape, were subjected to a tensile test in the same machine as the reinforcement bars. Since there were many difficulties with the production of the test specimens it affected the quality of them, and the results were not always trustworthy. Therefore, a decision

[4] This value should have been neglected since it is an outlier. The mean value neglecting this value would have been 189 GPa. However, throughout the hand calculations in this report the values in Table 10.5 have been used.

was made to only look at Young's modulus on all test specimens except for the last four NM specimens where ultimate stress and strain also was studied. Ideally should the NM specimens have been hardened in higher temperatures, but this was not possible. Therefore, the specimens all hardened in room temperature. The results of the tensile tests are presented in Table 10.6, Table 10.7 and Table 10.8.

Table 10.6 Results from tensile tests of S&P adhesive.

Test specimen	Young's Modulus tension, E [GPa]
S&P 1	3.7
S&P 2	3.9
S&P 3	3.8
S&P 4	3.6
S&P 5	3.4
S&P 6	3.4
Mean	**3.6**

Table 10.7 Results from tensile tests of NM adhesive.

Test specimen	Age [days] in room temperature around 20°C	Young's Modulus tension, E [GPa]
NM 1	14	3.5
NM 2	14	3.6
NM 3	14	3.7
NM 4	14	3.6
NM 5	49	3.5
NM 6	49	3.6
NM 7	49	3.5
NM 8	49	3.5
Mean 14 days	**14**	**3.6**
Mean 49 days	**49**	**3.5**

Table 10.8 Ultimate stress and strain for the NM test specimens tested at an age of 49 days.

Test specimen	Ultimate stress, σ_u [MPa]	Ultimate strain, ε_u
NM 5	32.9	10.7
NM 6	36.4	11.7
NM 7	40.3	13.5
NM 8	13.4	3.8

As can be seen in Table 10.6 and Table 10.7 the mean difference in stiffness between the two types of adhesives was small. Further, a small decrease in stiffness between 14 and 49 days could be observed for the NM adhesive. The last four NM specimens were also studied with respect to ultimate stress and strain and the results of the first three had quite small variation whereas the fourth specimen experienced much lower capacity. The fourth specimen had a large air bubble which affected the capacity and in which the failure took place; because of this, the ultimate stress and strain for this

specimen is not deemed to be representative for the adhesive. In Figure 10.3 stress versus strain results for the last four NM tests are presented.

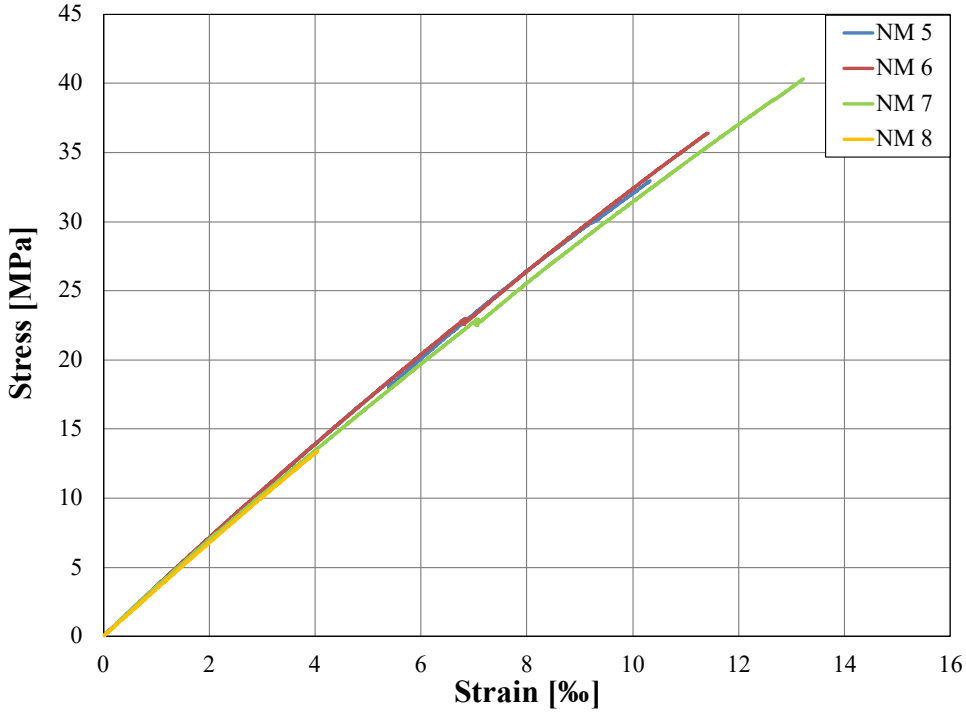

Figure 10.3 Stress versus strain diagram for the four NM adhesive tests done after 49 days.

As can be seen in Figure 10.3, the yellow curve (NM 8) ended much earlier than the other ones and this was because the air bubble affecting the capacity of this specimen. However, the shape of the stress-strain relation is the same as prescribed by the supplier with almost linear shape and abrupt end. The prescribed Young's modulus from tensile tests for specimens stored in air temperature in 7 days was 2.8-2.9 GPa which was somewhat smaller than the measured one in these tests but around the same level. The presented data in Table 10.8 for ultimate stress and strain are too uncertain due to the defects in form of air bubbles in the test specimens. Young's modulus from the different test presented in Table 10.6 and Table 10.7 though are trustworthy since it is based on the results in the early beginning of the test and the shape of the load versus displacement curve was almost linear for all tests.

10.2 Dynamic Test Results

The experimental part of this study started with the dynamic tests and the results are presented in this section. How the dynamic tests were conducted and all practical details treating set-up, cameras and test procedure are presented in Chapter 8 and Sections 8.7.1 and 8.8 in particular for the dynamic tests. The results presented are from the DIC data captured by the two high speed cameras and then processed in GOM Correlate 2018 (GOM, 2018). Throughout this section it will be referred to the two high speed cameras as camera 1 and camera 2. Camera 1 focused on the drop weight and recorded at 40 000 FPS while camera 2 focused on the left part of the beam recording slightly more than half of the beam at 5 000 FPS. The analyses that focus on the general behaviour of the beams will use data from camera 2. The analyses that focus on the drop weight uses instead data from camera 1 but some comparisons between the two

cameras are also made in these cases. The dynamic test results include impact force and impulse from the drop weight, beam midpoint deflection over time, deformed shape of beams, velocity of the drop weight, when and how the FRP delaminates (if debonding occurs), strain fields and failure mode tendencies.

10.2.1 Midpoint Deflection Over Time

In order to determine the midpoint deflection over time, a point was placed in the middle of the span in order to calculate its displacement. A point over the support was also taken in order to calculate the difference in displacement between midpoint and support. This was made to see how large the midpoint deflection was in relation to the support and was calculated as

$$u = u_{mid} - u_{support} \tag{10.1}$$

This makes it easier to see the plastic deformation which is the value the curve oscillates around. It should be noted that only the deformation in the left support was able to be calculated due to camera 2 capturing the left side of the beam. The deformation is assumed to be equal on both supports. Between 3 and 6 ms, depending on the drop weight height, there is a shift in the curve. This is because the beam is lifted up from its supports shortly after impact and the shift observed is obtained when the beam is pushed back in contact with the supports again. There it stops before the deformations increases further.

The deflection versus time relationships are presented in this section for beams subjected to drop weight from the same drop height as well as different drop heights but the same type of beam, i.e. unstrengthened and strengthened with the two different adhesives. The maximum deflection as well as the plastic deformation are also presented for the different beams. However, it is worth noticing that the plastic deformations presented were extracted by analysing an image prior to impact and an image after the impact test when the beam has been placed on its supports again. This means that the actual plastic deflection values, u_{pl}, that are presented in the tables throughout this section is not from the data used to plot the curves but how the beam has beam deformed comparing images when the beam was resting on its supports before and after impact. This also means that there might be deviations from the plastic deflection presented in the tables and the deformation that can be visually identifiable in the graphs. This could be due to repeated deformations obtained when the beam fell down to its supports again and in extreme cases receiving an additional impact when hitting the laboratory equipment. So, in the tables throughout this section both the visible plastic deformation in the deflection versus time relationships and the actual plastic deformation are presented. The visible plastic deformation is taken visually from the deflection versus time relationship and is therefore approximate.

For the unstrengthened beams the behaviour was similar for all four beams. The deflection increases rapidly, the maximum deflection was reached followed by oscillation around a certain deflection. This deflection, here denoted as visible plastic deformation, being the plastic deformation of the beam obtained due to the initial impact. With increasing drop weight height, the maximum deflection of the midpoint increased and also occurred later. The plastic deformation increased with increasing

drop weight height. However, for the highest drop height of 5.7 m, the oscillation obtained was more irregular and never clearly varied around a certain plastic deflection.

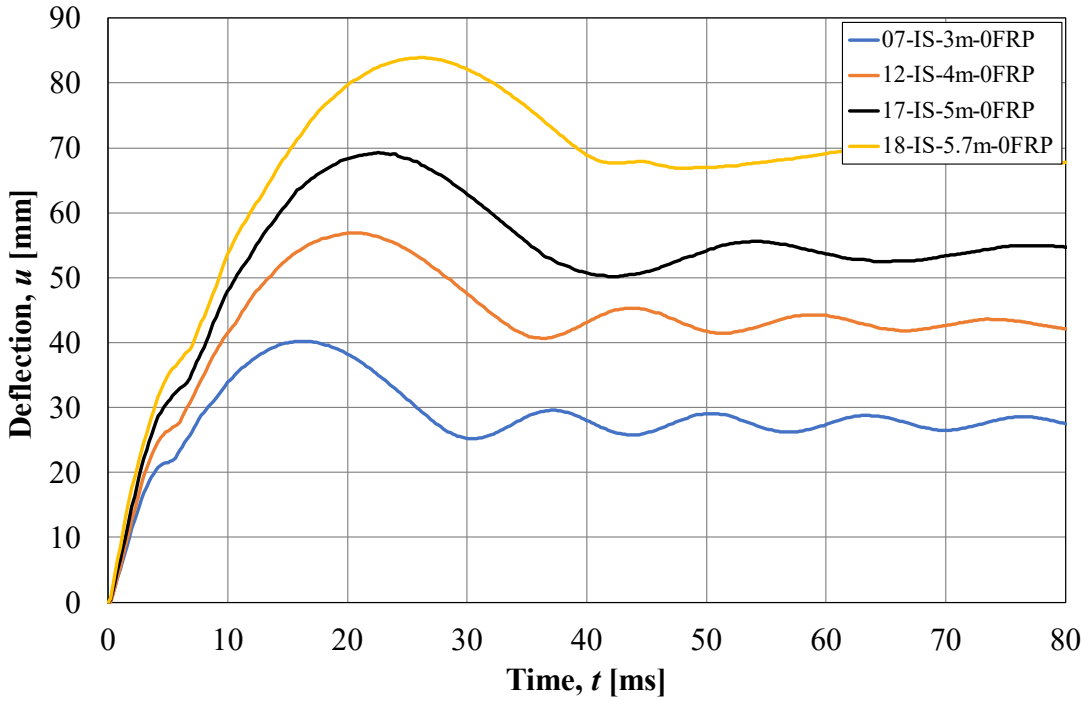

Figure 10.4 *Midpoint deflection over time for unstrengthened beams subjected to drop weight from various heights.*

Table 10.9 *Maximum and plastic midpoint deflection for relative deflection for unstrengthened beam.*

Beam	**Maximum deflection, u_{max} [mm]**	**Visible plastic deformation, u_{pl} [mm]**	**Actual plastic deflection, u_{pl} [mm]**
07-IS-3m-0FRP	40.2	28	27.9
12-IS-4m-0FRP	56.9	43	44
17-IS-5m-0FRP	69.3	54	56.7
18-IS-5.7m-0FRP	83.9	68	70.6

If studying the results of the beams subjected to the drop weight from a height of 3 m, visualized in Figure 10.5, it can be seen what kind of impact the FRP strengthening has on the structure. The maximum deflection is reduced a lot compared to an unstrengthened beam. The plastic deflection is also very noticeable where the FRP strengthening has had a massive effect on the remaining deflection after impact resulting in a much lower plastic deformation.

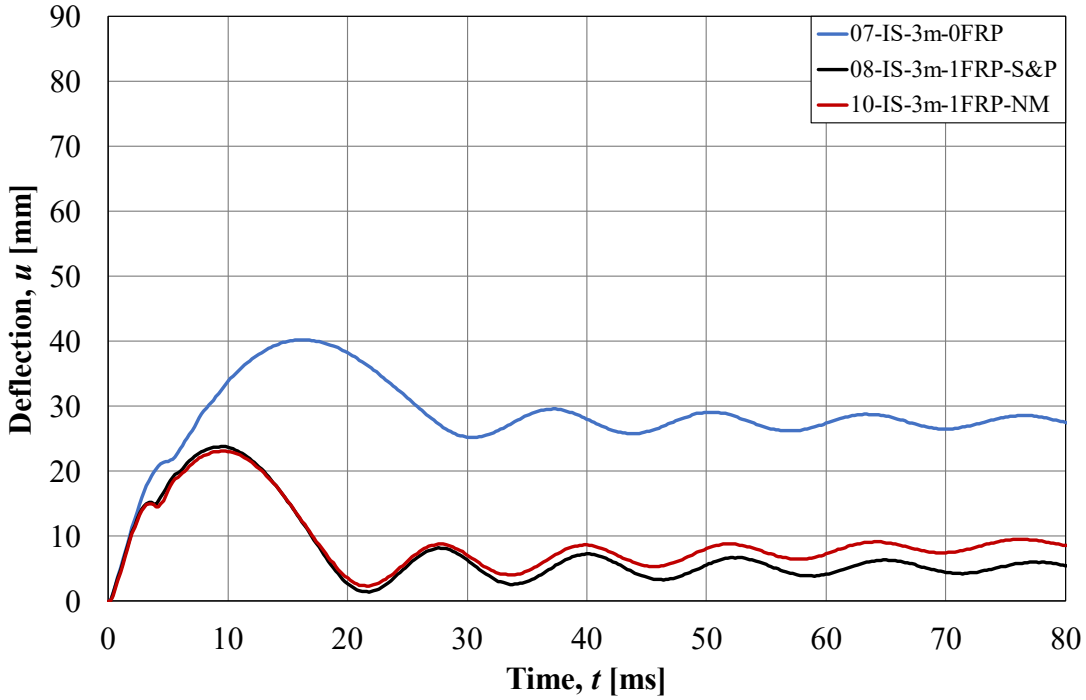

Figure 10.5 Midpoint deflection over time for beams subjected to drop weight from 3 m.

Table 10.10 Maximum and plastic midpoint deflection for relative deflection for beams subjected to a drop height of 3 m.

Beam	Maximum deflection, u_{max} [mm]	Visible plastic deformation, u_{pl} [mm]	Plastic deflection, u_{pl} [mm]
07-IS-3m-0FRP	40.2	28	27.9
08-IS-3m-1FRP-S&P	23.8	5	5.4
10-IS-3m-1FRP-NM	23.1	8	6.2

The results for the midpoint deflection over time for beams subjected to drop weight from 4 m are presented in Figure 10.6. For the FRP strengthened beams, a similar behaviour as for the 3 m drop height can be seen, i.e. the maximum deflection as well as the plastic deflection is reduced.

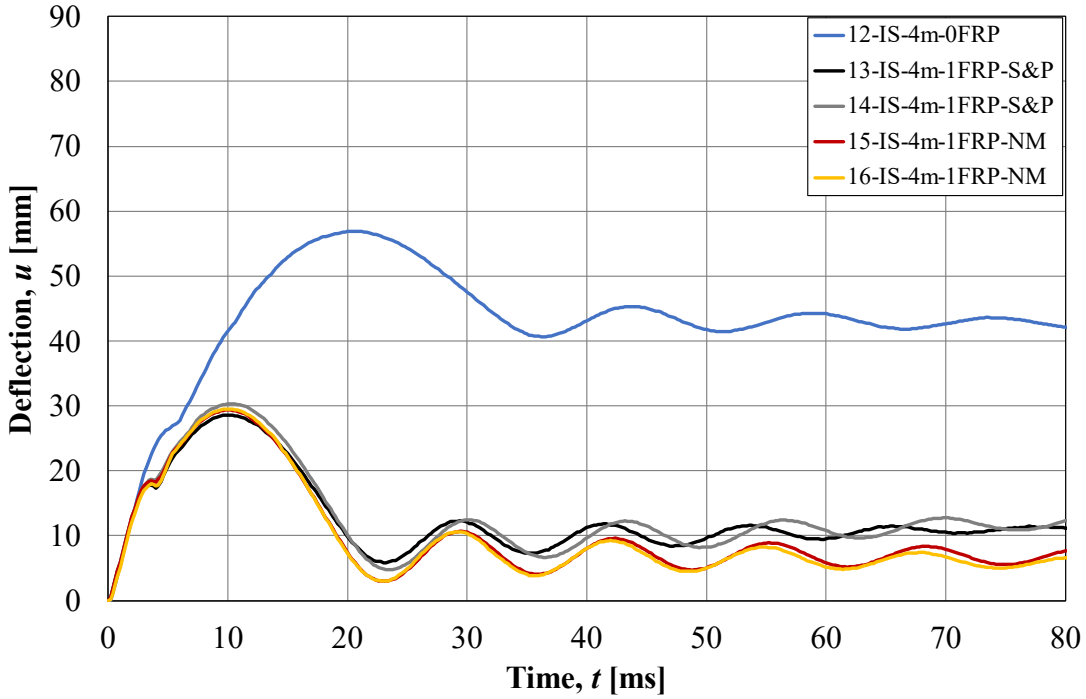

Figure 10.6 Midpoint deflection over time for beams subjected to drop weight from 4 m.

Table 10.11 Maximum and plastic midpoint deflection for relative deflection for beams subjected to a drop height of 4 m.

Beam	Maximum deflection, u_{max} [mm]	Visible plastic deformation, u_{pl} [mm]	Plastic deflection, u_{pl} [mm]
12-IS-4m-0FRP	56.9	42	44
13-IS-4m-1FRP-S&P	28.6	10	9.3
14-IS-4m-1FRP-S&P	30.3	10	7.4
15-IS-4m-1FRP-NM	29.4	6	7.6
16-IS-4m-1FRP-NM	29.5	6	6.9

The results for the midpoint deflection over time for beams subjected to a drop weight from 5 m are presented in Figure 10.7. Similarly, for the FRP strengthened beams subjected to a drop weight from 3 and 4 m, the maximum deflection and the plastic deflection is reduced. As can be seen throughout Figure 10.5 to Figure 10.7 the maximum deflection is reduced by roughly a factor 2 and the plastic deformations are reduced by an even higher factor in FRP strengthened beams. The damages on beam 21-IS-5m-1FRP-NM shows larger plastic deformations compared to the other FRP strengthened beams. The variation of the deformations increased with increasing drop height which can be seen when comparing the Figure 10.5 to Figure 10.7. For drop heights of 5 m, some beams obtained only minor damage while some were damaged

more severely, compare e.g. beam 20-IS-5m-1FRP-S&P with 21-IS-5m-1FRP-NM. Another aspect worth paying attention to is the fact that the visible plastic deformation that beam 19-IS-5m-1FRP-S&P oscillates around, is approximately 10 mm but the actual plastic deformation was 23.3 mm. In this case, the beam had such a strong rebound after impact that it flung upwards so much that it hit the tube rig. Due to this, the beam was subjected to a second impact which could help explain why the visible and the actually measured plastic deformation does not match.

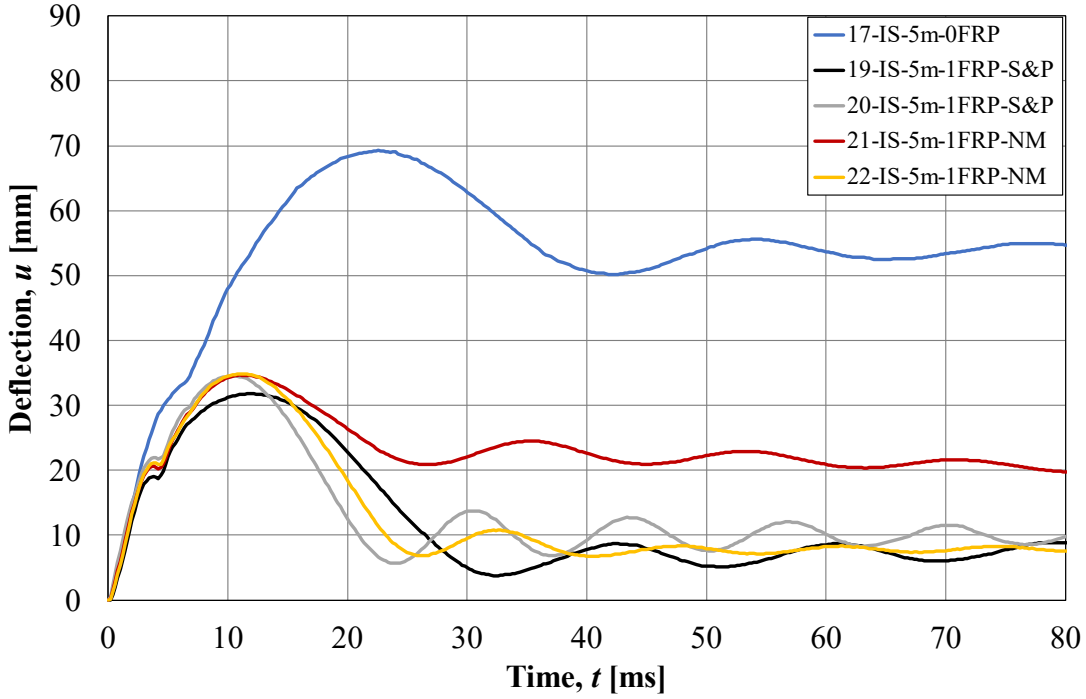

Figure 10.7 Midpoint deflection over time for beams subjected to drop weight from 5 m.

Table 10.12 Maximum and plastic midpoint deflection for relative deflection for beams subjected to a drop height of 5 m.

Beam	Maximum deflection, u_{max} [mm]	Visible plastic deformation, u_{pl} [mm]	Plastic deflection, u_{pl} [mm]
17-IS-5m-0FRP	69.3	54	56.7
19-IS-5m-1FRP-S&P	31.8	8	23.3
20-IS-5m-1FRP-S&P	34.5	10	8.3
21-IS-5m-1FRP-NM	34.7	21	25.7
22-IS-5m-1FRP-NM	34.9	8	6.8

The results for the midpoint deflection over time for beams subjected to 5.7 m drop height are presented in Figure 10.8. From this drop height the damages were very severe

for both strengthened and unstrengthened beams which resulted in difficulties extracting precise data. With such a large impact as it was from 5.7 m large diagonal shear type cracks struck out a large cone shaped piece of concrete. The large damages resulted in loss of data in the centre of the beam which made it hard for DIC and GOM Correlate to get information in that area of the beam overall and in some sequences was the data loss due to the cameras not being able to capture the damages from that drop height. This led to larger gaps where no information about the deflection was available and that is one explanation as to why the curves do not oscillates in the same way as the beams does from another drop height. In Table 10.13a large difference between the visible and the actual plastic deflection for beam 11-IS-5.7m-1FRP-NM can be seen. This could be explained by the similar reason as for beam 19-IS-5m-1FRP-S&P which hit the laboratory equipment when it flung upwards after impact.

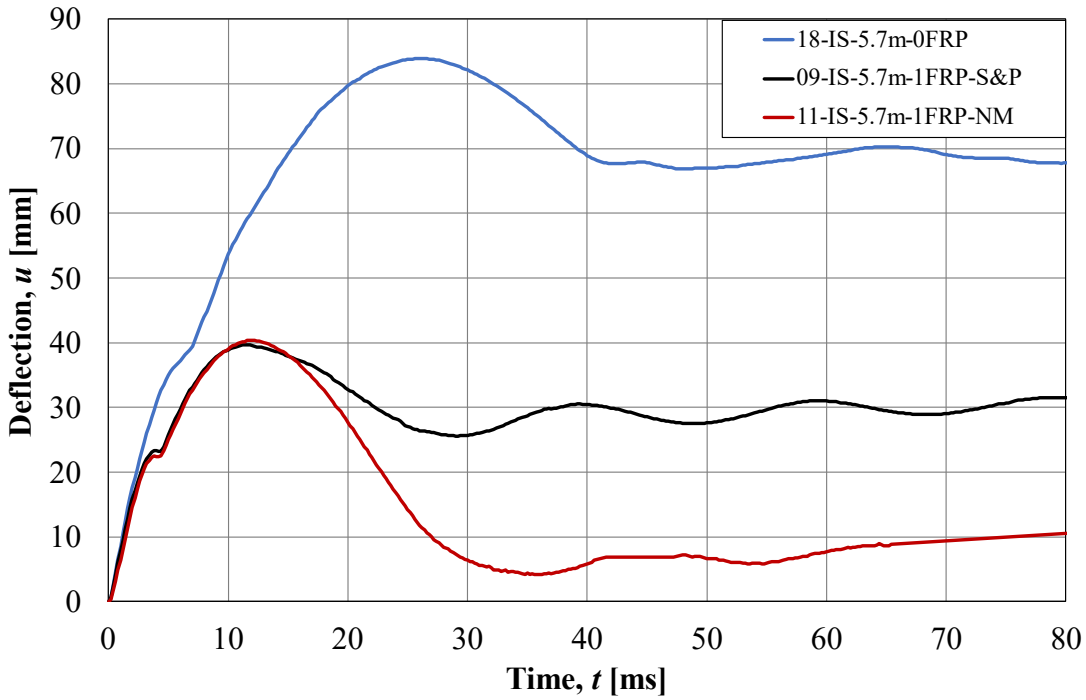

Figure 10.8 *Midpoint deflection over time for beams subjected to drop weight from 5.7 m.*

Table 10.13 *Maximum and plastic midpoint deflection for relative deflection for beams subjected to a drop height of 5.7 m.*

Beam	**Maximum deflection, u_{max} [mm]**	**Visible plastic deformation, u_{pl} [mm]**	**Plastic deflection, u_{pl} [mm]**
18-IS-5.7m-0FRP	83.9	68	70.6
09-IS-5.7m-1FRP-S&P	39.7	30	28.8
11-IS-5.7m-1FRP-NM	40.3	10	19

In Figure 10.9 and Figure 10.10, the strengthened beams are categorized depending on which type of adhesive that was used. The results are very similar and show no larger differences between the two adhesives except for an outlier (beam 21-IS-5m-1FRP-NM). Beams subjected to a drop weight from 5.7 m are excluded in this comparison.

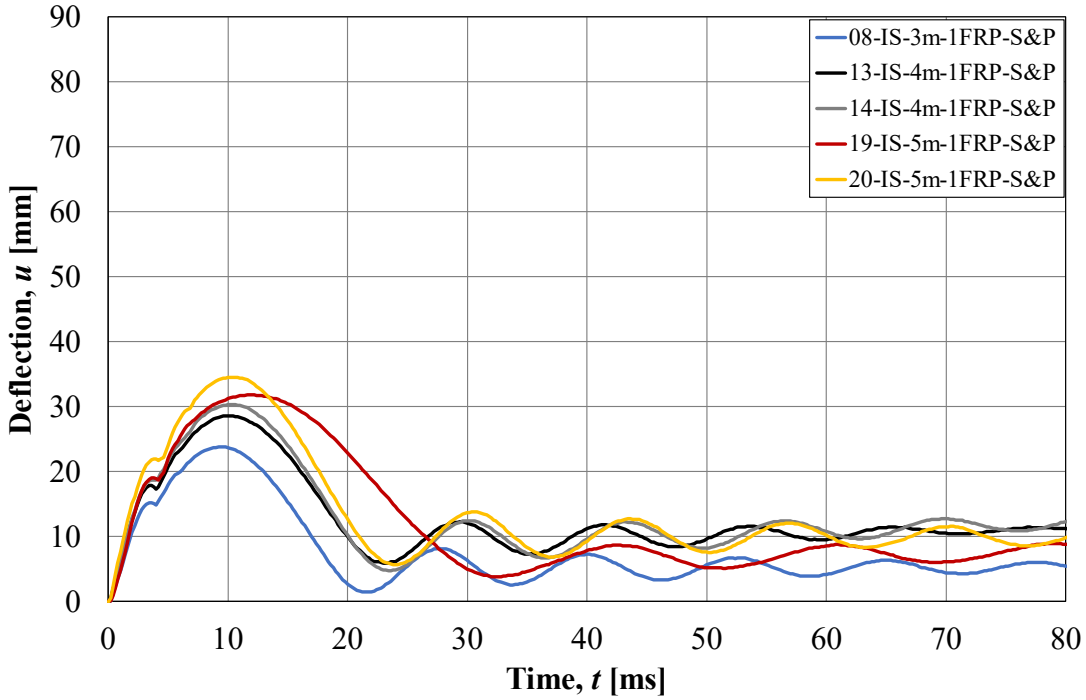

Figure 10.9 Midpoint deflection over time for strengthened beams with S&P adhesive.

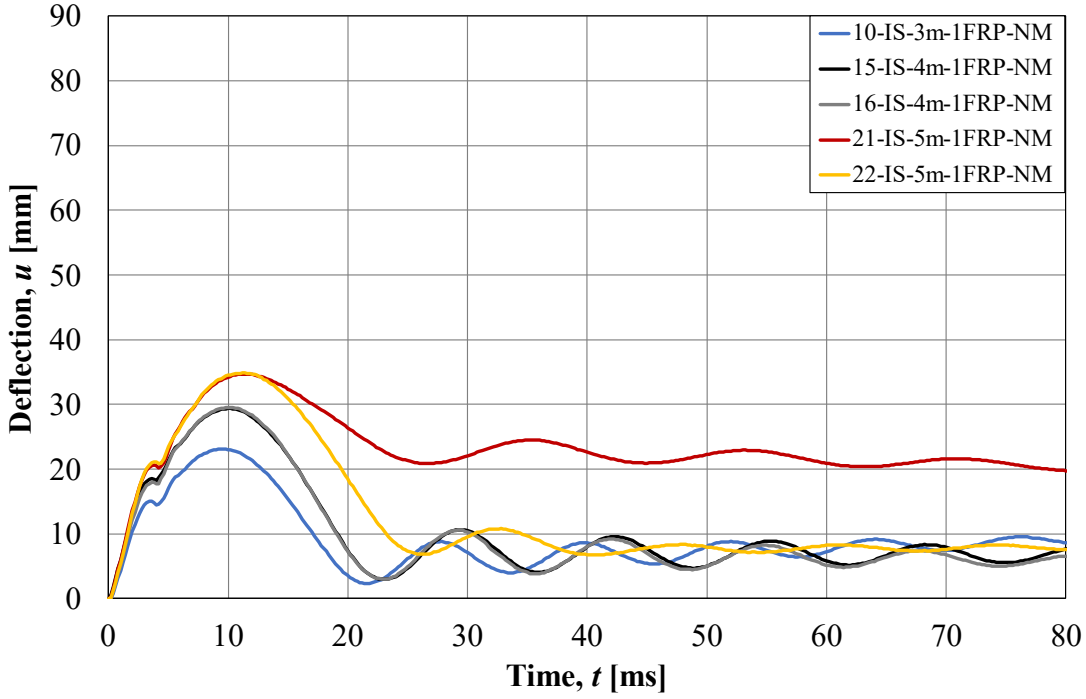

Figure 10.10 Midpoint deflection over time for strengthened beams with NM adhesive.

10.2.2 Failure Mode Tendencies

During the dynamic tests different types of failure modes were registered. This varied depending on whether the beams were unstrengthened or strengthened but also depending on the drop height. When failure modes are discussed here it is not referred to as a complete failure or collapse since all of the beams were tested statically after the dynamic tests and all showed some to considerable residual strength. Hence, this section is a review of what type of failure mode tendencies that could be observed from the drop weight tests and not referring to failure in its strict sense.

In this section the results from the analyses of dynamically loaded beams are presented. Images of the damages are presented, and the type of failure mode is stated. Many of the failure modes are referred to according to Figure 7.1 but some might deviate and those are explained either as variation of Figure 7.1 or using an entirely new description. Since the beams are dynamically loaded with a drop weight instead of statically loaded it might be difficult to fully match the failure modes described by Teng et al. (2003).

One failure mode not occurring during the dynamic tests were the shear crack mode, see mode c) illustrated in Figure 7.1; i.e. the type of shear failure mode starting close to the support where a diagonal shear crack is propagating from the plate end. In the dynamic tests a type of shear crack instead occurred where two diagonal shear cracks formed a cone-like shape at the impact area. This failure mode is deemed to be similar to failure mode g) denoted intermediate flexural-shear crack induced interfacial debonding. It did not always cause debonding and sometimes the FRP was still partially attached to the bottom side of the beam. Nevertheless, some form of shear cracks were frequently observed in many of the beams during the dynamic tests. Examples of this behaviour are illustrated in Figure 10.11 and Figure 10.12 with various degree of visibility. For drop heights of 3 and 4 m, the damages obtained could still be minor for the FRP strengthened beams, but the shear cracks were still very clear. For drop heights of more than 4 m, the damages were more severe.

Figure 10.11 Beam 14 showing cone-like shear cracks under the impact area.

Figure 10.12 Beam 22 showing cone-like shear cracks under the impact area to a more severe degree.

These shear cracks also caused debonding where the FRP sheet completely delaminated from the middle of the span towards one of the edges. This was very similar to the failure mode described as failure mode g) in Figure 7.1. This is visualized in Figure 10.13. The effect on whether the FRP sheet delaminated or not had a large effect

on the residual response in the upcoming static tests and it had both pros and cons if the FRP delaminated or not. This is further treated in the results section for the static tests in Section 10.3.

Figure 10.13 Beam 09 showing cone-like shear cracks under the impact area causing debonding. Similar to the failure mode described as intermediate flexural-shear crack induced interfacial debonding.

During the dynamic tests one incident of a partial rupture of FRP, failure mode a), was recorded for the beam 13-IS-4m-1FRP-S&P. Roughly half of the width of the FRP ruptured, which is visualized in Figure 10.14, while the other half remained intact. This type of behaviour only occurred once and no particular reason why this occurred for this beam was found.

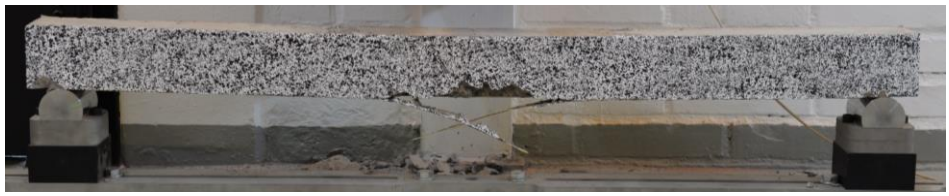

Figure 10.14 Beam 13 experiencing partial rupture of FRP.

The unstrengthened beams behaved in a similar way where they experienced flexural and shear cracks causing similar damages with increasing severity depending on the drop height. The unstrengthened beam subjected to a drop weight from 5.7 m experienced diagonal shear cracks that caused a large cone-like piece of concrete to come loose, resulting in the loss of a large part of the concrete in the midsection. Some of the unstrengthened beams after impact are visualized in Figure 10.15 and Figure 10.16.

Figure 10.15 Beam 12 after impact from 4 m.

Figure 10.16 Beam 18 after impact from 5.7 m.

As stated in the introduction of this section, no total failures were registered during the dynamic tests; instead all failures occurred during the upcoming static tests where the

residual strength were tested. However, tendencies were observed, as treated and visualized in this section, and these tendencies are summarized in Table 10.14. The table states which failure mode tendency and observations made from each dynamically loaded beam. The tested beams experienced different level of damages and to get an idea about how much mass was lost during testing, the beams were measured before and after both the dynamic and static testing. These results are presented in Appendix F .

Table 10.14 Failure mode tendencies for dynamically loaded beams.

Beam name	Failure mode tendency
07-IS-3m-0FRP	Flexural and shear cracks
08-IS-3m-1FRP-S&P	No tendencies
09-IS-5.7m-1FRP-S&P	Intermediate flexural-shear crack induced interfacial debonding
10-IS-3m-1FRP-NM	No tendencies
11-IS-5.7m-1FRP-NM	Intermediate flexural-shear crack induced interfacial debonding. Cracks propagating more than halfway between support and midpoint and causing partial debonding.
12-IS-4m-0FRP	Flexural and shear cracks
13-IS-4m-1FRP-S&P	Partial rupture of FRP
14-IS-4m-1FRP-S&P	Intermediate flexural-shear cracks. No debonding tendencies
15-IS-4m-1FRP-NM	Intermediate flexural-shear cracks. No debonding tendencies
16-IS-4m-1FRP-NM	Intermediate flexural-shear cracks. No debonding tendencies
17-IS-5m-0FRP	Flexural and shear cracks
18-IS-5.7m-0FRP	Diagonal cracks removing practically all concrete in a cone shape under the impact area
19-IS-5m-1FRP-S&P	Intermediate flexural-shear crack induced interfacial debonding. Cracks propagating halfway between support and midpoint and causing partial debonding.
20-IS-5m-1FRP-S&P	Intermediate flexural-shear cracks. Crack is propagating along FRP sheet but no debonding tendencies.
21-IS-5m-1FRP-NM	Intermediate flexural-shear crack induced interfacial debonding
22-IS-5m-1FRP-NM	Intermediate flexural-shear crack induced interfacial debonding. Cracks propagating halfway between support and midpoint and causing partial debonding.

10.2.3 Peak Force at Impact

Acceleration results for the drop weight from DIC was analysed in GOM Correlate 2018 to achieve the impact force and impulse which the beams were subjected to. Acceleration of the drop weight for each test was measured by assigning three facet points on the drop weight in GOM Correlate. Since acceleration is the second derivative of the displacement the noise is much larger than for the displacement and the velocity. To reduce the noise without losing the actual results, different techniques were tested. A decision was made that average of the three facet points was used when the acceleration data was studied. To minimize the noise, different levels of a sliding mean value were investigated where a sliding mean value over nine time steps (corresponds to a duration of 0.2 ms) was concluded as representative where the noise was minimized while the actual behaviour was still captured rather well. To ensure that this choice was a proper setting, two different beams were studied and the same conclusion was drawn. Further explanation of the study of the acceleration data is presented in Appendix B . The results for impact force presented in this section is based on data from Camera 1. This camera is faster than Camera 2, which was used to capture the acceleration of the drop weight in previous theses. Due to the noise and the processing of the data, the results presented in this section is not the true maximum value but more realistic than the results captured with Camera 2.

Impact force versus time is presented here where the maximum force is related to time 0 to be able to present results from different beams in the same diagram. A time period of approximately 2 ms before and 6 ms after the impact is illustrated. Impact force versus time for drop height 3 m is presented in Figure 10.17.

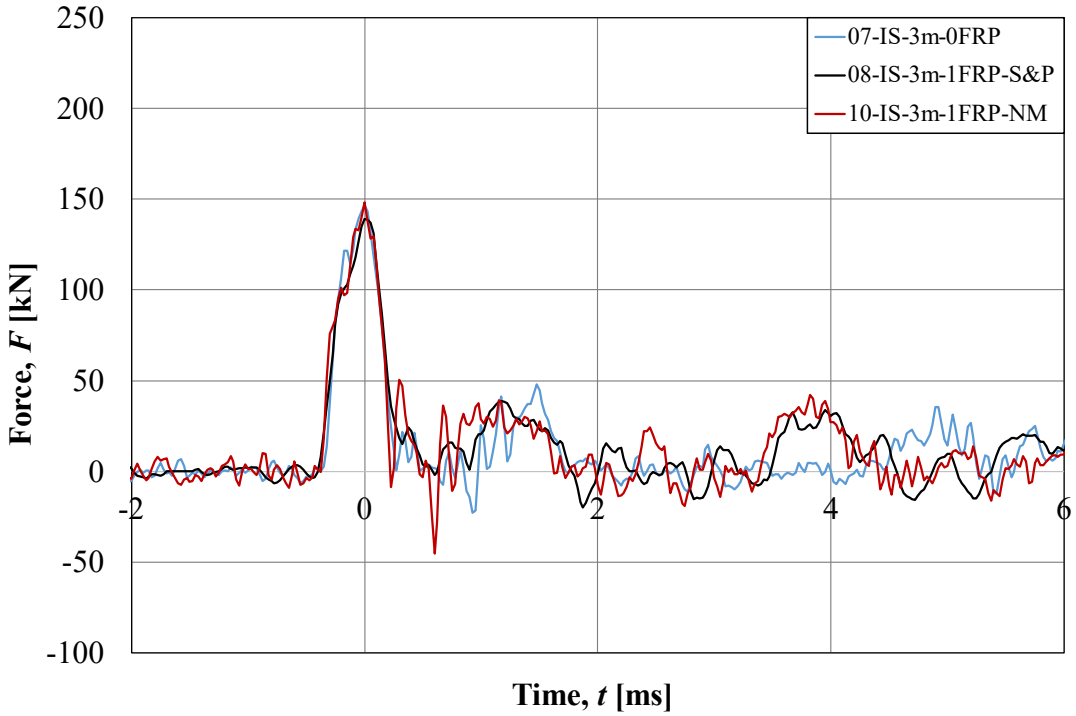

Figure 10.17 Impact force versus time for the three beams subjected to a drop weight from 3 m.

When studying the impact force for drop height of 3 m one can observe that the results had small deviations from each other before and during the first impact. The noise

before and during the first impact was small, but afterwards the results deviate more. This is reasonable since the impact has taken place and the beam and drop weight was moving together with smaller following impacts. The maximum impact force for all three beams was around 140-150 kN where the blue and red curve, representing beam 7 and 10 with no FRP and NM adhesive respectively, had a somewhat larger maximum value which can be seen in Figure 10.17. In Table 10.15, the maximum impact force is presented.

Table 10.15 Maximum impact force for beams subjected to drop weight from 3 m.

Beam name	Maximum impact force [kN]
07-IS-3m-0FRP	146
08-IS-3m-1FRP-S&P	139
10-IS-3m-1FRP-NM	148

For the height of 4 m, acceleration results from five different beams were studied. Impact force versus time is presented in Figure 10.18. For 4 m, the noise was small before and during the first impact but larger afterwards similar to the results presented in Figure 10.17 for 3 m but with larger variations after the first impact. The maximum impact force was around 180 kN for beam 13, 15 and 16 and somewhat lower, around 150 kN, for beam 12 and 14. In general the maximum impact force is markedly larger than the impact force for drop height 3 m, which is reasonable.

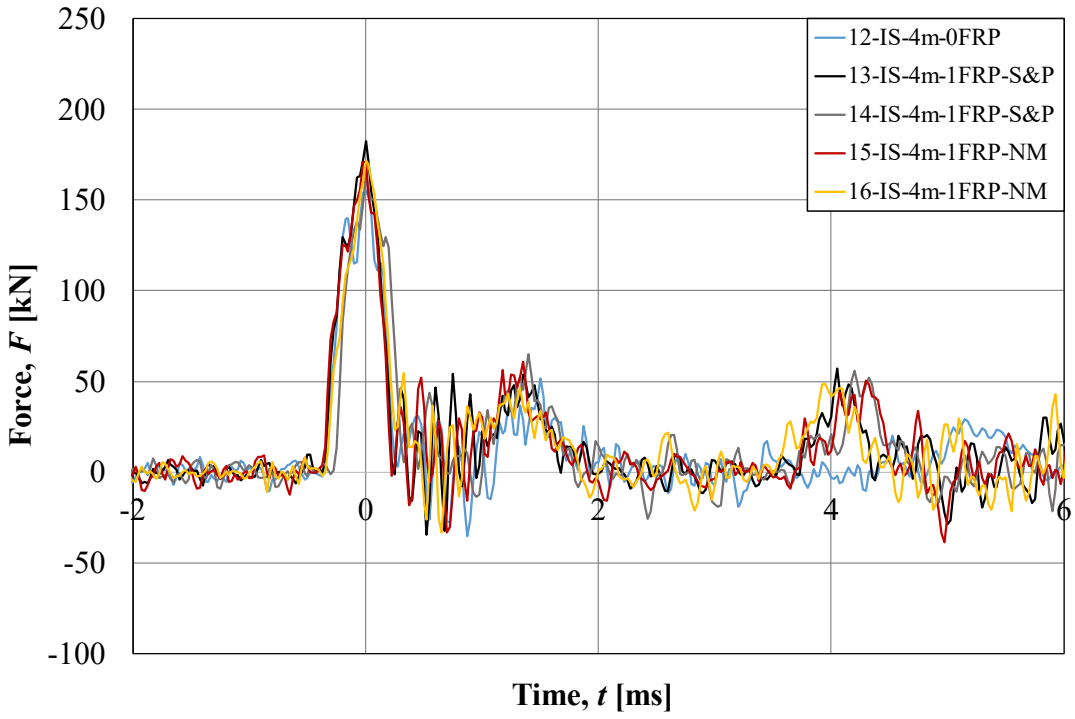

Figure 10.18 Impact force versus time for the three beams subjected to a drop weight from 4 m.

Maximum force for the different beams subjected to a drop weight from 4 m is presented in Table 10.20. From these results, it can be observed that the impact force for the FRP strengthened beams was larger than the impact force for the unstrengthened beam. Impact force for the FRP strengthened beams with adhesive NM, beam 15 and 16, was similar with a smaller variation than the impact force for beam 13 and 14 which

were strengthened using S&P adhesive. What could be noted about beam 13 is that this beam experienced partial rupture of the FRP during the drop weigh impact whereas beam 14 experienced no or small visible damages. If it would have been the other way around; i.e. that beam 14 experienced partial rupture instead, this could have been the reason why it got a smaller maximum impact force compared to the other beams with FRP. However, now this was not the case.

Beam 14 and 15 experienced the smallest maximum impact force of the FRP strengthened beams and if the strain field is studied in the time period close to impact some differences in strain distribution between these two and the other two FRP strengthened beams could be observed. In Table 10.16 and Table 10.17, the strain field for beam 14 and 15 are presented within a time period of 0.6 ms after impact.

Table 10.16 Strain fields from impact to 0.6 ms for beam 14-IS-4m-1FRP-S&P.

Time step [ms]	**Strain field**
1 %	**2 %**
0	
0.2	
0.4	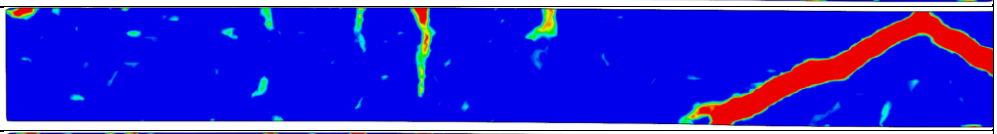
0.6	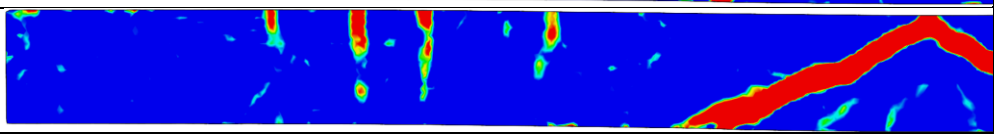

Early and large diagonal cracks could be observed and no bending cracks in the middle for beam 14. The strain field obtained in beam 15 was similar with the early diagonal cracks but also small bending cracks in the middle.

Table 10.17 Strain fields from impact to 0.6 ms for beam 15-IS-4m-1FRP-NM.

Time step [ms]	Strain field
1 %	2 %
0	
0.2	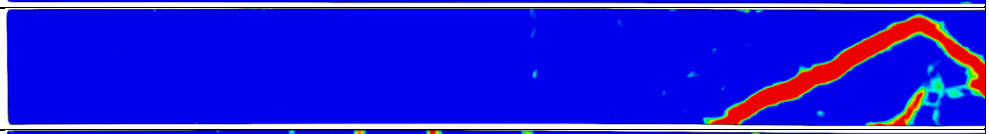
0.4	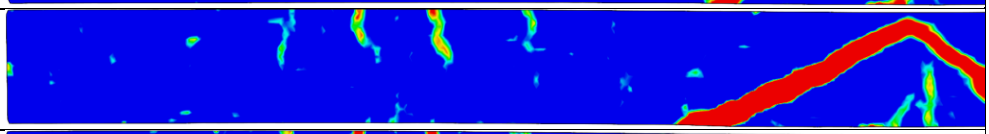
0.6	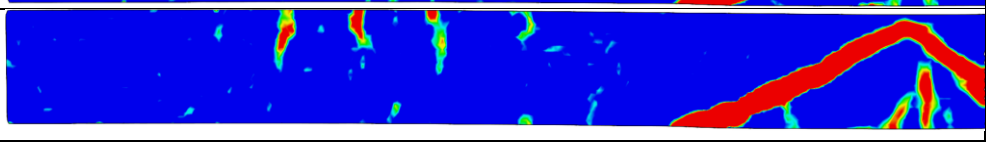

If instead beam 13 and beam 16 is studied one could observe that the early strain distribution is different to the general strain distribution for beam 14 and 15. Clearer bending cracks was registered and much smaller diagonal cracks. The strain distribution for beam 13 and 16 is presented in Table 10.18 and Table 10.19.

Table 10.18 Strain fields from impact to 0.6 ms for beam 13-IS-4m-1FRP-S&P.

Time step [ms]	Strain field
1 %	2 %
0	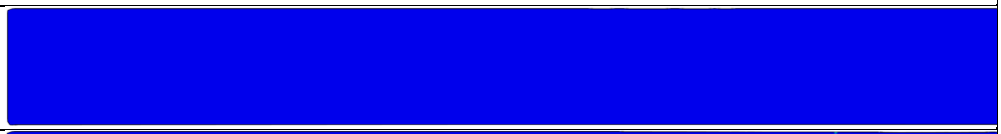
0.2	
0.4	
0.6	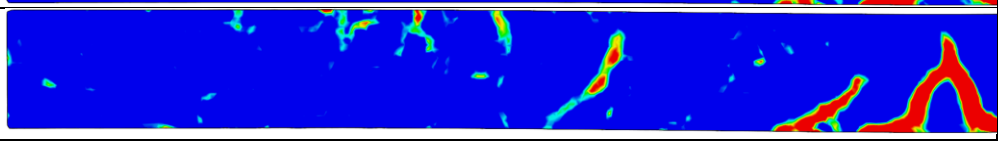

Table 10.19 Strain fields from impact to 0.6 ms for beam 13-IS-4m-1FRP-S&P.

Time step [ms]	Strain field
	1 % — 2 %
0	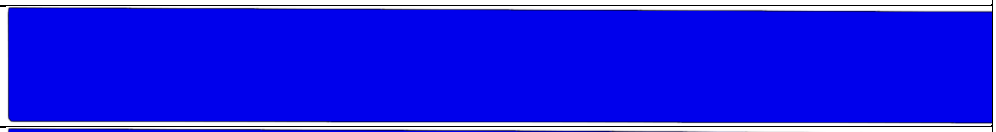
0.2	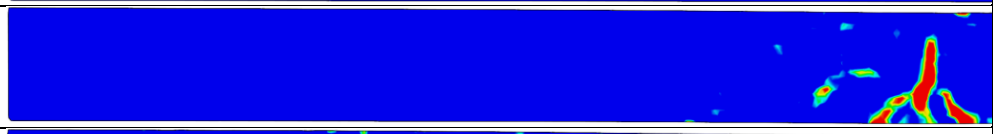
0.4	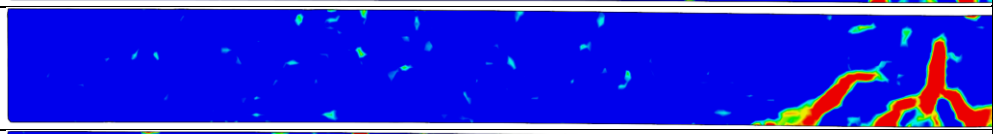
0.6	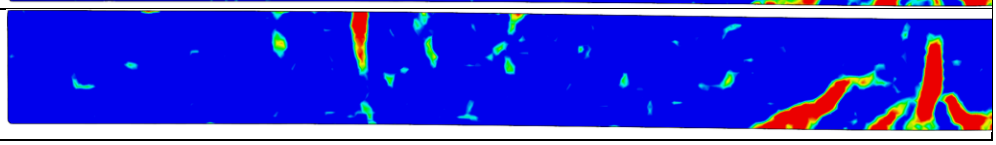

The general observation, when strain fields for the four beams is compared, is that beam 14 and 15 experienced early and large diagonal cracks and no or small bending cracks, whereas beam 13 and 16 experienced bending cracks and much smaller diagonal cracks. It was also a large difference between the two sets of beams in the inclination of the diagonal cracks. These observations do not explain why especially beam 14 experienced smaller maximum impact force compared to the other FRP strengthened beams but it is worth to be mentioned and could perhaps be a part of the explanation.

Table 10.20 Maximum impact force for beams subjected to drop weight from 4 m.

Beam name	Maximum impact force [kN]
12-IS-4m-0FRP	157
13-IS-4m-1FRP-S&P	182
14-IS-4m-1FRP-S&P	166
15-IS-4m-1FRP-NM	171
16-IS-4m-1FRP-NM	171

The next height studied was 5 m where the noise was a bit larger than for the two smaller heights of 3 and 4 m. However, the results are generally relatively close to each other before and during the first impact. In Figure 10.19 it is clear that the results varied considerably after the first impact. The beam and the drop weight moved together with smaller repeating impacts after the first one and the beams got damaged, which could be the reason why the results deviated from each other.

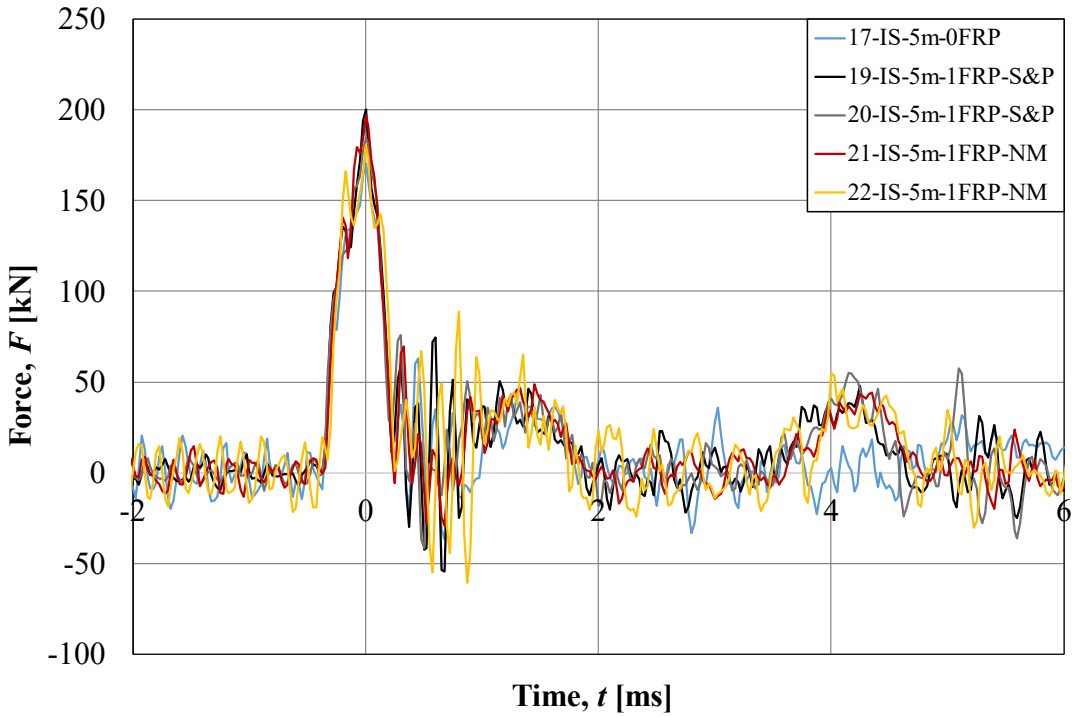

Figure 10.19 Impact force versus time for the three beams subjected to a drop weight from 5 m.

Maximum impact force is presented in Table 10.21. In general, the FRP strengthened beams got a larger maximum impact force than the unstrengthened one. For 5 m the impact force was around 170-200 kN compared to 140-150 kN for 3 m and 155-180 kN for 4 m drop height. Beam 19 and 21 were the beams with largest maximum impact force when 5 m drop height was studied but these experienced larger visible deformations than beam 20 and 22. For beam 19 and 21, the FRP debonded partially or fully but for beam 20 and 22 no such large deformations were observed. When comparing this observation with the results from drop weight height 4 m one can conclude that the largest maximum impact forces occurred for FRP strengthened beams where debonding or local rupture of FRP took place.

As mentioned previously for beams subjected to a drop weight from 4 m, early diagonal cracks occurred for beams with the smallest maximum impact force. When beam 19-22 was studied this observation was not seen. Shortly after impact all of the four beams developed diagonal cracks and no or small bending cracks appeared but there was no clear difference in the inclination of the cracks for the ones with smallest maximum impact force compared to the other two. The strain fields for the four FRP strengthened beams subjected to a drop weight are presented in Section 10.2.7 and Appendix C .

Table 10.21 Maximum impact force for beams subjected to drop weight from 5 m.

Beam name	Maximum impact force [kN]
17-IS-5m-0FRP	171
19-IS-5m-1FRP-S&P	200
20-IS-5m-1FRP-S&P	185
21-IS-5m-1FRP-NM	197
22-IS-5m-1FRP-NM	181

The last studied height was 5.7 m with results similar to the one from 5 m with small noise and variations before and during the first impact followed by large variations afterwards, see Figure 10.20. Maximum impact force was around 170-200 kN where the two FRP strengthened beams were very close to each other at 197 and 201 kN.

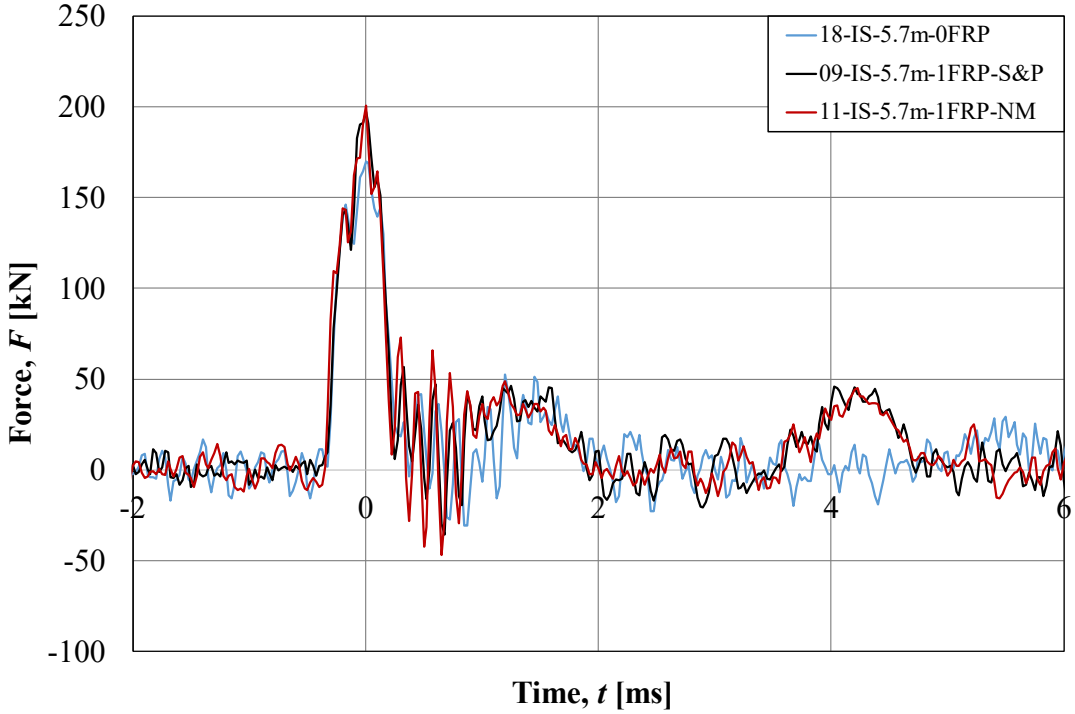

Figure 10.20 Impact force versus time for the three beams subjected to a drop weight from 5.7 m.

Similar to the results for 4 and 5 m drop height, the impact force for the unstrengthened beam was smaller than the FRP strengthened ones. Maximum impact force is presented in Table 10.22.

Table 10.22 Maximum impact force for beams subjected to drop weight from 5.7 m.

Beam name	Maximum impact force [kN]
18-IS-5.7m-0FRP	170
09-IS-5.7m-1FRP-S&P	197
11-IS-5.7m-1FRP-NM	201

As presented earlier in this section, Camera 1 registered 40 000 FPS, compared to Camera 2 which captured 5 000 FPS, and therefore Camera 1 had a bigger chance to capture the real peak values of the impact. In previous theses (Lovén & Svavarsdóttir, 2016; Lozano & Makdesi, 2017; Jönsson & Stenseke, 2018; Andersson & Pettersson, 2019; Nigani & Nordström, 2020), Camera 2 was used to capture the acceleration of the drop weight but in this project the use of Camera 1 gave the opportunity to obtain more detailed results than that of obtained using just Camera 2.

When acceleration data from Camera 2 was analysed and processed, different settings were compared to present the results in an optimal way. The process in GOM Correlate 2018 (GOM, 2018) was the same as for Camera 1. where three facet points

were placed on the drop weight and then the mean value over these three points was evaluated. Sliding mean value over 9 steps was used for Camera 1 but since Camera 2 captured much less frames per second than Camera 1 no sliding mean value was used for Camera 2. Two different beams were investigated with both sliding mean value over 3, 5, 7, 9 and 11 steps and only mean value over the three points in each step. The conclusion was that the best way to illustrate the acceleration data from Camera 2 was to only take the mean value over the three facet points in each step. Impact force data for Camera 2 for beams subjected to drop weight from 3 m is presented in Figure 10.21.

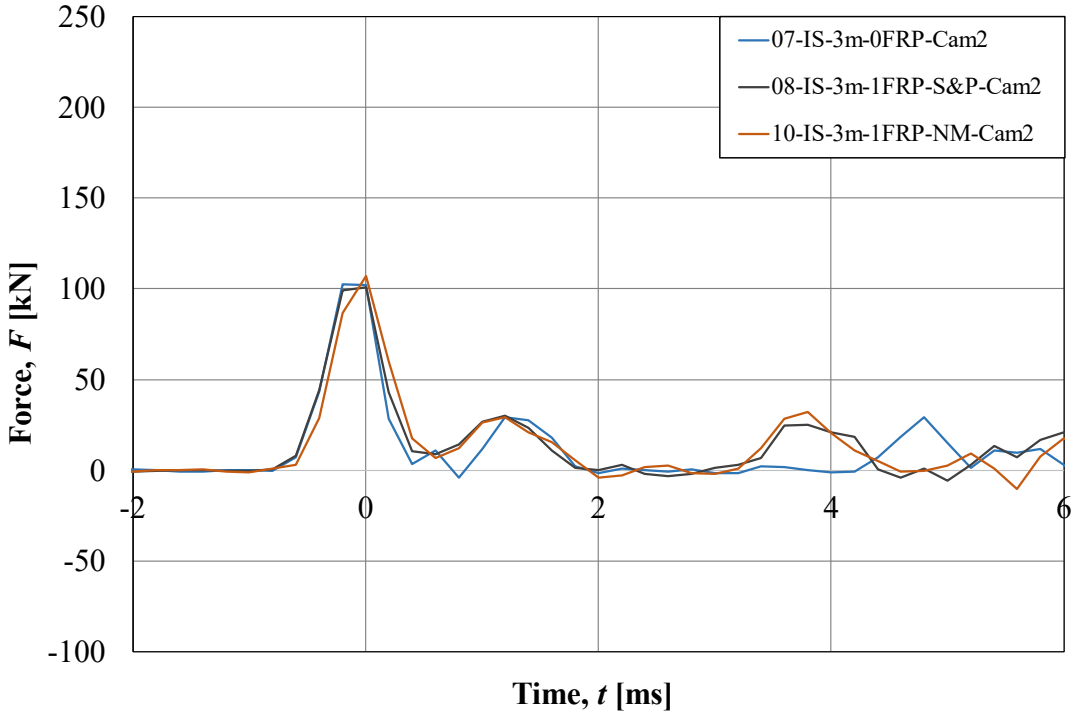

Figure 10.21 Impact force versus time for the three beams subjected to a drop weight from 3 m. Results from Camera 2.

The results presented in Figure 10.21 clearly illustrates that the noise is much smaller for Camera 2 than Camera 1. However, peak values are less distinct when using Camera 2, which also is clearly illustrated in Figure 10.21 where both the blue and the grey curve, representing beam 7 and 8 respectively, are almost horizontal at the top between the two largest values. In Figure 10.22, the impact force versus time is presented for beams subjected to drop weight from 3 m analysed with Camera 1 to be able to compare the results and see their behaviours separately.

To illustrate the differences between the captured behaviour when using Camera 1 or Camera 2, the impact force versus time is presented in Figure 10.23, for beams subjected to a drop weight from 3 m. When comparing the maximum impact force, obtained using the two cameras, a difference of around 50 kN can be observed. This, together with the illustrated horizontal peak in Figure 10.21, support the observation made above that Camera 2 does not thoroughly capture the real peak values. However, since the results from Camera 1 also includes much noise, the reliability on these results are not perfect either but they are deemed to be more reliable than the results from Camera 2.

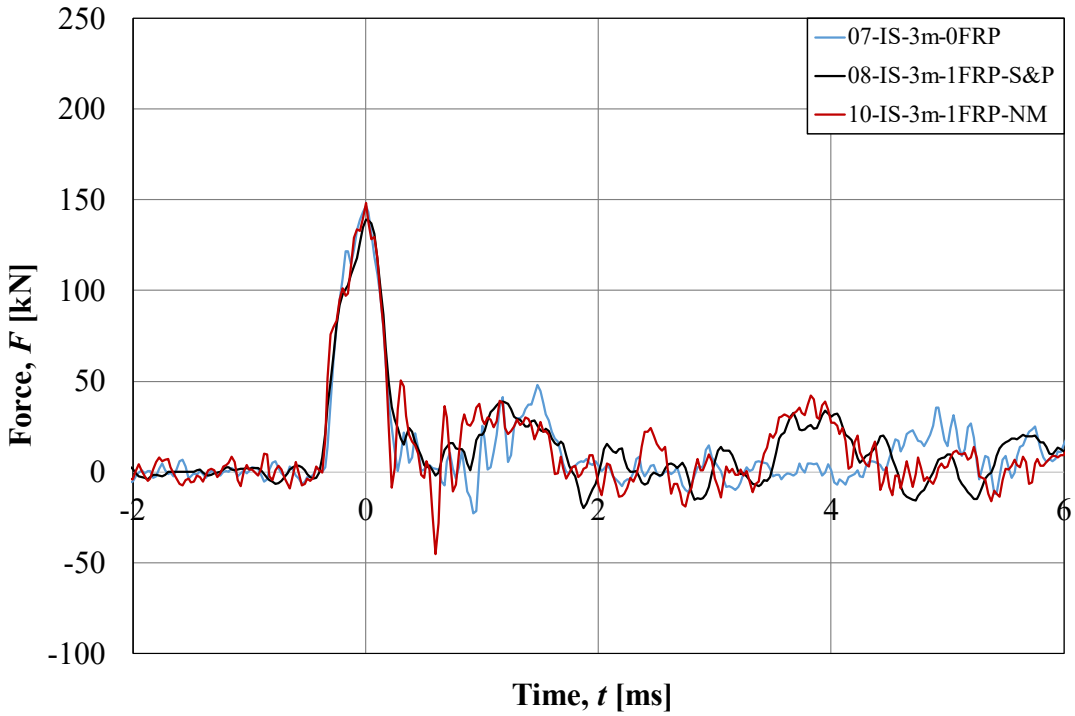

Figure 10.22 Impact force versus time for the three beams subjected to a drop weight from 3 m. Results from Camera 1.

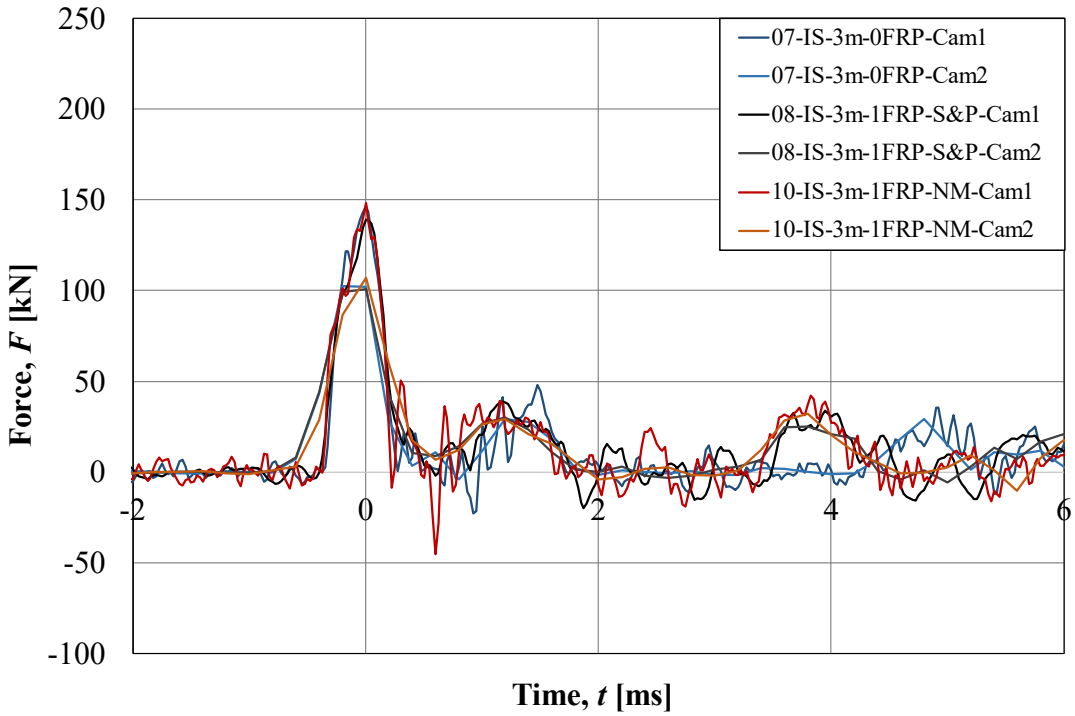

Figure 10.23 Impact force versus time for the three beams subjected to a drop weight from 3m. Comparison of results from both Camera 1 and 2.

10.2.4 Impulse at Impact

When studying the impact from the drop weight the impulse is also interesting and the impulse for all different test beams within this project is presented in this section. The impulse was calculated in a way similar to the procedure presented by Jönsson and Stenseke (2018) with total impact equal to one initial part and one post part. The initial part represents the clear first impact including the maximum impact force and the post part represent the following impulse until the impact force is zero. Impulse results presented in this section was based on the impact force results presented in Section 10.2.3 where results from Camera 1 was used. The impulse was obtained by integrating the impact force results over a specific time period. For further explanation of how the impulse was calculated and information about it, see Appendix E .

The impulse was calculated for each test beam and the results for beams subjected to a drop weight from 3 m are presented in Table 10.24. In Figure 10.24, the impact force and the total impulse are presented together over time. The time representing when maximum deflection occurred for the different beams studied is illustrated with a solid square in Figure 10.24 to Figure 10.27. These solid squares are presented to be able to easily compare the size of the impulse at the same time among the test specimens but also with the point dashed line representing the theoretical momentum of the drop weight, p_0, for the different heights. p_0 was calculated according to Equation (5.1). The values of p_0 for the different heights are also presented in Table 10.23 and can be compared to $I_{t(u_{max})}$, which is the impulse at the time of maximum deformation during impact.

Table 10.23 Theoretical momentum of the drop weight.

	3 m	**4 m**	**5 m**	**5.7 m**
$\boldsymbol{p_0}$	153 Ns	177 Ns	198 Ns	212 Ns

Table 10.24 Impulse results for beams subjected to a drop weight from 3 m.

Test beam	$\boldsymbol{I_{initial}}$ **[Ns]**	$\boldsymbol{I_{post}}$ **[Ns]**	$\boldsymbol{I_{t(u_{max})}}$ **[Ns]**	$\boldsymbol{\frac{I_{initial}}{I_{t(u_{max})}}}$	$\boldsymbol{I_{tot}}$ **[Ns]**	$\boldsymbol{\frac{I_{initial}}{I_{tot}}}$
07-IS-3m-0FRP	59	138	153	0.39	197	0.30
08-IS-3m-1FRP-S&P	61	178	152	0.40	240	0.26
10-IS-3m-1FRP-NM	62	167	151	0.41	229	0.27
Mean FRP	**62**	**173**	**152**	**0.41**	**234**	**0.27**
Mean	**61**	**161**	**152**	**0.40**	**222**	**0.28**

Small variations of initial impulse magnitude were observed where all three beams had an initial impulse of around 60 Ns. The post impulse though varied more where it was around 140 Ns for the unstrengthened beam and around 165-180 Ns for the two FRP strengthened beams. When comparing the impulse at the time of maximum deflection with the theoretical momentum of the drop weight of 150 Ns it is clear that similar values are obtained, see Figure 10.24.

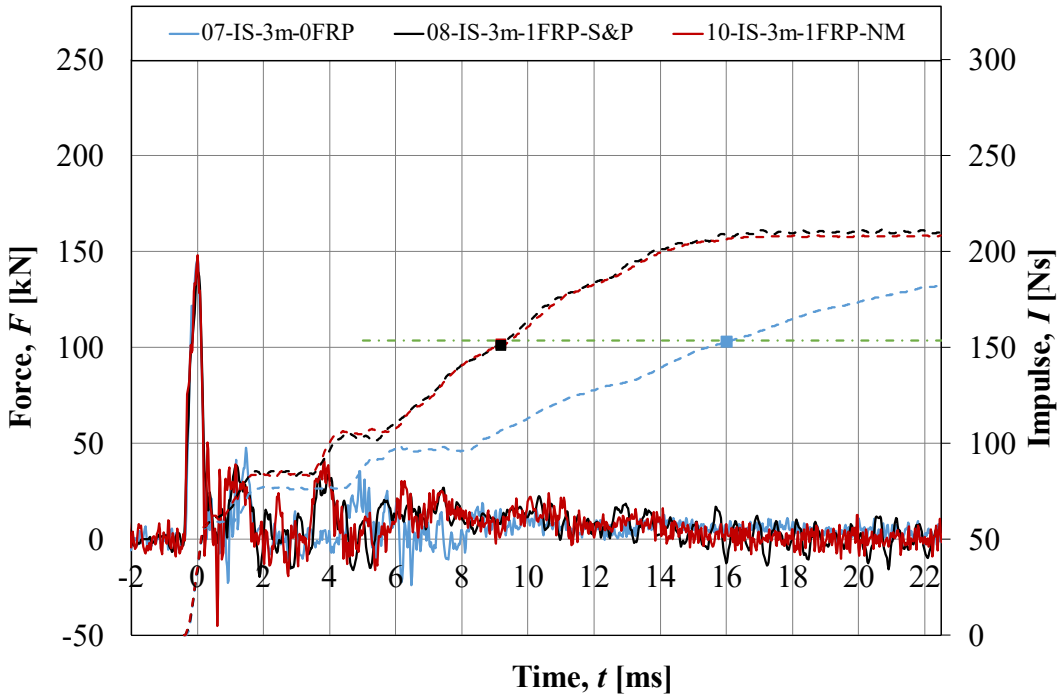

Figure 10.24 *Impact force versus time and impulse versus time for beams subjected to a drop weight from 3 m. Solid lines represent the impact force and dashed lines represents the impulse.*

In Table 10.25 is the results for beams subjected to a drop weight from 4 m presented. In Figure 10.25 is the impact force and the total impulse presented together over time.

Table 10.25 *Impulse results for beams subjected to a drop weight from 4 m.*

Test beam	$I_{initial}$ [Ns]	I_{post} [Ns]	$I_{t(u_{max})}$ [Ns]	$\frac{I_{initial}}{I_{t(u_{max})}}$	I_{tot} [Ns]	$\frac{I_{initial}}{I_{tot}}$
12-IS-4m-0FRP	66	120	174	0.38	186	0.35
13-IS-4m-1FRP-S&P	70	162	171	0.41	231	0.30
14-IS-4m-1FRP-S&P	66	170	173	0.38	236	0.28
15-IS-4m-1FRP-NM	69	177	172	0.40	245	0.28
16-IS-4m-1FRP-NM	68	171	171	0.40	239	0.29
Mean FRP	**68**	**170**	**172**	**0.40**	**238**	**0.29**
Mean	**68**	**160**	**172**	**0.39**	**227**	**0.3**

Regarding both the initial impulse and the post impulse, the variation was quite small. Beam 13 had a total impulse a bit smaller than the other beams but overall, the variations were small. The difference in post impulse between the unstrengthened beam and the FRP strengthened ones was around 50 Ns compared to 35 Ns difference for beams subjected to a drop weight from 3 m. As illustrated in Figure 10.25 the total impulse varied very little between the beams, especially until around 12-13 ms. The value of the total impulse at the time for maximum deflection for all beams subjected to a drop weight from 4 m was very close to the theoretical momentum of 177 Ns.

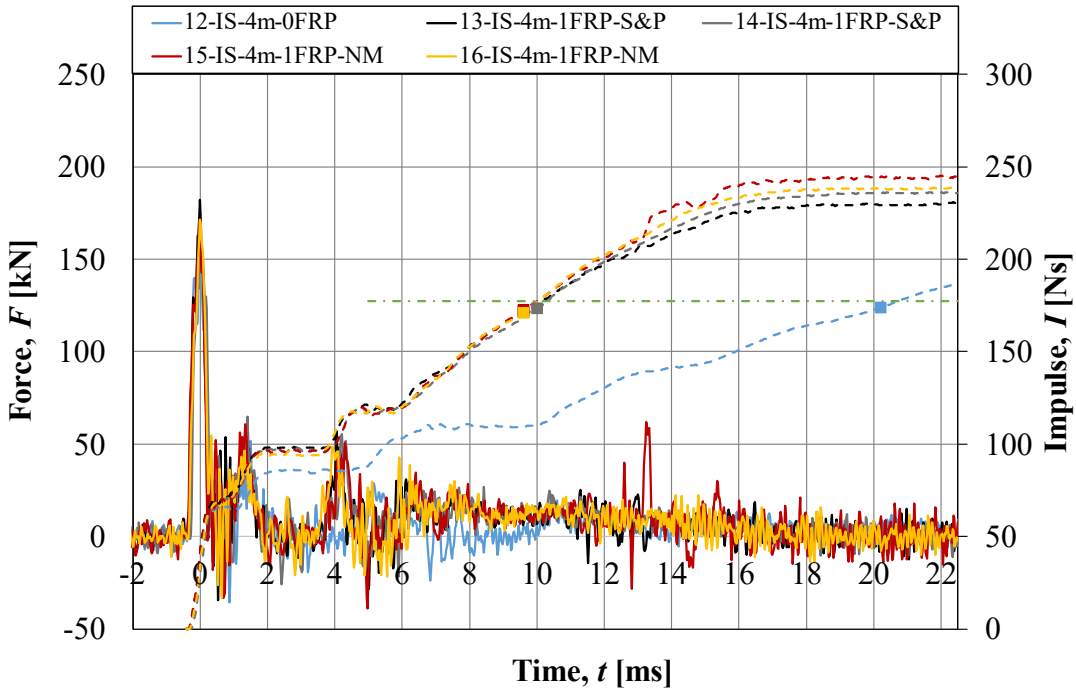

Figure 10.25 Impact force versus time and impulse versus time for beams subjected to a drop weight from 4 m. Solid lines represent the impact force and dashed lines represent the impulse.

The results for beams subjected to a drop weight from 5 m is presented in Table 10.26 and the impact force and impulse versus time is presented in Figure 10.26.

Table 10.26 Impulse results for beams subjected to a drop weight from 5 m.

Test beam	$I_{initial}$ [Ns]	I_{post} [Ns]	$I_{t(u_{max})}$ [Ns]	$\frac{I_{initial}}{I_{t(u_{max})}}$	I_{tot} [Ns]	$\frac{I_{initial}}{I_{tot}}$
17-IS-5m-0FRP	71	128	196	0.36	199	0.36
19-IS-5m-1FRP-S&P	76	164	188	0.40	240	0.32
20-IS-5m-1FRP-S&P	76	189	192	0.40	265	0.29
21-IS-5m-1FRP-NM	77	146	192	0.40	223	0.35
22-IS-5m-1FRP-NM	78	179	199	0.39	257	0.30
Mean FRP	**77**	**169**	**193**	**0.40**	**246**	**0.32**
Mean	**76**	**161**	**193**	**0.39**	**237**	**0.32**

The initial impulse had small variations and especially for the FRP strengthened beam where it varied between 76 and 78 Ns. The post impulse varied a bit more though where beam 18 was a bit higher than the other ones and 21 got a bit lower post impulse than the other beams which also could be seen in Figure 10.26. The value of the impulse at the time for maximum deflection was though very similar when comparing the beams to each other and to the theoretical value of the momentum of the drop weight of almost 200 Ns.

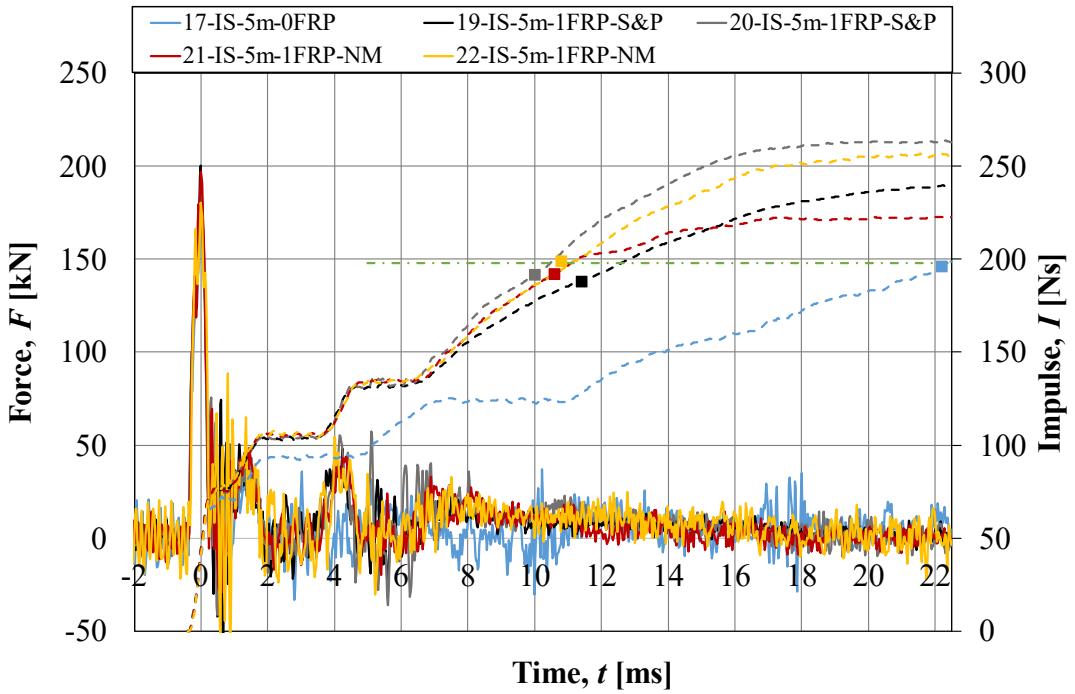

Figure 10.26 Impact force versus time and impulse versus time for beams subjected to a drop weight from 5 m. Solid lines represent the impact force and dashed lines represent the impulse.

Results for beams subjected to a drop weight from 5.7 m is presented in Table 10.27 and in Figure 10.27 is impact force and impulse versus time presented for the beams.

Table 10.27 Impulse results for beams subjected to a drop weight from 5.7 m.

Test beam	$I_{initial}$ **[Ns]**	I_{post} **[Ns]**	$I_{t(u_{max})}$ **[Ns]**	$\frac{I_{initial}}{I_{t(u_{max})}}$	I_{tot} **[Ns]**	$\frac{I_{initial}}{I_{tot}}$
18-IS-5.7m-0FRP	75	115	190	0.40	190	0.39
09-IS-5.7m-1FRP-S&P	80	155	207	0.39	235	0.34
11-IS-5.7m-1FRP-NM	79	185	203	0.39	264	0.30
Mean FRP	**79**	**170**	**205**	**0.39**	**249**	**0.32**
Mean	**78**	**152**	**200**	**0.39**	**230**	**0.34**

As seen in Table 10.27 the initial impulse had small variations between the FRP strengthened beams with a value around 79 Ns. The post impulse varied a bit more with a post impulse of 155 Ns for beam 9 and 185 Ns for beam 11. If the value of the impulse at the time of maximum deflection is studied instead one can see that the results was very close to each other for the two FRP strengthened beams subjected to a drop weight form 5.7 m but the impulse for the unstrengthened one was a bit lower. Comparing the theoretical value of the theoretical momentum of the drop weight to the corresponding impulse for the FRP strengthened beams shows very small variations.

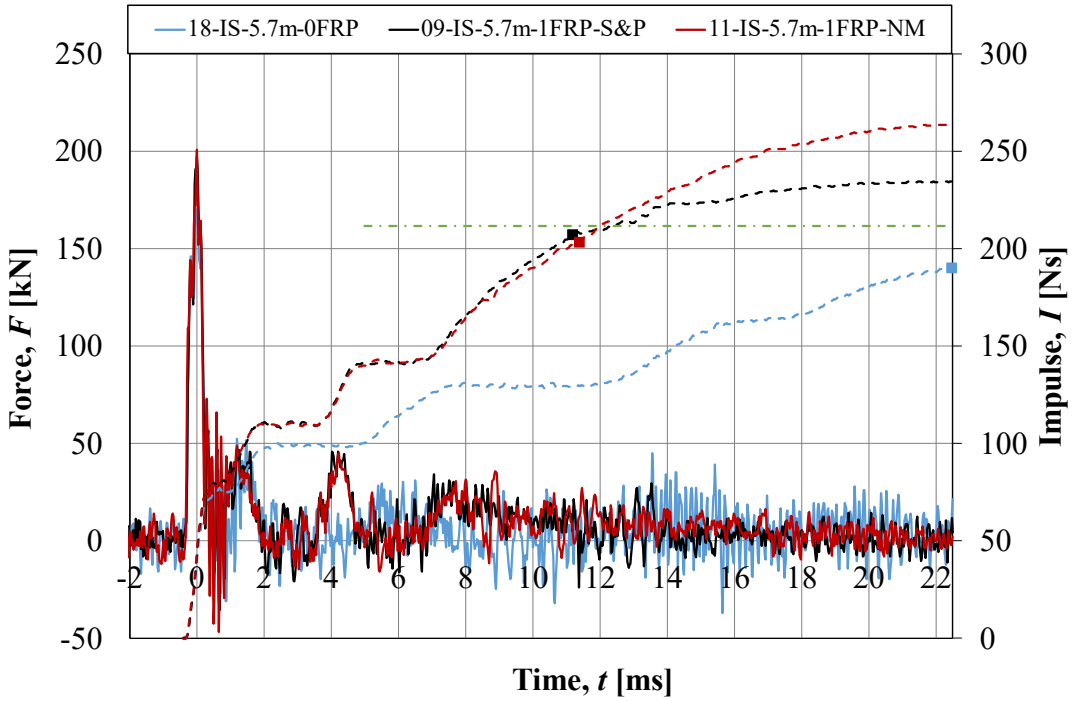

Figure 10.27 Impact force versus time and impulse versus time for beams subjected to a drop weight from 5.7 m. Solid lines represent the impact force and dashed lines represent the impulse.

The impulse was calculated with acceleration results from Camera 1. In previous theses the impulse was evaluated with result for acceleration from Camera 2 and in the following part of this section are the two cameras compared to validate the results from the two cameras. The impulse calculated for Camera 2 was done with an initial impulse calculated over 1.2 ms from -0.6 ms before maximum impact force to 0.6 ms after the maximum impact force and a post impulse from 0.6 ms to 22.5 ms after maximum impact force. Same procedure of processing the impact force as presented in Section 10.2.4 was used when impulse was calculated. Calculated initial and total impulse for Camera 1 and Camera 2 for beams subjected to a drop weight from 3 m is presented in Table 10.28 and Table 10.29, respectively.

Table 10.28 Comparison of initial impulse between Camera 1 and Camera 2 for beams subjected to a drop weight from 3 m.

Test beam	$I_{initial.cam\ 1}$ **[Ns]**	$I_{initial.cam\ 2}$ **[Ns]**	$\frac{I_{initial.cam\ 1}}{I_{initial.cam\ 2}}$
07-IS-3m-0FRP	59	57	1.03
08-IS-3m-1FRP-S&P	61	62	0.99
10-IS-3m-1FRP-NM	62	61	1.01
Mean FRP	**62**	**62**	**1.00**
Mean	**61**	**60**	**1.01**

Table 10.29 Comparison of total impulse between Camera 1 and Camera 2 for beams subjected to a drop weight from 3 m.

Test beam	$I_{tot.cam\ 1}$ **[Ns]**	$I_{tot.cam\ 2}$ **[Ns]**	$\frac{I_{tot.cam\ 1}}{I_{tot.cam\ 2}}$
07-IS-3m-0FRP	182	183	1.00
08-IS-3m-1FRP-S&P	211	210	1.00
10-IS-3m-1FRP-NM	208	208	1.00
Mean FRP	**210**	**209**	**1.00**
Mean	**201**	**200**	**1.00**

Since the initial impulse was not evaluated over the exact same time period the actual initial impulse perhaps could vary a bit from the results presented in Table 10.28 but the deviation should be small. A conclusion that could be drawn from results for 3 m drop height is that there are very small differences between the cameras when calculating the impulse. Calculated initial and total impulse for Camera 1 and Camera 2 for beams subjected to a drop weight from 4 m is presented in Table 10.30 and Table 10.31, respectively.

Table 10.30 Comparison of initial impulse between Camera 1 and Camera 2 for beams subjected to a drop weight from 4 m.

Test beam	$I_{initial.cam\ 1}$ **[Ns]**	$I_{initial.cam\ 2}$ **[Ns]**	$\frac{I_{initial.cam\ 1}}{I_{initial.cam\ 2}}$
12-IS-4m-0FRP	66	67	0.98
13-IS-4m-1FRP-S&P	69	69	1.00
14-IS-4m-1FRP-S&P	66	65	1.02
15-IS-4m-1FRP-NM	69	67	1.02
16-IS-4m-1FRP-NM	68	69	1.00
Mean FRP	**68**	**67**	**1.01**
Mean	**68**	**67**	**1.00**

Table 10.31 Comparison of total impulse between Camera 1 and Camera 2 for beams subjected to a drop weight from 4 m.

Test beam	$I_{tot.cam\ 1}$ **[Ns]**	$I_{tot.cam\ 2}$ **[Ns]**	$\frac{I_{tot.cam\ 1}}{I_{tot.cam\ 2}}$
12-IS-4m-0FRP	186	184	1.01
13-IS-4m-1FRP-S&P	231	230	1.00
14-IS-4m-1FRP-S&P	236	234	1.01
15-IS-4m-1FRP-NM	245	236	1.04
16-IS-4m-1FRP-NM	239	239	1.00
Mean FRP	**238**	**235**	**1.01**
Mean	**227**	**225**	**1.01**

The similarities were very clear for beams subjected to a drop weight from 4 m as well which is presented in Table 10.30 and Table 10.31. Calculated initial and total impulse for Camera 1 and Camera 2 for beams subjected to a drop weight from 5 m is presented in Table 10.32 and Table 10.33, respectively.

Table 10.32 Comparison of initial impulse between Camera 1 and Camera 2 for beams subjected to a drop weight from 5 m.

Test beam	$I_{initial.cam\ 1}$ **[Ns]**	$I_{initial.cam\ 2}$ **[Ns]**	$\frac{I_{initial.cam\ 1}}{I_{initial.cam\ 2}}$
17-IS-5m-0FRP	71	70	1.02
19-IS-5m-1FRP-S&P	76	76	1.00
20-IS-5m-1FRP-S&P	76	74	1.03
21-IS-5m-1FRP-NM	77	76	1.01
22-IS-5m-1FRP-NM	78	73	1.07
Mean FRP	**77**	**75**	**1.03**
Mean	**76**	**74**	**1.03**

Table 10.33 Comparison of total impulse between Camera 1 and Camera 2 for beams subjected to a drop weight from 5 m.

Test beam	$I_{tot.cam\,1}$ **[Ns]**	$I_{tot.cam\,2}$ **[Ns]**	$\frac{I_{tot.cam\,1}}{I_{tot.cam\,2}}$
17-IS-5m-0FRP	199	197	1.01
19-IS-5m-1FRP-S&P	240	239	1.01
20-IS-5m-1FRP-S&P	265	264	1.01
21-IS-5m-1FRP-NM	223	224	1.00
22-IS-5m-1FRP-NM	257	255	1.01
Mean FRP	**246**	**245**	**1.01**
Mean	**237**	**236**	**1.01**

Similar to the beams subjected to a drop weight from 3 and 4 m are the results very close to each other with small deviations of only some percentages. Calculated initial and total impulse for Camera 1 and Camera 2 for beams subjected to a drop weight from 5 m is presented in Table 10.34 and Table 10.35, respectively.

Table 10.34 Comparison of initial impulse between Camera 1 and Camera 2 for beams subjected to a drop weight from 5.7 m.

Test beam	$I_{initial.cam\,1}$ **[Ns]**	$I_{initial.cam\,2}$ **[Ns]**	$\frac{I_{initial.cam\,1}}{I_{initial.cam\,2}}$
18-IS-5.7m-0FRP	75	73	1.03
09-IS-5.7m-1FRP-S&P	80	81	0.98
11-IS-5.7m-1FRP-NM	79	79	1.00
Mean FRP	**79**	**80**	**0.99**
Mean	**78**	**78**	**1.00**

Table 10.35 Comparison of total impulse between Camera 1 and Camera 2 for beams subjected to a drop weight from 5.7 m.

Test beam	$I_{tot.cam\,1}$ [Ns]	$I_{tot.cam\,2}$ [Ns]	$\frac{I_{tot.cam\,1}}{I_{tot.cam\,2}}$
18-IS-5.7m-0FRP	190	192	0.99
09-IS-5.7m-1FRP-S&P	235	236	0.99
11-IS-5.7m-1FRP-NM	264	267	0.99
Mean FRP	**249**	**251**	**0.99**
Mean	**230**	**232**	**0.99**

For the drop height 5.7 m the variations similar to the other heights with very small variations between the two cameras and overall, the results for both the initial and the total impulse were very close to each other. A conclusion that could be drawn is that when the impulse is evaluated, results from either Camera 1 or Camera 2 works fine.

10.2.5 Deformed Shape of Beams

The deformed shape of the beams was analysed for different beams. The deformed shape shows both the actual deflection of all sections but also how the impact is transferred through the structure and how the deflection propagates from the midspan of the beam towards the support. This was made by making a section along the length of the beam in GOM Correlate and register the deflection along this section. The values of the analysis were then extracted for the first 2 ms. Since camera 2, the slower one with 5 000 FPS, recorded slightly more than half of the beam the spacing between the images are 0.2 ms. The extracted data was used to plot the graphs for both actual and relative deflection along the section for different drop heights and are presented in this section. The relative deflection means that all curves in the graph are related to the corresponding maximum value of each curve resulting in each curve has the value 1.0 at the point of maximum deflection. This is a good way to understand how the shape of the beams develops over time but in a more dramatic way.

Figure 10.28 and Figure 10.29 shows the deflection of the beams 07-IS-3m-0FRP and 08-IS-3m-1FRP-S&P, which are an unstrengthened and strengthened beam, respectively, subjected to a drop weight from the drop height of 3 m. When comparing Figure 10.28 and Figure 10.29 it can be seen that the deformations are similar to their magnitude in the midspan but that the unstrengthened beam experiences a somewhat larger deflection in the last timestep. This is also shown in Figure 10.5 where the midpoint deflection of the strengthened beam starts to increase at a slower rate compared to the unstrengthened beam around a time period of 2 ms after impact.

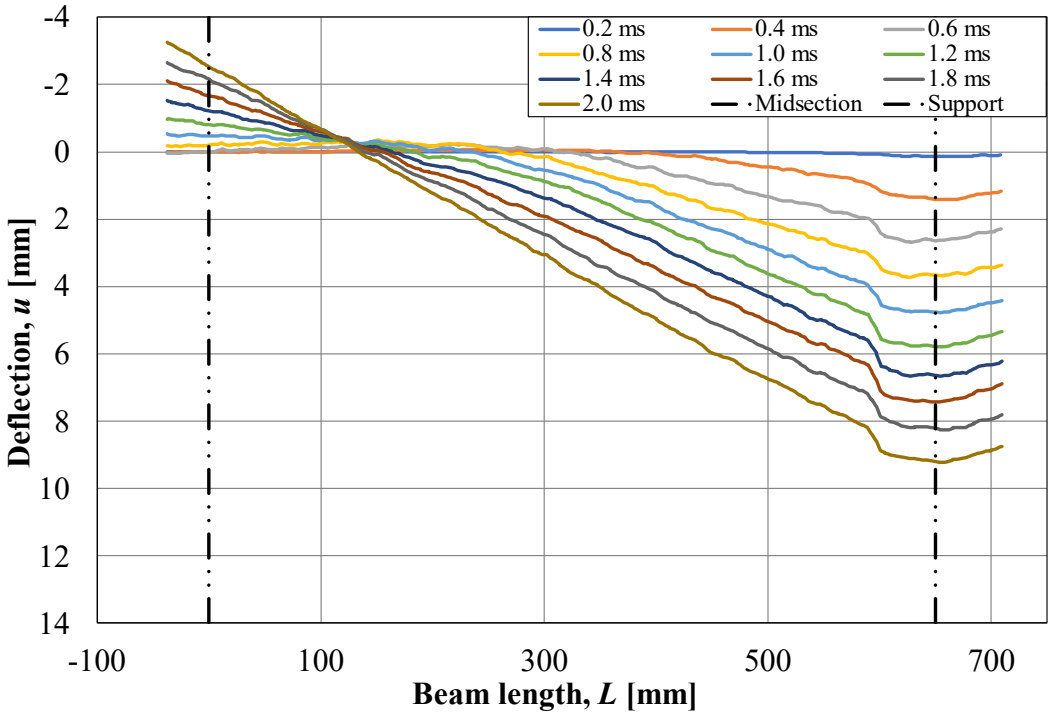

Figure 10.28 Deformed shape of unstrengthened beam subjected to drop weight from 3 m, beam 07-IS-3m-0FRP, for the first 2 ms after impact.

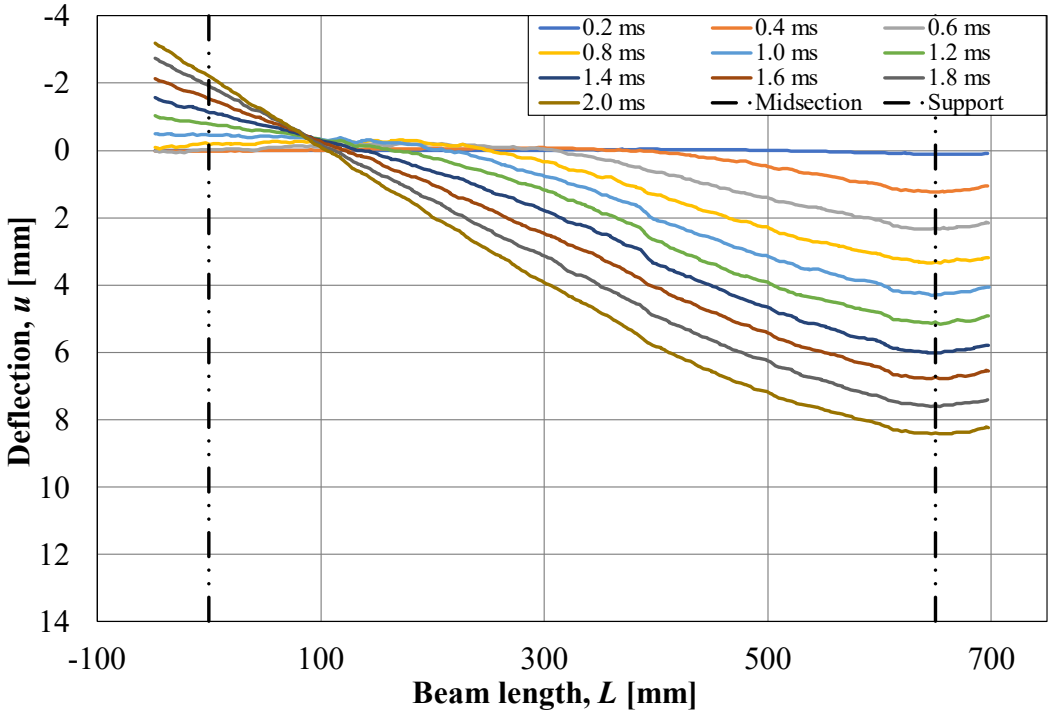

Figure 10.29 Deformed shape of FRP strengthened beam subjected to drop weight from 3 m, beam 08-IS-3m-1FRP-S&P, for the first 2 ms after impact.

However, there is another aspect which is worth noticing for the deformed shape of the beams and that is that the unstrengthened beams experienced a more triangular deformed shape compared to the strengthened beams; for the latter, the deformed shape was smoother resulting in a more parabolic shape. The different shapes of the beams

also resulted in that the deflection in midspan was higher in the unstrengthened beams while the average deflection of the FRP strengthened beams were higher. To compare this, deflections at different sections are compared in Table 10.36.

Table 10.36 Deflection at certain sections after 2 ms.

Beam	Deflection 2 ms after impact 300 mm from support [mm]	Deflection 2 ms after impact 400 mm from support [mm]	Deflection 2 ms after impact 500 mm from support [mm]	Deflection 2 ms after impact in the middle of the beam [mm]
07-IS-3m-0FRP	3.1	5.0	6.8	9.2
08-IS-3m-1FRP-S&P	3.9	5.8	7.2	8.4

The results from the deformed shape analysis are also presented here for beams 17-IS-5m-0FRP and 20-IS-5m-1FRP-S&P, which are an unstrengthened and strengthened beam, respectively, subjected to a drop weight from the drop height of 3 m. The deformed shapes for the two beams are presented in Figure 10.30 and Figure 10.31. The deflection in midspan was larger for the unstrengthened beam compared to the FRP strengthened beam. However, it was only towards the last two timesteps that the difference in the magnitude of the deflection in midspan was apparent.

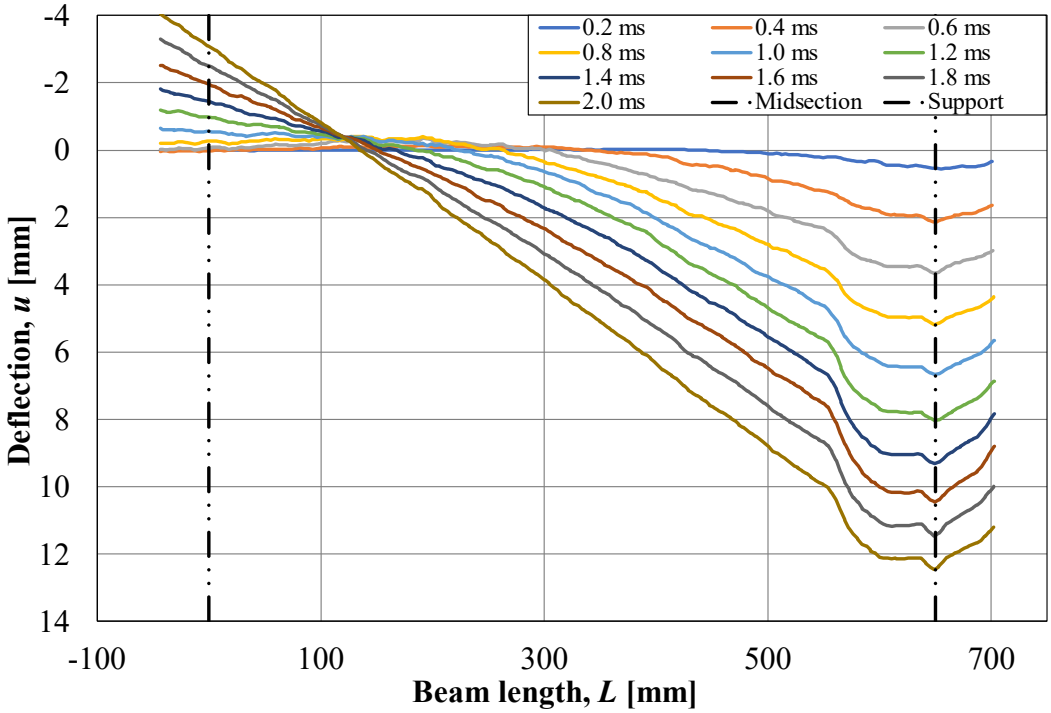

Figure 10.30 Deformed shape of FRP strengthened beam subjected to drop weight from 5 m, beam 17-IS-5m-0FRP, for the first 2 ms after impact.

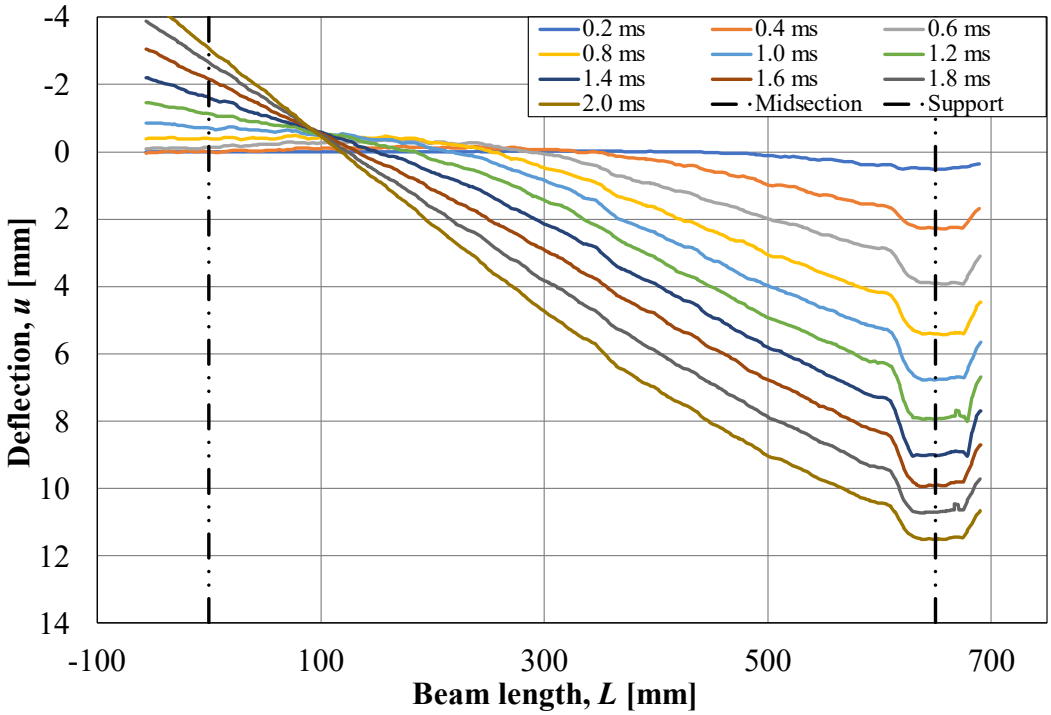

Figure 10.31 Deformed shape of FRP strengthened beam subjected to drop weight from 5 m, beam 20-IS-5m-1FRP-S&P, for the first 2 ms after impact.

Based on the general shape of the beams subjected to a drop weight from 5 m, it can be seen that for the unstrengthened beam the deformed shape is yet again more triangular than for the FRP strengthened beam which has a more parabolic shape. Similar to the 3 m case, this results in a larger average deflection along the section for the FRP strengthened beam compared to the unstrengthened beam. The deformation around the impact area also increases with increasing drop height, where the FRP strengthened beam experiences smaller deformations of the drop weight. This results in that the length from the support of which the FRP strengthened beam has a higher average deflection decreases. This is shown in Table 10.37 where for a lower drop height the effect of difference for the deformed shape was greater.

Table 10.37 Deflection at certain sections after 2 ms.

Beam	Deflection 2 ms after impact 300 mm from support [mm]	Deflection 2 ms after impact 400 mm from support [mm]	Deflection 2 ms after impact 500 mm from support [mm]	Deflection 2 ms after impact in the middle of the beam [mm]
17-IS-5m-0FRP	3.9	6.3	8.8	12.4
20-IS-5m-1FRP-S&P	4.7	7.0	9.0	11.5

The relative deflection of the four beams commented above are also compared. In Figure 10.32 and Figure 10.33, beams subjected to drop weight from 3 m are compared. Here, the triangular shape compared to the parabolic shape is also more apparent. The

reason why the first time step at 0.2 ms in Figure 10.33 behave differently is probably simply due to the fact that it is difficult to capture the impact exactly when it is happening. In this case the frame was just at impact but since the deflections are so small the noise is large in comparison to the other times steps resulting in that specific time step appearing in a deviating way in the graph.

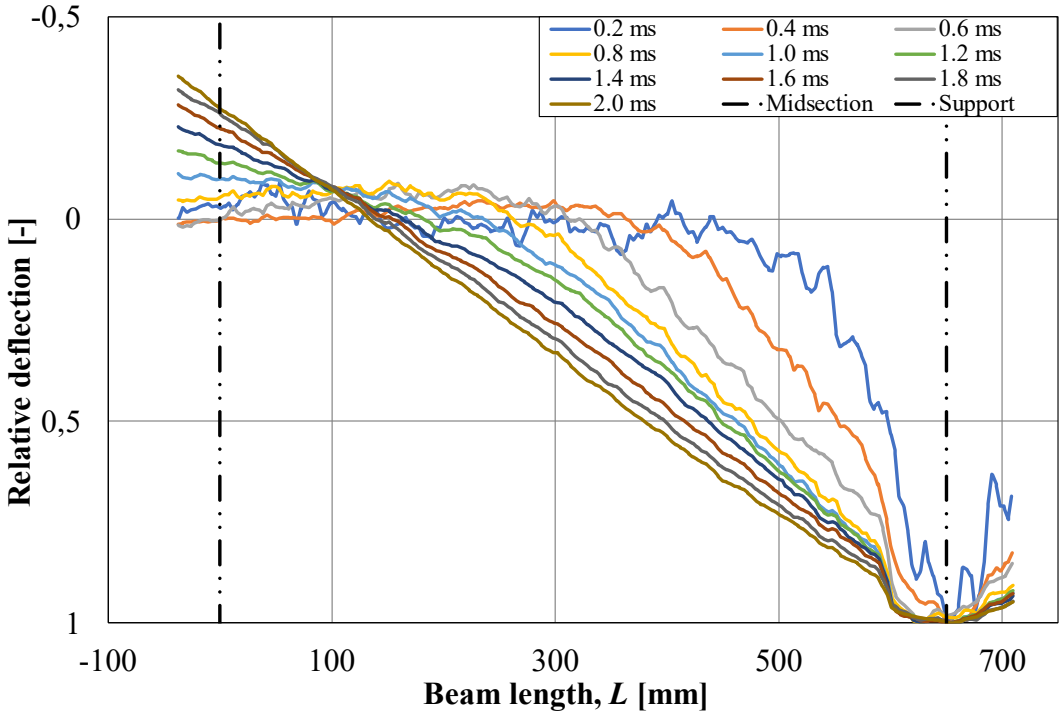

Figure 10.32 Deformed shape with relative deflection of unstrengthened beam subjected to drop weight from 3 m, beam 07-IS-3m-0FRP, for the first 2 ms after impact.

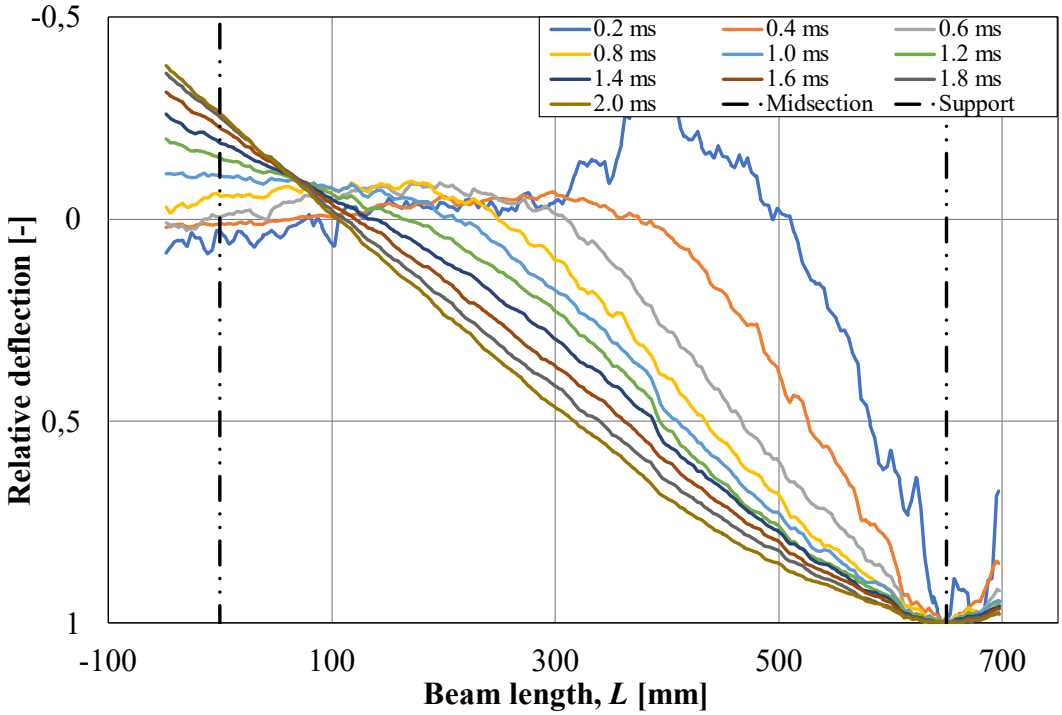

Figure 10.33 Deformed shape with relative deflection of FRP strengthened beam subjected to drop weight from 3 m, beam 08-IS-3m-1FRP-S&P, for the first 2 ms after impact.

For the case with a drop weight from 5 m drop height the same behaviour, triangular compared to parabolic shape, can be seen in Figure 10.34 and Figure 10.35. Comparing the deflections between the two drop heights it can be seen that from a lower drop height the FRP strengthening is delaying the developing of a plastic hinge. The larger load carrying capacity of the FRP compared to the reinforcement results in something in between a plastic hinge and elastic response. For the higher drop height, the plastic hinge develops in the midspan but the FRP delays the development to a higher degree.

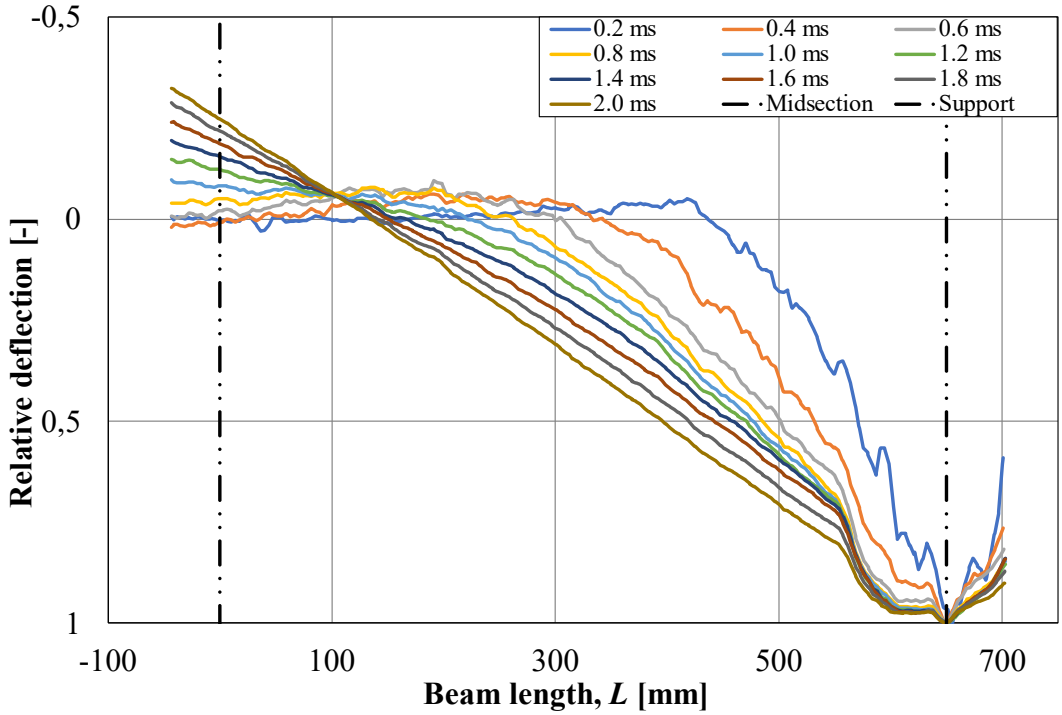

Figure 10.34 Deformed shape with relative deflection of unstrengthened beam subjected to drop weight from 5 m, beam 17-IS-5m-0FRP, for the first 2 ms after impact.

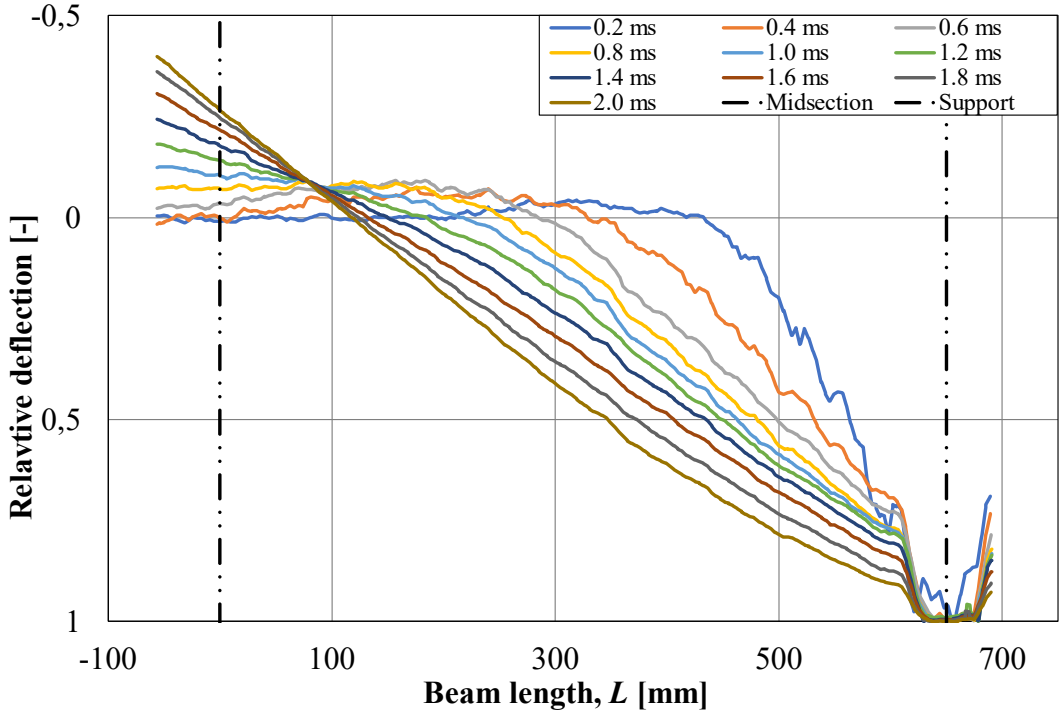

Figure 10.35 Deformed shape with relative deflection of FRP strengthened beam subjected to drop weight from 5 m, beam 20-IS-5m-1FRP-S&P, for the first 2 ms after impact.

10.2.6 Drop Weight Velocity

The velocity of the drop weight for the drop test were extracted from GOM Correlate by extracting the velocity of three points and then calculating the mean value of these points. The velocities were compared between the different beams subjected to the same drop height or with the same adhesive but from different drop heights. A selection of these is presented in this section, all results are also presented in Appendix D . Since two high-speed cameras with different frames per second were used, the velocities from the different cameras were compared.

In Figure 10.36 and Figure 10.37 the velocity of the drop weight from 4 m are presented. What can be seen is that the velocity is reduced faster after the drop weight impacts the beam if the beam is strengthened with FRP. What also can be seen is that the difference between the two different adhesives is very small. All the four strengthened beams behave in a very similar manor. Something worth noticing in Figure 10.37, where the velocities of the drop weight are compared between the two cameras, is that the results are very similar but with a little more noise for Camera 1.

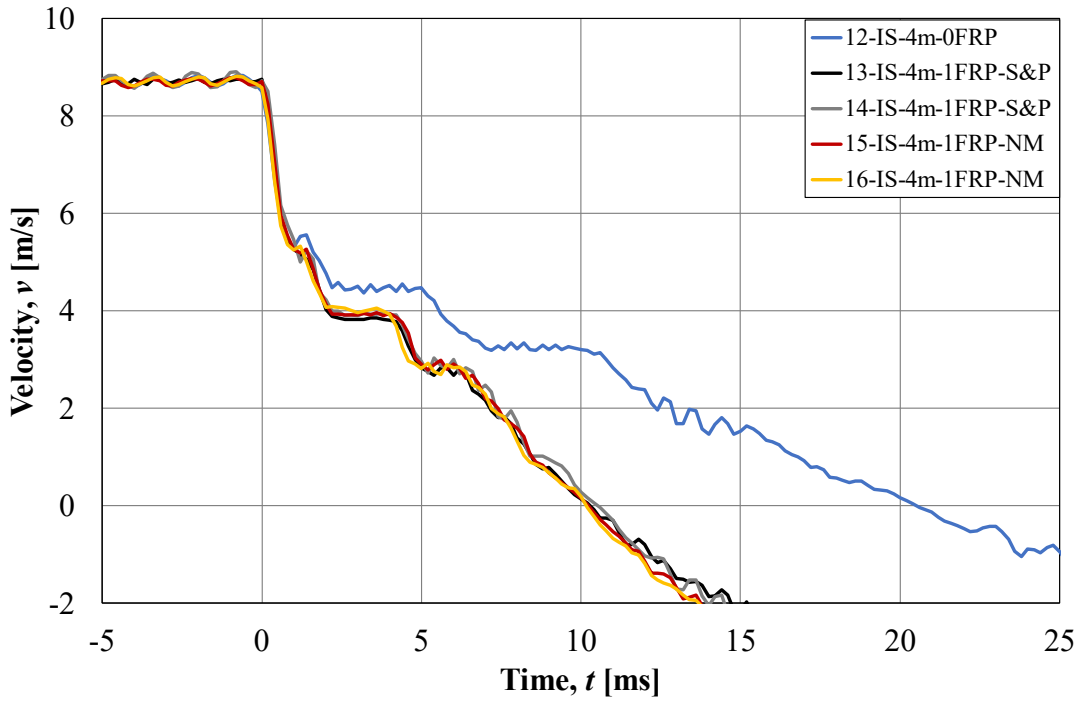

Figure 10.36 Velocity of drop weight from a drop height of 4 m from Camera 2.

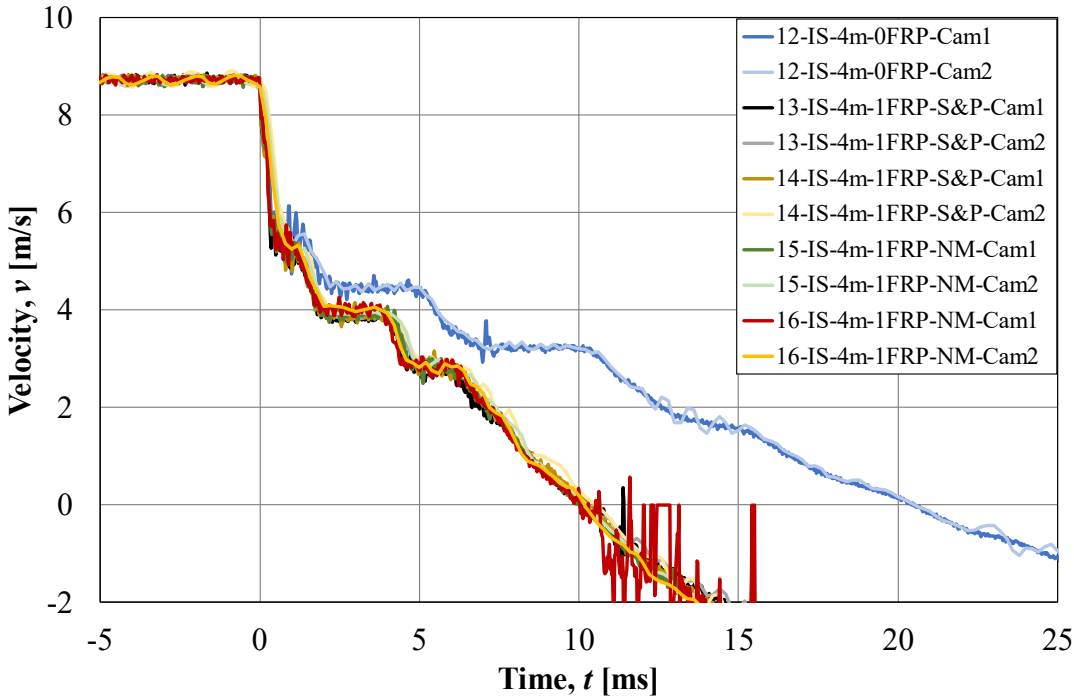

Figure 10.37 Comparison of the velocity of the drop weight between the two high speed cameras from a drop height of 4 m.

The results were very similar with varying drop heights. The initial velocity was higher, but the behaviour was the same where the FRP strengthened beams reduced the velocity of the drop weight faster compared to an unstrengthened beam. Figure 10.38 shows the velocity from the drop height of 5 m. After about 7 ms, the results of the four strengthened beams become less gathered than from a drop height of 4 m. This is something that was noticed in general that with increasing drop height the results differed more, even though the scatter is rather small. To see all of the graphs showing the results from the evaluation of the drop weight velocity the reader is referred to Appendix D .

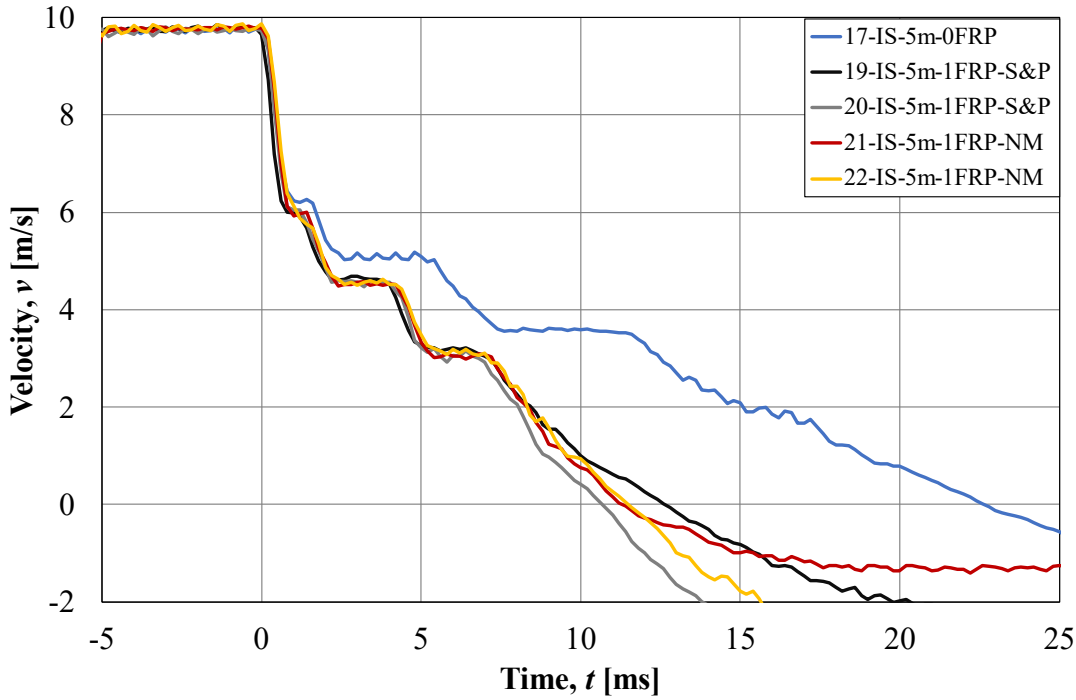

Figure 10.38 Velocity of drop weight from a drop height of 5 m from Camera 2.

The mean velocity 3 ms before impact was calculated for the different beams and these are presented in Table 10.38 to Table 10.41 for the different drop heights. The velocities from both cameras together with the calculated velocity, using gravitational acceleration g as 9.81 m/s^2, are presented. What can be seen when studying the values of the velocities is that the measured values match well with the calculated value. However, for all heights the calculated value is slightly higher than the measured ones. The measured ones match very well between themselves and the values between the two cameras are practically the same. If the maximum and minimum values were studied during the 3 ms before impact then these values could differ between the two cameras where Camera 1 showed a larger variation, probably due to increased noise for this camera. But since the mean values were studied it can be said that the velocities match well for all beams.

Table 10.38 Meassured and calculated velocities from a drop height of 3 m.

Beam name	Velocity Camera 1 [m/s]	Velocity Camera 2 [m/s]	Calculated velocity [m/s]
07-IS-3m-0FRP	7.60	7.58	7.67
08-IS-3m-1FRP-S&P	7.60	7.59	
10-IS-3m-1FRP-NM	7.59	7.59	

Table 10.39 Meassured and calculated velocities from a drop height of 4 m.

Beam name	Velocity Camera 1 [m/s]	Velocity Camera 2 [m/s]	Calculated velocity [m/s]
12-IS-4m-0FRP	8.73	8.71	8.86
13-IS-4m-1FRP-S&P	8.73	8.72	
14-IS-4m-1FRP-S&P	8.75	8.73	
15-IS-4m-1FRP-NM	8.71	8.70	
16-IS-4m-1FRP-NM	8.73	8.71	

Table 10.40 Meassured and calculated velocities from a drop height of 5 m.

Beam name	Velocity Camera 1 [m/s]	Velocity Camera 2 [m/s]	Calculated velocity [m/s]
17-IS-5m-0FRP	9.77	9.77	9.90
19-IS-5m-1FRP-S&P	9.78	9.78	
20-IS-5m-1FRP-S&P	9.74	9.74	
21-IS-5m-1FRP-NM	9.79	9.78	
22-IS-5m-1FRP-NM	9.80	9.79	

Table 10.41 Meassured and calculated velocities from a drop height of 5.7 m.

Beam name	Velocity Camera 1 [m/s]	Velocity Camera 2 [m/s]	Calculated velocity [m/s]
18-IS-5.7m-0FRP	10.38	10.37	10.54
09-IS-5.7m-1FRP-S&P	10.43	10.43	
11-IS-5.7m-1FRP-NM	10.39	10.38	

10.2.7 Strain Fields

In this section, strain fields for beams subjected to drop weight form 3 m and 5 m are presented. Results from major strain in GOM Correlate 2018 (GOM,2018) for all three beams for drop height 3 m is presented and three out of five beams subjected to drop weight from 5 m are presented; one unstrengthened and two with FRP strengthening, one with S&P and one with NM. The legend was limited to minimum value 1 % and maximum value 2 % to get rid of the noise and show the general strain field. Strain field for beam 07-IS-3m-0FRP is presented in Table 10.42.

Table 10.42 Strain fields from impact to maximum deformation for beam 07-IS-3m-0FRP.

Time step [ms]	Strain field
1 %	2 %
0.2	
0.4	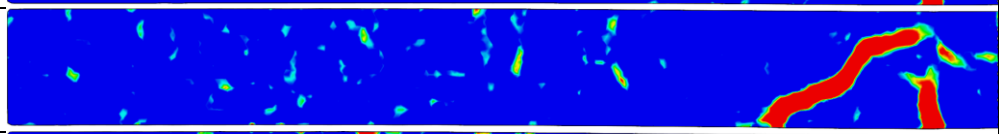
0.6	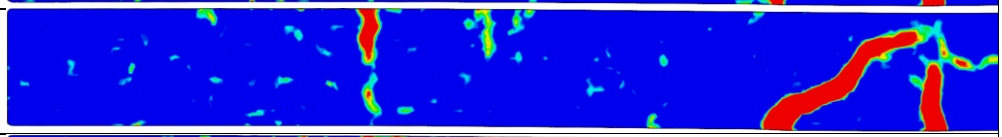
0.8	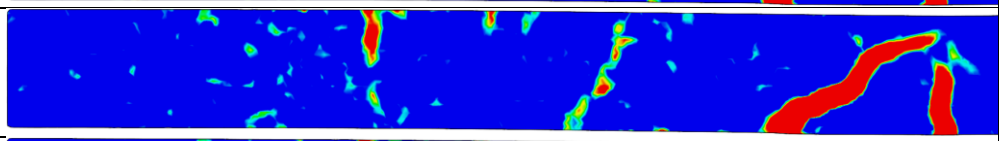
1.0	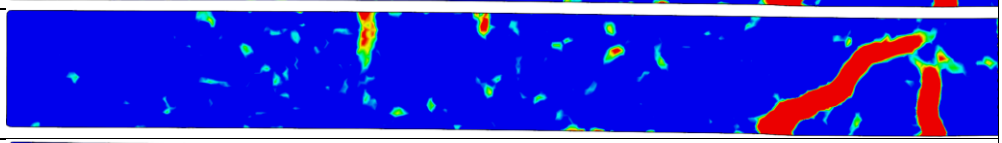
1.6	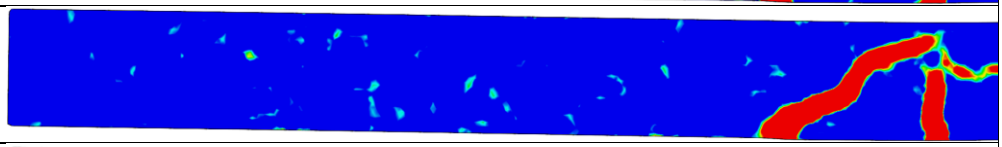
2.0	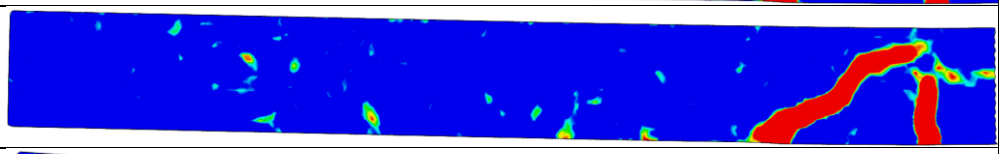
16	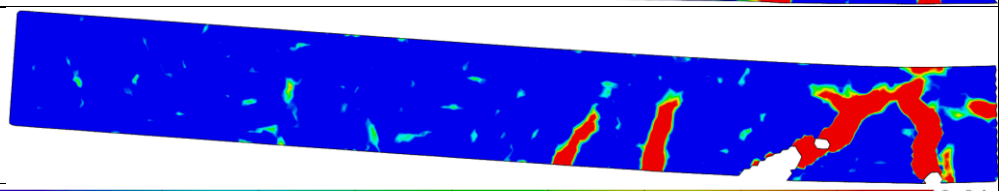
1 %	2 %

The presented strain fields in Table 10.42 clearly show a bending crack in the middle of the beam which increased with time together with a diagonal crack. At 16 ms, the maximum deformation was reached, and large deformations had occurred; two more bending cracks had also developed at the bottom of the beam. An interesting observation is the cracks propagating from the top surface at 0.6 ms until 1.0 ms and then disappear. These cracks can be connected with the observations discussed in Section 10.2.5 where the deformed shape close to the impact is studied. In Table 10.43, strain fields for beam 08-IS-3m-1FRP-S&P are presented. The major strains for the unstrengthened beam are larger than the strains presented in Table 10.43 for an FRP strengthened beam.

Table 10.43 Strain fields from impact to maximum deformation for beam 08-IS-3m-1FRP-S&P.

Time step [ms]	Strain field
1 %	2 %
0.2	
0.4	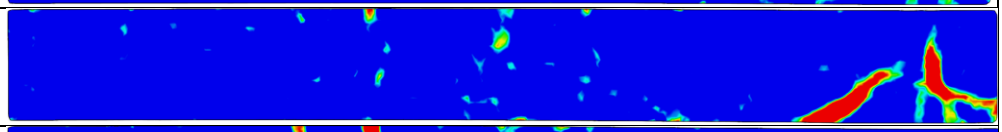
0.6	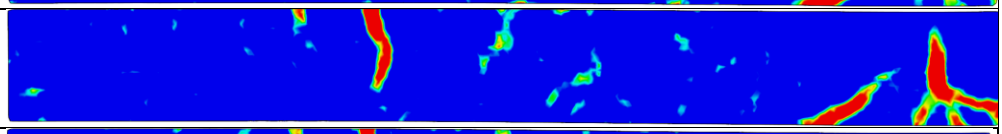
0.8	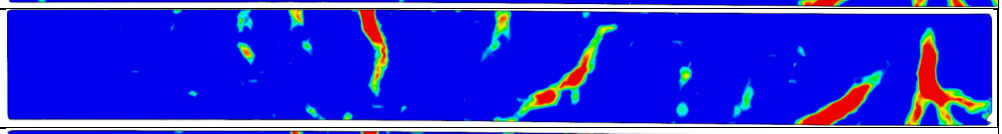
1.0	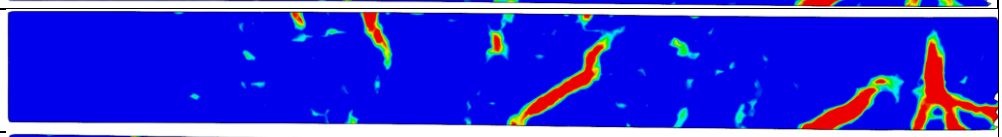
1.6	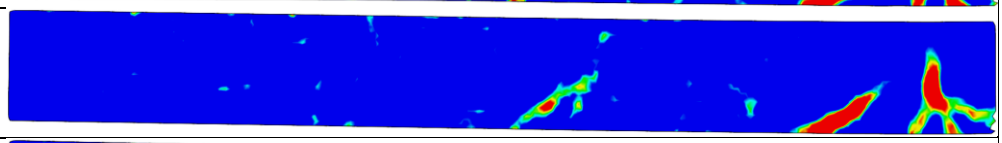
2.0	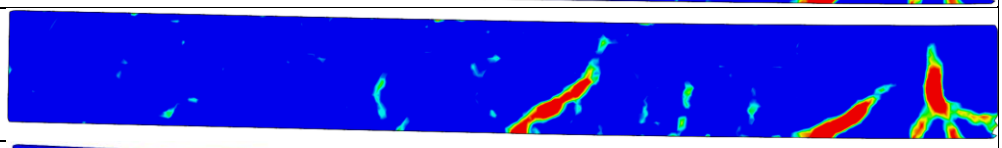
9.2	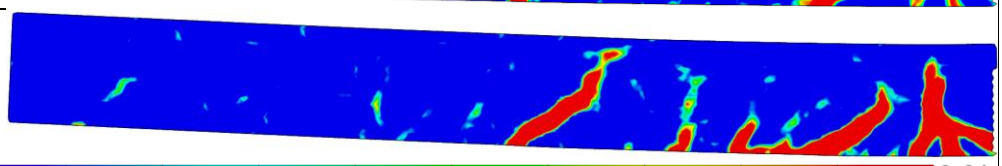
1 %	2 %

Another difference between the unstrengthened beam in Table 10.42 and the FRP strengthened beam in Table 10.43 was that the FRP strengthened beam overall showed a tendency to develop more and smaller cracks; particularly in the middle of the beam. For this beam, the cracks propagating from the upper surface was also observed between 0.6 ms and 1.0 ms; however, from 1.6 ms and forward they were not visible anymore. Strain fields for the second FRP strengthened beam subjected to a drop weight from 3 m, beam 10-IS-3m-1FRP-NM is presented in Table 10.44.

Table 10.44 Strain fields from impact to maximum deformation for beam 10-IS-3m-1FRP-NM.

Time step [ms]	Strain field
1 %	2 %
0.2	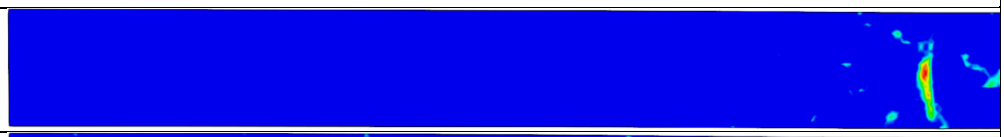
0.4	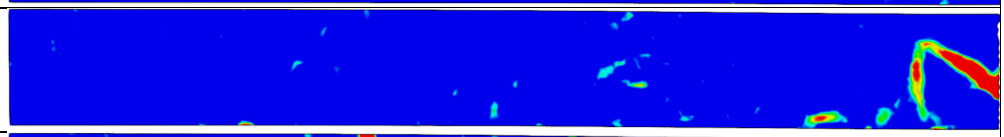
0.6	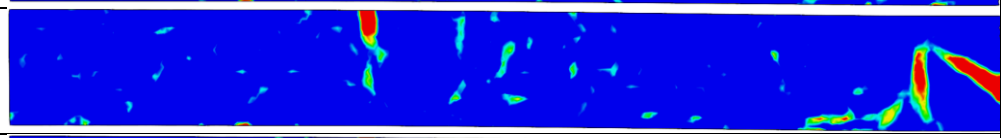
0.8	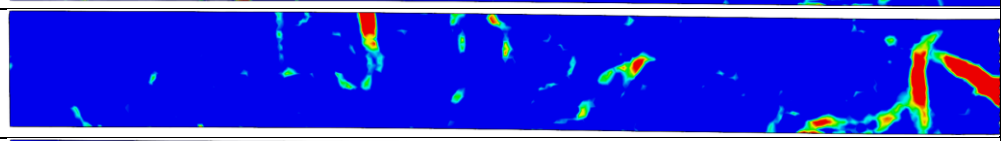
1.0	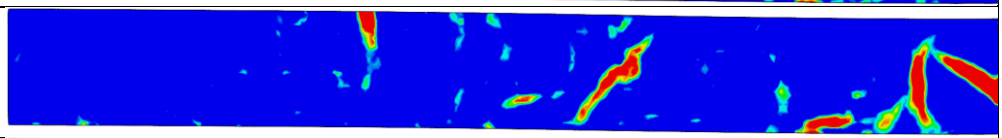
1.6	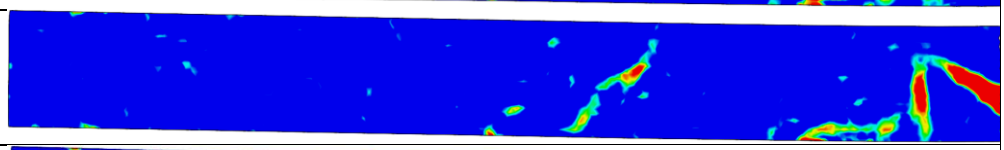
2.0	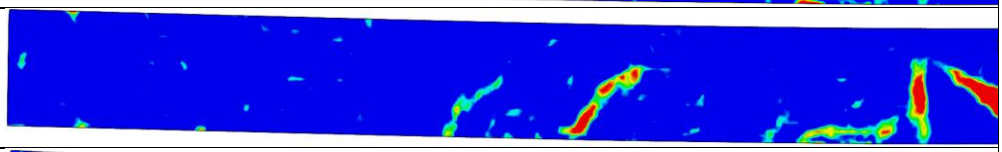
9.4	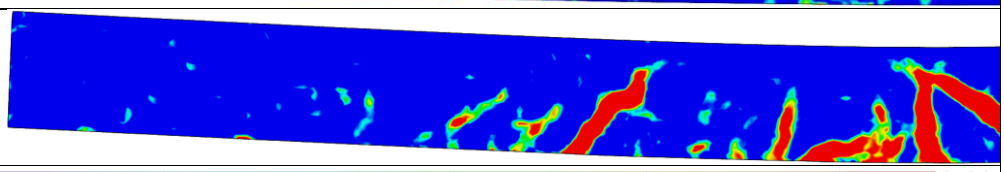
1 %	2 %

The strain fields presented for beam 10 is similar to those in the FRP strengthened beam with S&P adhesive with smaller but more cracks than the unstrengthened one. Maximum deflection occurred at around the same time for the both FRP strengthened beams. Again, the observation with cracks from the upper surface was done but this time possibly a bit smaller compared to the ones for beam 7 and beam 8.

If instead 5 m drop height is studied the strain fields for unstrengthened beam, 17-IS-5m-0FRP, is presented in Table 10.45. After 0.4 ms, the beam experienced both a bending crack in the middle and a diagonal crack.

Table 10.45 Strain fields from impact to maximum deformation for beam 17-IS-5m-0FRP.

Time step [ms]	Strain field
1 %	2 %
0.2	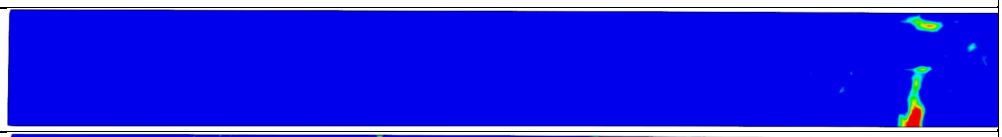
0.4	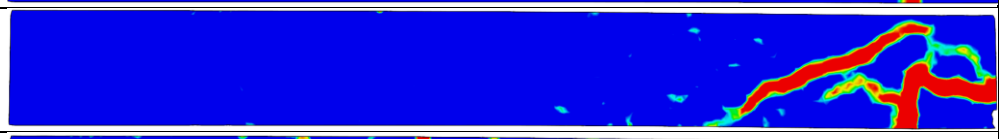
0.6	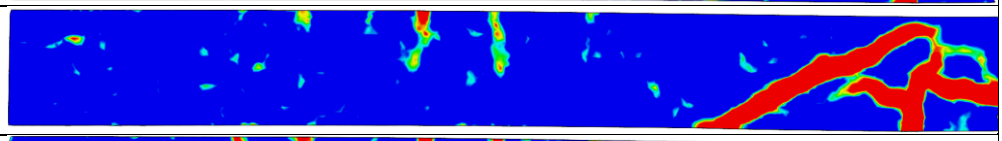
0.8	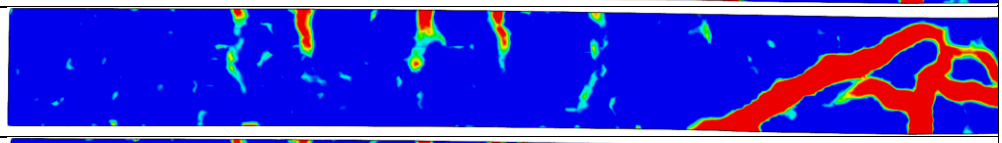
1.0	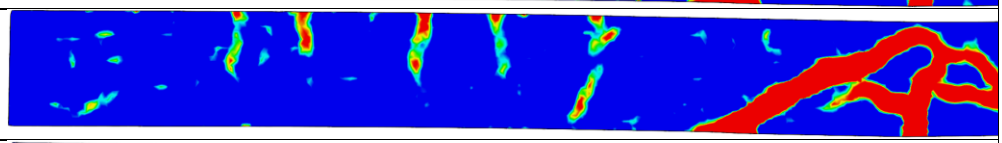
1.6	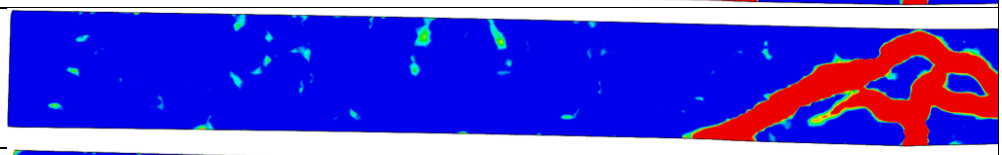
2.0	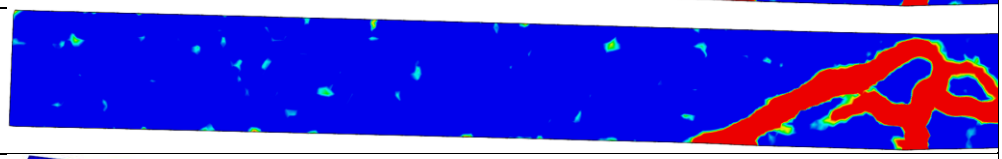
22.6	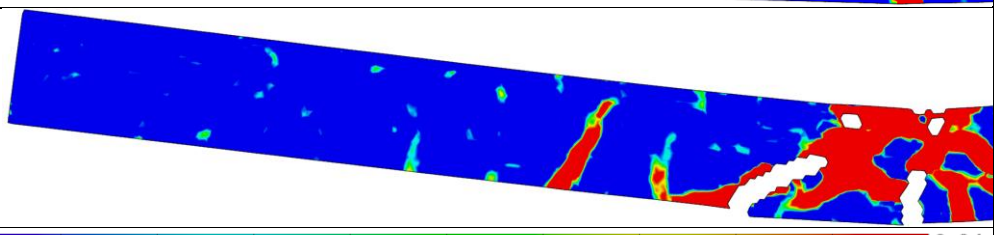
1 %	2 %

In general, strains were larger for the unstrengthened beam subjected to a drop weight from 5 m compared to the one subjected to a drop weight from 3 m; this is deemed to be reasonable. The results also showed that the concrete cracked more than in case with 3 m, which is illustrated with larger red zones and cracks developing horizontally together with white parts at the final step which was where very large cracks had developed or concrete had fell down.

Strain fields for one FRP strengthened beam with S&P adhesive subjected to drop weight from 5 m is presented in Table 10.46. The strains were larger for this beam compared to the corresponding one subjected to a drop weight from 3 m presented in

Table 10.43 which is reasonable since the impact force was larger. The strains were smaller in general compared to the unstrengthened beam for drop height 5 m, in particular the bending crack in the middle.

Table 10.46 Strain fields from impact to maximum deformation for beam 19-IS-5m-1FRP-S&P.

Time step [ms]	Strain field
	1 % — 2 %
0.2	
0.4	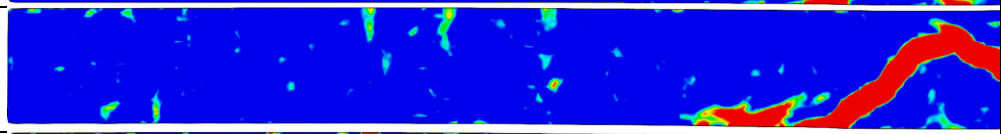
0.6	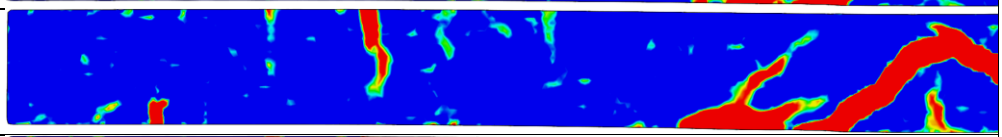
0.8	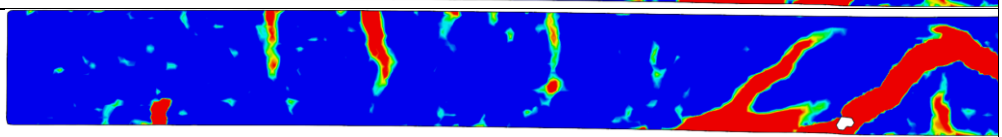
1.0	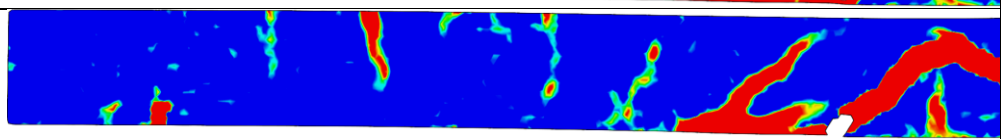
1.6	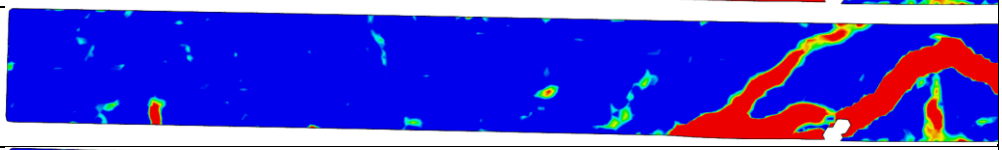
2.0	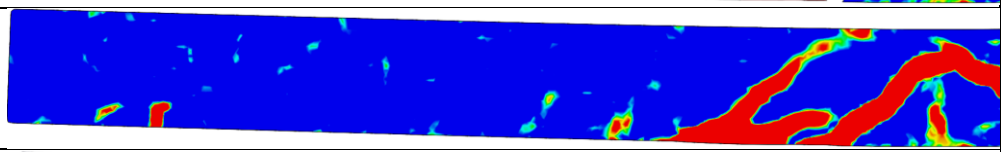
11.6	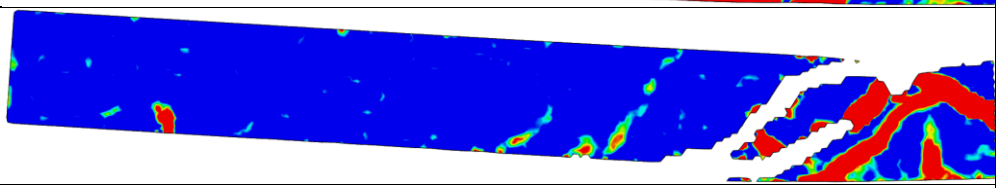
	1 % — 2 %

Two large diagonal cracks developed and between them were also large strains occurring at the bottom side of the surface, clearly illustrated from time 0.8 ms to 2.0 ms in Table 10.46. Within this area the FRP debonded and parts of the concrete were pulled off from the beam by the FRP. The FRP did not entirely debond from the beam but debonded almost all the way to the left support with large deformations. At time 11.6 ms, large deformations had taken place which can be seen as the white parts in Table 10.46, where cracks through the entire section had occurred.

The strain field for beam 21-IS-5m-1FRP-NM is presented in Table 10.47. This beam showed a very small, or almost none, tendency to develop a bending crack in the middle of the beam; this was a big difference compared to the unstrengthened beam for the same drop height. Similar to the beam with S&P adhesive for drop height 5 m, presented in Table 10.46, this beam also developed two diagonal cracks; however, they were much closer positioned to each other in this beam compared to the one with S&P adhesive. All beams presented in Table 10.45 to Table 10.47 showed the same behaviour with cracks propagating from the upper surface from 0.6 ms, except for beam 21 where such cracks started to appear at 0.4 ms, and then disappeared at 1.6 ms. As discussed in Section 10.2.5 this phenomenon is connected to the force distribution and deformation in the beam during the time immediately after impact.

Table 10.47 Strain fields from impact to maximum deformation for beam 21-IS-5m-1FRP-NM.

Time step [ms]	**Strain field**
	1 % — **2 %**
0.2	
0.4	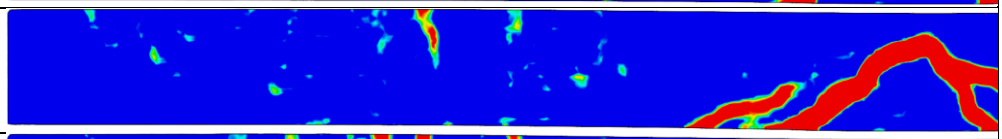
0.6	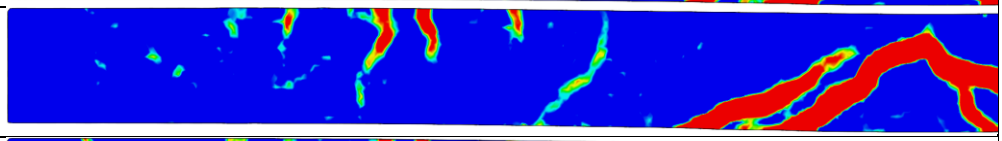
0.8	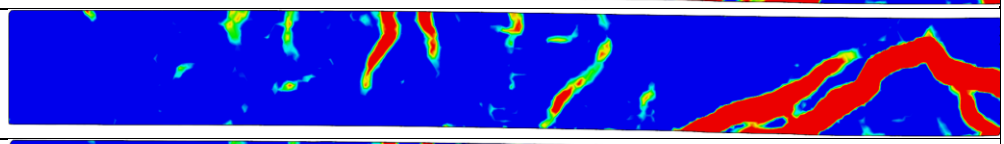
1.0	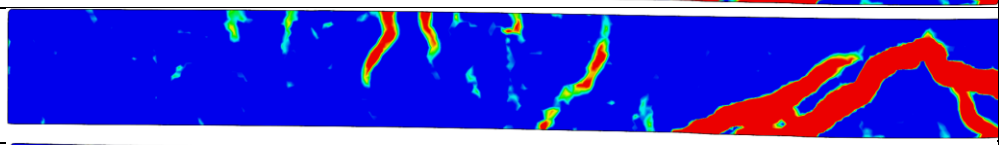
1.6	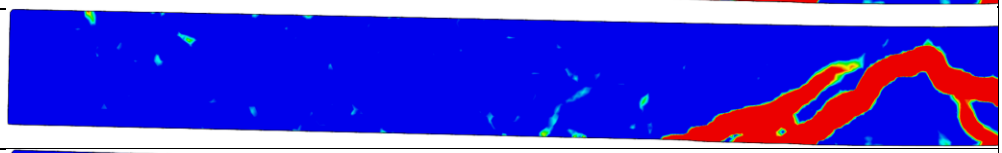
2.0	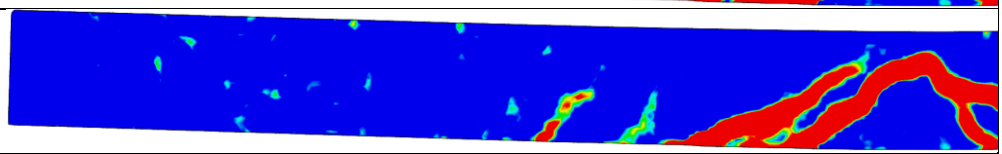
10.8	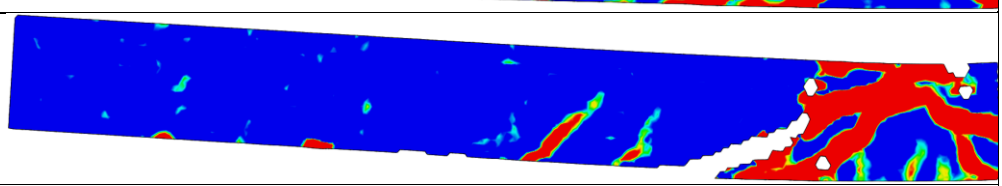
	1 % — **2 %**

Strain fields for the rest of the beams for drop height 5 m together with strain fields for beams for drop height 4 m and 5.7 m is presented in Appendix C .

10.2.8 Debonding of FRP

In most cases, debonding of the FRP strengthening did not occur until the static testing of the beams when they were loaded until failure. In some cases, though, the FRP strengthening also debonded during the drop weight tests. Since Camera 2 captured the left side of the beam, details about FRP debonding on the right side were not documented in the tests. Two beams were observed to experience complete debonding of FRP and one partial rupture of the beam in the middle of the span. Development of the debonding over time and information about the debond propagation is presented in Table 10.48.

Table 10.48 Information about debonding of FRP strengthening for the beams which experienced debonding during the impact tests.

Beam	Time from impact to start of debond [ms]	Time from impact to entire debond [ms]	Direction of debond propagation
21-IS-5m-1FRP-NM	7.0	11.0	From the middle to the left support
09-IS-5.7m-1FRP-S&P	7.4	10.8	From the middle to the left support

10.3 Static Test Results

In this section the results from the static tests are presented. All beams were tested statically where the residual strength was of interest for the beams that had previously been subjected to a drop weight. The results presented here are load deflection curves, strain fields at key moments during the static tests, internal work and plastic rotation capacity. The static tests proceeded until rupture of one reinforcement bar in all cases but two. In the first case, another failure mode occurred related to a shear type failure mode and in the second case, the beam had a very low residual strength and therefore just experienced large deformations at a very low load in a protracted process. In both cases, the tests were stopped when the static load applied had dropped to a low level. This happened for two beams from the drop height of 5.7 m where the test was eventually stopped.

10.3.1 Load Deflection

All of the 22 beams were tested statically where sixteen of them were subjected to a drop weight before the static test and the rest six were only tested statically. The six reference beams were both strengthened and unstrengthened beams and the results from the static tests for these, in form of load versus deflection, are presented in Figure 10.39.

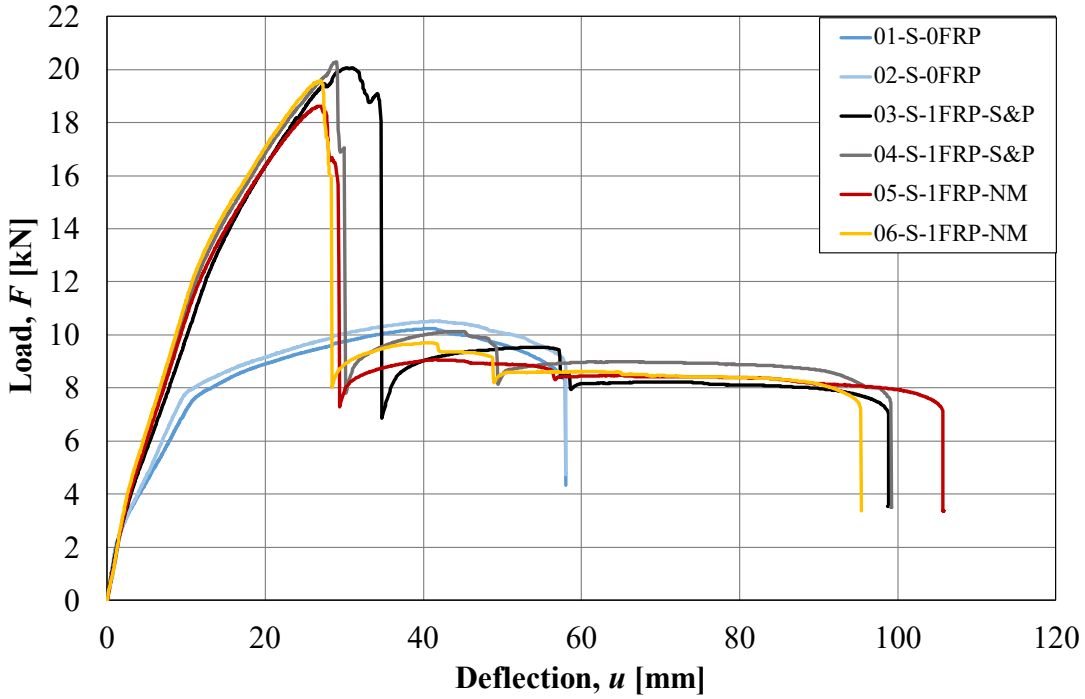

Figure 10.39 Load versus deflection curves for the six reference beams.

As can be seen in Figure 10.39, the maximum load for FRP strengthened beams was significantly larger than for unstrengthened beams with a maximum about 18-20 kN instead of about 10 kN. The top value was at the time immediately before debonding of the FRP and afterwards a large drop in load can be seen. The load level after debonding was almost at the same level as the unstrengthened beams, which is illustrated in Figure 10.39 where the blue curves are the unstrengthened beams. The maximum deflection at failure was also significant larger for the FRP strengthened beams compared to the unstrengthened beams. If the unstrengthened beams are studied, the maximum deflection at failure reached about 55-60 mm. The corresponding values for the FRP strengthened beams was about 95-105 mm, which thus provides a considerably larger deformation capacity. The ultimate load and deformation capacity for the reference beams are presented in Table 10.49.

These results point out the fact, for the structures studied here, that a structure with FRP absorbs a much larger amount of energy compared to an unstrengthened one since both the maximum load capacity and the deformation capacity was larger. This is clearly illustrated as the area under the graph for the strengthened and unstrengthened beams.

Table 10.49 Ultimate load and deflection for reference beams.

Test beam	Ultimate load [kN]	Maximum deflection [mm]
01-S-0FRP	10.2	58
02-S-0FRP	10.5	58
03-S-1FRP-S&P	20.1	99
04-S-1FRP-S&P	20.3	99
05-S-1FRP-NM	18.6	106
06-S-1FRP-NM	19.6	95

The rest of the beams were tested in both static and dynamic testing where the presented results in Figure 10.40 are load versus deflection for beams subjected to drop weight from 3 m height.

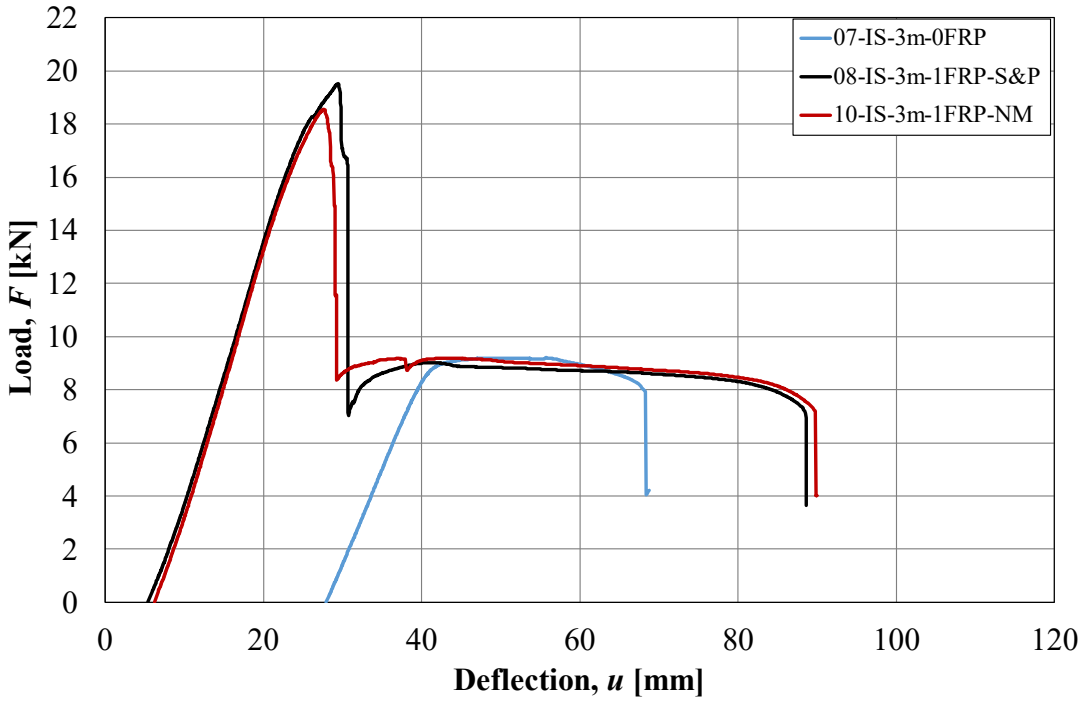

Figure 10.40 Load versus deflection for beams subjected to a drop weight from 3 m tested statically until failure.

As can be seen in Figure 10.40, each beam had a plastic deformation from the drop weight tests included in this figure. For the FRP strengthened beams this deformation was around 5-10 mm while for the unstrengthened one around 25-30 mm. The maximum load capacity for the strengthened beams was at the same level as the reference beams in Figure 10.39 and the deformation capacity was a bit smaller but around the same level. For beams subjected to a drop weight from 3 m the results in Figure 10.40 clearly illustrates that the load capacity when debonding occur was the same as for an unstrengthened one. Considering that the absorbed energy, i.e. the area under the graph, is much larger for the FRP strengthened beams than the unstrengthened beam illustrated in red, black and blue, respectively. The results for ultimate load and deformation capacity together with initial plastic deformation from drop weight tests are presented in Table 10.50.

Table 10.50 Initial deformation together with test results from static loading for beams subjected to a drop weight from 3 m.

Test beam	Initial deformation [mm]	Ultimate load [kN]	Maximum deflection [mm]
07-IS-3m-0FRP	28	9.2	69
08-IS-3m-1FRP-S&P	5.4	19.5	89
10-IS-3m-1FRP-NM	6.2	18.5	90

Test results from static testing of beams subjected to a drop weight from 4 m are presented in Figure 10.41. The blue curve illustrates the test results from the unstrengthened beam and the rest the FRP strengthened beams. The plastic deformation from drop weight tests was very similar between the four FRP strengthened beams and the ultimate load also had small deviations except for number 16, the yellow curve.

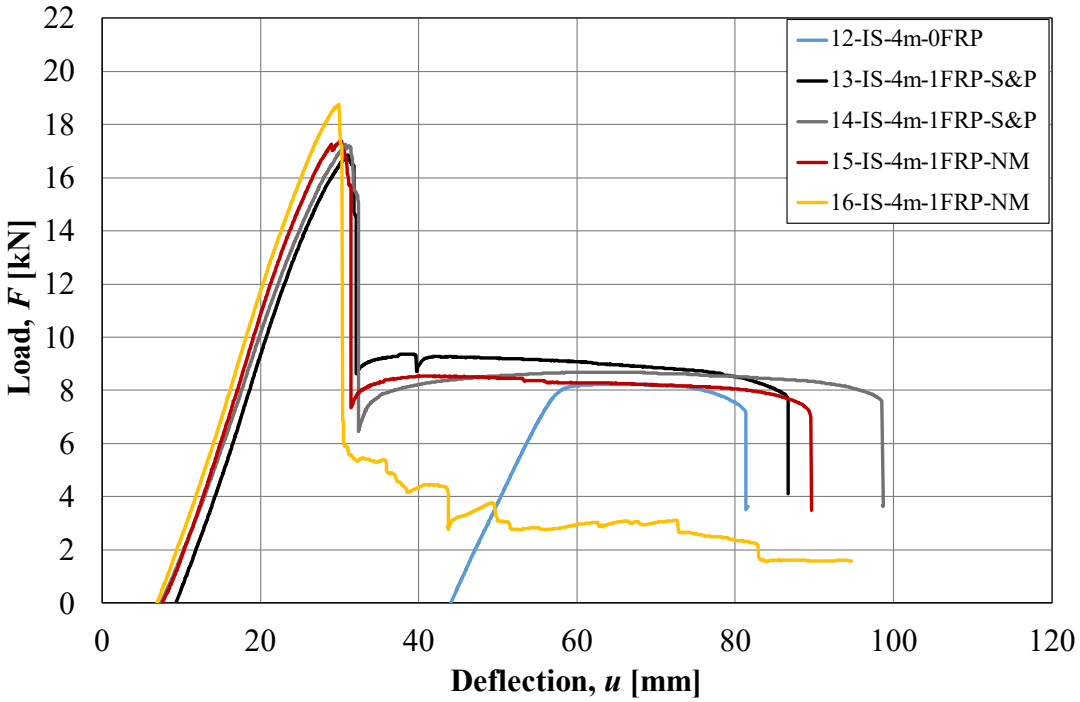

Figure 10.41 Load versus deflection curves for beams subjected to a drop weight from 4 m tested statically until failure.

The plastic deformation for the strengthened beams was around 10 mm, which is similar to the results for drop weight from 3 m presented in Figure 10.40, and the ultimate load was a bit lower, but in the same region when the two drop heights are compared. Similar to the tests from 3 m, the capacity when debonding of FRP occurred, was at the same level as for the unstrengthened beam and the ultimate deformation capacity was larger than for the unstrengthened beam, which clearly illustrates the advantage of the FRP. The ultimate load and deformation capacity are presented in Table 10.51.

Table 10.51 Initial deformation together with test results from static loading for beams subjected to a drop weight from 4 m.

Test beam	Initial deformation [mm]	Ultimate load [kN]	Maximum deflection [mm]
12-IS-4m-0FRP	44	8.2	82
13-IS-4m-1FRP-S&P	9.3	16.9	87
14-IS-4m-1FRP-S&P	7.4	17.2	99
15-IS-4m-1FRP-NM	7.6	17.4	90
16-IS-4m-1FRP-NM[5]	6.9	18.8	95

As can be seen in Figure 10.41, when maximum load capacity was reached for beam 16 followed by a large drop, presented with the yellow curve, it never reached the load capacity of an unstrengthened beam as the rest of the beams but successively decreased until test was ended at around 2 kN. This beam got a shear failure and the FRP debonding never occurred. The drop in load around 4 kN and deformation of 45 mm was achieved since the machine had settings to automatically stop when load went below 4 kN but this test was manually re-started again and continued until the load reached below 2 kN at which time it was finally stopped.

Results for statically tested beams subjected to a drop weight from 5 m presented a larger scatter compared to results from the lower drop heights. The grey curve in Figure 10.42 represents beam 20, which reached a similar ultimate load and deformation capacity as the FRP strengthened beams subjected to a drop weight from 4 m. Beam 20 and 22 shows a clear drop in load when debonding of FRP occurred whereas beam 19 and 21 experienced more severe damages from drop weight impact resulting in partial or total debonding of FRP already in the dynamic tests.

[5] This beam experienced shear failure. The test was ended manually when the load reached below 2 kN.

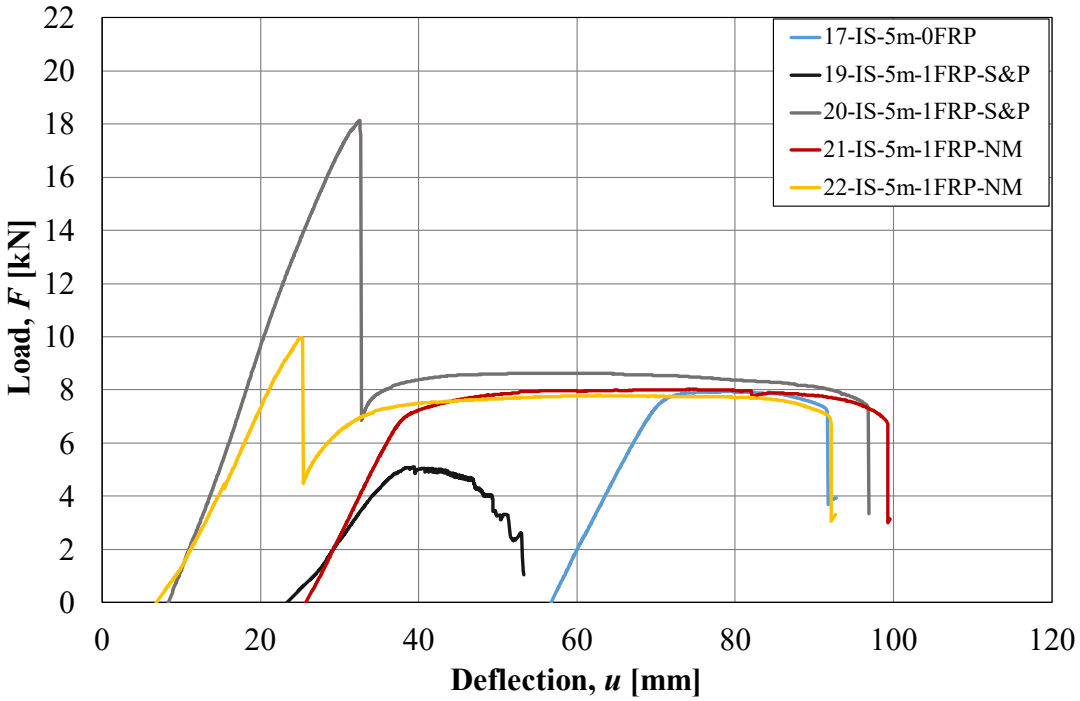

Figure 10.42 Load versus deflection curves for beams subjected to drop weight from 5 m tested statically until failure.

When unstrengthened and FRP strengthened beams are compared the results in Figure 10.42 presents a much larger deformation capacity for the strengthened ones compared to the unstrengthened beam, i.e., these beams absorbed much more energy than the unstrengthened one. The initial deformation together with the ultimate load and deformation capacity is presented in Table 10.52.

Table 10.52 Initial deformation together with test results from static loading for beams subjected to a drop weight from 5 m.

Test beam	Initial deformation [mm]	Ultimate load [kN]	Maximum deflection [mm]
17-IS-5m-0FRP	57	7.9	93
19-IS-5m-1FRP-S&P[6]	23	5.1	53
20-IS-5m-1FRP-S&P	8.3	18.1	97
21-IS-5m-1FRP-NM	26	8.0	100
22-IS-5m-1FRP-NM	6.8	10	95

The maximum height available in test laboratory was 5.7 m, which was used for drop weight tests on three beams before statically tests until final failure was reached. Load versus deflection curves for these three beams are presented in Figure 10.43. When 5.7 m was used as drop height the beams experienced very severe damages with plastic deformation of around 70 mm for the unstrengthened beam and 20-30 mm for the FRP

[6] The test for this beam was ended when the load reached below 2 kN.

strengthened beams. Beam number 9 had an ultimate load capacity at about 8 kN whereas the other two beams reached a load capacity of about 5 kN. During the dynamic tests, large parts of concrete were crushed by the drop weight impact, which resulted in some difficulties with the load application when the beams were later tested statically. Therefore, the load cell was placed either in the centre of the beam as usual or in the centre of the damaged zone when very large deformation already had taken place. The shift from the centre in longitudinal direction was at maximum 3 cm.

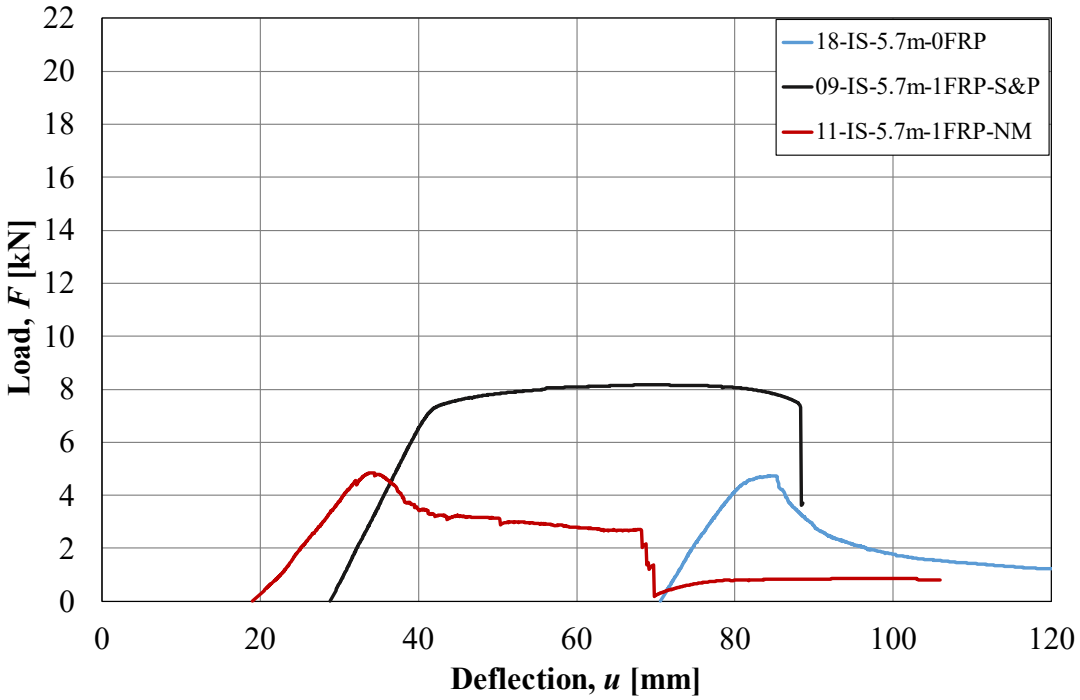

Figure 10.43 Load versus deflection curves for beams subjected to drop weight from 5.7 m tested statically until failure.

Also, in this case, the FRP strengthening showed advantages with larger or similar ultimate load capacity and larger deformation capacity than the unstrengthened beam. The initial deformation together with ultimate load and deformation capacity is presented in Table 10.53.

Table 10.53 Initial deformation together with test results from static loading for beams subjected to a drop weight from 5.7 m.

Test beam	Initial deformation [mm]	Ultimate load [kN]	Maximum deflection [mm]
18-IS-5.7m-0FRP[7]	71	4.7	120
09-IS-5.7m-1FRP-S&P	29	8.2	89
11-IS-5.7m-1FRP-S&P[8]	19	4.9	106

[7, 8] The test for this beam was ended when the load reached below 1 kN.

Load versus deflection curves for all of the FRP strengthened beams using S&P adhesive, tested either only statically or both statically and dynamically, are presented in Figure 10.44. The red curve, representing beam 19, is the only curve where debonding of FRP did not occur. For the green curve, representing beam 9, debonding of FRP occurred during the drop weight test and therefore no large peak value with following drop is illustrated for this beam. The rest of the beams experienced a similar behaviour to each other with only small deviations in ultimate load capacity and deformation capacity. What can be noted is that the capacity of the beams subjected to a drop weight impact from 3 m or 4 m were similar to that obtained in beams subjected to static loading only; the ultimate load capacity obtained, though, was somewhat lower.

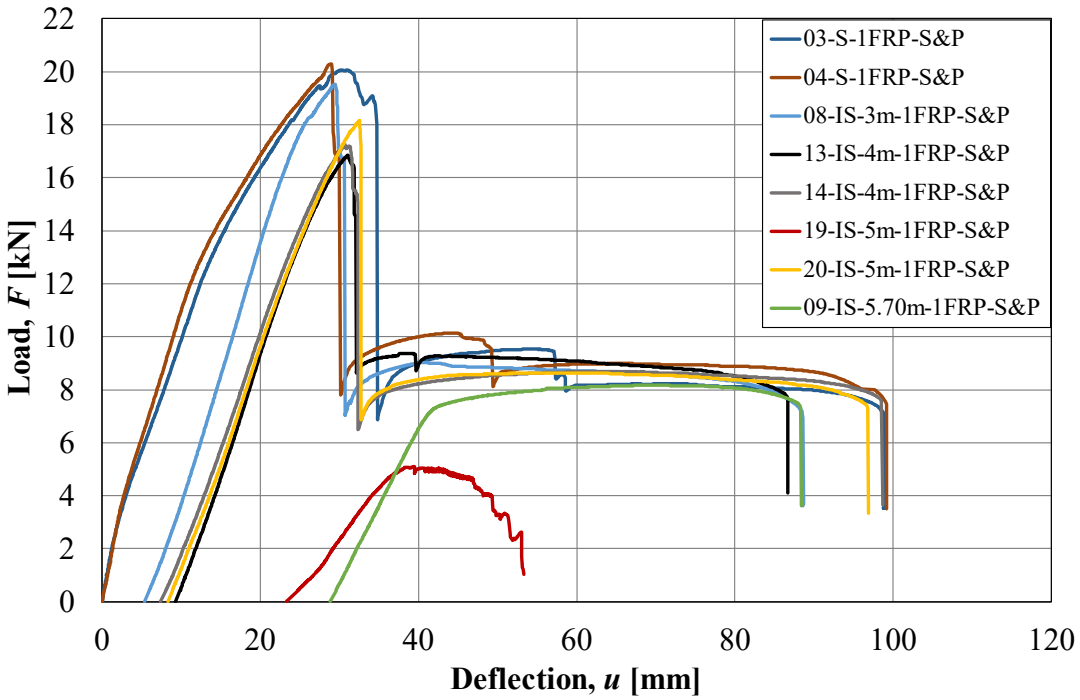

Figure 10.44 Load versus deflection curves for all FRP strengthened beams with S&P adhesive.

Test results for the FRP strengthened beams with NM adhesive showed a similar response as that obtained using S&P adhesive. Load deflection curves for all FRP strengthened beams with NM adhesive are presented in Figure 10.45. Results for beams subjected to a drop weight from 3 and 4 m were very similar to the results for the beams only statically loaded with almost the same ultimate load capacity with small deviations and a similar deformation capacity about 90-100 mm.

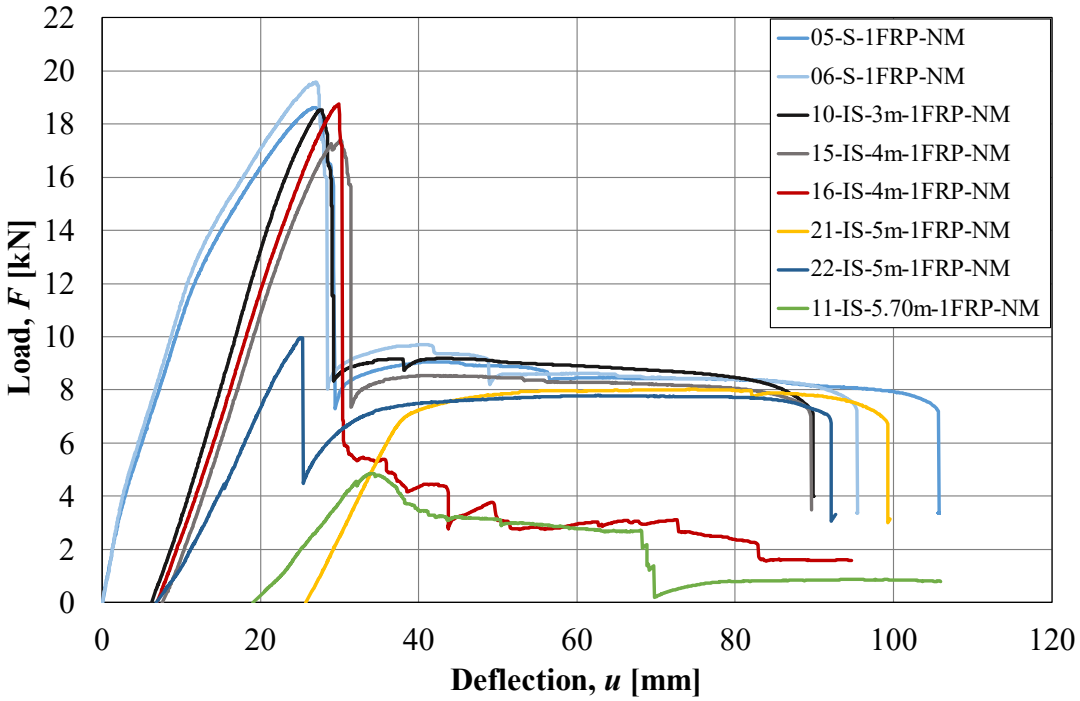

Figure 10.45 Load versus deflection curves for all FRP strengthened beams with NM adhesive.

A summary of all unstrengthened beams is presented in Figure 10.46. The results show that the ultimate load capacity decreases with impact loading and increasing height. What also can be seen, though, is that the deformation capacity increases with impact loading.

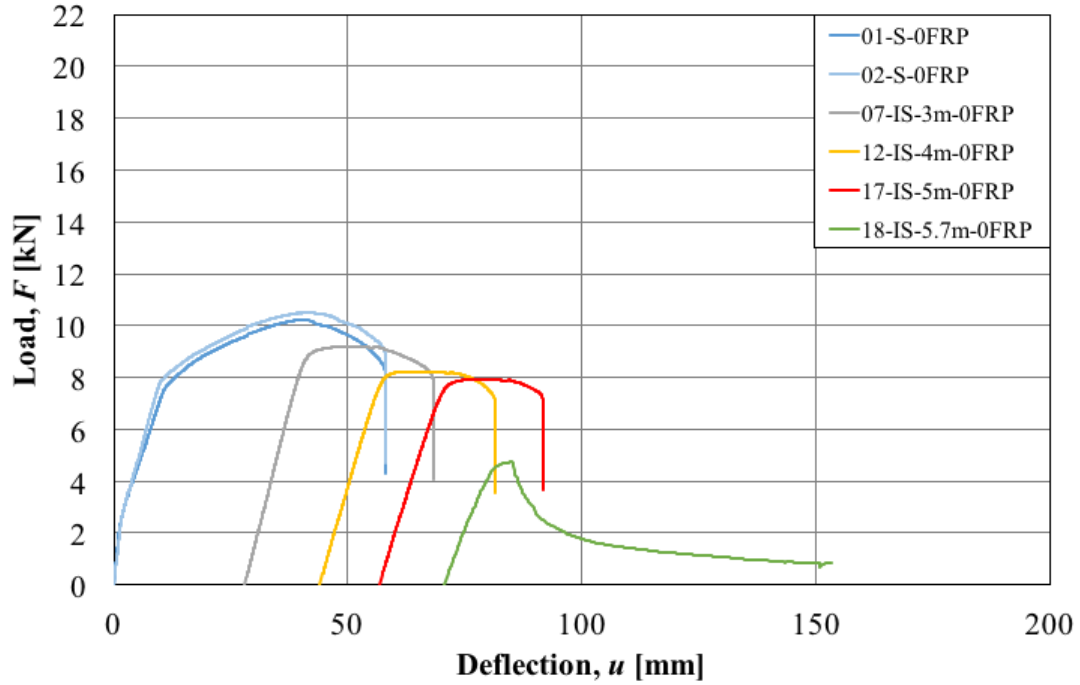

Figure 10.46 Load versus deflection curves for all unstrengthened beams.

10.3.2 Strain Fields

In this section, strain fields from the static tests are presented. In Table 10.54, the results for beams subjected to static loading only are presented together with the corresponding ultimate load and deflection. A general observation from the strain fields of the beams from the experiments was that the debonding of FRP started to propagate from the middle of the beam towards the end of the FRP sheet, both for the beams only loaded statically and the beams which first were subjected to a drop weight and later loaded statically.

Table 10.54 Strain fields at maximum force and deflection for only statically loaded beams.

0.2 % — 3.0 %	
01-S-0FRP F_{max}= 10.2 kN u_{max}= 58 mm	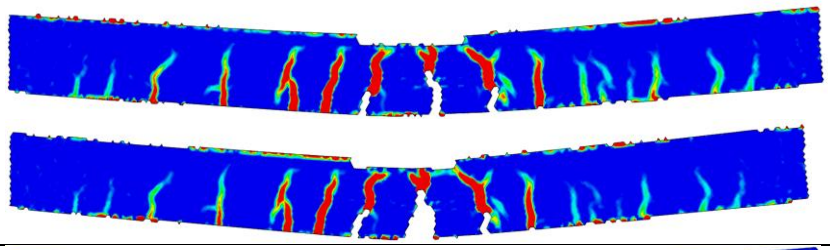
02-S-0FRP F_{max}= 10.5 kN u_{max}= 58 mm	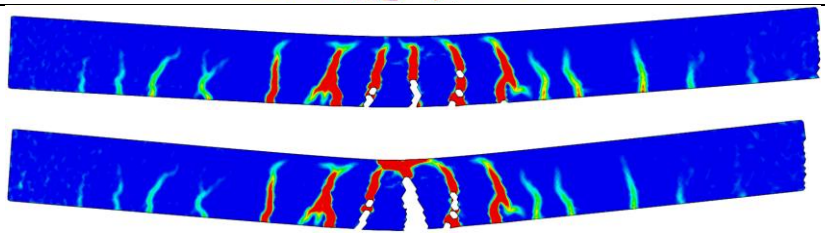
03-S-1FRP-S&P F_{max}= 20.1 kN u_{max}= 99 mm	This image, sought to illustrate the strain field at maximum force, was not able to be captured in GOM Correlate due to intense sunlight. 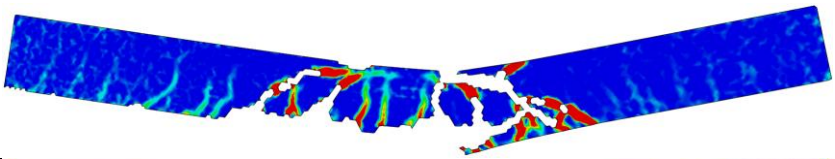
04-S-1FRP-S&P F_{max}= 20.3 kN u_{max}= 99 mm	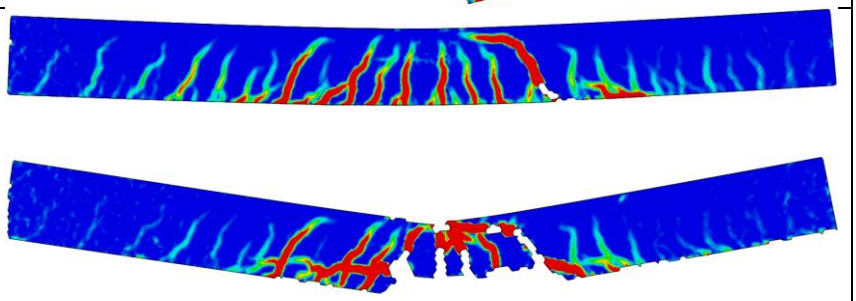
05-S-1FRP-NM F_{max}= 18.6 kN	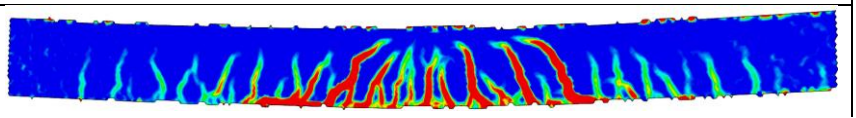

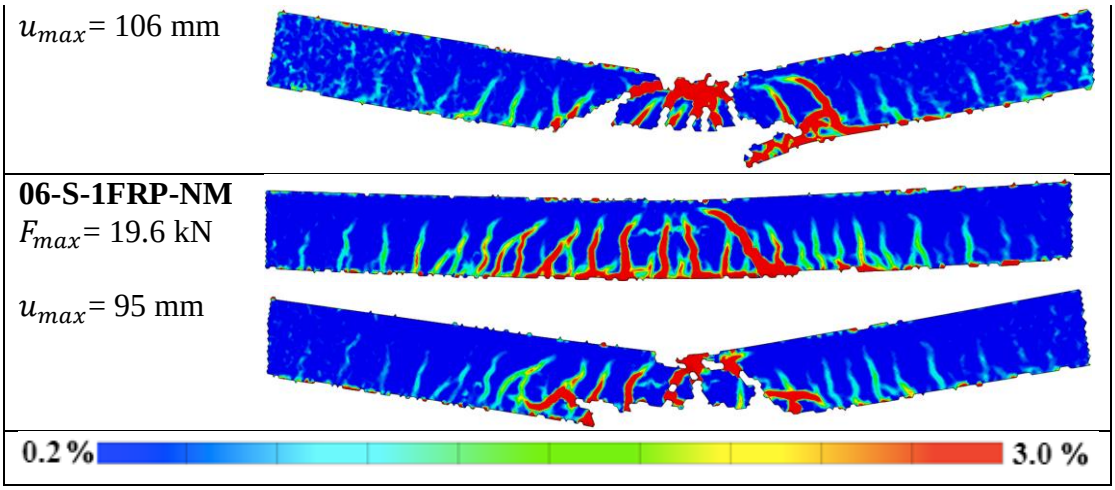

As can be seen in Table 10.54 the beams that were only statically loaded had different strain fields depending on if they were strengthened with FRP or not. It was a clear difference with much more cracks for beam 3-6, i.e. the FRP strengthened ones, compared to beam 1-2, which were unstrengthened; up to twice as many for the former cases. Another difference can be observed by studying the pictures for maximum deflection for each beam in Table 10.54, it was a significant difference in how much the reinforcement was exposed when unstrengthened and FRP strengthened beams are compared. When the FRP debonded, a large part of the concrete cover was also pulled off by the FRP, which created a large distance with exposed reinforcement. One consequence of this was that the reinforcement lost much or all of its bond with the concrete within this region, which hence meant that it here could utilize maximum plastic behaviour. The region where the reinforcement could yield without reduced or no influence of concrete was significant and increased when the FRP pulled of the concrete cover which was a great advantage. The corresponding strain fields for beams subjected to a drop weight from 4 m are presented in Table 10.55. Strain fields for the rest of the heights are presented in Appendix H .

Table 10.55 Strain fields at maximum force and deflection for beams subjected to a drop weight from 4 m before statically loading.

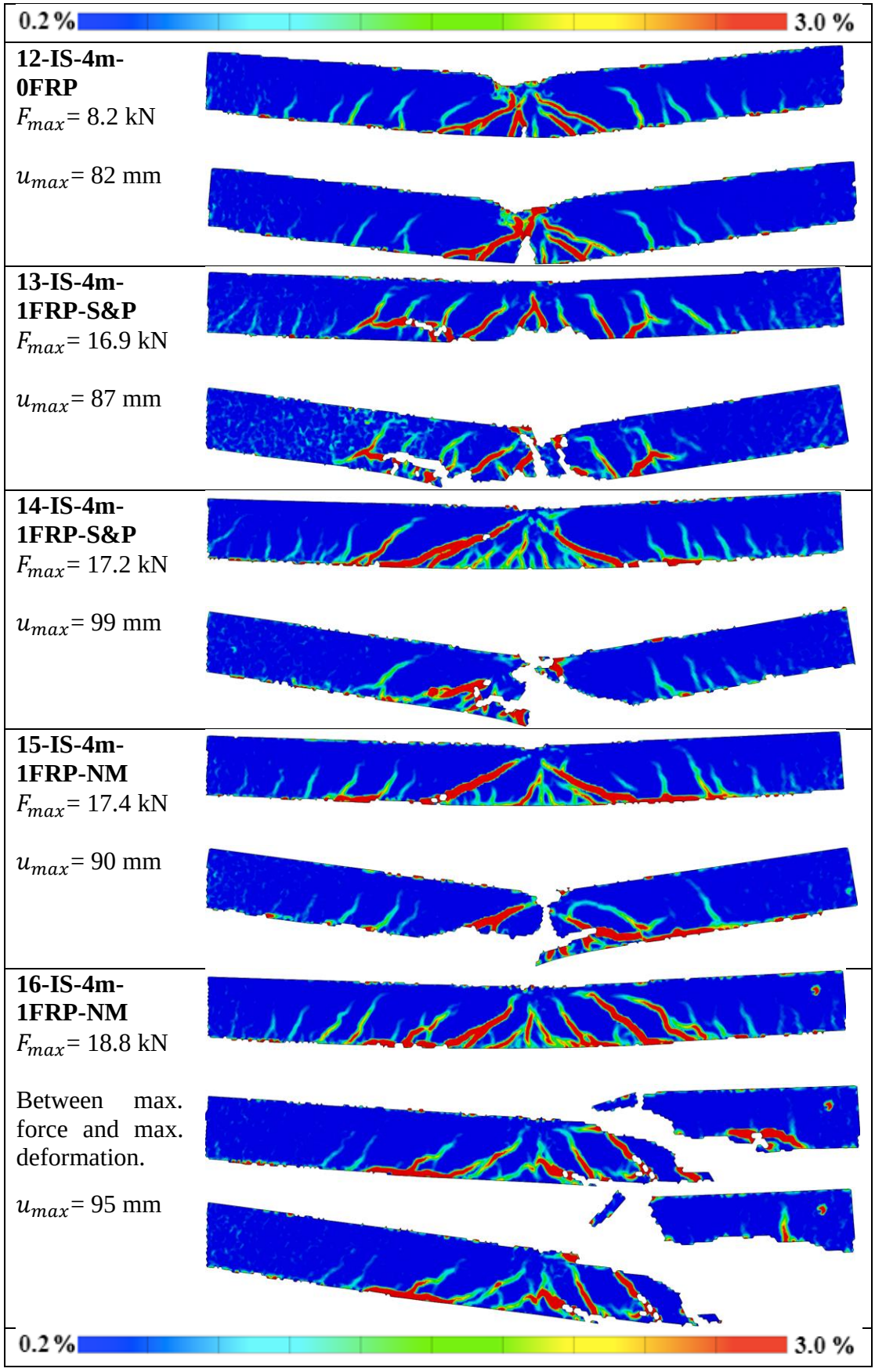

As can be seen in Table 10.55 the FRP strengthened beams obtained larger deformations than the unstrengthened beam prior to failure. The debonding of the FRP occurred during static testing, i.e. the FRP was still attached after the drop weight impact. For beams subjected to a drop weight, the increase in cracks for FRP strengthened beams compared to unstrengthened beams was not as significant as for the beams subjected to static loading only, but in all cases the number of cracks was equal or larger for the FRP strengthened ones. The observation with the FRP pulling of the concrete cover and creating a larger plastic region for the reinforcement was observed for all FRP strengthened beams except for beam 16, where debonding never occurred (shear failure). A conclusion could be made that beams with FRP strengthening subjected to a drop weight impact and then statically loaded develop equal amount or more cracks than the unstrengthened beams. Another conclusion that could be made is that the FRP pulled off the concrete cover and the possibility for a larger plastic region for the reinforcement was created in those cases.

For many of the beams with the FRP strengthening, entire debonding or rupture of FRP did not occur during the drop weight tests, in most of these cases the debonding instead occurred during the static testing except for in some exceptional cases such as for beam 16. The strain fields before and after debonding for beams subjected to a drop weight from 4 m is presented in Table 10.56. For some of the beams the debonding took place partially in several sequences and in such cases the different stages are presented. Strain fields before and after debonding for the rest of the beams is presented in Appendix H .

Table 10.56 Strain fields immediately before and after debonding of FRP for beams subjected to a drop weight from 4 m.

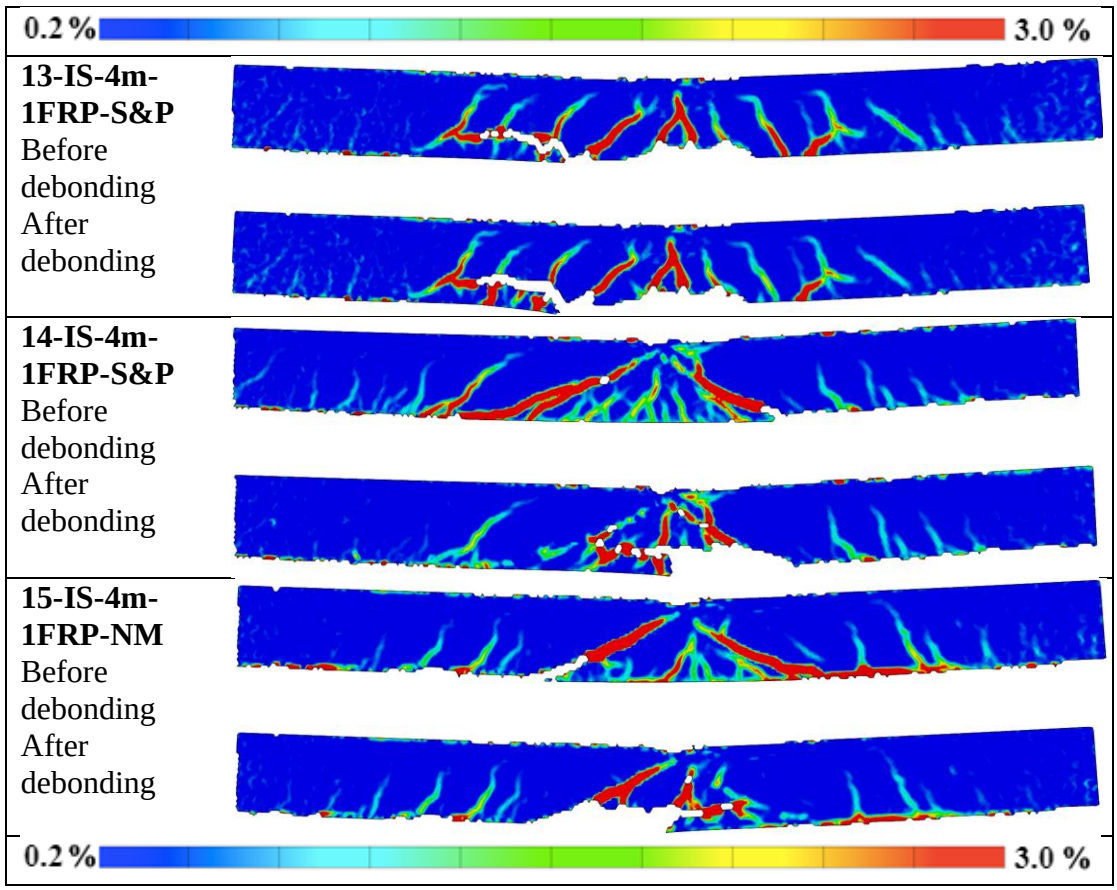

When the strain fields in Table 10.56 is studied the first observation is the already mentioned consequence regarding the FRP pulling of concrete. If beam 13 is studied, very small differences before and after debonding can be observed; this is due to the partial rupture of the FRP which occurred during the drop weight impact. If the number of cracks is studied, one can observe significantly more cracks for beam 14 before debonding compared to after debonding. However, for beam 13 and 15 this was not observed to the same extent.

To summarize, one conclusion that could be made, based on observations of the strain fields from the static testing, is that FRP strengthened beams develop equal amount or more cracks compared to the unstrengthened beams. For beams that were only statically loaded, significantly more cracks appeared when FRP strengthening was used. Further, for beams subjected to drop weight impact, the number of cracks was at least equal if not larger for the FRP strengthened beams compared to the unstrengthened ones. Another conclusion that could be made is that the FRP pulled off the concrete cover and the reinforcement experienced no bonding with the concrete over a large distance, which meant that the reinforcement could be utilized more effectively. As a result, this lead to a larger deformation capacity.

10.3.3 Internal Work

The internal work was calculated both for statically only loaded beams as well as for the dynamically and statically loaded beams. The method used for calculating the internal work is in correspondence with Section 5.4 as the area under the load-deflection relationship as presented throughout Section 10.3.1. For the statically only loaded beams, plastic internal work as well as the elastic internal work at different load levels are presented in this section together with the total internal energy. For the dynamically loaded beams the approximated internal work consumed in the impact is also presented together with the plastic internal work at different load levels.

The different load levels were 100 % to 75 % with 5 percent intervals and the area was taken in accordance with Figure 4.6 for the statically only loaded beams. Here, the first point was set at the corresponding load level in the ascending branch for state II stiffness and the second point at the descending branch. This procedure is presented in Appendix I . For the beams subjected to impact prior to being loaded statically the procedure was somewhat different. This was due to the fact that the internal work consumed at the impact needed to be taken into consideration. To understand the procedure for calculating the internal work from the impact the reader is directed to Appendix J and to see how the plastic internal work at different load levels were calculated for the residual internal energy see Appendix J .

The load level chosen as 100% is the load level of beam 02-S-0FRP, which is used as reference for the unstrengthened beams. As can be seen in Figure 10.39, the load-deflection relationship for the two unstrengthened beams were very similar and either one, or a mean value could have been chosen but the maximum load reached by beam 02-S-0FRP marks the 100 % level. As can be seen in e.g. Figure 10.39, the ascending branch after debonding for the FRP strengthened beams did not reach the recently stated load level 100% and sometimes not even a load value of 75 %. Consequently, if the descending branch for FRP strengthened beams after debonding did not reach a certain

load level interval, the corresponding place in the tables in this section is marked with "-". The internal work for the different beams is presented in Table 10.57 to Table 10.61.

For the beams subjected to static loading only in Table 10.57 it can be seen that the total internal work increased massively with FRP strengthening, generally, around a factor 2 compared to that of the unstrengthened beams. This large increase is partly due to the large internal energy gained before debonding of FRP and partly due to the increased ultimate deflection for FRP strengthened beams compared to the unstrengthened beams.

Table 10.57 Internal work at different load levels for beams subjected to static loading only.

Beam name	$W_{pl,95\%}$ $W_{el,95\%}$ **[J]**	$W_{pl,90\%}$ $W_{el,90\%}$ **[J]**	$W_{pl,85\%}$ $W_{el,85\%}$ **[J]**	$W_{pl,80\%}$ $W_{el,80\%}$ **[J]**	$W_{pl,75\%}$ $W_{el,75\%}$ **[J]**	W_{tot} **[J]**
01-S-0FRP	305	374	412	436	443	495
	73	67	62	58	52	
02-S-0FRP	393	441	465	471	481	524
	69	65	59	52	43	
03-S-1FRP-S&P	-	625	632	635	926	1016
	-	55	48	45	40	
04-S-1FRP-S&P	494	531	537	542	976	1017
	53	49	43	38	34	
05-S-1FRP-NM	-	-	473	566	939	1018
	-	-	45	41	38	
06-S-1FRP-NM	-	451	518	525	896	955
	-	49	47	41	36	

For the beams subjected to impact loading from a drop height of 3 m prior to static loading the internal work is presented in Table 10.58. There it can be seen that the internal work from the impact is similar but that the plastic residual internal work is higher than the unstrengthened beam with about a factor of 1.5. This total residual internal work, in the tables, donated $W_{pl.stat}$, is the residual internal work after the internal work consumed by the impact. This is illustrated and explained further in Appendix J .

Table 10.58 Internal work obtained due to drop weight impact and residual internal energy at different load levels. Beams subjected to drop weight from 3 m.

Beam name	W_{imp} **[J]**	$W_{pl,85\%}$ **[J]**	$W_{pl,80\%}$ **[J]**	$W_{pl,75\%}$ **[J]**	$W_{pl,stat}$ **[J]**
07-IS-3m-0FRP	369	156	212	232	378
08-IS-3m-1FRP-S&P	306	188	482	548	575
10-IS-3m-1FRP-NM	331	267	499	543	565

For the beams subjected to impact loading from a drop height of 4 m prior to static loading the internal work is presented in Table 10.59. There it can be seen that the internal work from the impact is higher for the unstrengthened beam. The plastic residual internal work is higher for the FRP strengthened beams with exception for beam 16. This beam had a dominant shear crack after the impact and during the static loading the beam experienced some type of shear failure and did not have the same type of protracted descending branch as the other FRP strengthened beams. This resulted in a considerable decrease of the internal work compared to the other FRP strengthened beams.

Table 10.59 Internal work obtained due to drop weight impact and residual internal energy at different load levels. Beams subjected to drop weight from 4 m.

Beam name	W_{imp} **[J]**	$W_{pl,85\%}$ **[J]**	$W_{pl,80\%}$ **[J]**	$W_{pl,75\%}$ **[J]**	$W_{pl,stat}$ **[J]**
12-IS-4m-0FRP	519	-	-	155	338
13-IS-4m-1FRP-S&P	379	342	493	530	538
14-IS-4m-1FRP-S&P	379	-	482	591	609
15-IS-4m-1FRP-NM	393	-	253	492	544
16-IS-4m-1FRP-NM	393	-	-	-	245

For the beams subjected to impact loading from a drop height of 5 m prior to static loading the internal work is presented in Table 10.60. For these beams there is a larger spread between the beams. This is mainly due to beam 19 and 20 performed poor and very well respectively. Beam 19 had practically no residual strength compared to the other beams since it experienced an additional impact when it hit the experimental equipment. Beam 20 had a large maximum load capacity, practically twice as large, compared to the other beams subjected to a drop weight from 5 m.

Table 10.60 Internal work obtained due to drop weight impact and residual internal energy at different load levels. Beams subjected to drop weight from 5 m.

Beam name	W_{imp} **[J]**	$W_{pl,85\%}$ **[J]**	$W_{pl,80\%}$ **[J]**	$W_{pl,75\%}$ **[J]**	$W_{pl,stat}$ **[J]**
17-IS-5m-0FRP	647	-	-	106	353
19-IS-5m-1FRP-S&P	572	-	-	-	43
20-IS-5m-1FRP-S&P	379	-	437	572	600
21-IS-5m-1FRP-NM	498	-	-	318	450
22-IS-5m-1FRP-NM	373	-	-	-	484

For the beams subjected to impact loading from a drop height of 5.7 m prior to static loading the internal work is presented in Table 10.61. The internal work from the impact was larger for the unstrengthened beam compared to the FRP strengthened beams. For the residual internal work, the results are scattered and vary depending on the residual strength, which were higher for beam 9 while the two other beams subjected to a drop weight from 5.7 m had very low residual strength. What can be seen in Table 10.61 is that the internal work consumed in the impact is very high and the residual internal work is very low for the unstrengthened beam, beam 18. The damages of beam 18 were severe and the residual stiffness was low, which resulted in a large amount of estimated internal energy consumed in the impact. The internal work for beam 18 is likely overestimated which should be kept in mind when evaluating the results. How the internal work was estimated is presented in Appendix J .

Table 10.61 Internal work obtained due to drop weight impact and residual internal energy at different load levels. Beams subjected to drop weight from 5.7 m.

Beam name	W_{imp} **[J]**	$W_{pl,85\%}$ **[J]**	$W_{pl,80\%}$ **[J]**	$W_{pl,75\%}$ **[J]**	$W_{pl,stat}$ **[J]**
18-IS-5.7m-0FRP	813	-	-		81
09-IS-5.7m-1FRP-S&P	548	-	-	303	341
11-IS-5.7m-1FRP-NM	524	-	-	-	100

In Table 10.62 to Table 10.64 a comparison between beams of the same type is presented. Here, the internal work from impact and residual internal work are compared with the internal work from the beams subjected to static loading only.

Table 10.62 Internal work comparison for unstrengthened beams.

Beam name	W_{imp} **[J]**	$W_{pl,stat}$ **[J]**	$W_{imp+pl,stat}$ **[J]**	W_{stat} **[J]**
01-S-0FRP	-	-	-	495
02-S-0FRP	-	-	-	524
07-IS-3m-0FRP	369	378	747	-
12-IS-4m-0FRP	519	338	857	-
17-IS-5m-0FRP	647	353	1000	-
18-IS-5.7m-0FRP	813	81	894	-

Table 10.63 Internal work comparison for FRP strengthened beams with S&P adhesive.

Beam name	W_{imp} **[J]**	$W_{pl,stat}$ **[J]**	$W_{imp+pl,stat}$ **[J]**	W_{stat} **[J]**
03-S-1FRP-S&P	-	-	-	1016
04-S-1FRP-S&P	-	-	-	1017
08-IS-3m-1FRP-S&P	306	575	881	-
13-IS-4m-1FRP-S&P	379	538	917	-
14-IS-4m-1FRP-S&P	379	609	988	-
19-IS-5m-1FRP-S&P	572	43	615	-
20-IS-5m-1FRP-S&P	379	600	979	-
09-IS-5.7m-1FRP-S&P	548	341	889	-

Table 10.64 Internal work comparison for FRP strengthened beams with NM adhesive.

Beam name	W_{imp} [J]	$W_{pl,stat}$ [J]	$W_{imp+pl,stat}$ [J]	W_{stat} [J]
05-S-1FRP-NM	-	-	-	1018
06-S-1FRP-NM	-	-	-	955
10-IS-3m-1FRP-NM	331	565	896	-
15-IS-4m-1FRP-NM	393	544	937	-
16-IS-4m-1FRP-NM	393	245	638	-
21-IS-5m-1FRP-NM	498	450	948	-
22-IS-5m-1FRP-NM	373	484	857	-
11-IS-5.7m-1FRP-NM	524	100	524	-

The internal energy that was approximately consumed in the impact was compared to the energy in a plastic impact according to Section 5.5.2. The theoretical energy from the impact theory is calculated with Equation (5.21). In this equation, the mass of body two, i.e. the beam, was determined according to Appendix F where the weights of the beams were noted before and after each test. The weights differ slightly but the difference is minor and therefore the theoretical energy is presented as the mean value for each drop height and not for every single beam. The masses in Equation (5.21) are multiplied with the corresponding transformations factor, κ_m.The theoretical energies from the impact as well as the kinetic energy from the drop weight, denoted E_{k0} in Section 5.5, are presented in Table 10.65

Table 10.65 Theoretical energy from plastic impact drop for different drop heights.

	Drop height 3 m	Drop height 4 m	Drop height 5 m	Drop height 5.7 m
Theoretical energy from plastic impact, $E_{k,pl,12}$ [J]	375	500	624	711
Kinetic energy from the drop weight, E_{k0} [J]	589	785	981	1118

What can be seen when comparing the theoretical energy from a plastic impact to the energy that was estimated from the impact is that the energies corresponded well for the unstrengthened beams. If instead the FRP strengthened beams are analysed, it can be seen that the estimated energy from the drop weight impact was smaller than the theoretical. This difference could partly be due to the underestimation of the internal resistance during dynamic loading, e.g. neglecting some strain rate effects. Another reason to the difference could be that all dynamic loading cannot be treated as a

characteristic impulse, it is only the initial peak which could be said to be a characteristic impulse.

10.3.4 Plastic Rotation Capacity

In this section, the plastic rotation capacity obtained for all test beams is presented, both the beams only loaded statically, and the beams subjected to a drop weight and later loaded statically until failure. The deformation at different load levels on the descending branch was obtained from the load versus deflection data presented in Section 10.3.1 and from the stadium II stiffness curve's intersection point with the load level. The difference between those two values were divided by half the beam length to calculate the plastic rotation. All the beams subjected to a drop weight was related to a reference beam which was only statically loaded to be able to calculate the two values of deformation needed. For further explanation of how the plastic rotation was calculated, see Appendix K .

The plastic rotation was calculated for different load levels, the same load levels as stated in Section 10.3.3. In cases where the beam did not reach the corresponding reference beam's load levels, "-" is used to mark this in the following tables. Plastic rotation for the six beams loaded statically are presented in Table 10.66.

Table 10.66 Plastic rotation for the six reference beams only loaded statically.

Test beam	$\boldsymbol{\theta_{pl,100\%}}$ **[mrad]**	$\boldsymbol{\theta_{pl,95\%}}$ **[mrad]**	$\boldsymbol{\theta_{pl,90\%}}$ **[mrad]**	$\boldsymbol{\theta_{pl,85\%}}$ **[mrad]**	$\boldsymbol{\theta_{pl,80\%}}$ **[mrad]**	$\boldsymbol{\theta_{pl,75\%}}$ **[mrad]**
01-S-0FRP	-	24.5	30.0	33.3	35.4	36.2
02-S-0FRP	22.1	29.8	33.8	35.9	36.5	37.4
03-S-1FRP-S&P	-	-	36.5	37.1	37.2	64.8
04-S-1FRP-S&P	-	28.2	31.1	31.5	32.0	70.0
05-S-1FRP-NM	-	-	-	29.1	37.2	71.7
06-S-1FP-NM	-	-	25.6	31.2	31.7	65.4
Mean no FRP	**22.1**	**27.1**	**31.9**	**34.6**	**35.9**	**36.8**
Mean FRP	**-**	**28.2**	**31.1**	**32.2**	**34.5**	**68.0**
Mean	**22.1**	**27.5**	**31.4**	**33.0**	**35.0**	**57.6**

When comparing the rotation capacity for the unstrengthened beams with the FRP strengthened beams one can observe that the values were very similar down to a load level of 80 %; after that, though, they differed a lot. At a load level of 75 %, the mean for unstrengthened beams was 36.8 mrad and for the FRP strengthened beams the mean

value was 68.0 mrad. Plastic rotation results for beams subjected to a drop weight from 3 m are presented in Table 10.67. For beams subjected to a drop weight from 3 m the results were similar at a load level of 85 % but increasing difference between unstrengthened and FRP strengthened beams with decreasing load level as presented in Table 10.67.

Table 10.67 Plastic rotation at different load levels for beams subjected to a drop weight from 3 m.

Test beam	$\boldsymbol{\theta_{pl,100\%}}$ **[mrad]**	$\boldsymbol{\theta_{pl,95\%}}$ **[mrad]**	$\boldsymbol{\theta_{pl,90\%}}$ **[mrad]**	$\boldsymbol{\theta_{pl,85\%}}$ **[mrad]**	$\boldsymbol{\theta_{pl,80\%}}$ **[mrad]**	$\boldsymbol{\theta_{pl,75\%}}$ **[mrad]**
07-IS-3m-0FRP	-	-	-	37.1	42.6	45.4
08-IS-3m-1FRP-S&P	-	-	-	26.9	53.3	59.8
10-IS-3m-1FRP-NM	-	-	-	35.8	56.8	61.2
Mean no FRP	**-**	**-**	**-**	**37.1**	**42.6**	**45.4**
Mean FRP	**-**	**-**	**-**	**31.4**	**55.1**	**60.5**
Mean	**-**	**-**	**-**	**33.3**	**50.9**	**55.5**

Plastic rotation results for beams subjected to a drop weight from 4 m are presented in Table 10.68. For beams subjected to a drop weight from 4 m, several of the beams did not reach up to a load level higher than 80 %, and only beam 13 reached 85 %. The results for 80 % varied a bit where beam 15 was much lower than the two beams with S&P adhesive. For 75 % the FRP strengthened had a significantly larger rotation than the unstrengthened one.

Table 10.68 Plastic rotation at different load levels for beams subjected to a drop weight from 4 m.

Test beam	$\boldsymbol{\theta_{pl,100\%}}$ **[mrad]**	$\boldsymbol{\theta_{pl,95\%}}$ **[mrad]**	$\boldsymbol{\theta_{pl,90\%}}$ **[mrad]**	$\boldsymbol{\theta_{pl,85\%}}$ **[mrad]**	$\boldsymbol{\theta_{pl,80\%}}$ **[mrad]**	$\boldsymbol{\theta_{pl,75\%}}$ **[mrad]**
12-IS-4m-0FRP	-	-	-	-	-	51.9
13-IS-4m-1FRP-S&P	-	-	-	42.8	56.5	60.3
14-IS-4m-1FRP-S&P	-	-	-	-	58.0	68.5
15-IS-4m-1FRP-NM	-	-	-	-	34.6	58.2
16-IS-4m-1FRP-NM	-	-	-	-	-	-
Mean no FRP	**-**	**-**	**-**	**-**	**-**	**51.9**
Mean FRP	**-**	**-**	**-**	**42.8**	**49.7**	**62.3**
Mean	**-**	**-**	**-**	**42.8**	**49.7**	**59.7**

Plastic rotation results for beams subjected to a drop weight from 5 m are presented in Table 10.69. For beams subjected to a drop weight from 5 m two of the beams did not even reach 75 % and only one reached 80 % so there were only a few results to present. The results varied and no significant difference between unstrengthened and FRP strengthened beams was observed.

Table 10.69 Plastic rotation at different load levels for beams subjected to a drop weight from 5 m.

Test beam	$\theta_{pl,100\%}$ [mrad]	$\theta_{pl,95\%}$ [mrad]	$\theta_{pl,90\%}$ [mrad]	$\theta_{pl,85\%}$ [mrad]	$\theta_{pl,80\%}$ [mrad]	$\theta_{pl,75\%}$ [mrad]
17-IS-5m-0FRP	-	-	-	-	-	57.2
19-IS-5m-1FRP-S&P	-	-	-	-	-	-
20-IS-5m-1FRP-S&P	-	-	-	-	53.1	66.2
21-IS-5m-1FRP-NM	-	-	-	-	-	57.5
22-IS-5m-1FRP-NM	-	-	-	-	-	-
Mean no FRP	**-**	**-**	**-**	**-**	**-**	**57.2**
Mean FRP	**-**	**-**	**-**	**-**	**53.1**	**61.9**
Mean	**-**	**-**	**-**	**-**	**53.1**	**60.3**

Plastic rotation results for beams subjected to a drop weight from 5.7 m are presented in Table 10.70. Only one of the beams subjected to a drop weight from 5.7 m reached a level of 75 % which was number 9 strengthened with FRP but not one of the other beams reached a load level of 75 %.

Table 10.70 Plastic rotation at different load levels for beams subjected to a drop weight from 5.7 m.

Test beam	$\theta_{pl,100\%}$ [mrad]	$\theta_{pl,95\%}$ [mrad]	$\theta_{pl,90\%}$ [mrad]	$\theta_{pl,85\%}$ [mrad]	$\theta_{pl,80\%}$ [mrad]	$\theta_{pl,75\%}$ [mrad]
18-IS-5.7m-0FRP	-	-	-	-	-	-
09-IS-5.7m-1FRP-S&P	-	-	-	-	-	58.7
11-IS-5.7m-1FRP-NM	-	-	-	-	-	-
Mean no FRP	**-**	**-**	**-**	**-**	**-**	**-**
Mean FRP	**-**	**-**	**-**	**-**	**-**	**58.7**
Mean	**-**	**-**	**-**	**-**	**-**	**58.7**

11 Comparison of Experimental Results with Predictions and Results from other Studies

Predictions were done to complement the experimental testing and when the experimental results were evaluated the theoretical predictions could be validated if they give the same results. Both static and dynamic predictions were done in Chapter 9 and are compared with the experimental results and presented in Section 11.1 and 11.2. A comparison of the results from this project with the thesis made by Nigani & Nordström (2020) was also done and is presented in Section 11.3.

11.1 Static Response

The predicted response regarding load versus deflection curves, ultimate moment and load capacity and plastic rotation are compared with the results from the experiments. Some of the predicted results took the FRP strengthening into consideration, and some neglected it to get the capacity of an unstrengthened reference beam. It would have been preferred, though in some cases to be able to take the properties of the FRP and the adhesive into consideration in a more accurate way.

11.1.1 Load versus Deflection and Ultimate Load

When comparing the actual load versus deflection curves from experimental results for unstrengthened beams one can observe that the actual ultimate load was larger than the predicted capacity. The blue curves in Figure 11.1 representing the experimental test results show a stiffness in between the predicted stiffness for stadium I and stadium II as described in Section 9.1.3.

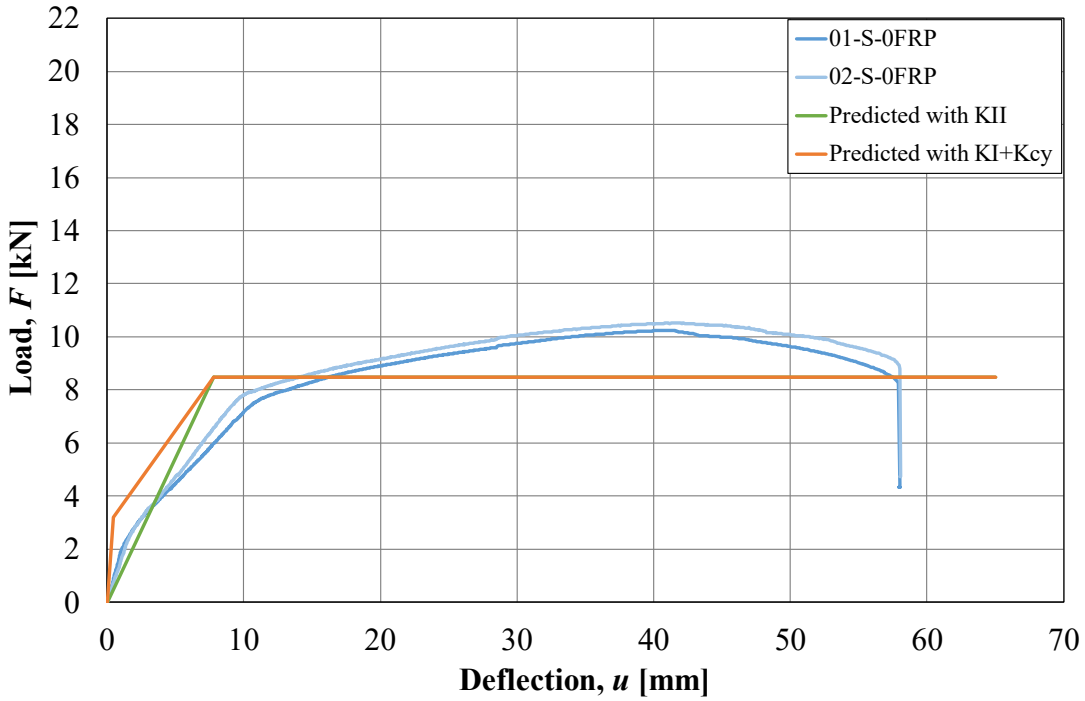

Figure 11.1 Predicted load versus deflection curve and experimental results for unstrengthened beams.

The ultimate load capacity from experimental testing is presented together with the predicted ultimate load capacity in Table 11.1. A comparison of the experimental results with the theoretical predicted capacity calculated in Appendix M is also presented.

Table 11.1 Comparison of ultimate load capacity for experimental results and theoretical predictions for unstrengthened beams.

	$F_{u,exp}$ [kN]	$F_{u,theory}$ [kN]	$\frac{F_{u,exp}}{F_{u,theory}}$
01-S-0FRP	10.2	8.5	1.20
02-S-0FRP	10.5	8.5	1.24

Predicted response for load versus deflection for FRP strengthened adhesive together with experimental results for FRP strengthened beams with S&P adhesive is presented in Figure 11.2. The predicted response is based on Eurocode 2 method, see Section 9.1.1, calculated in Appendix M .

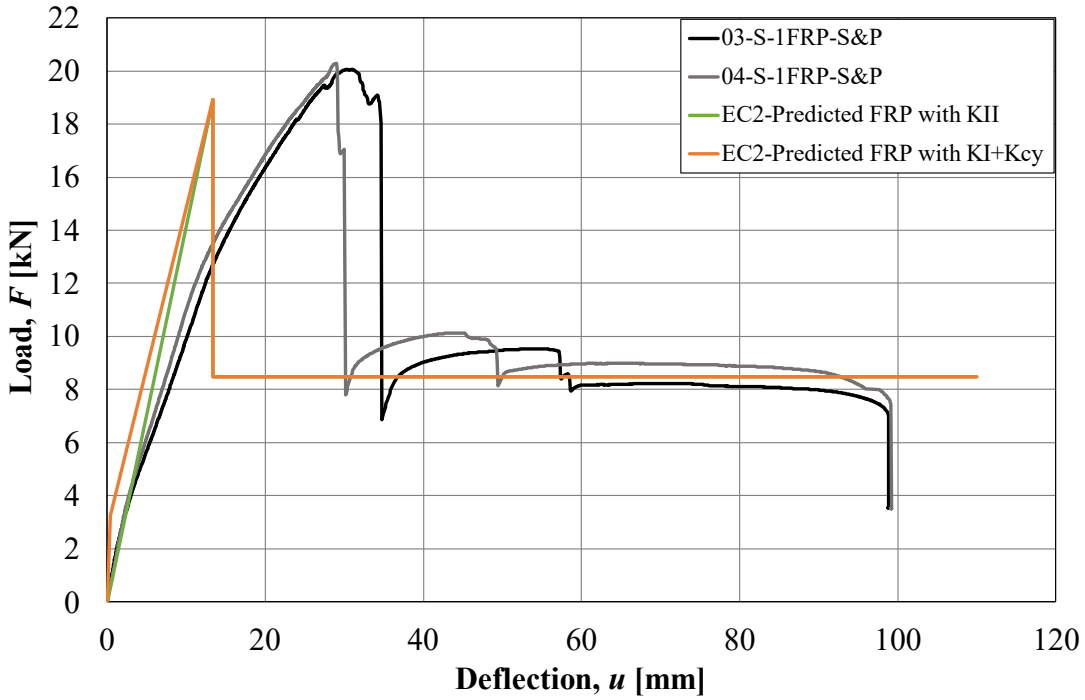

Figure 11.2 Predicted load versus deflection curve using EC2 and experimental results for FRP strengthened beams with S&P adhesive.

Again, one can observe that the predicted ultimate load was smaller than the predicted capacity. The stiffness in the predicted response is generally larger than the actual response from the testing beams. However, the predicted load capacity after debonding was similar to the actual capacity which can be seen in Figure 11.2 where the orange curve representing the predicted capacity is between the grey and black curve. The theoretical predictions are presented for three different methods in Table 11.2. Ultimate load from experimental testing and theoretical predictions for FRP strengthened beams with S&P adhesive are presented in Table 11.3.

Table 11.2 Theoretical predicted capacities of ultimate load capacity for three methods.

Method	$F_{u,theory}$ **[kN]**
EC2	18.9
Kompositförstärkning betong	21.5
FIB	17.5

Table 11.3 Comparison of ultimate load capacity for experimental results and theoretical predictions for FRP strengthened beams with adhesive S&P.

	$F_{u,exp.}$ **[kN]**	$\frac{F_{u,exp}}{F_{u,theory.EC2}}$	$\frac{F_{u,exp}}{F_{u,theory.Komp.}}$	$\frac{F_{u,exp}}{F_{u,theory.FIB}}$
03-S-1FRP-S&P	20.1	1.06	0.93	1.15
04-S-1FRP-S&P	20.3	1.07	0.94	1.16

Results in Table 11.3 show that Eurocode 2 and FIB underestimate the ultimate load capacity whereas Kompositförstärkning overestimates it. Figure 11.3 is similar to Figure 11.2 but the experimental results come from the beams strengthened with FRP and the adhesive NM. For this case the prediction with Eurocode 2 was closer to the actual ultimate load capacity.

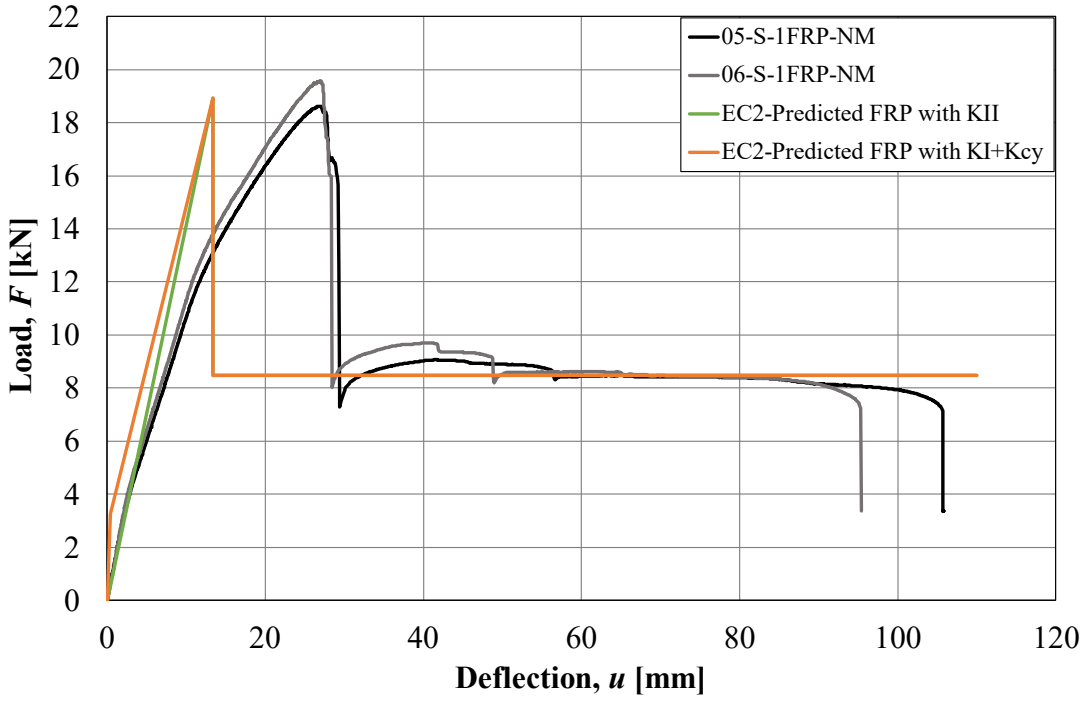

Figure 11.3 Predicted load versus deflection curve and experimental results for FRP strengthened beams with NM adhesive.

The load capacity after debonding of FRP for the experimental results was close to the predicted capacity at a level of slightly above 8 kN. In Table 11.4 is the ultimate load capacity and the theoretical predicted capacity for Eurocode 2, Kompositförstärkning

and FIB presented. EC2 and FIB underestimated the ultimate load capacity and Kompositförstärkning overestimated it. When comparing the theoretical predictions one can observe that EC2 was closest to the actual response.

Table 11.4 Comparison of ultimate load capacity for experimental results and theoretical predictions for FRP strengthened beams with adhesive NM.

	$F_{u,exp.}$ [kN]	$\frac{F_{u,exp}}{F_{u,theo.EC2}}$	$\frac{F_{u,exp}}{F_{u,theo.Komp.}}$	$\frac{F_{u,exp}}{F_{u,theo.FIB}}$
05-S-1FRP-NM	18.6	0.98	0.87	1.06
06-S-1FRP-NM	19.6	1.04	0.91	1.12

11.1.2 Plastic Rotation Capacity

Plastic rotation capacity was predicted with three different methods and the comparison of those predictions with experimental results for the beams only loaded statically for different load levels are presented in Figure 11.4. For the calculated predicted responses with the three methods used, the FRP was not taken into consideration. Presented values in Figure 11.4 are mean values from the two corresponding beams to each category. If one of the two beams beam did not reach up to the studied load level, then the presented value was taken from the one which reached the actual load level.

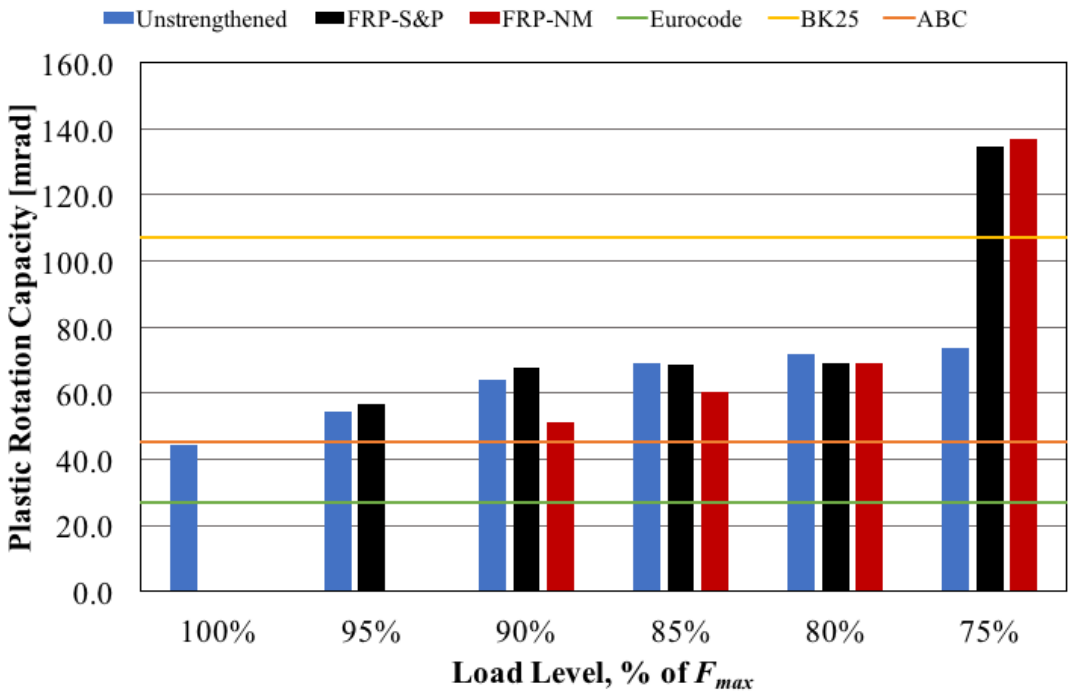

Figure 11.4 Predicted rotation capacity and rotation capacity at different load levels from experimental results for only statically loaded beams.

As can be seen in Figure 11.4 the predicted response for BK25-method was much larger than the experimental results for all load levels but 75%. Predicted rotation capacity calculated with BK25-method was around 107 mrad. ABC-method predicted a rotation capacity of around 45 which is slightly larger than the capacity of the unstrengthened

beam for load level of 100% but an underestimation for the rest of the cases. For the FRP strengthened beams was the predicted capacity with BK25 larger than the actual capacity in all load levels above 75 % but at 75 % the actual capacity of the test beams was around 135-140 mrad. None of the methods is clearly close to the plastic rotation from the test results, ABC-method was closest but underestimated the capacity in all cases but one.

11.2 Dynamic Response

In this section the dynamic behaviour is compared to the theoretically predicted dynamic behaviour. This was of interest because it showed how well the theoretical models used in this project comply with the results gained from the dynamic tests. Here the dynamic results for midpoint deflection over time and the drop weight velocity for the four different drop heights are compared.

11.2.1 Comparisons Made

It was found during the static test that the resistance of the statically loaded unstrengthened beams exceeded the theoretically predicted static resistance, see Section 11.1.1. The predicted static strength resulted in deflections larger than the measured ones due to underestimation of the resistance of the beam and therefore another type of comparison was also made. This second type of comparison was made using an increased resistance of the beam. In this comparison, a resistance R_2 was chosen in the 2DOF model so that the maximum deflection obtained in the calculations was the same as that observed in the dynamic tests. Figure 11.5 illustrates the resistances and their bi-linear responses used for the 2DOF prediction and comparison using the 2DOF model together with the static response for the unstrengthened beams from the statically only loaded beams. For the comparison using the 2DOF model the maximum deflection corresponds with the maximum deflections stated in Section 10.2.1.

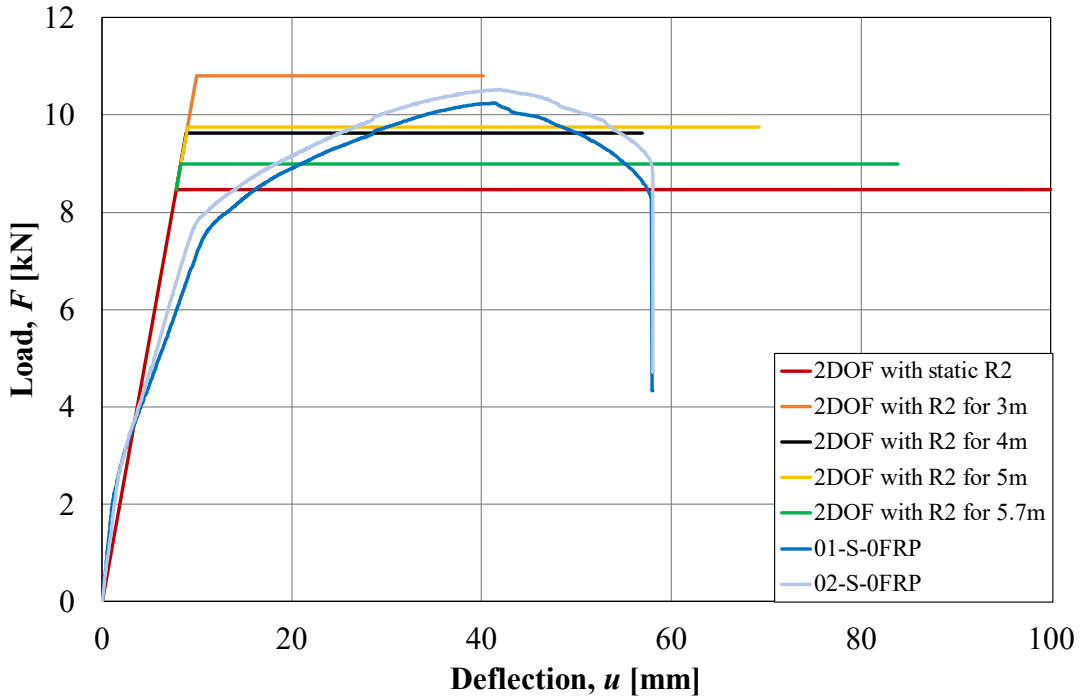

Figure 11.5 Bi-linear responses for the two types of predictions together with the actual responses for the two beams loaded statically only.

For the second type of prediction, using backwards calculations to comply with the measured dynamic behaviour, the beam had different resistance naturally but also the actual measured velocities from the experiments were used. The stiffness used for the bi-linear response was the same in both predictions according to Section 6.4.2 but for the second prediction the resistance of body 2, i.e the beam, was higher.

11.2.2 Midpoint Deflection Over Time

In this section the midpoint deflection over time is compared with the results from the dynamic tests. The results are presented and compared for the unstrengthened beam together with the two predicted results presented in Section 9.2 for each drop height. The comparisons for the different drop heights are presented in Figure 11.6 to Figure 11.9.

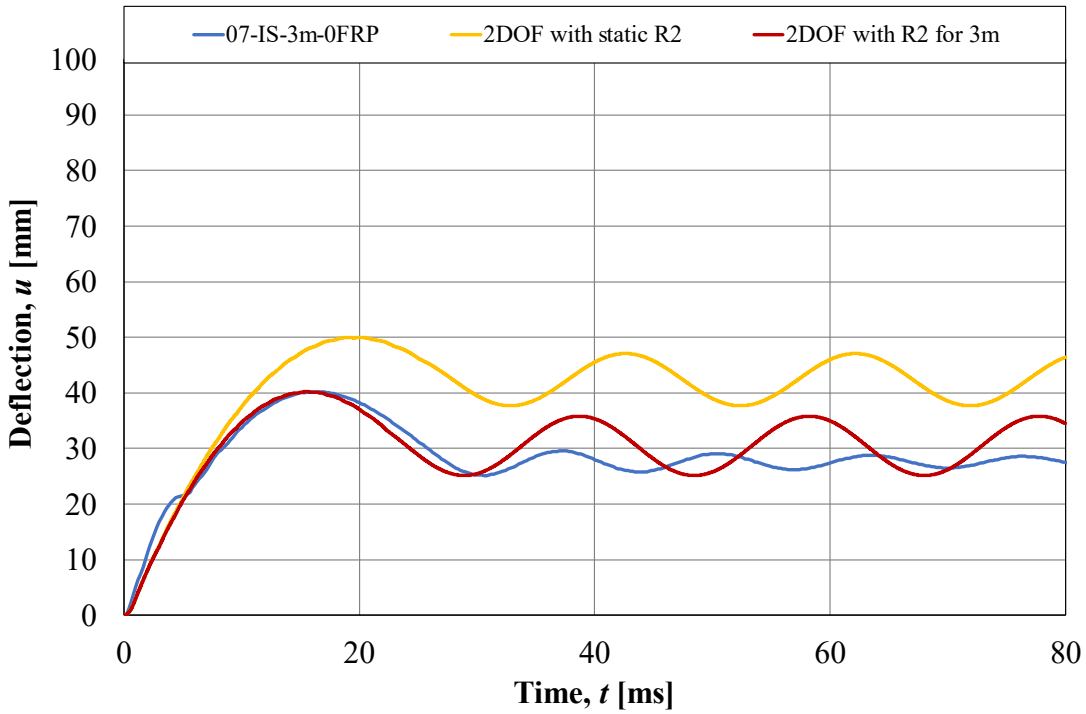

Figure 11.6 Comparison of predicted midpoint deflection versus time and actual results from experimental testing for beams subjected to a drop weight from 3 m.

Figure 11.6 shows the results of the drop height 3 m where it can be seen that, as expected, the predicted static resistance of the beam leads to too high deflections, both maximum and plastic. The static resistance was clearly an underestimation which was expected since the maximum capacity was known and larger for the unstrengthened beams under static loading compared to the theoretically predicted. When a beam resistance was used to match the maximum deflection instead the behaviour up to the maximum deflection was very similar and after the point of maximum deflection the predicted response oscillated more and around a larger plastic deformation compared to the real response.

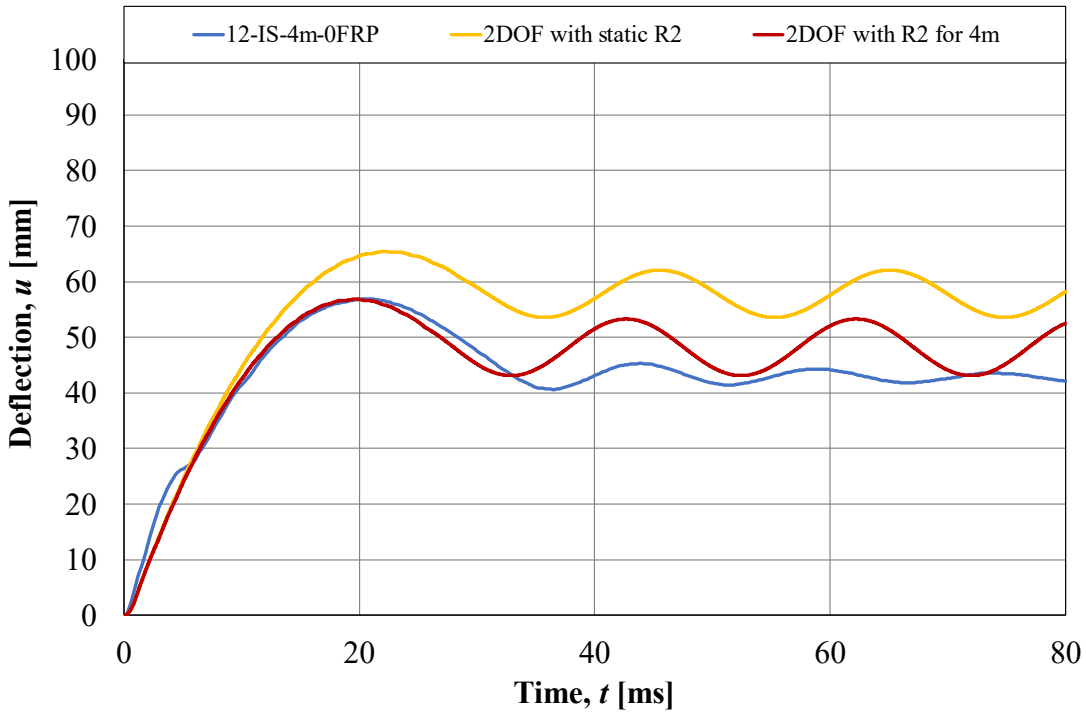

Figure 11.7 Comparison of predicted midpoint deflection versus time and actual results from experimental testing for beams subjected to a drop weight from 4 m.

Figure 11.7 shows the results of the drop height 4 m where the same pattern between predicted and actual response was found. When the beam resistance was increased the maximum deflection as well as the point of maximum deflection matched but after that point the predicted plastic deformation is overestimated.

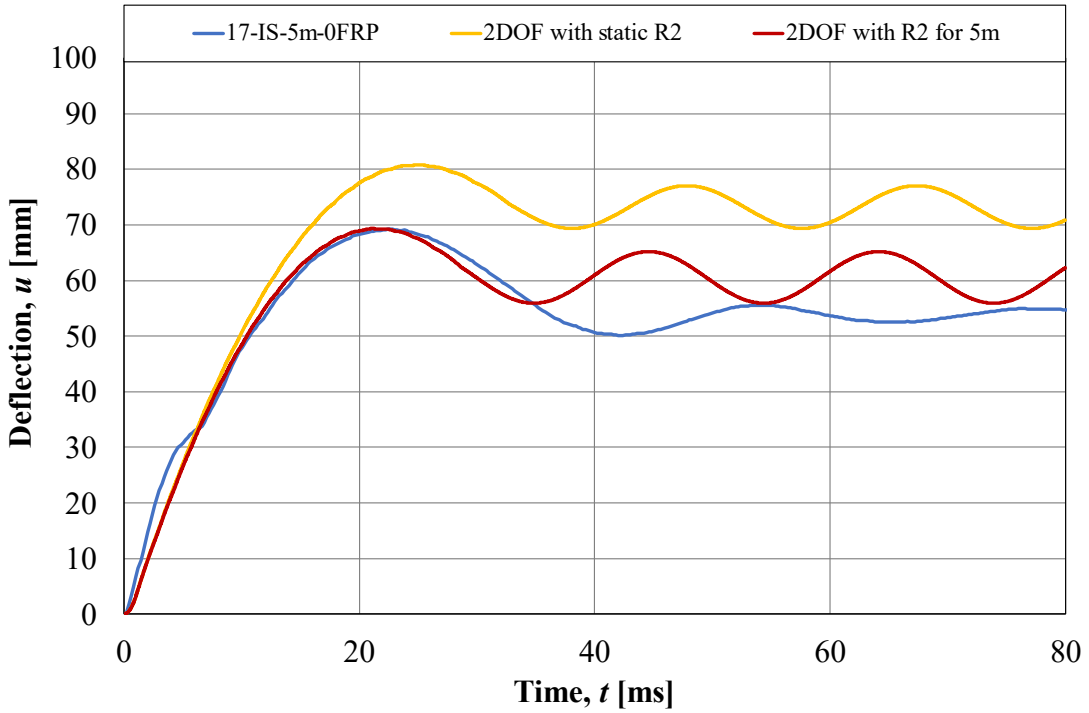

Figure 11.8 Comparison of predicted midpoint deflection versus time and actual results from experimental testing for beams subjected to a drop weight from 5 m.

Figure 11.8 shows the results of the drop height 5 m and once again similar type of response was obtained as the results from drop heights 3 and 4 m.

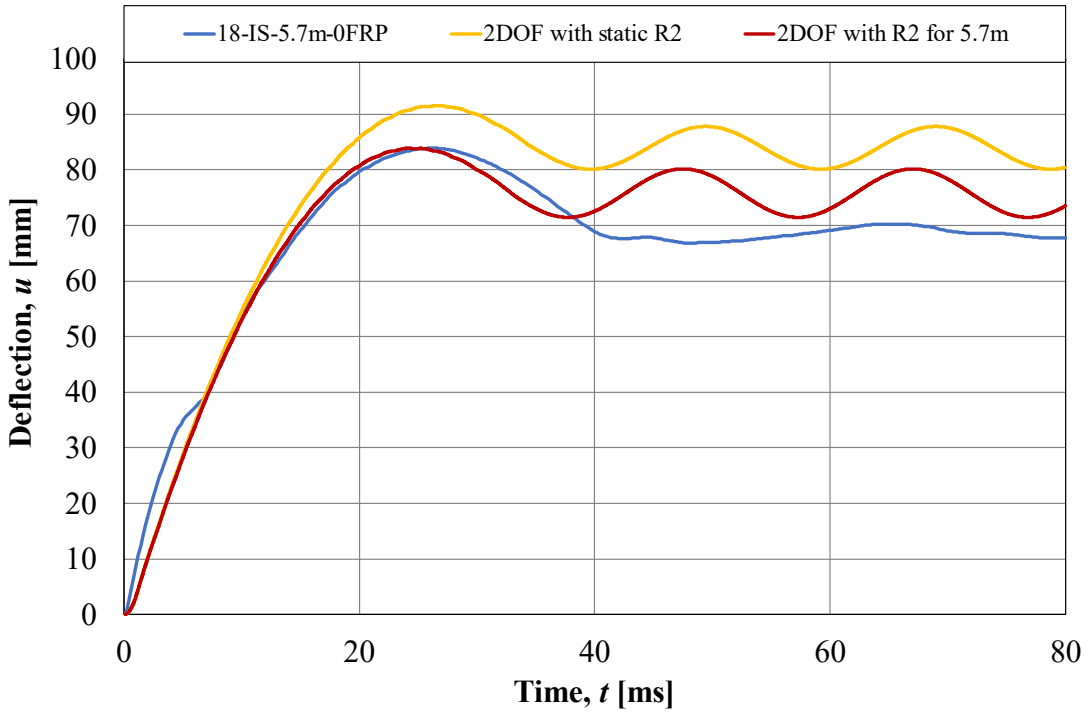

Figure 11.9 Comparison of predicted midpoint deflection versus time and actual results from experimental testing for beams subjected to a drop weight from 5.7 m.

From a drop height of 5.7 m, see Figure 11.9, the curve of the measured data looks different from the others. This was because of data missing in some loading steps due to damages of the beam where not all images captured information due to small pieces obscured the camera at certain images. Therefore, the results could not be fully trusted when it came to oscillation. However, the plastic deformation in general could still be trusted.

What can be seen in the predictions made for the midpoint deflection versus time relationship is that the maximum deflection obtained using the predicted static resistance gives un underestimation of results compared to the resistance used to get the same maximum deflection as in the dynamic tests. This is natural since the prediction of static resistance of the beam was underestimated. The predicted results using the statically predicated resistance experienced their maximum later which is reasonable since the deflection continued to increase after the second prediction achieved its maximum value. Something else worth noticing was that the difference between predicted beam resistance and the resistance needed in order to obtain the same deformation in the 2DOF model decreased with increasing drop height. This was probably due to the fact the difference between the two resistances decreased for increasing drop height in general, see Appendix L for values of beam resistances.

Consequently, the predicted and actual midpoint deflection over time was different to some degrees. Mainly the fact that the statically predicted resistance of the beam was an underestimation and that the model yields larger predicted plastic deformations compared to the actual response, even if the resistance is matched to result in the same maximum deformation. The overestimation of maximum and plastic deformations in the model has been observed in previous theses as well. The model does not capture the entire behaviour of the system, one aspect not included in the model is strain rate effects. This could be one of the reasons for the difference in results between predicted and actual results.

11.2.3 Drop Weight Velocity

In this section the dynamic test results regarding the drop weight velocity are compared with the predicted drop weight velocity and the drop weight velocity from the second type of comparison described in Section 11.2.1. The comparisons are presented in Figure 11.10 to Figure 11.13.

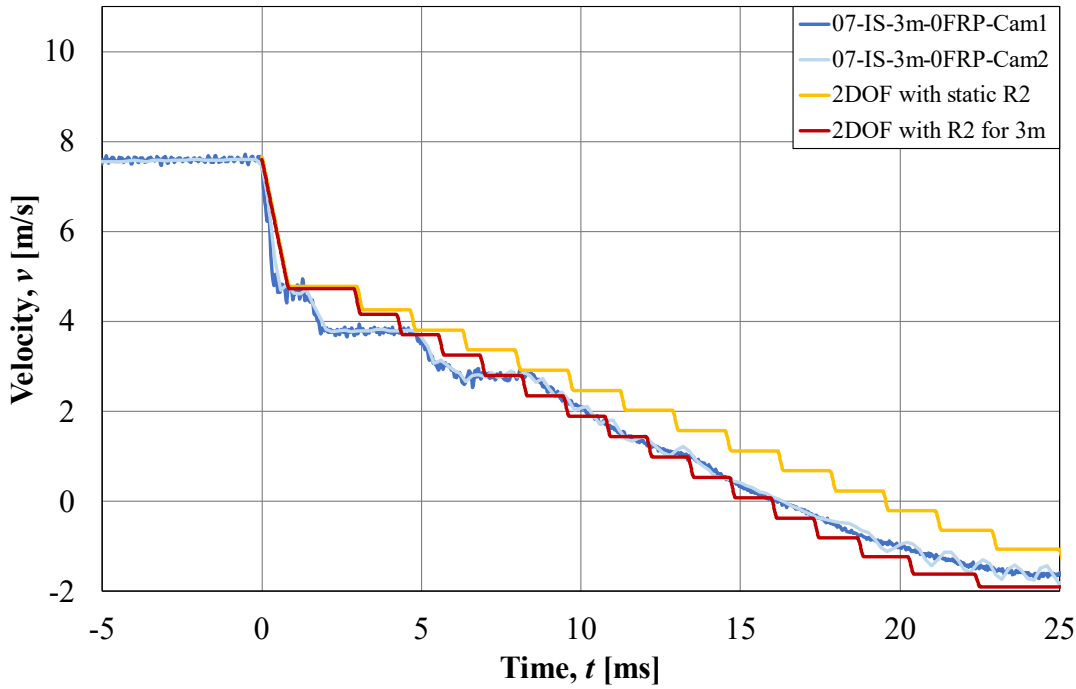

Figure 11.10 Comparison of predicted drop weight velocity versus time and actual results from experimental testing for beams subjected to a drop weight from 3 m.

Figure 11.10 shows the predictions compared to the measured values for the drop weight velocity from a drop height of 3 m. The values of the velocity were very similar between the predictions and measured values. However, the shape of the velocity versus time relationship differs. In the first few milliseconds after impact the curves complied well but after the first millisecond or two after impact the measured values showed less and longer periods with a constant velocity and not the same constant stepwise decrease in velocity as the predicted ones.

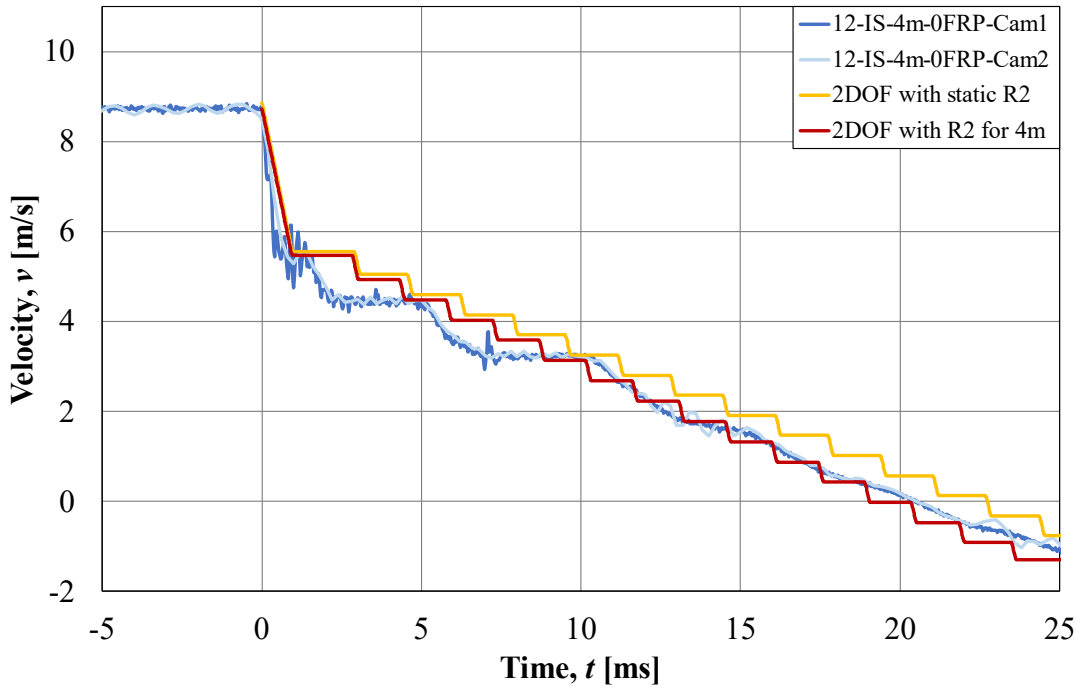

Figure 11.11 Comparison of predicted drop weight velocity versus time and actual results from experimental testing for beams subjected to a drop weight from 4 m.

In the comparison for the 4 m case, visualized in Figure 11.11, the measured drop weight velocity showed, similarly as for the 3 m case, that the values of the measured velocity complied well with the predicted ones but the shape was not the same. Instead of the stepwise degrease predicted the measured values showed a smoother decrease.

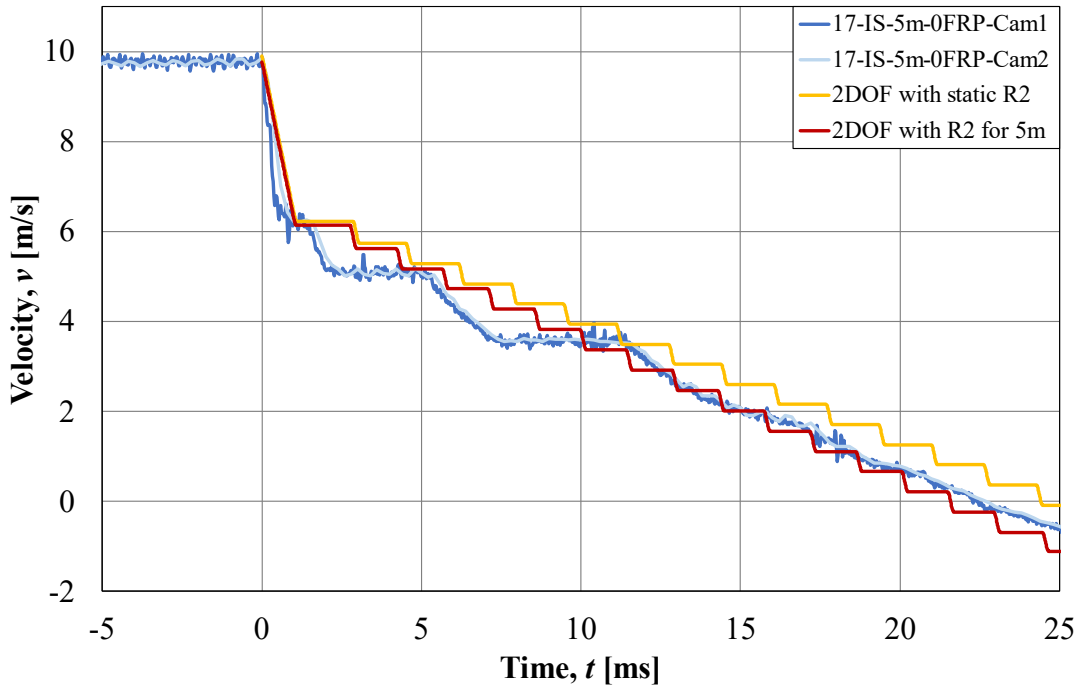

Figure 11.12 Comparison of predicted drop weight velocity versus time and actual results from experimental testing for beams subjected to a drop weight from 5 m.

Figure 11.12 visualizing the comparison for the 5 m drop height case showed the similar type of results as for the 3 and 4 m cases.

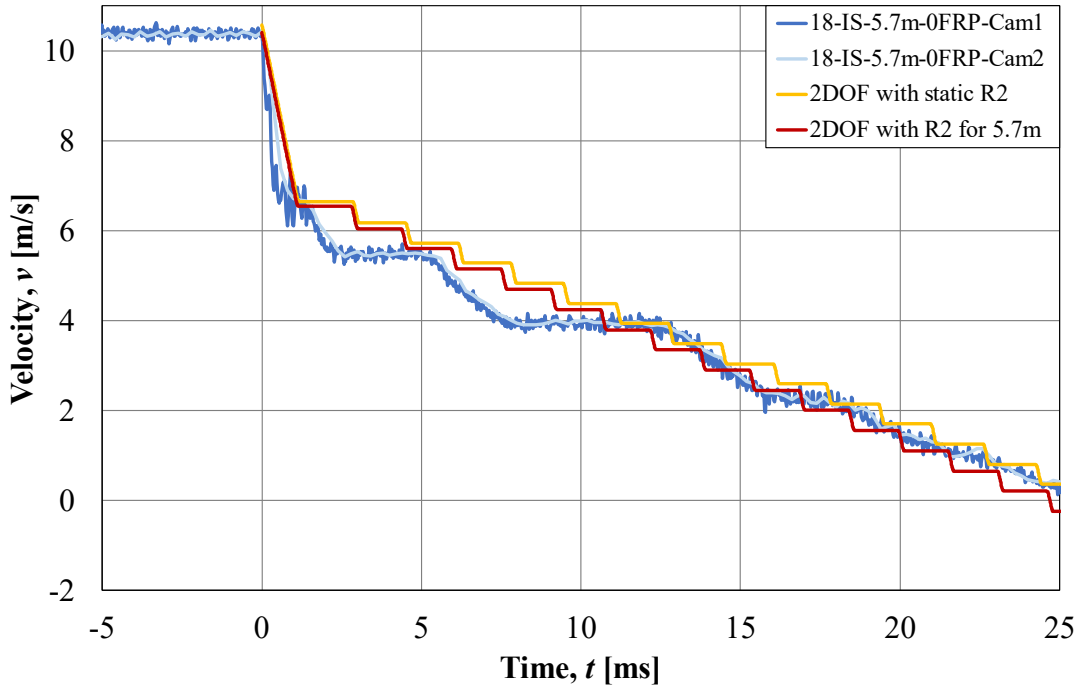

Figure 11.13 Comparison of predicted drop weight velocity versus time and actual results from experimental testing for beams subjected to a drop weight from 5.7 m.

The results of the final drop height of 5.7 m, visualized in Figure 11.13, showed similar response as described above for the lower heights. Since the measured values had fewer and longer periods where the velocity was constant, the difference between measured and predicted values were the largest at a point shortly after 5 ms where the drop weight and beam were in contact for the measured case. This was the case for all drop heights but in general the measured velocities complied very well with the predicted ones. Naturally the predicted response using the higher beam resistance complied to a higher degree with the measured values. Overall, both methods to predict the dynamic behaviour are well suited to predict the velocity.

11.3 Comparison of Experimental Results with Previous Study

Previous experimental study with FRP strengthened concrete beams was made in 2020 at Chalmers by Nigani and Nordström (2020). In Figure 11.14 results from the experimental study presented in this thesis is compared with previous study made in 2020 for beams that were subjected to static loading only.

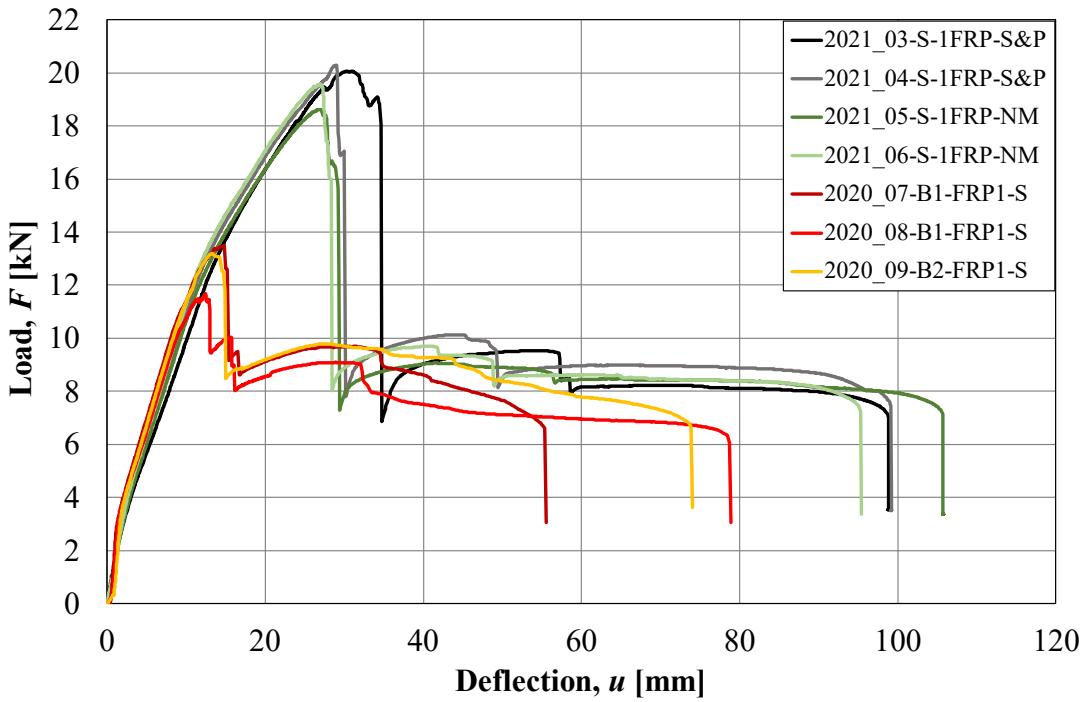

Figure 11.14 Comparison of load versus deflection for beams only statically loaded presented in this thesis (2021) and from Nigani & Nordström (2020).

As seen in Figure 11.14 the ultimate load was significantly higher 2021 and debonding occurred at a significantly larger deformation. The ultimate deformation capacity was also larger when results from this project is compared with the previous study from 2020. If the load capacity after debonding is studied one can observe that it was around the same level in both test-series. In Figure 11.15 is a comparison of results for beams subjected to a drop weight from 3 m from this project compared to corresponding tests in Nigani & Nordström (2020).

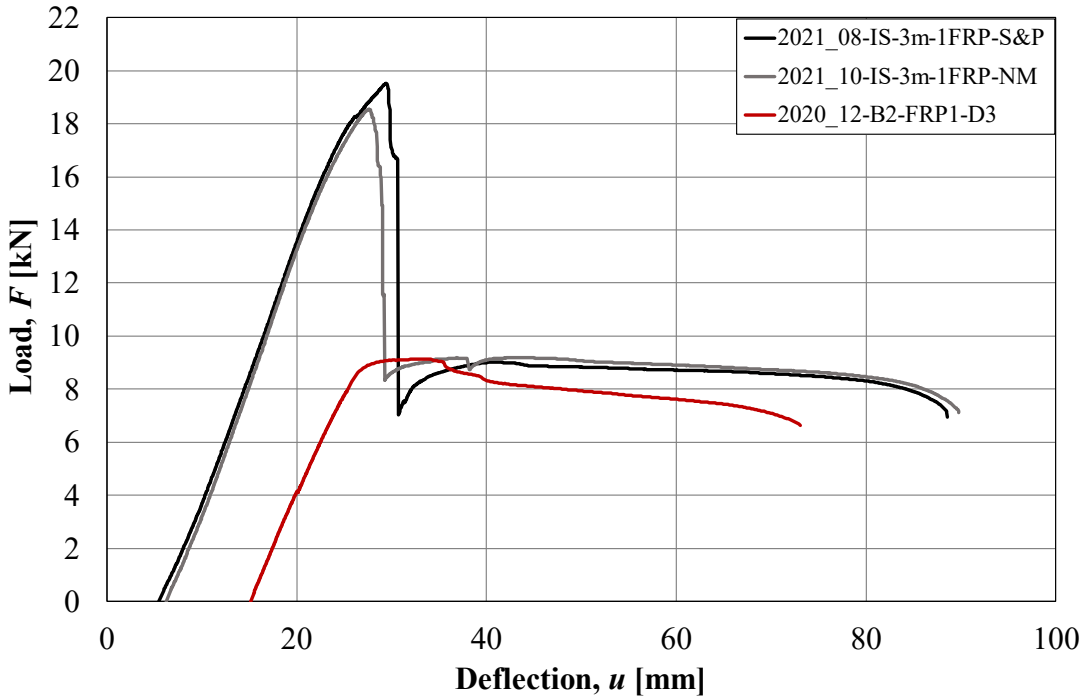

Figure 11.15 Comparison of load versus deflection for beams subjected to a drop weight from 3 m presented in this thesis (2021) and from Nigani & Nordström (2020).

When comparing results for beams subjected to a drop weight from 3 m one can observe that debonding of FRP had taken place already in the drop weight tests made by Nigani & Nordström (2020). In this thesis (2021), though, the debonding of FRP occurred during the static tests. The results in Figure 11.15 show that the residual plastic deformation from the drop weight was smaller in this project and the ultimate deformation capacity was larger compared to the results from Nigani & Nordström (2020). A comparison of load versus deflection for beams subjected to a drop weight from 4 m is presented in Figure 11.16.

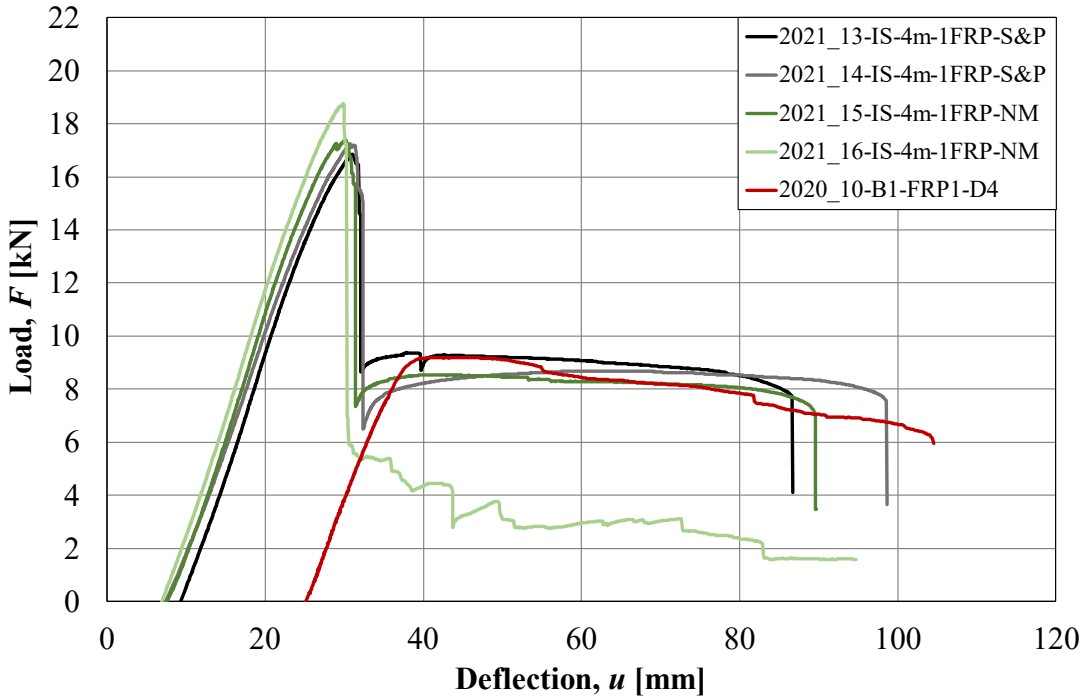

Figure 11.16 Comparison of load versus deflection for beams subjected to a drop weight from 4 m presented in this thesis (2021) and from Nigani & Nordström (2020).

When studying the results in Figure 11.16 one could observe that debonding of FRP occurred during the drop weight tests for Nigani & Nordström (2020) but in this project (2021) all beams experienced debonding during the static tests. One could observe a significantly smaller residual plastic deformation from the drop weight tests for beams in this project compared to the one in Nigani & Nordström (2020). The ultimate load capacity was much larger for beams in this project since debonding of FRP first occurred at static testing. To summarize, beams within this project developed larger ultimate load and deformation capacity than the studied beams in Nigani & Nordström (2020) and debonding of FRP occurred much later. A conclusion that can be made is that the preparations of the surface, on which the FRP was applied on, affected the results of great level in a positive way. The preparations prevented early debonding of FRP since the adhesion became much better.

12 Discussion

In this work several aspects regarding the structural response of a FRP strengthened reinforced concrete structure have been investigated. From both the dynamic and static tests, many observations have been made and it has been observed that FRP has proven to give a desired response in many of the aspects investigated in this work.

One key aspect regarding FRP strengthening is the fact that beams strengthened with FRP developed a significantly higher number of cracks. An increase in number of cracks increases the possibility to achieve a higher rotation capacity and therefore also achieve larger deformations. This was proven to be the case in this study where the FRP strengthened beams had the possibility to achieve larger deformations. For all beams where the number of cracks could be counted, the FRP strengthened beams showed up to a factor of 2 more cracks and never less cracks than the unstrengthened beams. The difference was largest between the statically only loaded beams; with increasing drop height, though, the difference in the number of cracks decreased. Where a form of shear failure occurred the FRP strengthened beam did not achieve a larger deformation capacity than their unstrengthened counterpart. This, though, only occurred for one of the beams, but it showed the importance of taking all type of failure modes into consideration.

Another key aspect that gave a larger deformation capacity was the fact that the FRP sheet ripped off some concrete when debonding occurred. The sheet often ripped off the concrete in the middle of the span where the stresses were the highest and the cracks were the densest. This response was advantageous since the reinforcement in tension then became fully exposed, leading to an increased length of reinforcement with no or reduced bond. A result of this was that the reinforcement was able to elongate practically unhindered in this plastic region with a largely increased plastic length. This was very distinct during the static tests, where the residual strength was measured, and the beams achieved very large deformations. The debonding occurred mainly during the static tests. However, it was also observed during the dynamic loading but only during two instances.

Another aspect which proved to be vital in order to increase the capacities of FRP strengthened beams and enhance their structural response was to make the bonding as good as possible. The grinding of the surface was most definitely an important step to enhance the behaviour of the FRP strengthened beam. This procedure gave a very good bonding and delayed debonding compared to an untreated or minorly treated surface. The comparison with the results for previous year's thesis showed the importance of a treated surface in order to achieve good bonding.

Prior to the tests, one uncertainty regarding the FRP strengthened beams was the structural response after debonding. Optimally, the beam believed to have a response of an unstrengthened beam after debonding, but this was not sure beforehand. However, in this work it was seen that the structural response after debonding returned to a similar response to that of an unstrengthened beam. However, as discussed, due to the increased number of cracks and the local removal of concrete cover during debonding, the plastic deformation capacity in the FRP strengthened beams also increased compared to the unstrengthened beams.

FRP strengthened beams that previously had been subjected to a drop weight from the higher drop heights could also achieve a lower residual strength than the unstrengthened counterpart. This was the case for beam 19 which has throughout the results chapter given peculiar results. It has previously been stated that a possible reason for this was that after the drop weight impact the beam flung upwards and severely hit the experimental equipment. One of the FRP strengthened beams subjected to an impact from 5.7 m achieved lower ultimate deformation than its unstrengthened counterpart but for the same drop height another FRP strengthened beam achieved almost twice the load capacity than that of the unstrengthened beam. So, the results of the residual strength and ultimate deformation capacity for beams subjected to drop weight from the higher heights were somewhat scattered. However, in general, the results showed the same tendencies.

During the dynamic testing of the beams, several beams developed diagonal shear cracks after that the drop weight caused spalling of the concrete below the area of impact. The FRP proved important in order to prevent spalling and stay together. This gave the beam still some residual strength even though it might had gotten severely damaged. Probably can FRP give an enhanced ability for concrete structures to keep the concrete intact and maintain load carrying capacity.

During the project several different and interesting failure modes and tendencies to failure modes were observed. The beams were strong in flexure and experienced on several occasions shear like failures or tendencies to failure. During static loading flexural and flexural-shear cracks in the middle of the beam propagated towards the end of the FRP sheet and caused debonding. Dynamic loading gives another structural response which might trigger different types of failure modes. The deformed shape shortly after impact is not triangular under dynamic loading and therefore cracks on the top edge could be observed. The cone shaped damages caused by the drop weight might be the reason for debonding during the static tests for beams previously subjected to impact. The diagonal shear cracks propagated towards the edges in a similar way as for the statically only loaded beams.

In Section 7.3, several measures to enhance the load carrying capacity of the beams are presented; i.e. anchors, U-jackets and stirrups. Those are all measures that would enhance the capacities of the beams. Anchors would most likely delay or perhaps hinder debonding of the FRP sheet which the literature treated in the report validate. This could lead to an even higher load carrying capacity and might result in even more cracks, which proved to be important for the large deformation capacity. Something worth noticing is that with enhanced response in flexure, which FRP gives, other failure modes might become governing. It was also seen, as mentioned throughout the report, that from the drop weight impact, diagonal shear type cracks developed under the impact zone. So, other measures might be needed to not experience other types of failure than bending, for example failure in shear. Stirrups is one measure which could enhance the structural response of the FRP strengthened beams from this study. Another measure could be the use of U-jackets which enhance both the flexural, by delaying debonding, and shear behaviour of beams. When structures are strengthened with FRP in flexure it is important to keep in mind that possible undesired structural responses could appear.

Studying the two types of adhesives, no significant differences in responses for the test beams or material tests were observed. There were some differences in elastic modulus when material tests were compared with the specified properties by the supplier but these differences could be connected to the problems with the test specimens so no further conclusions could be drawn. One aspect worth mentioning, though, was that the NM adhesive were supposed to be heat cured but it was not done in this work, and this could perhaps have affected the results in some way. But for the applications studied in this project and the future development and areas of use, a production process including heat curing is not believed to be appropriate.

Two cameras were used with different properties, and one consequence with the faster camera was that the maximum impact force was captured more precisely than what has been done in previous, similar, test-series carried out at Chalmers. The results from the faster camera also led to more precise results compared to the previous theses regarding acceleration and impact force (Lovén & Svavarsdóttir, 2016; Lozano & Makdesi, 2017; Jönsson & Stenseke, 2018; Andersson & Pettersson, 2019; Nigani & Nordström, 2020). The peak values of the impact force were closer to the real values compared to the ones from previous years which sometimes had an almost horizontal peak. The total impulse on the other hand was very similar when the two cameras were compared, so this observation verifies the impulse evaluation for results captured by the slower camera in previous theses, referred to above.

When the results of internal work of the beams were analysed, it was seen that for beams subjected to static loading only, the internal work for a FRP strengthened beam was significantly larger than for an unstrengthened beam; about twice the internal energy was observed in the static tests. This was due to an increased load capacity until debonding and larger ultimate deflection, which together gave a very large contribution to the internal energy compared to the unstrengthened beams. The results for the beams subjected to impact loading prior to the static loading showed that for an unstrengthened beam the internal work increased compared to when subjected to static loading only. However, the same effect was not observed for the FRP strengthened beams. In some cases, where the beams had previously been subjected to impact loading, similar or lower levels of total internal work were observed. It was observed though, that the estimation of internal work from the impact was similar to the theoretical one for the unstrengthened beams while the FRP strengthened beams had lower estimated internal works compared to the theoretical value. The difference between the theoretical and estimated values, and the lower total internal work for FRP strengthened beams previously subjected to impulse loading could be due to several reasons. One could be because of difficulties in the procedure of estimation of the internal work consumed in the impact. Both difficulties regarding the stiffnesses used in the approximation as well as that the assumption that the reference beams were representative. The difference could be due to effects from dynamic loading which created a more beneficial situation for the unstrengthened beams. However, this needs to be investigated further. To summarize, for unstrengthened beams an impulse loading was always beneficial from an energy point of view. However, for FRP strengthened beams the effect is not beneficial, but the consequences were minor. Even though the differences in consequences from an impulse loading, the FRP strengthened beams was always, except for some extreme cases, able to absorb approximately the same amount of energy as their unstrengthened counterpart for the same load situation. These exceptions were failure in shear or a very low residual capacity.

One group of structures designed for withstanding impulse loading, e.g. shock waves are for example embassies, civil defence shelters and fortifying facilities. One difference between these structures and other types of structures that could be retrofitted with FRP, e.g. bridges or columns, is that the structures mentioned first has people seeking protection or working there. If FRP strengthening is used in structures like these, secondary aspects need to be taken into consideration. One of these aspects arises when the FRP sheet delaminates. It was seen throughout the tests that when the FRP sheet delaminates it does so with a large force. This is very reasonable and expected since there are large amounts of energy being released at the point of debonding. In order to maintain people's safety and comfort in a facility being strengthened with FRP the potential debonding of FRP sheets needs to be considered. This could perhaps be handled by having some form of internal protection, e.g. a net hindering the flick of the FRP sheet at debonding, and potential concrete debris being ripped off the concrete surface. For structures like bridges or similar, this aspect is most likely not a problem to the same extent.

Throughout this work, FRP strengthened concrete structures has showed good and desirable response. However, it might not always be this case for impulse loaded reinforced concrete structures strengthened with FRP. There could be a situation where the design of the beam and the configuration of reinforcement influences the beam in such a way that the load capacity after debonding is decreased as well as there is a decrease in ultimate deformation capacity, which results in an issue at the point of debonding. When the FRP debonds, which it might eventually do, a large amount of energy will be released. This energy needs to be absorbed by the structure, in this case by the reinforcement. If the amount of reinforcement was lower or damaged, e.g. corroded, compared to the reinforcement amount used in this work, and a scenario where debonding occurs, the energy needs to be absorbed by the structure and a consequence of this could potentially be a rupture of a reinforcement bar. It could be this case as stated if the amount of reinforcement is decreased or if the reinforcement is damaged which makes the structure more vulnerable to the large release of energy. It could also be for a case where the maximum load and the ultimate deflection coincides more. The capacity of a structure is then utilized more when the large amount of energy is being released at the point of a potential debonding and the structure is then more vulnerable. For this latter case, this potential aspect about the debonding and the release of energy could be problematic. This could have catastrophic effects for a structure and therefore needs to be investigated more thoroughly.

13 Conclusions

The main aim in this work was to get a better understanding of the structural response of an impact loaded reinforced concrete structure strengthened with FRP. This was done by experimental testing tests of reinforced concrete beams where the beams were tested statically only of subjected to a drop weight impact followed by static loading. DIC was used to capture the structural response of the beams.

FRP strengthening of reinforced concrete beams leads to more cracks and a larger plastic region where the reinforcement can elongate more compared to an unstrengthened beam. This leads to an increased deformation capacity and hence also an increase in internal energy.

Treating the surface where the FRP is to be fastened was crucial to gain a good bonding. A well-treated surface enhances the structural response and delays debonding of the FRP sheet. A suitable treatment method is grinding of the surface.

The maximum load capacity increased with FRP strengthening and when debonding occurred the structural response followed the response of an unstrengthened beam. In this work, the FRP strengthened beams gave in general an enhanced structural response. However, in a few cases a dominant shear crack occurred during the impact or large damages of the concrete resulting in practically no compressive zone occurred. This led to that some beams did not experience the enhanced response of FRP strengthening

For impulse loaded beams in this study, the plastic deformation was reduced if FRP strengthening was used. It is beneficial with a dynamic loading followed by a static loading for unstrengthened beams considering the total internal work of the beams. Up to a drop height of 5 m the total absorption of energy increased with increasing drop height. For the drop height of 5.7 m the total absorption of energy for the unstrengthened beam did not continue to increase but it was still larger than for the case with only static loading. For FRP strengthened beams is it not beneficial but the total internal work is not in general lower than its unstrengthened counterpart for the same load scenario given that exceptions does not occur as explained above. For beams subjected to a drop weight from 3 or 4 m the total internal energy is larger for FRP strengthened beams. For a drop height of 5 m the total internal work was similar between unstrengthened and FRP strengthened beams and for 5.7 m the FRP strengthened beams had lower absorption of energy. However, for beams subjected to a drop weight from 5.7 m the results were scattered among the three specimens and more specimens are needed to draw conclusions from this height.

Material tests were made to investigate the properties of the concrete, reinforcement and adhesives. To be able to draw conclusions from the material tests, regarding the epoxy dogbones, improvements are needed for the test specimens. If trustworthy results from the epoxy tests can be achieved, then the properties of the adhesives can influence the choices in design of FRP strengthening.

Two high-speed cameras were used: one with 40 000 FPS and one with 5 000 FPS. The faster camera gave more precise results regarding acceleration and impact force and was mainly used to evaluate this while the slower camera was used to register deformations and strain fields in the tested beams. The initial peak at impact differed,

a higher load of about 50 % was obtained using the faster camera, but total impulse under the dynamic loading showed similar results with both cameras. The latter, thus validates impulse results from previous theses that used the slower camera.

14 Future Studies

This work has dealt with reinforced concrete beams strengthened with FRP subjected to impulse followed by static loading, and in addition beams subjected to static loading only. Several aspects not treated in this work needs to be investigated and aspects treated needs further investigations. Even though this project has investigated different drop heights and adhesives, the experimental study was limited to investigating certain aspects. It would therefore be interesting to see how different geometries of the beams as well as other reinforcement configurations would influence the structural response. In this study, the FRP strengthening resulted in overall improved and desired behaviour but with another design of the beams, other types of adhesives or other types of FRP, the general results might differ. For future studies it would be very interesting to see different types of adhesives with more diversified properties tested as well as other types of FRP. A more conventional method in civil engineering is strengthening with carbon FRP and it would be interesting to see the response with this type also. CFRP would perhaps increase the number of possible adhesives since it is more common. But the choice of FRP will partly depend on what is sought in form of load capacity, energy absorption and failure mode.

A study investigating different ratios of reinforcement is a needed. This is because of the theory that the structural response of FRP strengthened reinforced concrete structures is probably largely influenced by the configuration and amounts of reinforcement. With a lower reinforcement ratio, the structure could be more sensitive to a potential debonding of the FRP. Connected to this are scenarios where the FRP is more dominant. For example, with a reinforced concrete beam with stirrups and twice the amount of FRP, then the release of energy at debonding is significantly larger and a structure's ability to handle the absorption of energy may become more critical.

Another interesting aspect for a future study would be to further investigate the potential damage on the reinforcement due to FRP debonding. Non-linear finite element analyses to model and study how the reinforcement is affected by the debonding of FRP, but also non-linear finite element analyses of the problem at a larger scale would be interesting and probably needed in order to be able to predict these types of problems in an accurate way.

Improvements of the methods used to predict both static and dynamic responses are needed. In the static predictions the load capacity is underestimated and in the dynamic predictions, both the maximum and plastic deflections are overestimated. In these improved methods the influence of the FRP strengthening is needed, and optimally would be an accurate way to predict the response of the FRP and the adhesive.

Additional strengthening of the beams, e.g. the usage of anchors for the FRP would be interesting. The literature study concludes that the usage of end anchors gives a higher load carrying capacity, delays or hinders debonding and potentially gives a more ductile response, therefore further study within this area would be of high interest.

15 References

Al-Emrani, M., Engström, B., Johansson, M., & Johansson, P. (2013). *Bärande konstruktioner Del 1*. Göteborg: Division of Structural Engineering.

Amran Mugahed, Y,M., Alyousef, R., Rashid, R., Alabduljabbar, H. (2018). Properties and applications of FRP in strengthening RC structures: A review. *Structures 16 (2018)*. 208-238. https://doi.org/10.1016/j.istruc.2018.09.008

Andersson, M., Pettersson, E. (2019). *Reinforced Concrete Beams Subjected to Drop-Weight Impact Experimental study of the influence of reinforcement properties on the structural response* (Master's thesis, Chalmers University of Technology, Institution of Architecture and Civil Engineering).

Camata, G., Spacone, E., Zarnic, R. (2006). Experimental and nonlinear finite element studies of RC beams strengthened with FRP plates. *Composites: Part B*, 2006(38), 277-288. doi:10.1016/j.compositesb.2005.12.003.

CEN. (2005). *SS-EN 1992-1-1:2005: Design of concrete structures – Part 1-1: General rules and rules for buildings*. European Committee of Standardization.

- (2019a). *SS-EN 12350-2:2019: Testing fresh concrete – Part 2: Slump-test*. European Committee of Standardization
- (2019b). *SS-EN 12390-3:2019: Testing hardened concrete – Part 3: Compressive strength of test specimens.* European Committee of Standardization.

Domone, I., Illston, J. (2010). *Construction Materials: Their Nature and Behaviour*. Spon Press.

El-Hacha, R., Wight, R C., Green, M F. (2001). Prestressed fibre-reinforced polymer laminates for strengthening structures. *Progress in Structural Engineering and Materials*, 2001(3), 111-121, DOI: 10.1002/pse.76.

Engström, B. (2015). *Design and analysis of continuous beams and columns.* Göteborg: Division of Structural Engineering.

Fib. (2001). *Externally bonded FRP reinforcement for RC structures*. Fédération internationale du béton. doi.org/10.35789/fib.BULL.0014

Fortifikationsförvaltningen. (1973). *Provisoriska anvisningar för dimensionering av armerade betongkonstruktioner som skydd mot verkan av konventionella vapen inom närmissområde*. Fortifikationsförvaltningen. Befästningsavdelningen, Publ. No. 25:1 Bk/1973.

Huang, X., Zhou, Y., Xing, F., Wu, Y., Sui, L., Han, N. (2019). Reliability-based design of FRP flexural strengthened reinforced concrete beams: Guidelines assessment and calibration. *Engineering Structures*, 2020(209), https://doi.org/10.1016/j.engstruct.2019.109953

Johansson, M. (2000). *Structural Behavior in Concrete Frame Corners of Civil Defence Shelters*. (PhD thesis, Chalmers University of Technology, Department of Structural Engineering).

- (2014). *Beräkningsmetodik stötlast*. [Unpublished manuscript].

Johansson, M., Hallgren, M., Ansell, A., Magnusson, J., Leppänen, L. (2021*). Plastisk deformationsförmåga och tvärkraftsrespons hos impulsbelastade betongkonstruktioner* (Publication No. ACE 2021:5). [To be published during 2021]. Chalmers University of Technology.

Johansson, M., Laine, L. (2012). *Bebyggelsens motståndsförmåga mot extrem dynamisk belastning, Del 3 – Kapacitet hos byggnader*. Gothenburg: Swedish Civil Contingencies Agency.

Jönsson, J., Stenseke, A. (2018). *Concrete Beams Subjected to Repeated Drop-Weight Impact and Static Load: Assessment of structural response in experimental testing and predicted response with numerical analyses* (Master's thesis, Chalmers University of Technology, Institution of Architecture and Civil Engineering).

Kishi, N., Komuro, M., Kawarai, T,. Mikami, H. (2020). Low-Velocity Impact Load Testing of RC Beams Strengthened in Flexure with Bonded FRP Sheets. *Journal of Composites for Construction*. *24(5)*. https://doi.org/10.1061/(ASCE)CC.1943-5614.0001048

Lam, L., Teng J.G. (2001). Strength of RC Cantilever Slabs Bonded with GFRP strips. *Journal of Composites for Construction*, 5(4), 221-227.

Lozano Mendoza, F., Makdesi Aphram, J. (2017). *Concrete Beams Subjected to Drop-Weight Impact and Static Load: Structural behavior and plastic rotation capacity from experiments and finite element analysis* (Master's thesis, Chalmers University of Technology, Institution of Architecture and Civil Engineering).

Lu, X.Z., Teng, J.G., Ye, L.P., Jiang, J.J. (2005). Bond-slip models for FRP sheets/plates bonded to concrete. *Engineering Structures*, 2005(27), 920-937. doi:10.1016/j.engstruct.2005.01.014

Löfgren, I,. Forbes Olesen, J., Flansbjer, M. (2004). *Application of WST-method for fracture testing of fibre-reinforced concrete.* Göteborg: Department of Structural Engineering and Mechanics.

Nigani Zeleke. Y., Nordström, G. (2020). *FRP Strengthened RC Beams Subjected to Drop Weight Impact and Static load Experimental study for structural response* (Master's thesis, Chalmers University of Technology, Institution of Architecture and Civil Engineering).

Nils Malmgren. (2011). *Datablad NM Laminering 625* [Product sheet]. http://www.nilsmalmgren.se/Datablad/TDS%20S%20NM%20Laminering%20625.pdf

Nordin, H. (2003). Fibre Reinforced Polymers in Civil Engineering: Flexural Strengthening of Concrete Structures with Prestressed Near Surface Mounted CFRP Rods (Licentiate thesis, Luleå University of Technology, Department of Civil and Mining Engineering).

Norimitsu, K., Masato, K,. Tomoki, K,. Mikami, H. (2020). Low-Velocity Impact Load Testing of RC Beams Strengthened in Flexure with Bonded FRP Sheets. *Journal of Composites for Construction*, 25(5), DOI: 10.1061/(ASCE)CC.1943-5614.0001048. https://doi.org/10.1061/(ASCE)CC.1943-5614.0001048. CC BY 4.0.

Pham, T., Hao, H. (2016a). Review of Concrete Structures Strengthened with FRP Against Impact Loading. *Structures 7 (2016)*. 59-70. http://dx.doi.org/10.1016/j.istruc.2016.05.003

- (2016b). Impact Behaviour of FRP-Strengthened RC Beams without Stirrups. *Journal of Composites for Construction*. DOI: 10.1061/(ASCE)CC.1943-5614.0000671
- (2017). Behavior of fiber-reinforced polymer-strengthened reinforced concrete beams under static and impact loads. *International Journal of Protective Structures*. 8(1), 3-24. DOI: 10.1177/2041419616658730

Saatci, S., Vecchio, F.J. (2009). Effects of Shear Mechanisms on Impact Behavior of Reinforced Concrete Beams. *ACI Structural Journal*, 106(1), 78-86.

Smith, S.T., Teng, J.G. (2002a). FRP-strengthened RC beams. I: review of debonding strength models. *Engineering Structures*, 2002(24), 385-395. PII: S0141-0296(01)00105-5

- (2002b). FRP-strengthened RC beams. II: assessment of debonding strength models. *Engineering Structures*, 2002(24), 397-417. PII: S0141-0296(01)00106-7

Svensk Byggtjänst. (1990). Betonghandbok. Svensk Byggtjänst.

S&P. (n.d.). *S&P Resin 55 HP – Epoxy Adhesive (Saturant) & Primer* [Product sheet]. https://www.sp-reinforcement.eu/sites/default/files/field_product_col_doc_file/r_resin-hp-55_pub_br_pers_resin-hp-55-hp55_eu_en.pdf

Tang, T., Saadatmanesh, H. (2003). Behavior of Concrete Beams Strengthened with Fiber-Reinforced Polymer Laminates under Impact Loading. *Journal of Composites for Construction*, 7(3), 209-218. DOI: 10.1061/(ASCE)1090-0268(2003)7:3(209).

Teng, J.G., Smith, S.T., Yao, J., Chen, J.F. (2003). Intermediate crack-induced debonding in RC beams and slabs. *Construction and Building Materials*, 2003(17), 447-462. doi:10.1016/S0950-0618(03)00043-6

Teng, J.G., Lam, L., Chan, W,. Wang, J. (2000). Retrofitting of Deficient RC Cantilever Slabs Using GFRP Strips. *Journal of Composites for Construction*, 4(2), 75-84.

Tschegg, E. K. (1991). *New equipments for fracture test on concrete*. Munich: Carl Hanser Verlag.

Täljsten, B., Blanksvärd, T., Sas, G. (2016). *Kompositförstärkning av betong*. Stockholm: AB Svensk Byggtjänst och författarna.

Wu, H-C., Eamon, C. (2017). *Strengthening of Concrete Structures using Fiber Reinforced Polymers (FRP): Design, Construction and Practical Applications.* Cambridge. Woodhead Publishing

Yang J. (2021). *Strengthening Reinforced Concrete Structures with FRP Composites*. New Series No 4919, 33 pp. + papers. PhD thesis. Chalmers University of Technology.

Ye, Z., Zhao, D., Sui, L., Huang, Z., Zhou, X. (2020). Behaviors of Large-Rapture-Strain Fiber-Reinforced Polymer Strengthened Reinforced Concrete Beams Under Static and Impact Loads. *Structural Materials*. 7:578749, doi: 10.3389/fmats.2020.578749

Zoghi, M. (2014). *The International Handbook of FRP Composites in Civil Engineering*. Taylor and Francis Group.

Appendix A Facet Analysis

When GOM Correlate 2018 was used to analyse the frames from the testing the programme divided the captured area into smaller facets. Settings for these facets was needed to be properly done to capture the behaviour of the beam in an accurate way and create a mesh used in the programme. To find the most accurate settings a facet analysis was done where facet size and point distance were varied. Facet size can be described as the length of the side of each facet with the unit pixels. Point distance is the other factor and describes the distance between the centre point of each facet with the unit pixels. See Figure A.1 for illustration of the two factors.

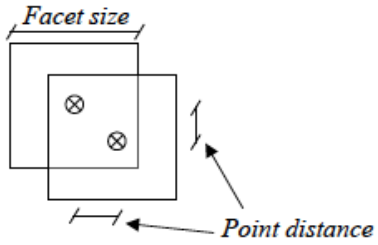

Figure A.1 Illustration of facet size and point distance (Jönsson & Stenseke, 2018).

To find the best settings different combinations of facet size and point distance was investigated. Strain fields for a beam was studied were the upper and lower limit for the major strain was set to 5 % and 1 % respectively to get rid of the noise. High accuracy computation was used. Then the analysis was done trying to find the settings presenting the results in most accurate way without too much noise. The different combinations studied firstly are presented in Table A.1 and Table A.2.

Table A.1 Strain fields for different facet sizes and point distance equal to five.

Facet size [Pixels]	**Point distance = 5 [Pixels]**
10	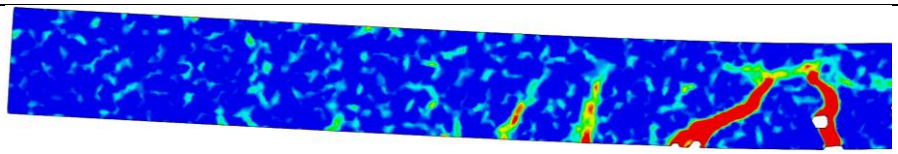
15	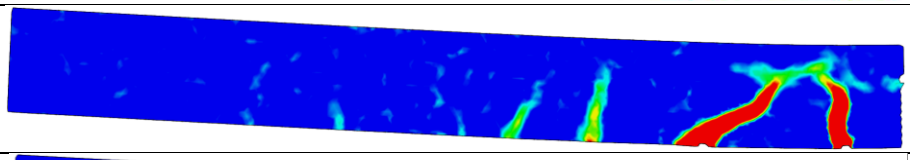
20	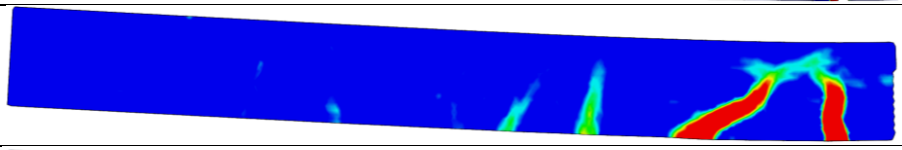
25	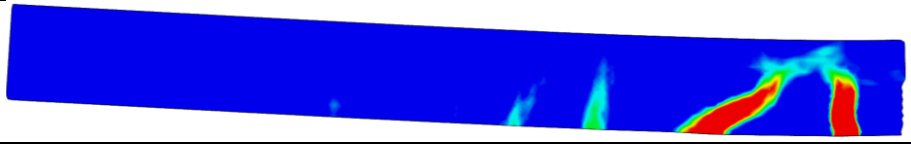

Table A.2 Strain fields for different facet sizes and point distance equal to ten.

Facet size [Pixels]	Point distance = 10 [Pixels]
15	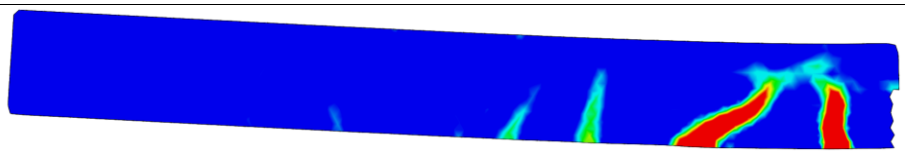
20	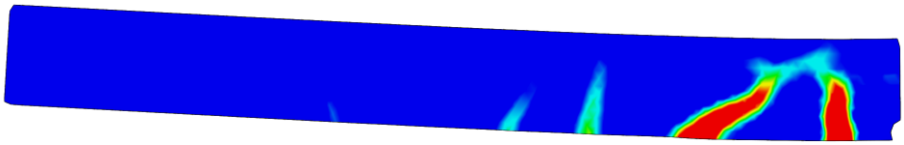
25	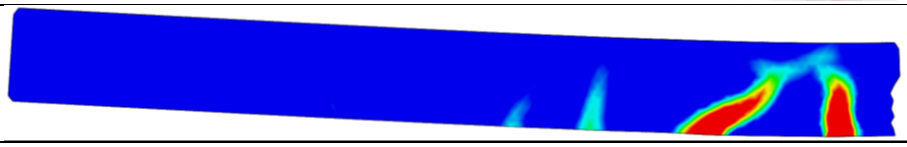

After studying the first 7 alternatives, a point distance of 5 pixels was decided to be the best setting but the facet size around 15 was investigated further. The other combinations studied are presented in Table A.3 and the final and best setting for facet size was concluded to be 16 pixels. Final settings for the dynamic tests were: facet size 16 pixels and point distance 5 pixels.

Table A.3 Strain fields for different facet sizes and point distance equal to five.

Facet size [Pixels]	Point distance = 5 [Pixels]
12	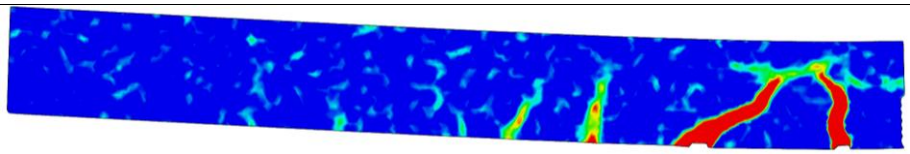
14	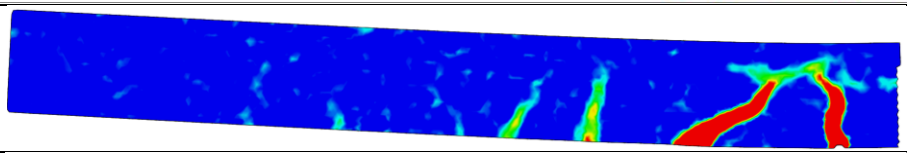
16	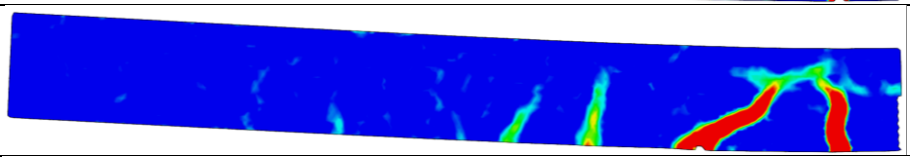
18	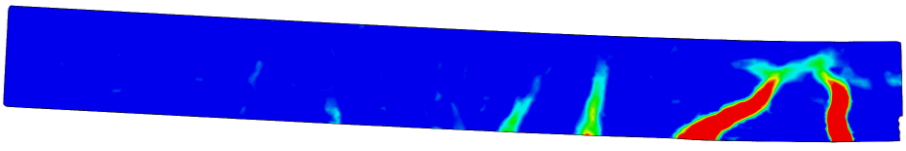

DIC during the static tests calibrated itself and the settings use were: facet size 17 pixels and point distance 14 pixels.

Appendix B Postprocessing of acceleration data from Camera 1

When acceleration data from Camera 1 was analysed it had to be post processed to be able to present the behaviour without too much noise but still capture the real behaviour in the most accurate way possible. For each test, three facet points were placed on the drop weight and acceleration data was measured in all these points. A mean value of these three facet points was deemed to be enough to represent the behaviour of the drop weight. To reduce the noise and capture the real values different types of sliding mean value over several steps was used on the mean value from the facet points. The sliding mean value was calculated as the mean value over several steps symmetrically distributed before and after the studied time step. For example, a sliding mean value over three steps around 10 ms means, a mean value of acceleration data in 9.975, 10 and 10.025 ms.

Two beams were studied to confirm which sliding mean value was most appropriate. Sliding mean value over 5, 7, 9, 11 and 13 steps was compared where the impact was in focus. Around 2 ms before impact and 8 ms after impact was studied and compared, where the noise before impact was tried to be minimized and the peak values was supposed to be at a reasonable level. For both 5 and 7 steps sliding mean value the noise and the impact behaviour was deemed to be too unrealistic but for 9 steps sliding mean value, the noise was found to be acceptable small and the impact had a reasonable shape. When increasing the steps to 11 and 13 the decrease in noise was negligible small but the peak values were further reduced. The conclusion drawn from this was that a sliding mean value over 9 steps was the best choice to treat the acceleration data before using them to calculate the impact force. Results from the investigations of the two beams are presented in Figure B.1 and Figure B.2.

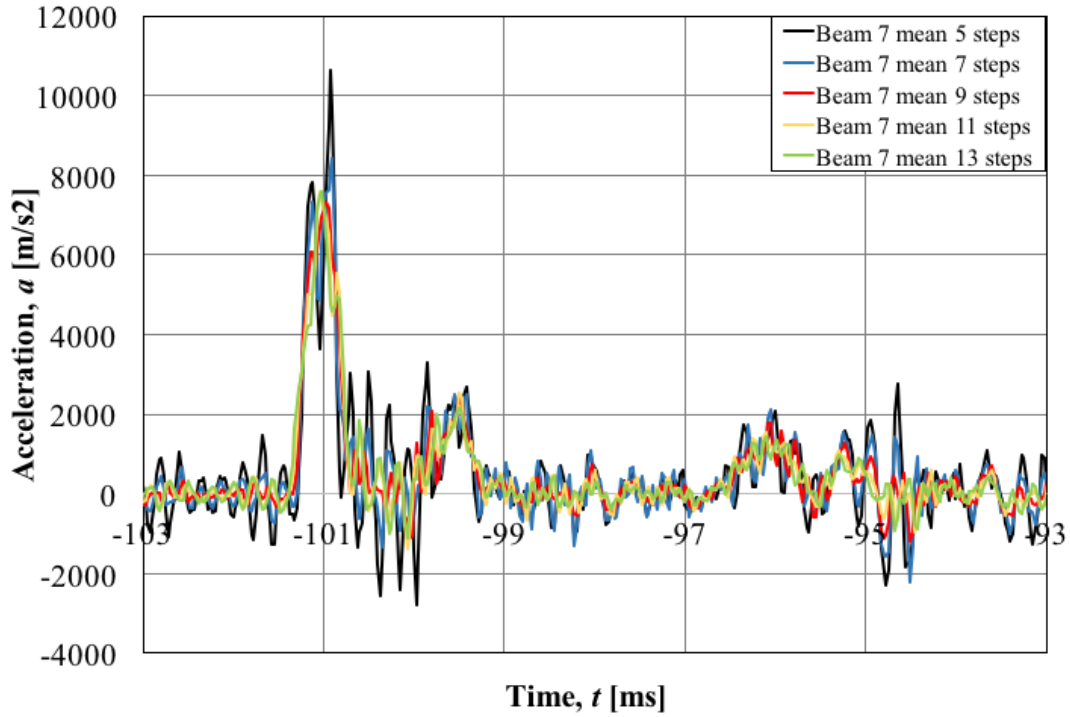

Figure B.1 *Comparison of different number of steps for sliding mean value for beam 7.*

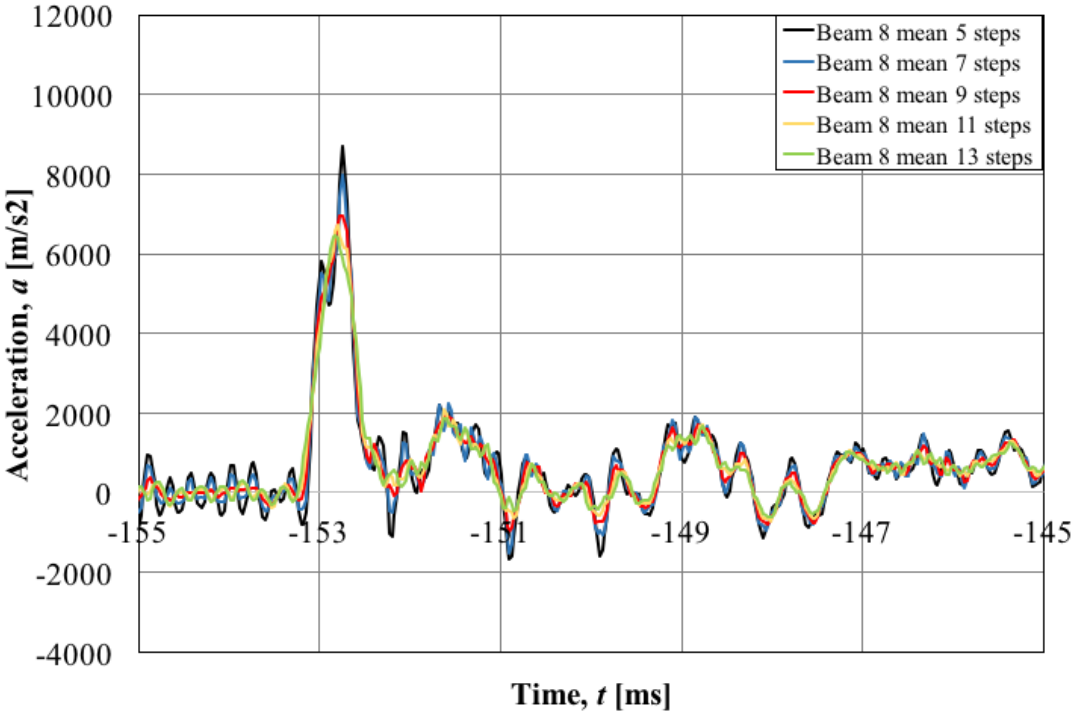

Figure B.2 *Comparison of different number of steps for sliding mean value for beam 8.*

Appendix C Strain Fields Dynamic

Strain field results presented in this appendix complement the results presented in Section 10.2.7. Strain fields for all beams are presented here.

Table C.1 Strain fields from impact to maximum deformation for beam 07-IS-3m-0FRP.

Time step [ms]	Strain field
1 %	2 %
0.2	
0.4	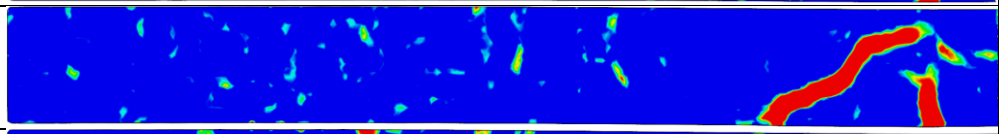
0.6	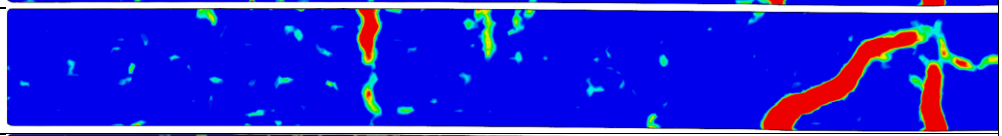
0.8	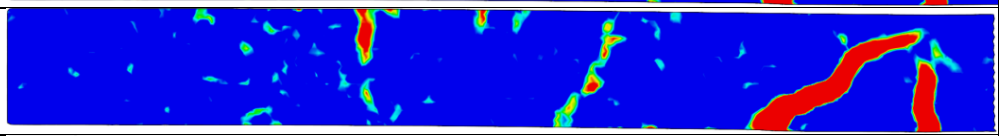
1.0	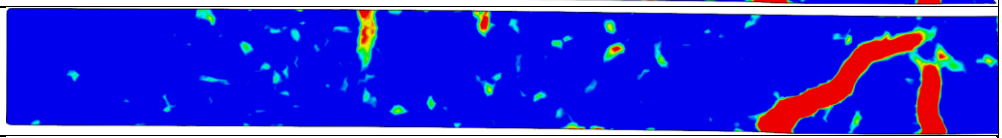
1.6	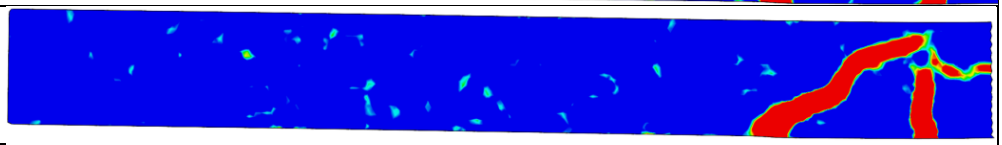
2.0	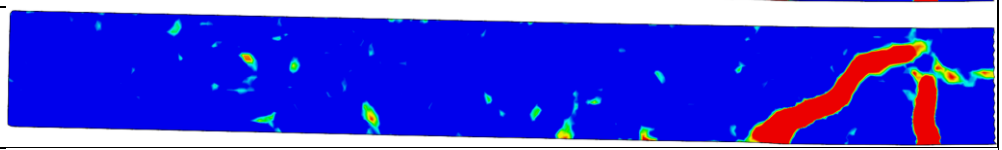
16	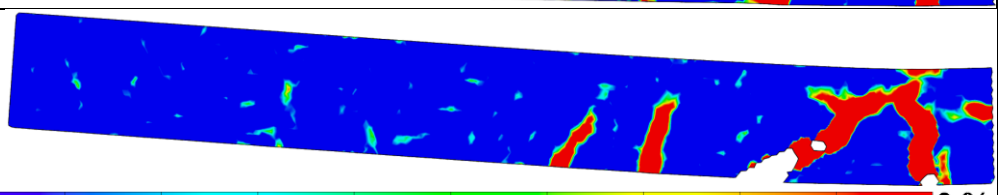
1 %	2 %

Table C.2 *Strain fields from impact to maximum deformation for beam 08-IS-3m-1FRP-S&P.*

Time step [ms]	**Strain field**
1 %	**2 %**
0.2	
0.4	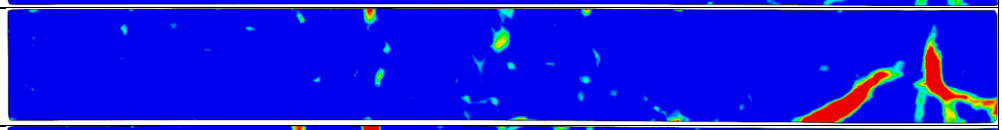
0.6	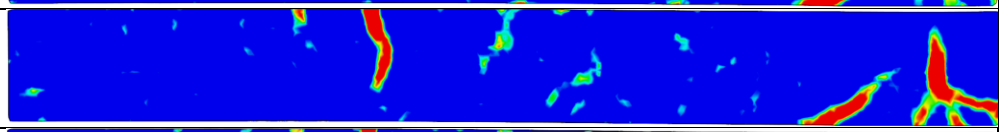
0.8	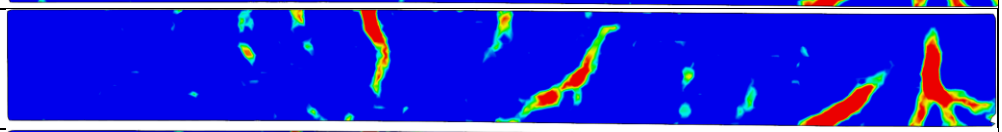
1.0	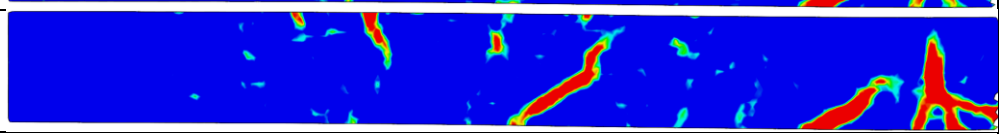
1.6	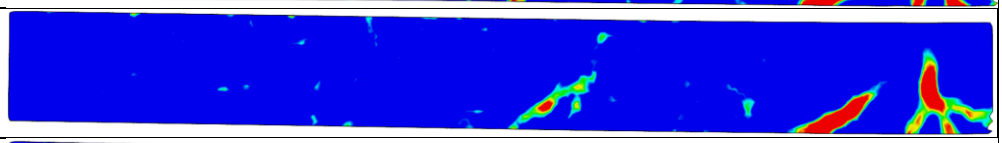
2.0	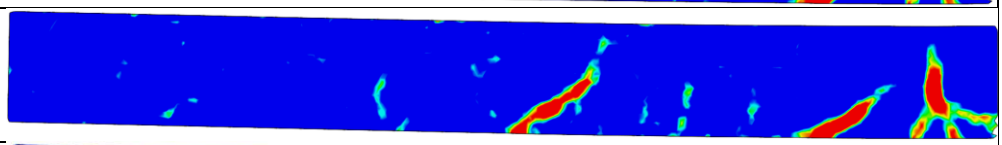
9.2	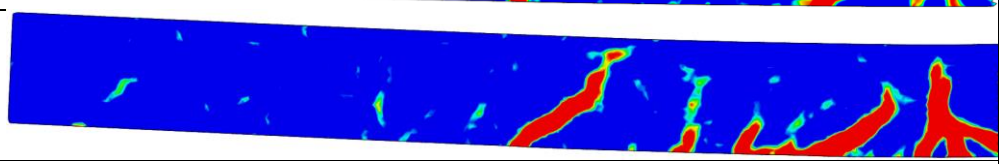
1 %	**2 %**

Table C.3 *Strain fields from impact to maximum deformation for beam 10-IS-3m-1FRP-NM.*

Time step [ms]	**Strain field**
1 %	**2 %**
0.2	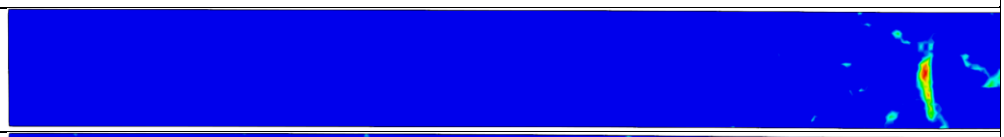
0.4	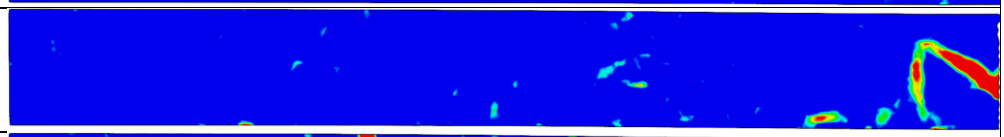
0.6	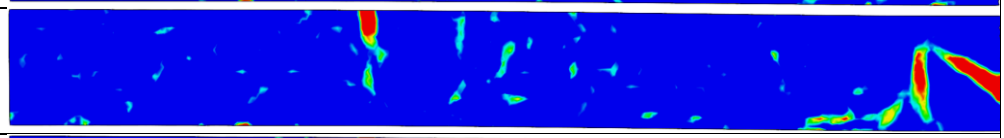
0.8	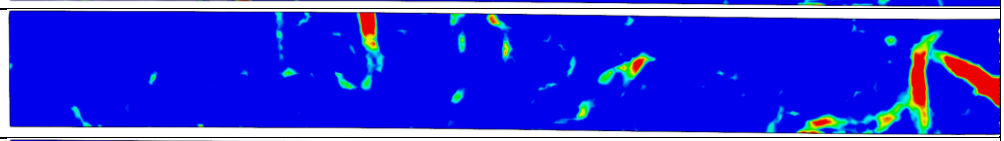
1.0	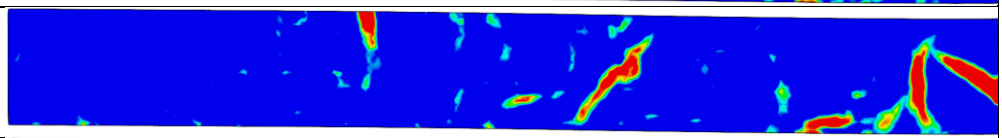
1.6	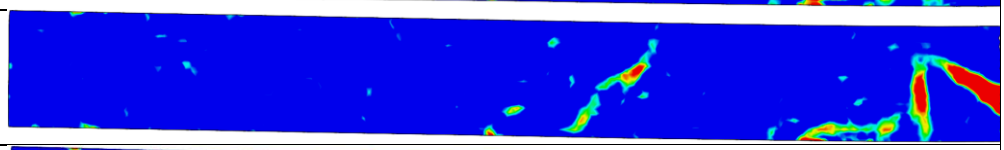
2.0	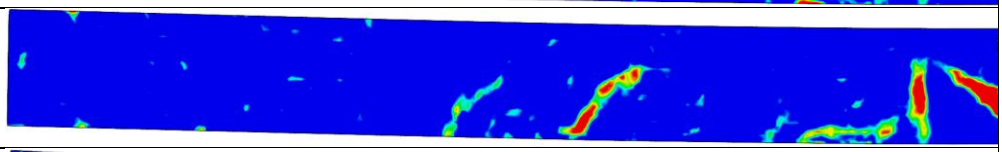
9.4	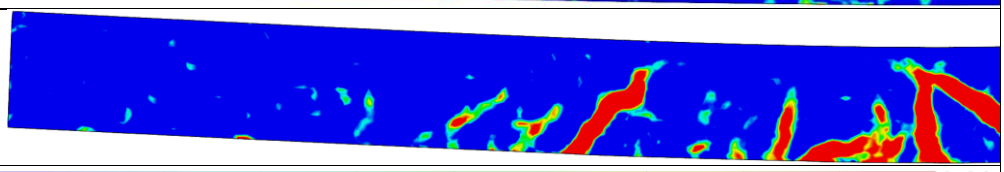
1 %	**2 %**

Table C.4 *Strain fields from impact to maximum deformation for beam 12-IS-4m-0FRP.*

Time step [ms]	Strain field
	1 % — 2 %
0.2	
0.4	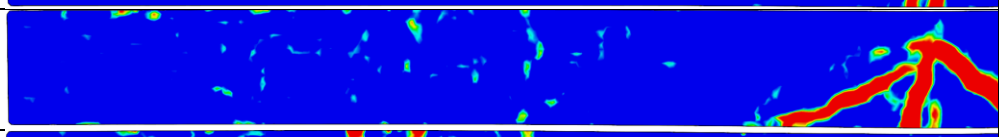
0.6	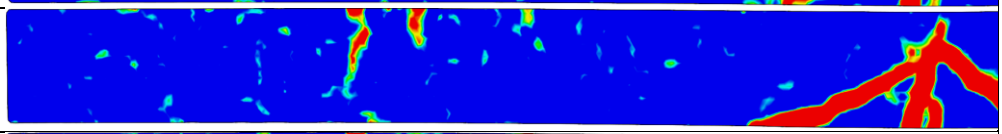
0.8	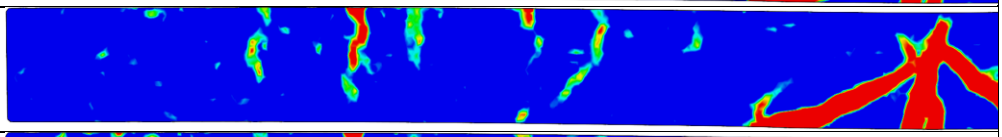
1.0	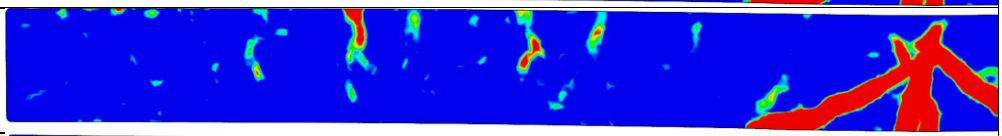
1.6	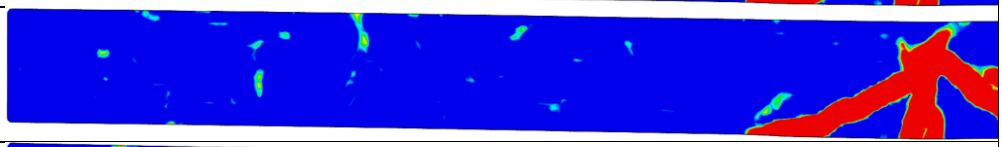
2.0	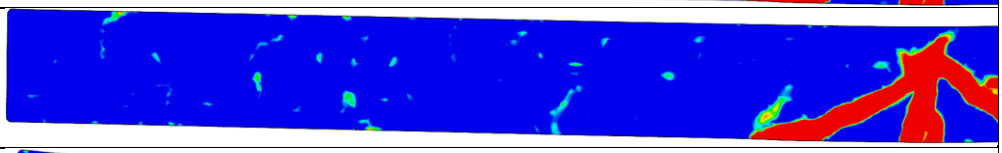
20.4	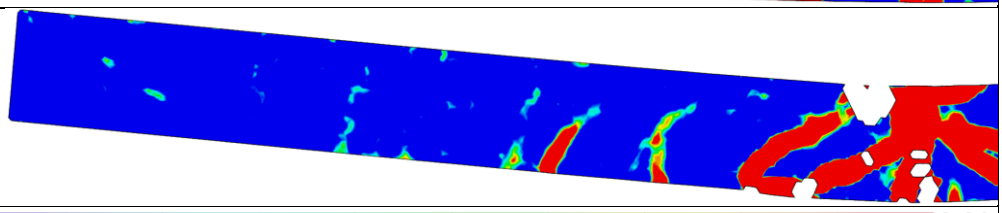
	1 % — 2 %

Table C.5 *Strain fields from impact to maximum deformation for beam 13-IS-4m-1FRP-S&P.*

Time step [ms]	Strain field
1 %	2 %
0.2	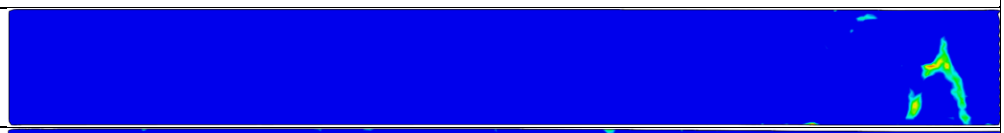
0.4	
0.6	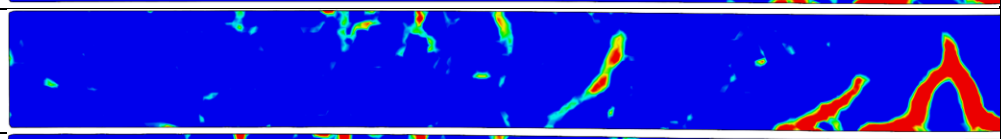
0.8	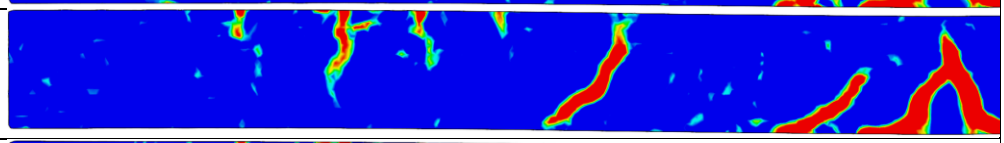
1.0	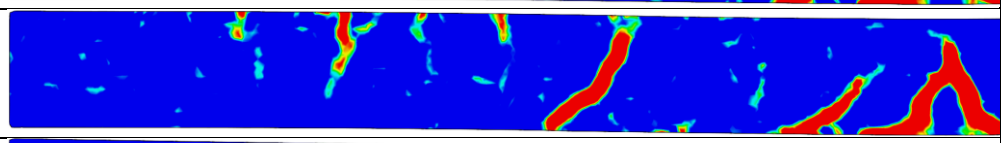
1.6	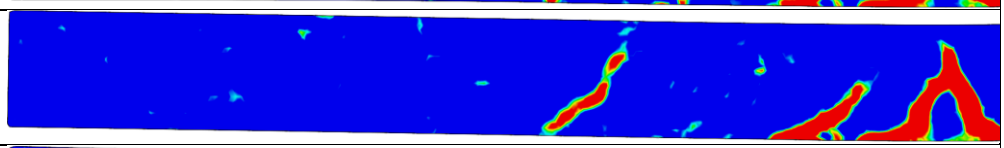
2.0	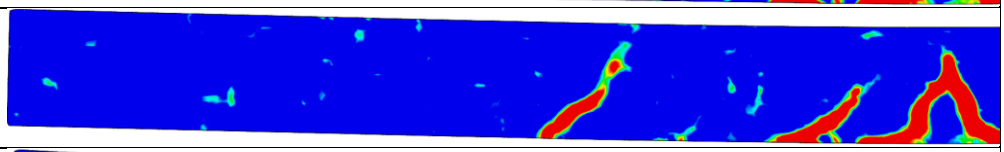
9.8	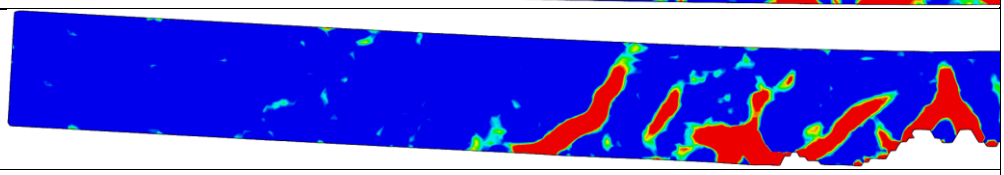
1 %	2 %

Table C.6 *Strain fields from impact to maximum deformation for beam 14-IS-4m-1FRP-S&P.*

Time step [ms]	Strain field
	1 % — 2 %
0.2	
0.4	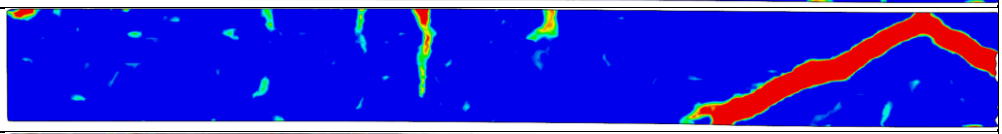
0.6	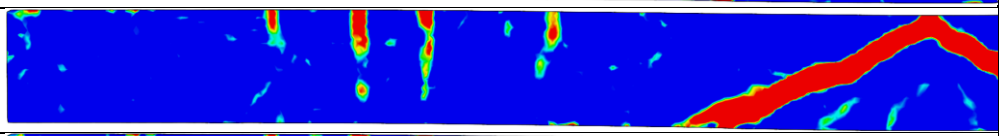
0.8	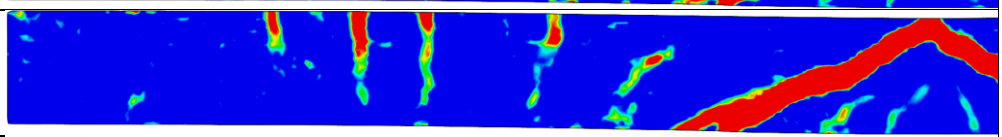
1.0	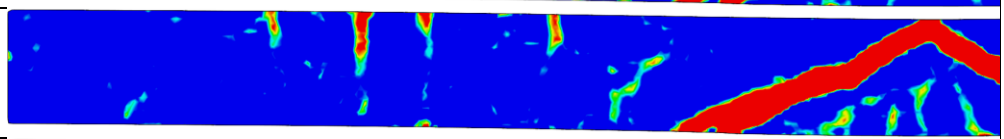
1.6	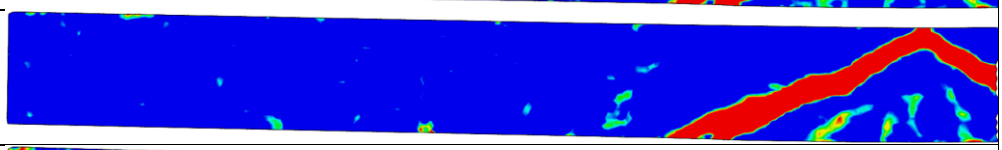
2.0	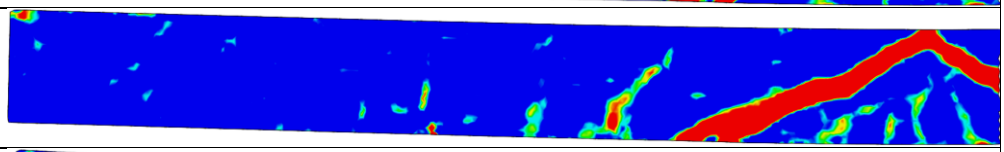
10.2	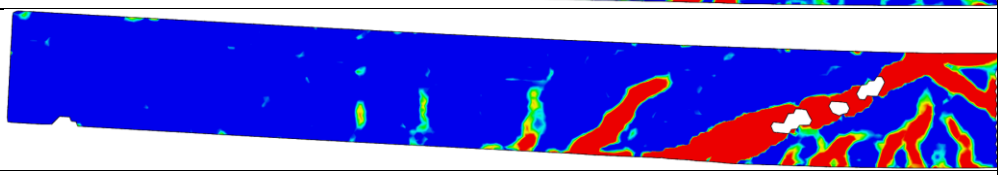
	1 % — 2 %

Table C.7 *Strain fields from impact to maximum deformation for beam 15-IS-4m-1FRP-NM.*

Time step [ms]	Strain field
1 %	2 %
0.2	
0.4	
0.6	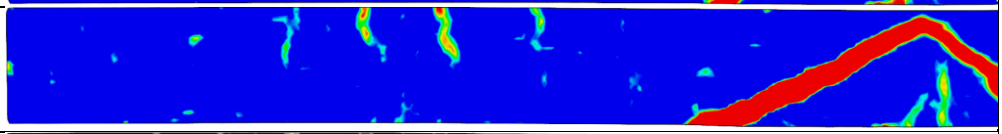
0.8	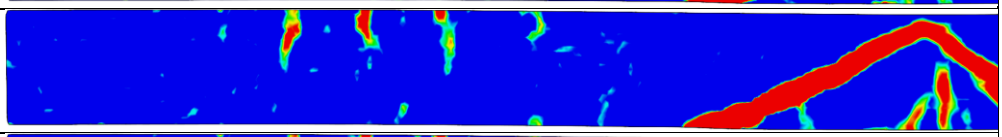
1.0	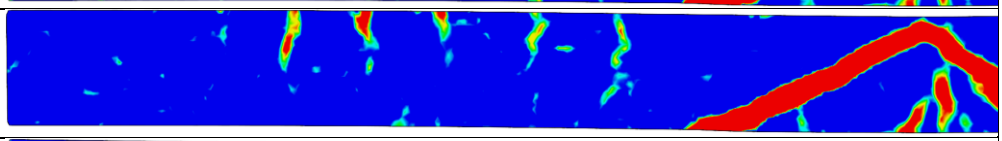
1.6	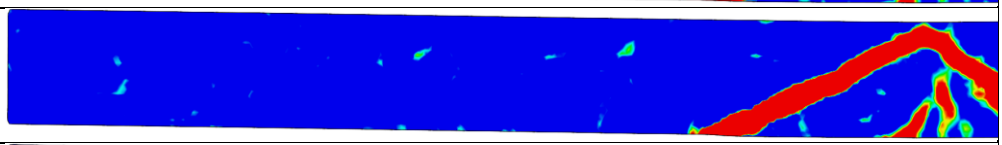
2.0	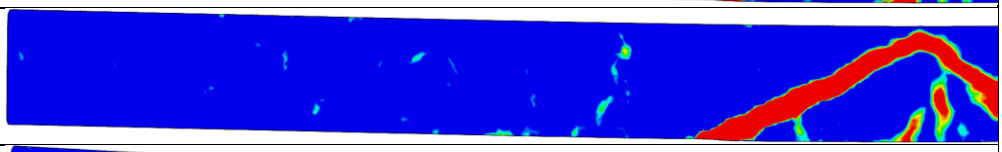
10.0	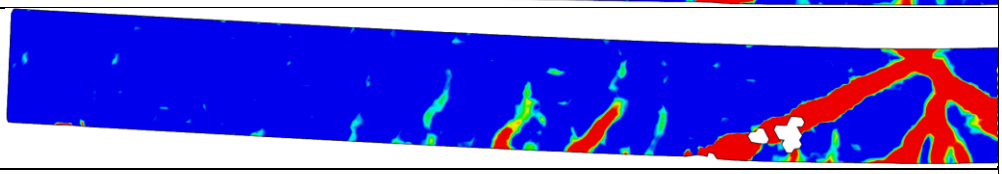
1 %	2 %

Table C.8 *Strain fields from impact to maximum deformation for beam 16-IS-4m-1FRP-NM.*

Time step [ms]	Strain field
1 %	2 %
0.2	
0.4	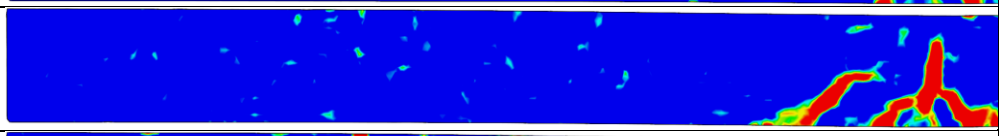
0.6	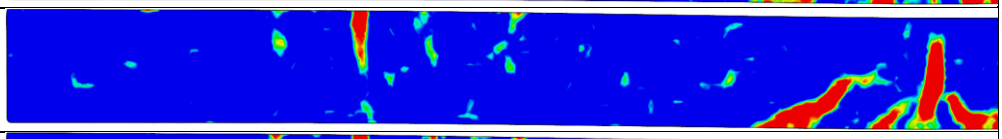
0.8	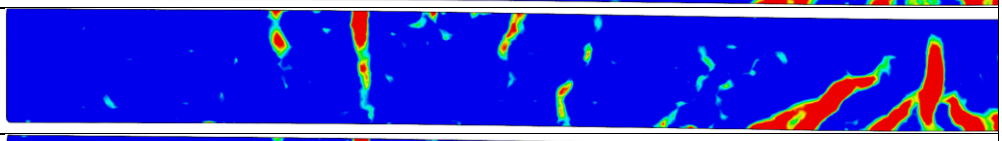
1.0	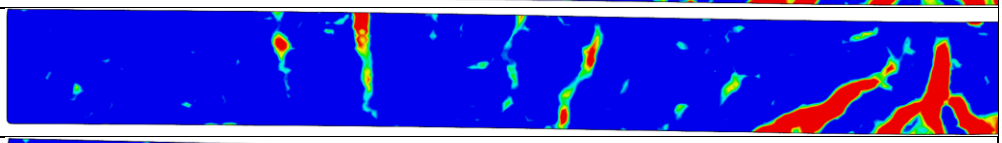
1.6	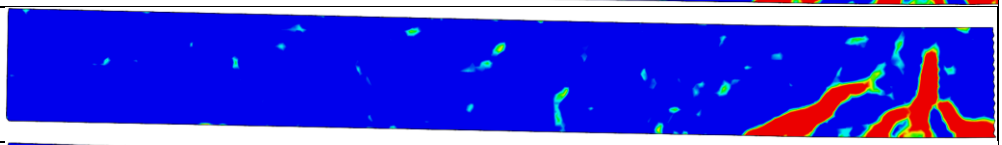
2.0	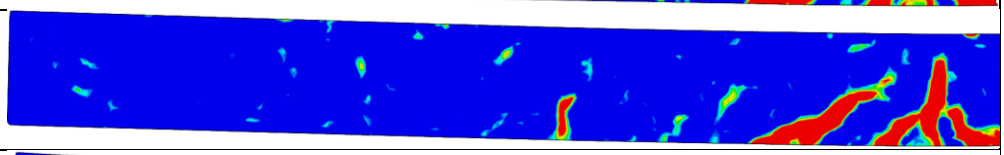
9.8	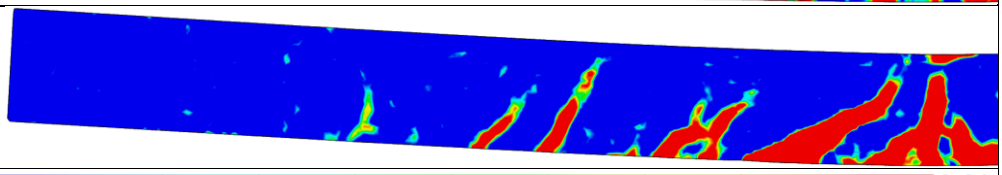
1 %	2 %

Table C.9 *Strain fields from impact to maximum deformation for beam 17-IS-5m-0FRP.*

Time step [ms]	Strain field
	1 % — 2 %
0.2	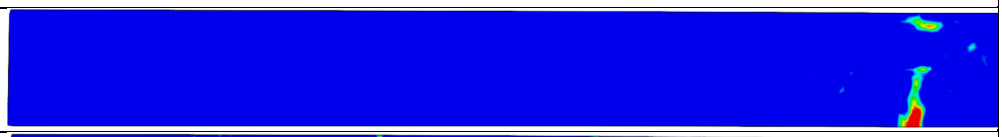
0.4	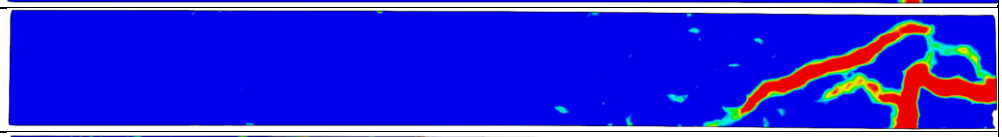
0.6	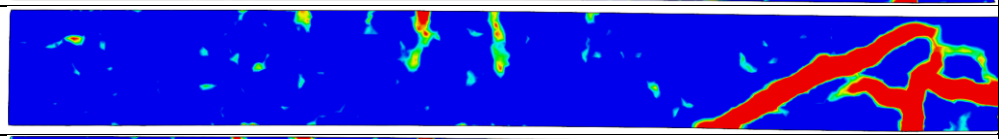
0.8	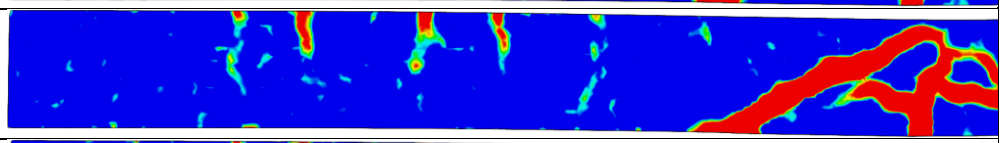
1.0	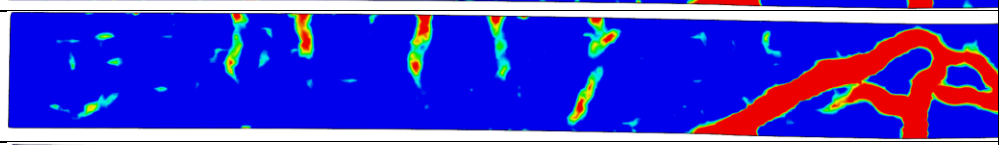
1.6	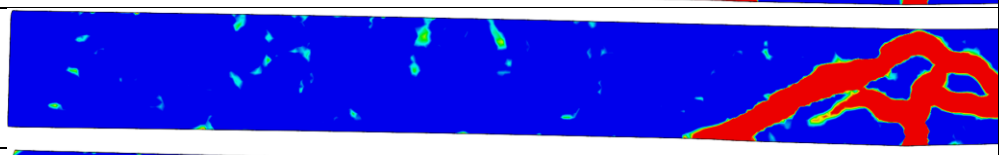
2.0	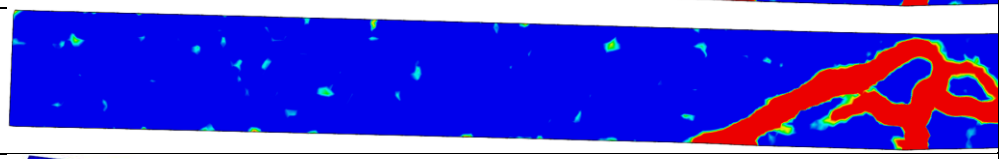
22.6	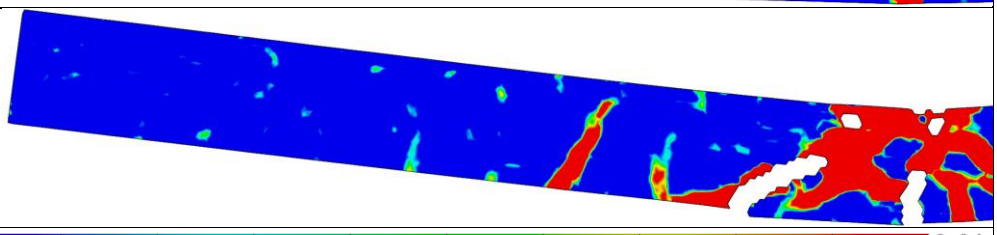
	1 % — 2 %

Table C.10 *Strain fields from impact to maximum deformation for beam 19-IS-5m-1FRP-S&P.*

Time step [ms]	Strain field
	1 % — 2 %
0.2	
0.4	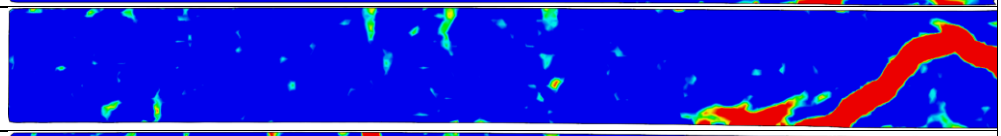
0.6	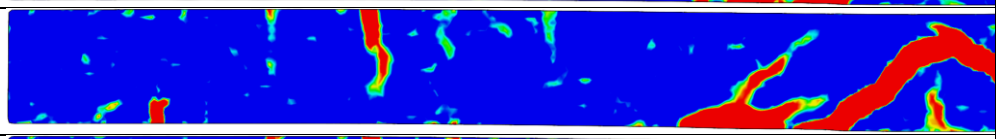
0.8	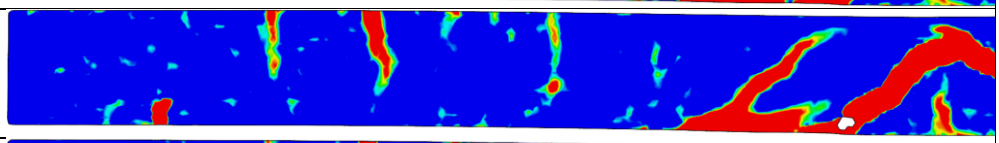
1.0	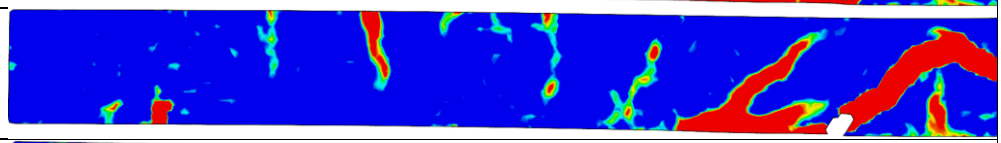
1.6	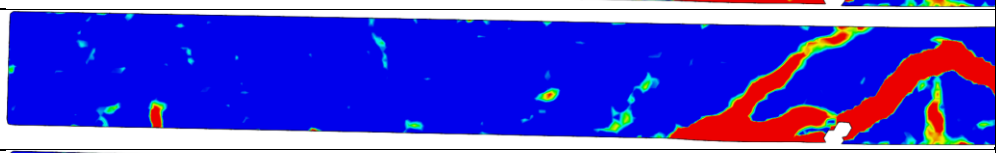
2.0	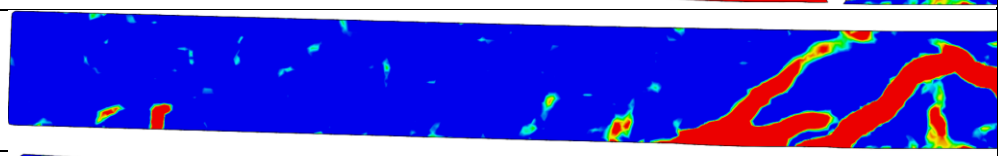
11.6	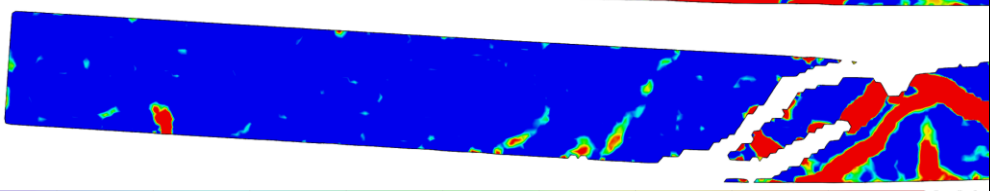
	1 % — 2 %

Table C.11 Strain fields from impact to maximum deformation for beam 20-IS-5m-1FRP-S&P.

Time step [ms]	Strain field
	1 % — 2 %
0.2	
0.4	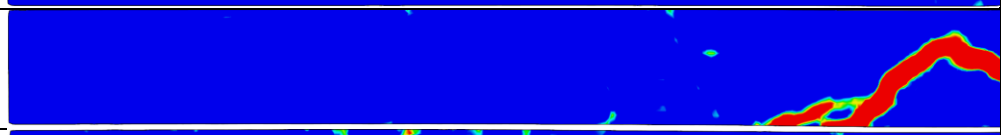
0.6	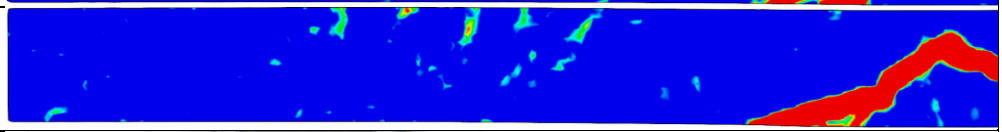
0.8	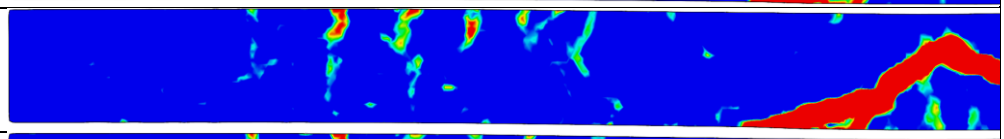
1.0	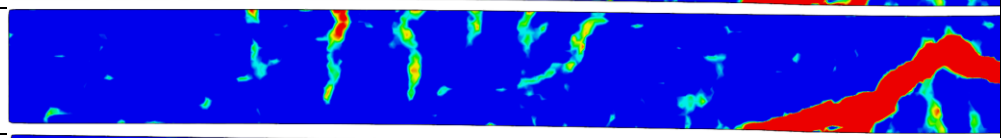
1.6	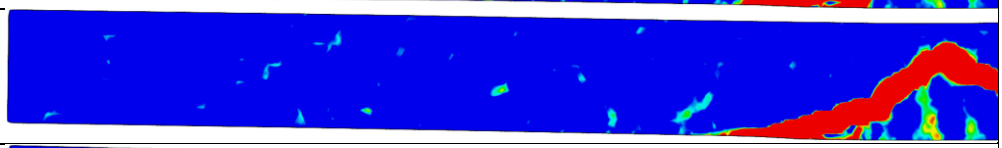
2.0	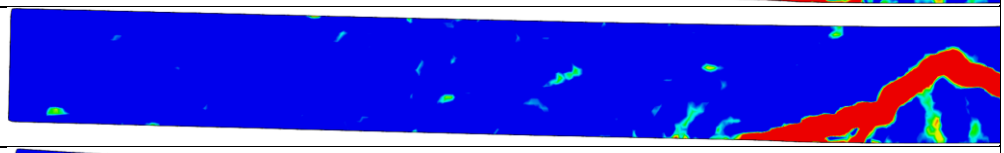
10.4	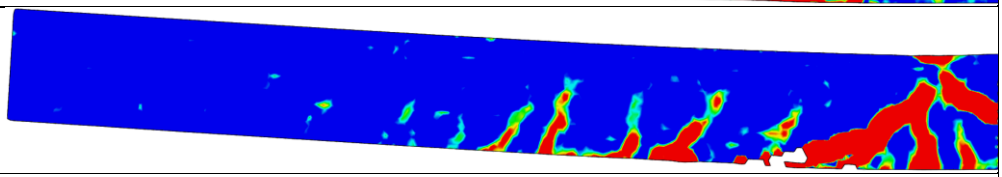
	1 % — 2 %

Table C.12 Strain fields from impact to maximum deformation for beam 21-IS-5m-1FRP-NM.

Time step [ms]	**Strain field**
1 %	**2 %**
0.2	
0.4	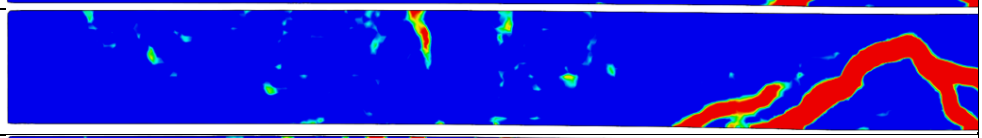
0.6	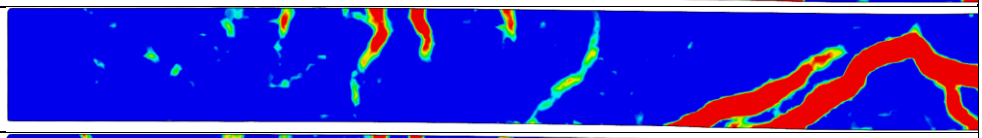
0.8	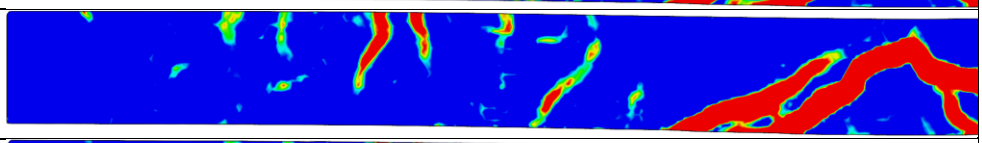
1.0	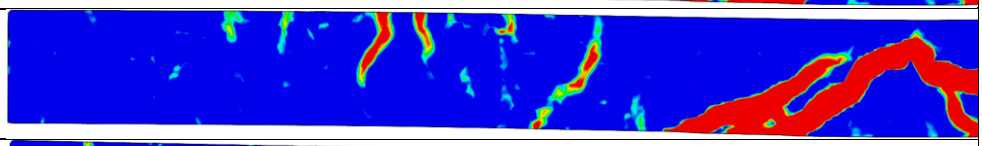
1.6	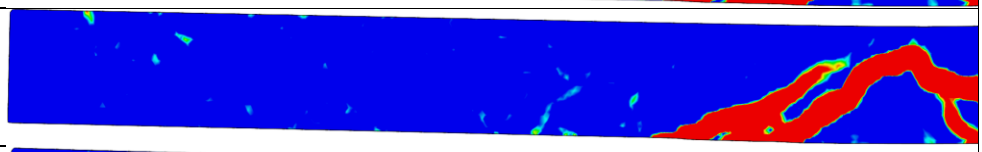
2.0	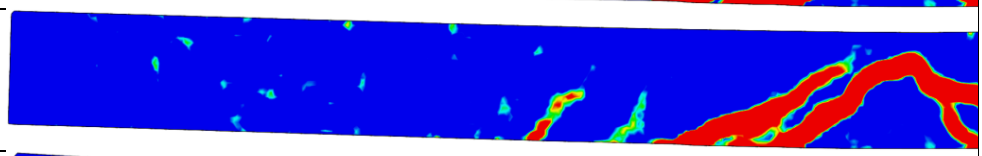
10.8	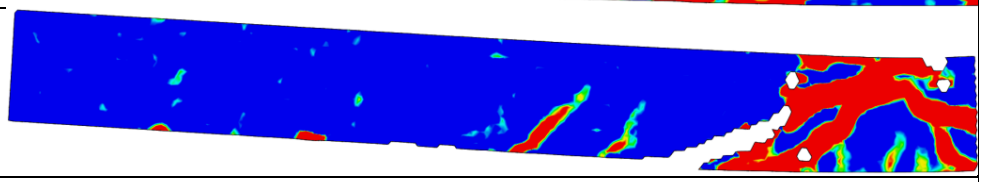
1 %	**2 %**

Table C.13 Strain fields from impact to maximum deformation for beam 22-IS-5m-1FRP-NM.

Time step [ms]	Strain field
	1 % — 2 %
0.2	
0.4	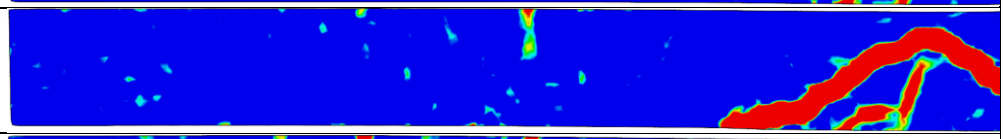
0.6	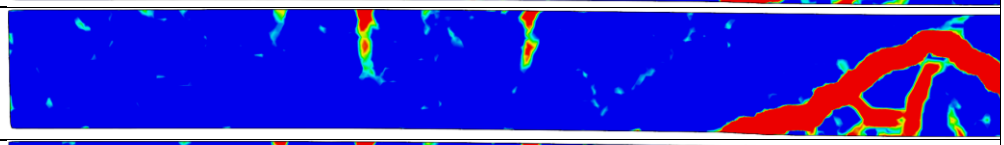
0.8	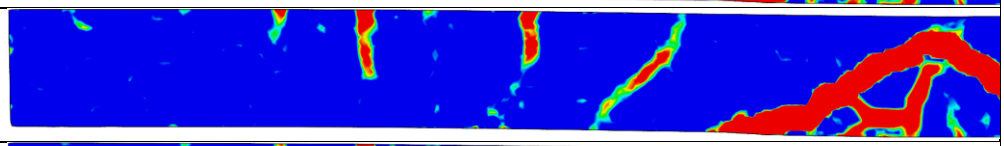
1.0	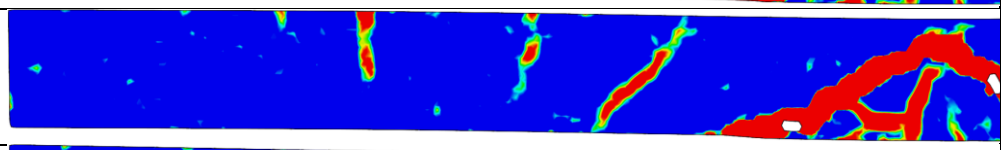
1.6	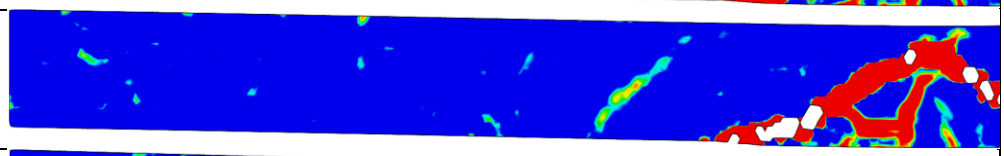
2.0	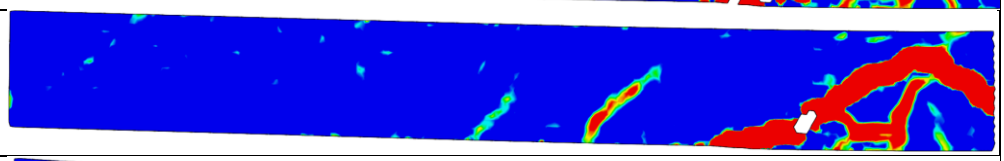
11.0	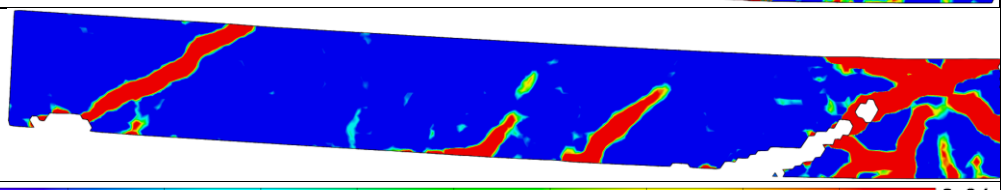
	1 % — 2 %

Table C.14 Strain fields from impact to maximum deformation for beam 18-IS-5.7m-0FRP.

Time step [ms]	Strain field
	1 % — 2 %
0.2	
0.4	
0.6	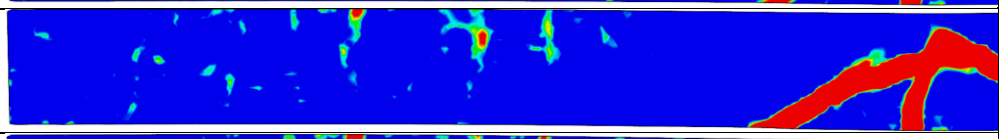
0.8	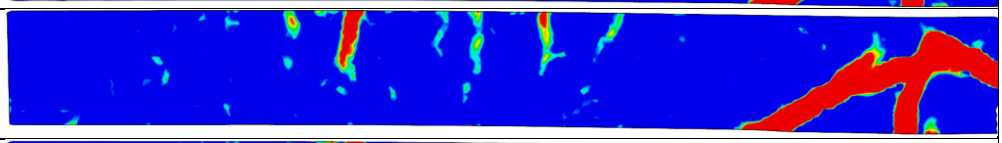
1.0	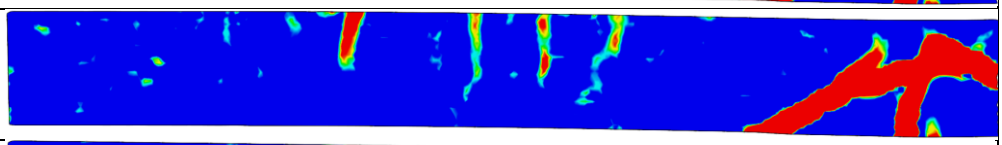
1.6	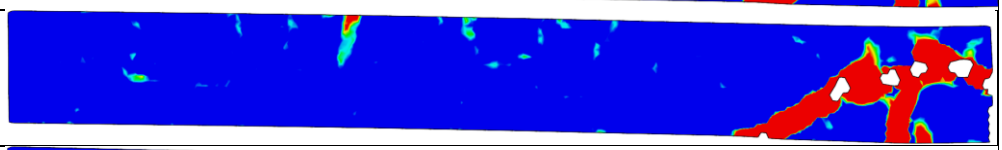
2.0	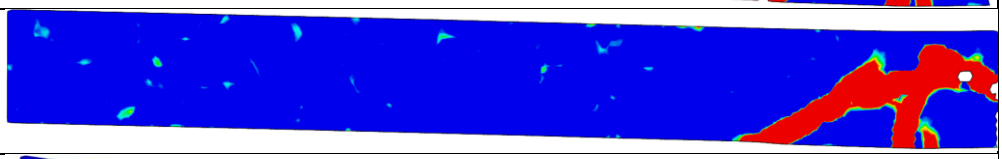
26.2	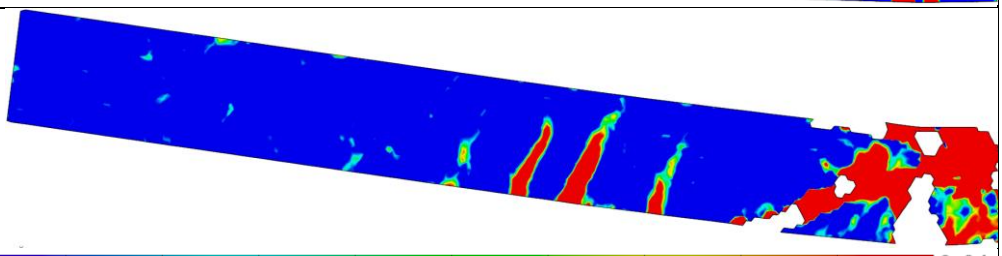
	1 % — 2 %

Table C.15 Strain fields from impact to maximum deformation for beam 09-IS-5.7m-1FRP-S&P.

Time step [ms]	Strain field
	1 % — 2 %
0.2	
0.4	
0.6	
0.8	
1.0	
1.6	
2.0	
11.6	
	1 % — 2 %

Table C.16 Strain fields from impact to maximum deformation for beam 11-IS-5.7m-1FRP-NM.

Time step [ms]	Strain field
	1 % — 2 %
0.2	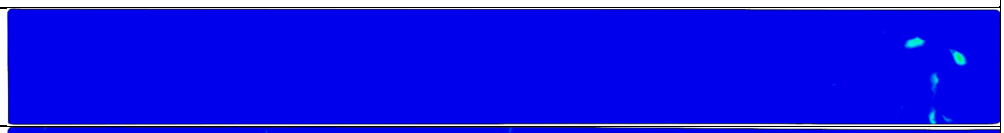
0.4	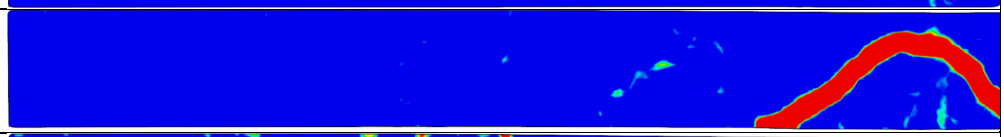
0.6	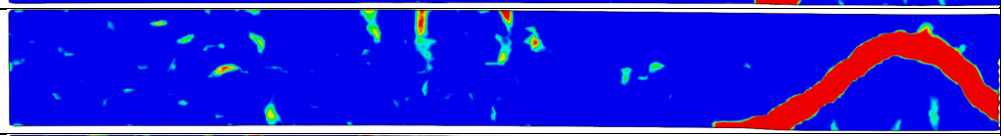
0.8	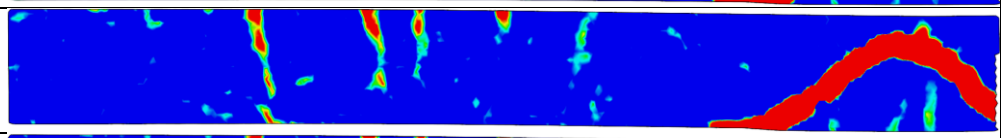
1.0	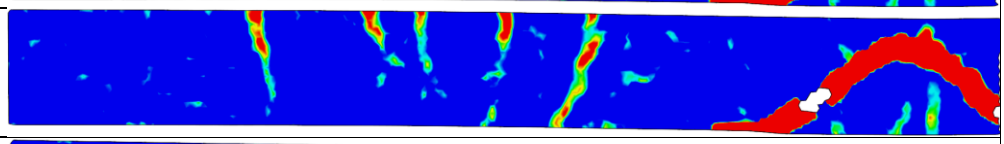
1.6	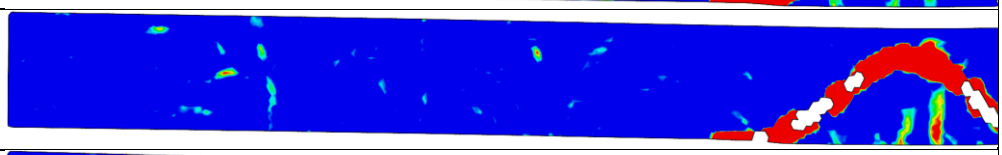
2.0	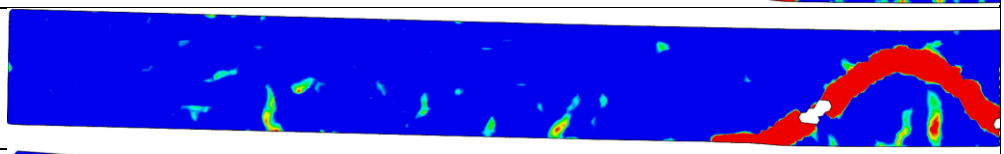
12.2	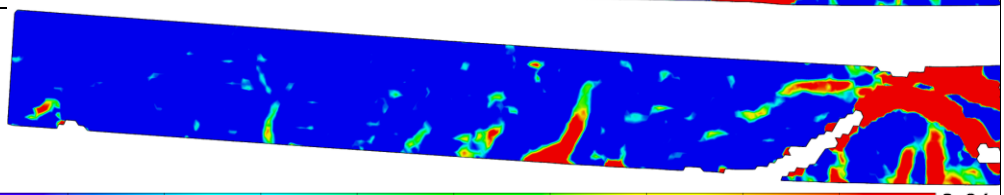
	1 % — 2 %

Appendix D Drop Weight Velocity

In this appendix the graphs with the drop weight velocities are presented that were not treated in the dynamic results section together with the rest of the results for drop weight velocities. The drop weight velocities were extracted from GOM Correlate where three facet points were placed on the drop weight and a mean value from these points were the value used for the acceleration. Both cameras were used to extract the velocities from the different heights where camera 1 being the faster camera with 40 000 FPS and Camera 2 being the less fast with 5 000 FPS. The graphs are presented in an order which is Camera 2, Camera 1 and then a comparison between the two with increasing drop height. This is for the drop heights that are not represented in the dynamic results section. If a graph is presented in the dynamic results section, it is simply removed from the order just stated.

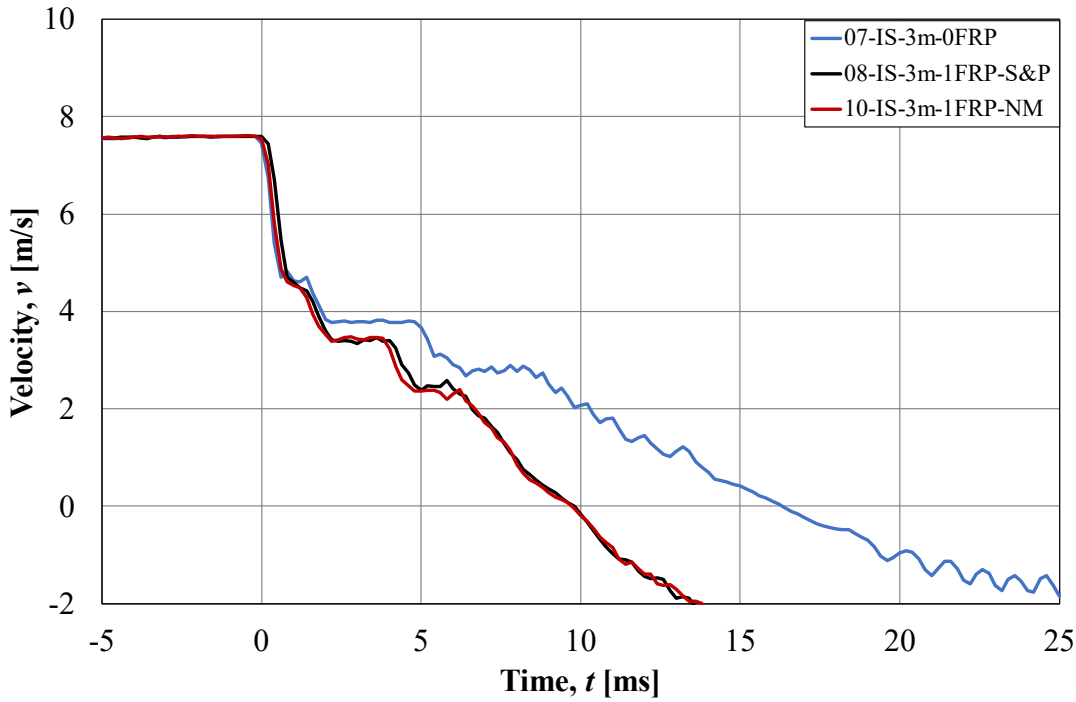

Figure D.1 Velocity of drop weight from a drop height of 3 m from Camera 2.

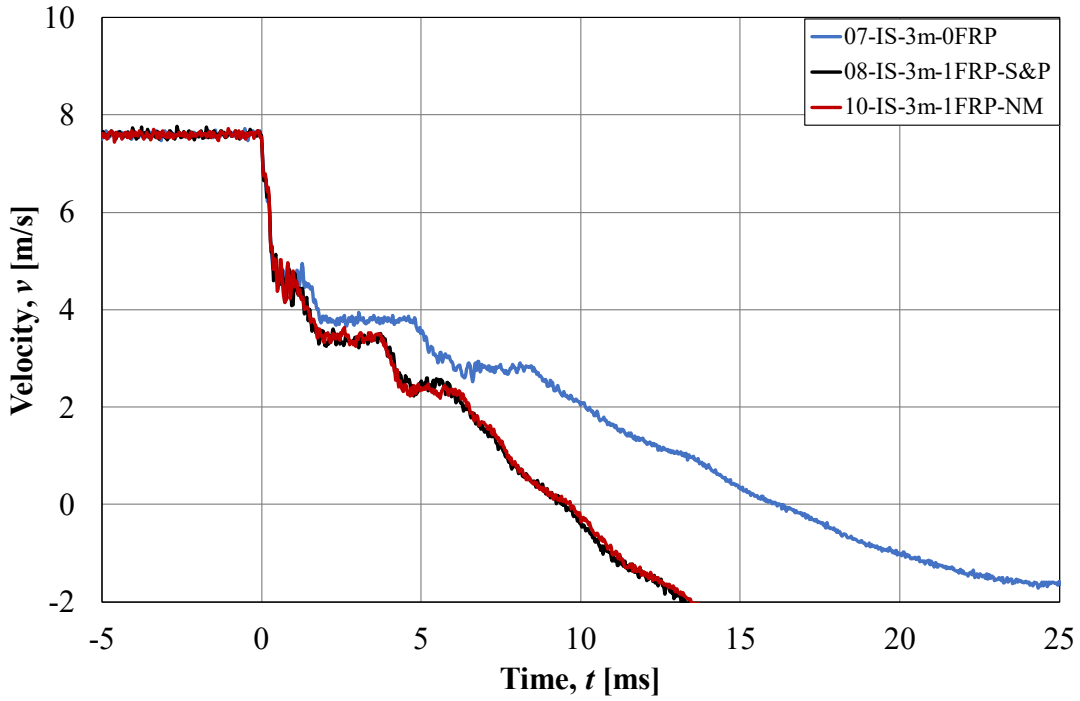

Figure D.2 Velocity of drop weight from a drop height of 3 m from Camera 1.

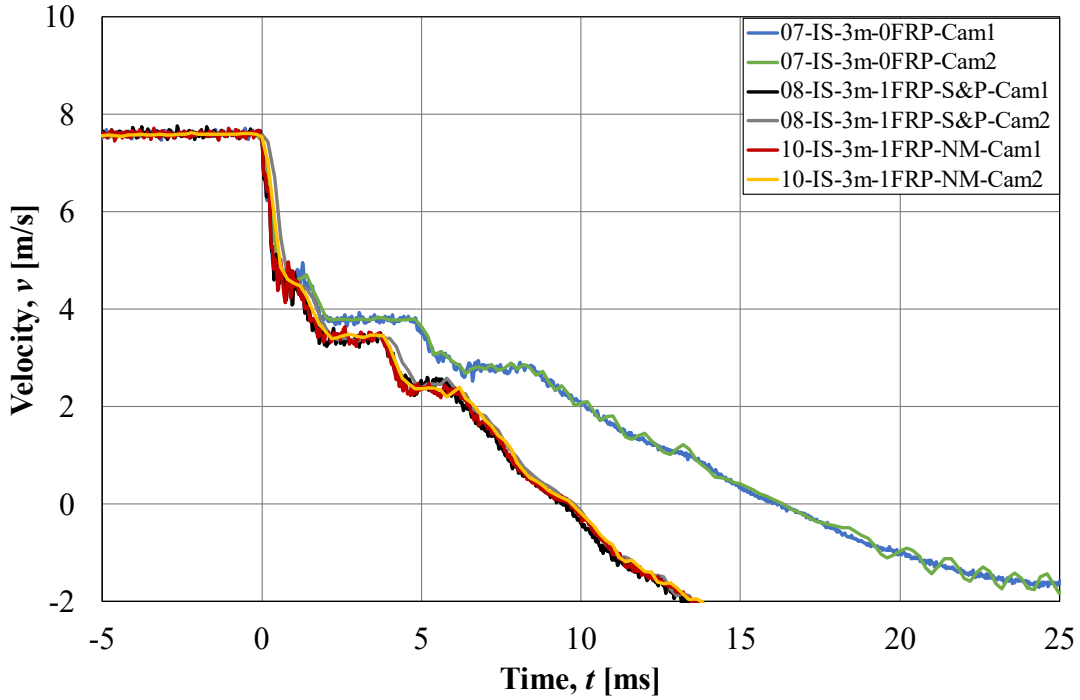

Figure D.3 Comparison of the velocity of the drop weight between the two high speed cameras from a drop height of 3 m.

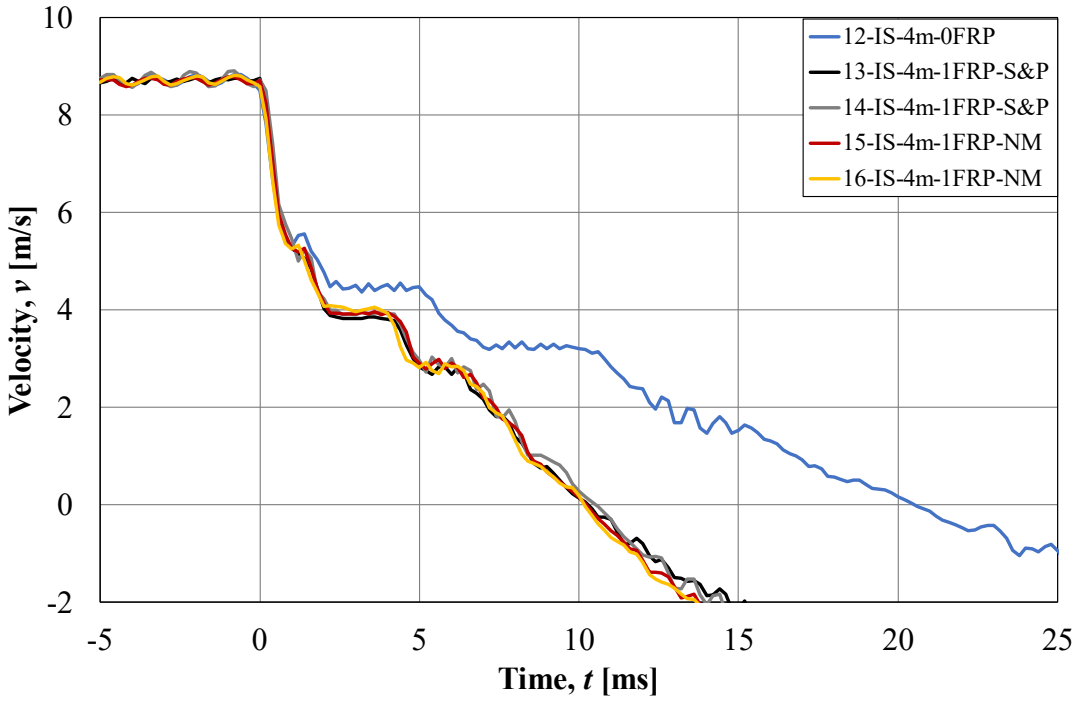

Figure D.4 Velocity of drop weight from a drop height of 4 m from Camera 2.

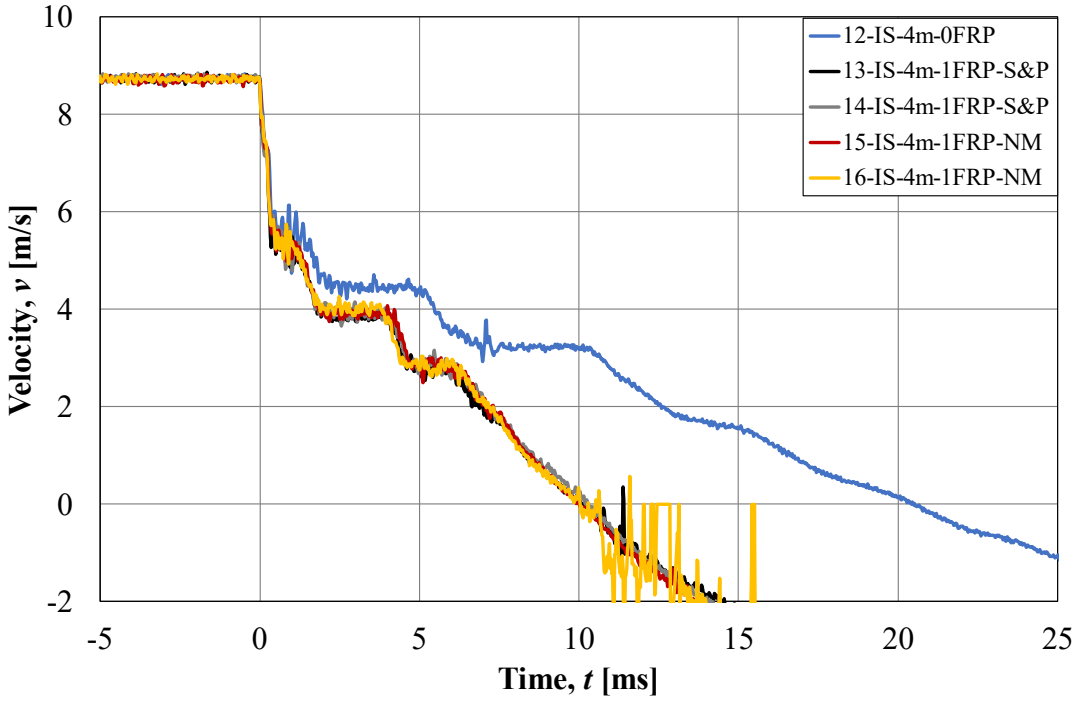

Figure D.5 Velocity of drop weight from a drop height of 4 m from Camera 1.

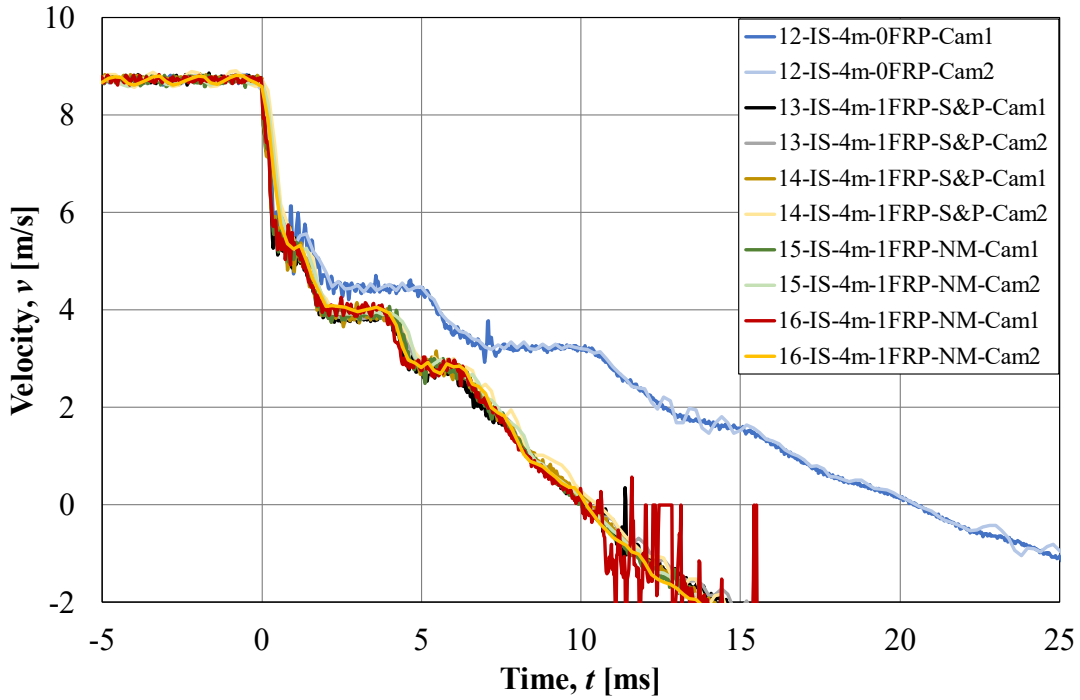

Figure D.6 Comparison of the velocity of the drop weight between the two high speed cameras from a drop height of 4 m.

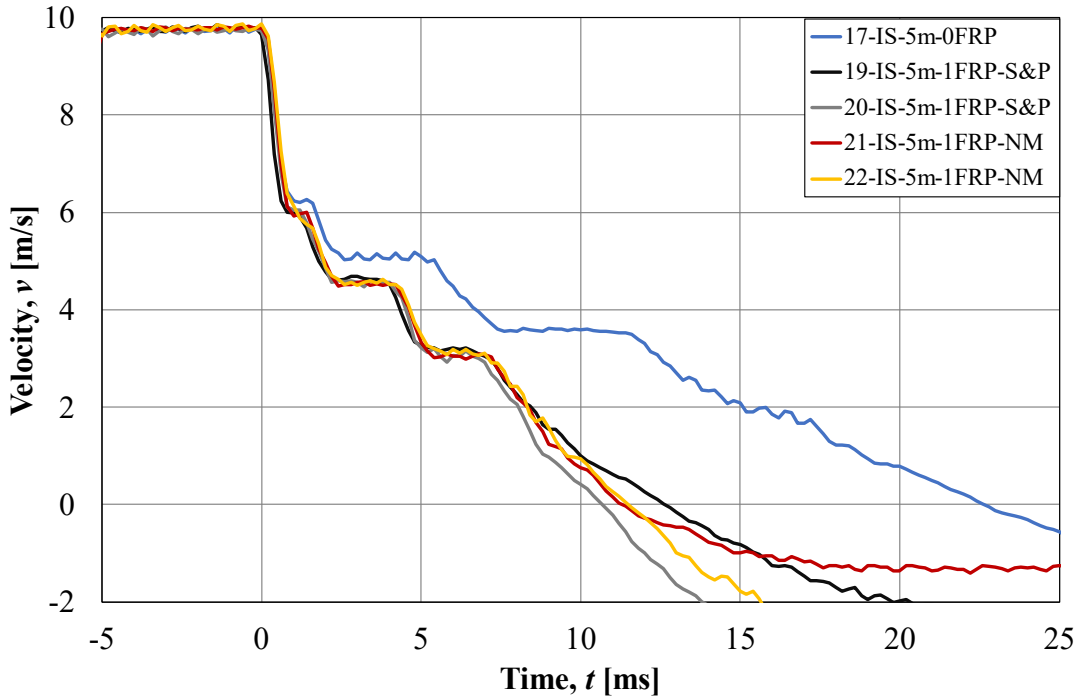

Figure D.7 Velocity of drop weight from a drop height of 5 m from Camera 2.

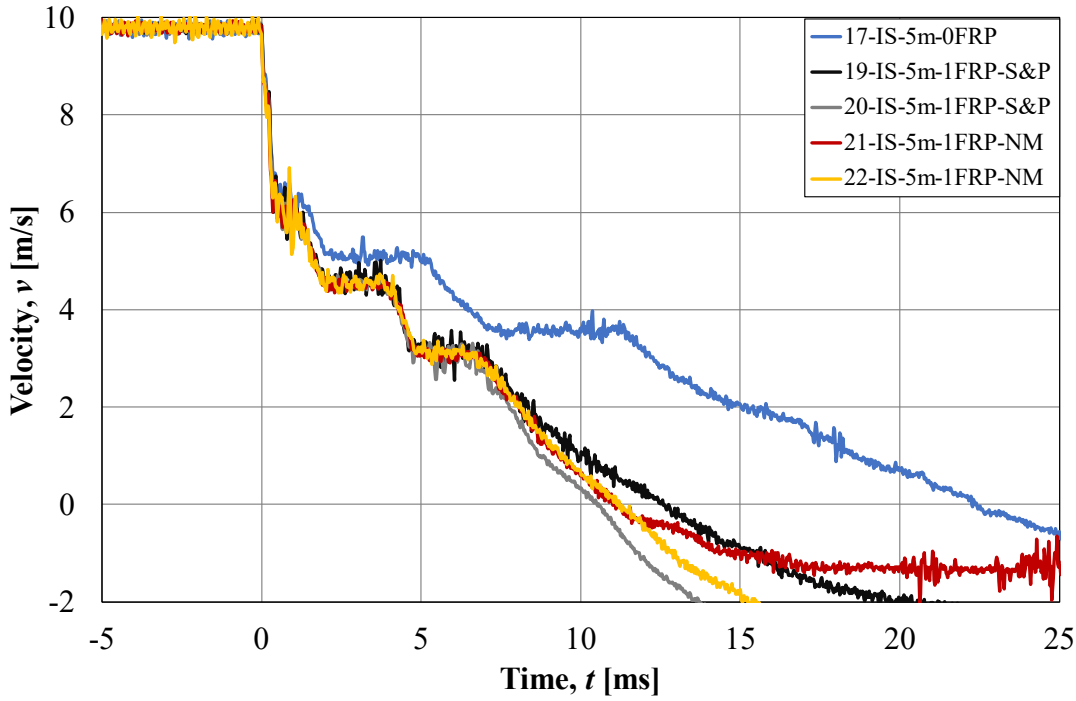

Figure D.8 *Velocity of drop weight from a drop height of 5 m from Camera 1.*

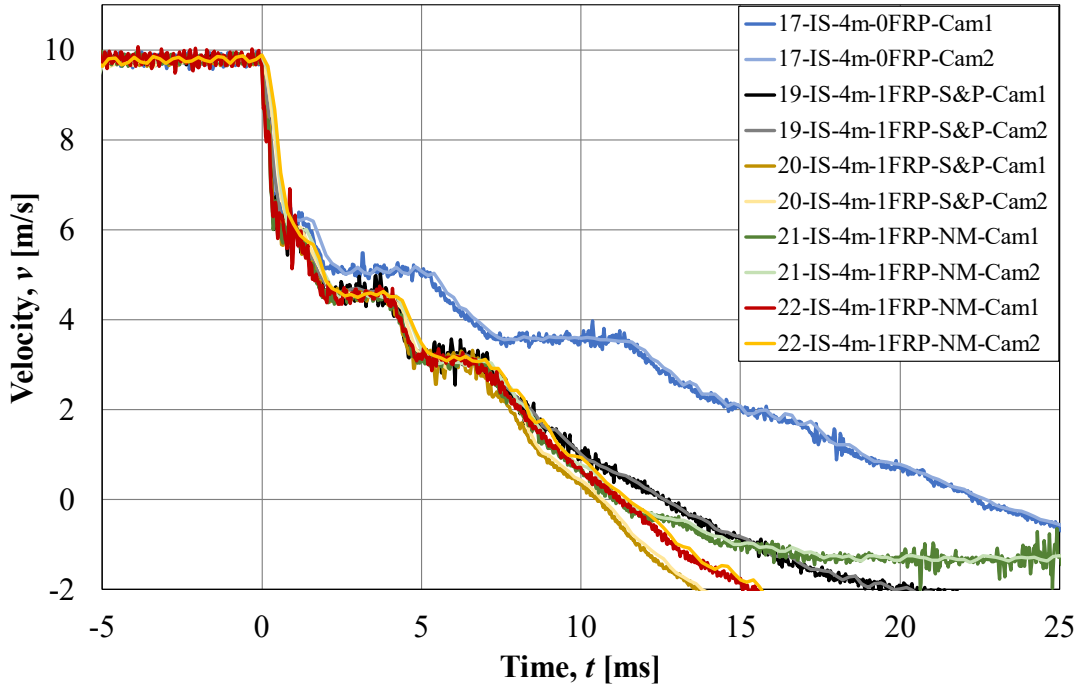

Figure D.9 *Comparison of the velocity of the drop weight between the two high speed cameras from a drop height of 5 m.*

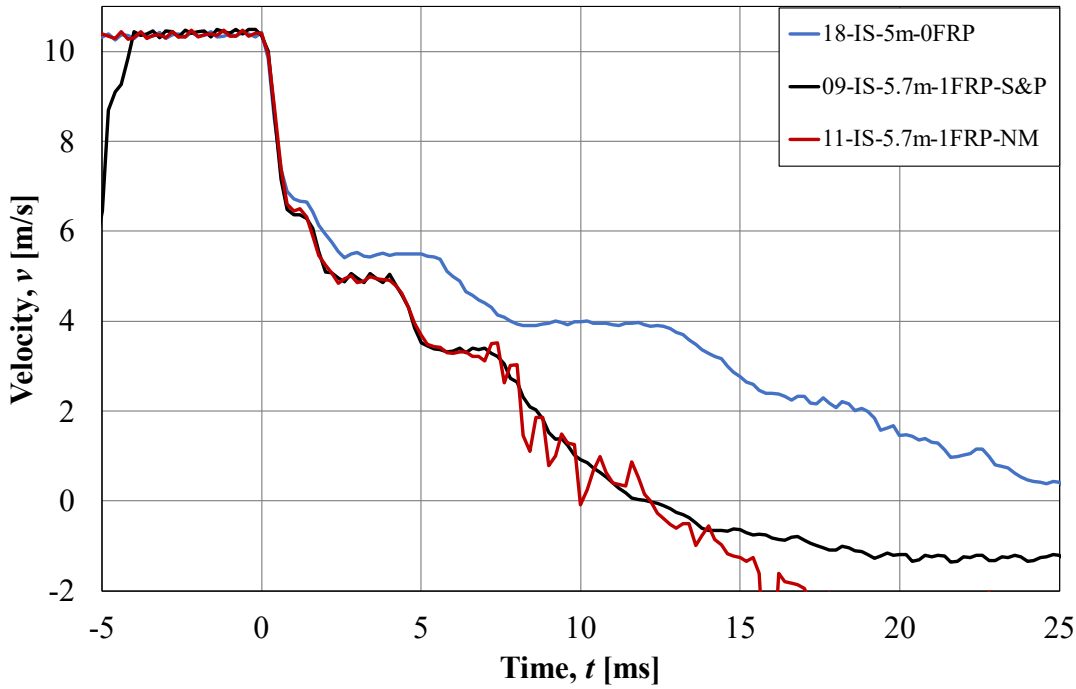

Figure D.10 Velocity of drop weight from a drop height of 5.7 m from Camera 2.

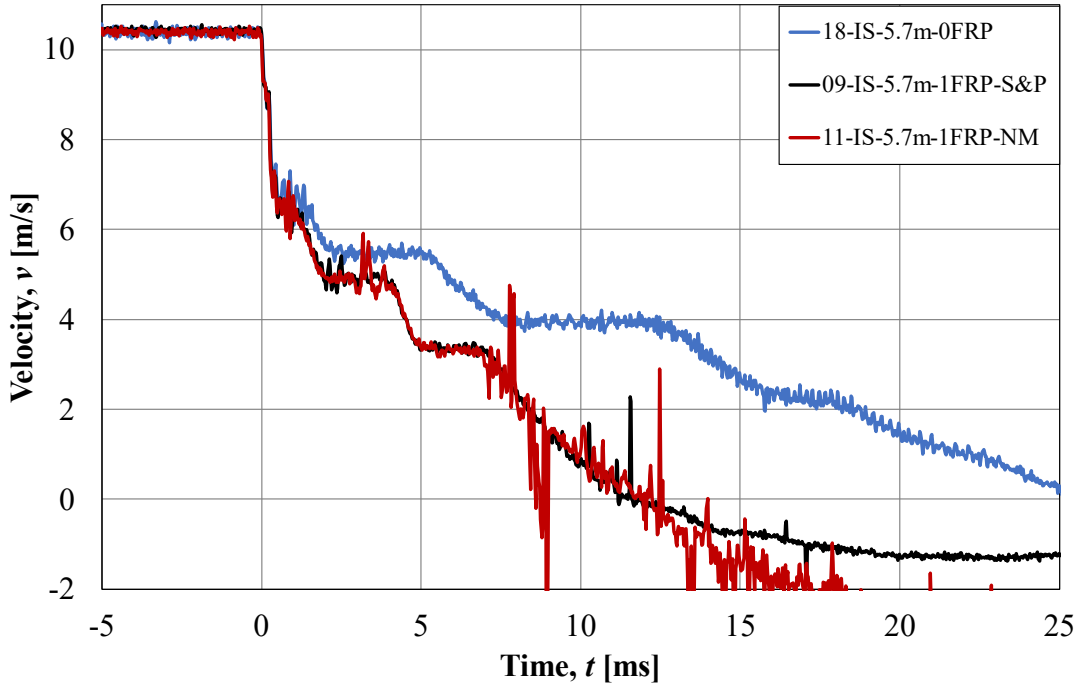

Figure D.11 Velocity of drop weight from a drop height of 5.7 m from Camera 1.

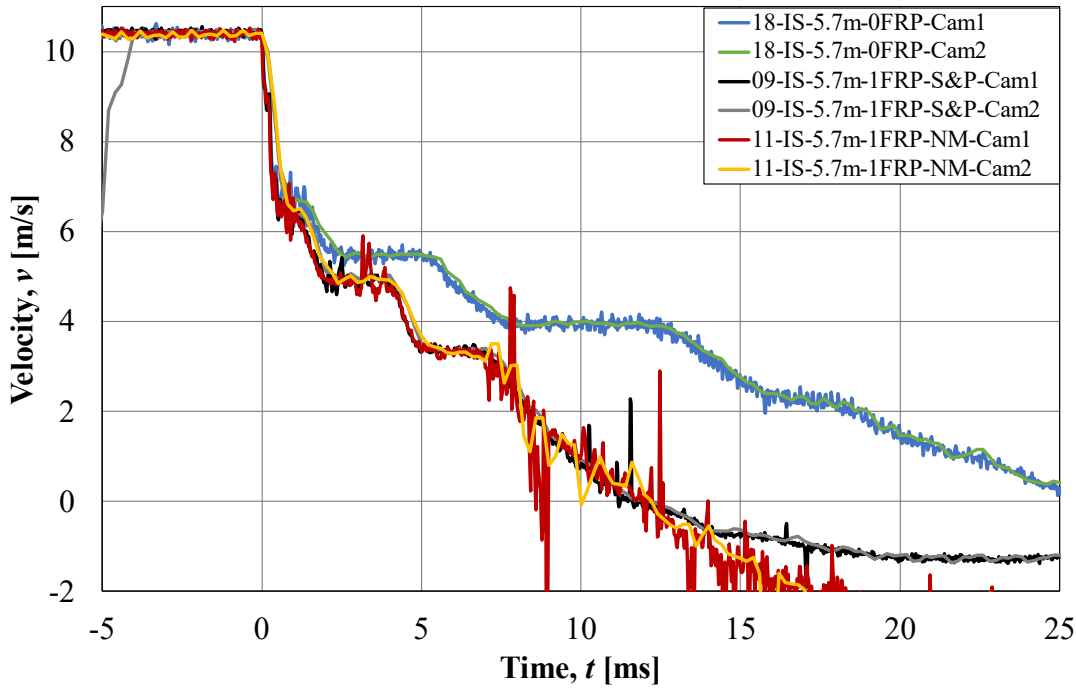

Figure D.12 Comparison of the velocity of the drop weight between the two high speed cameras from a drop height of 5.7 m.

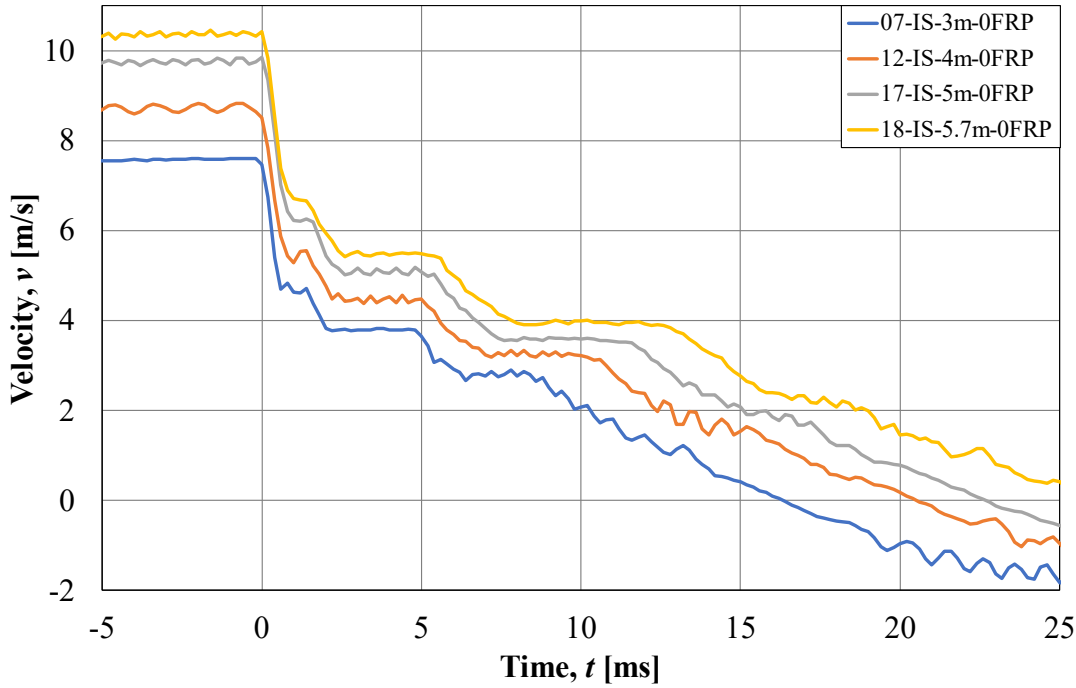

Figure D.13 Velocity of drop weight for unstrengthened beams from Camera 2.

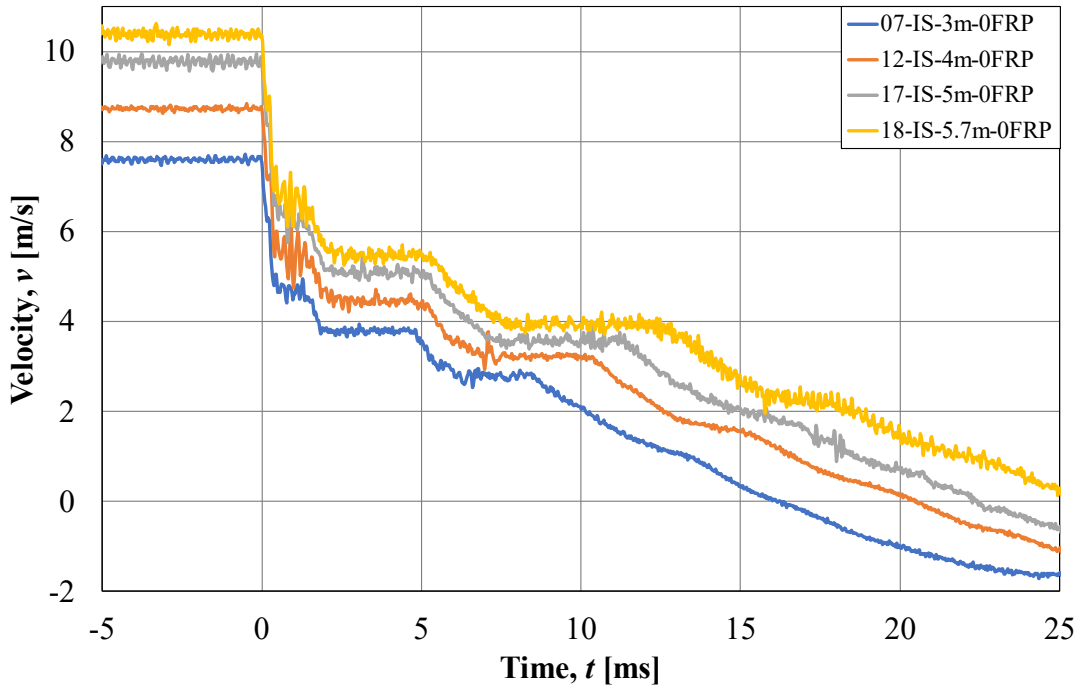

Figure D.14 Velocity of drop weight for unstrengthened beams from Camera 1.

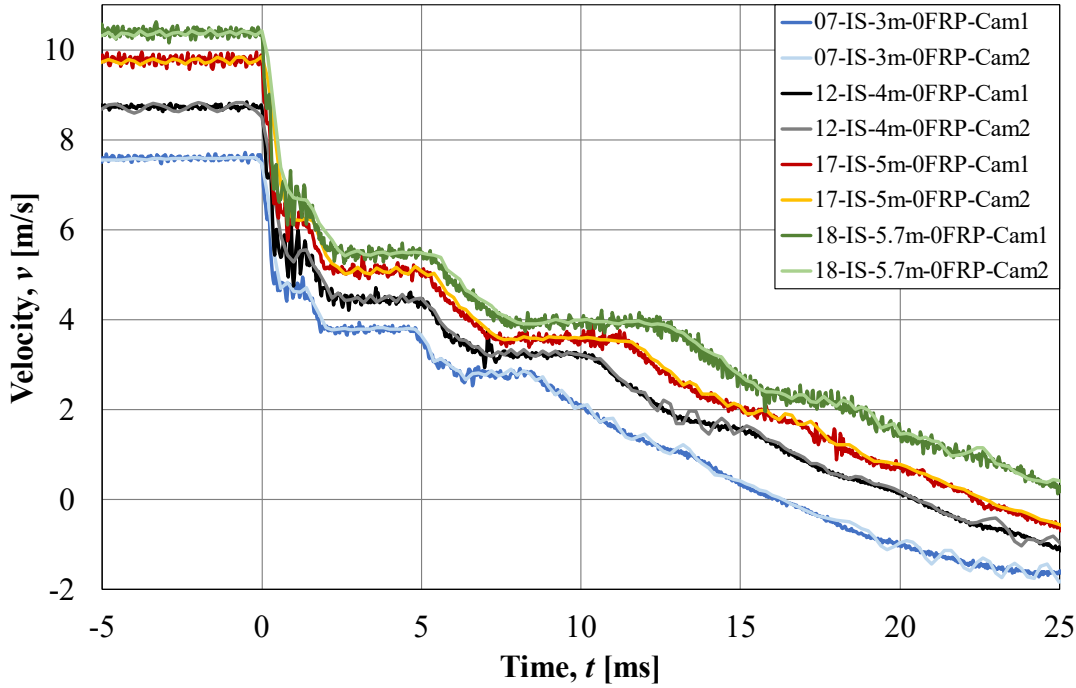

Figure D.15 Comparison of the velocity of the drop weight between the two high speed cameras for unstrengthened beams.

Appendix E Impulse

In this section is the procedure of the calculation of impulse presented. The impact force results presented in Section 10.2.3 from Camera 1 was used where a mean value of three facet points on the drop weight was established and then the acceleration data was post processed with a sliding mean value over nine time steps. The impulse was calculated by calculation of the area under the curve for the impact force in each time step followed by summarizing of the different areas. Jönsson & Stenseke (2018) proposed a procedure where the total impulse was divided into an initial part and one post part which is similar to the procedure done within this project. Their procedure is schematically illustrated in Figure E.1.

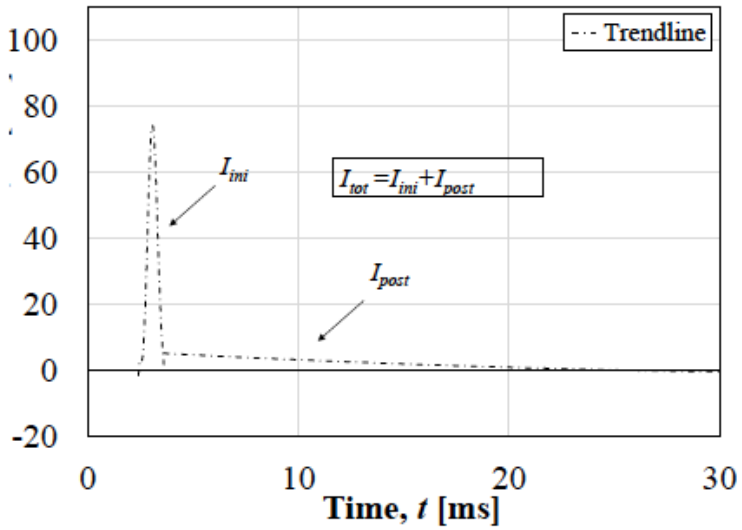

Figure E.1 *Illustration of impulse with one initial part and one post part (Jönsson & Stenseke, 2018).*

The initial part represented the peak with maximum impact force and the post part represented the impulse after the initial impulse until impulse equal to zero. Figure E.1 just present the concept with one initial part and one post part, the calculated impulse was based on the actual results from impact force and was not simplified to two triangles as illustrated in Figure E.1. The initial peak was calculated between 0.4 ms before maximum impact force and 0.5 ms after the maximum impact force. The post part was calculated from 0.5 ms after maximum impact force until the impulse was zero or close to zero, concluded to be at 22.5 ms. All values of impulse were considered when the total impulse was calculated even if a negative impulse could be confusing, but it was in order to reduce the effect of noise. The same procedure was done for all beams. Later was the development of the impulse presented by plotting the sum of the total impulse together with impact force versus time in the same figure as presented in Figure E.2.

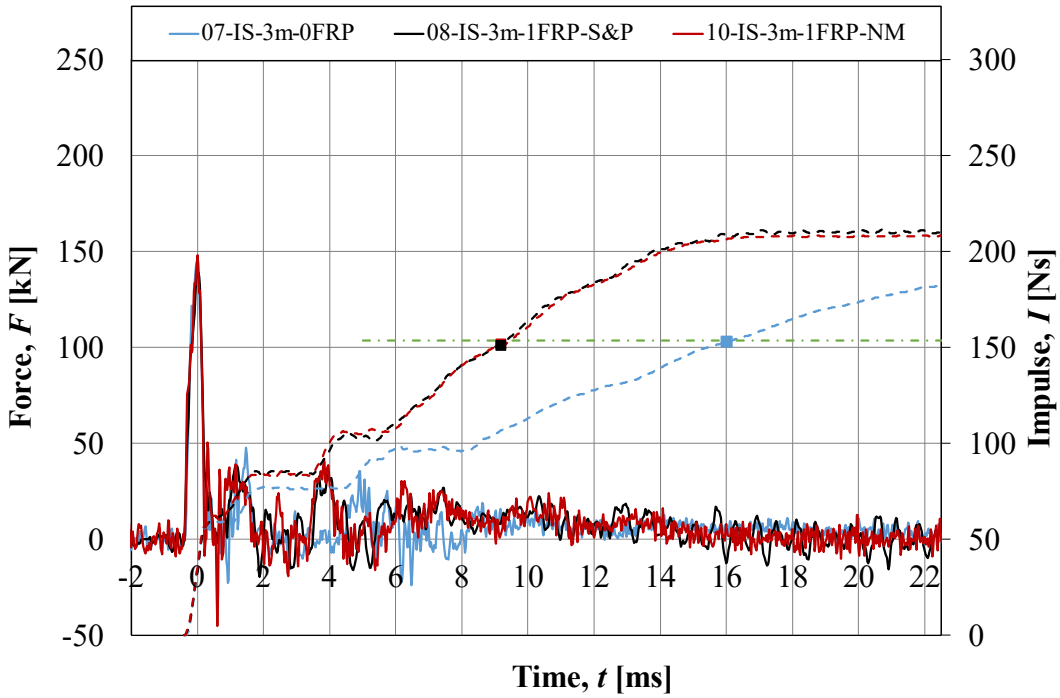

Figure E.2 Total impulse together with the impact force versus time.

Appendix F Beam Damages

All beams weight was registered both before and after the dynamic and static testing to be able to measure how much material damages the beams experienced during the different tests. The results are presented in Table F.1.

Table F.1 Summary of beam damages during the experimental tests.

Test beam	Weight before testing [kg]	Weight after dynamic testing [kg]	Weight loss after dynamic testing [g]	Weight after static testing [kg]	Total weight loss [kg]
01-S-0FRP	34.04	-	-	33.98	0.060
02-S-0FRP	34.30	-	-	34.28	0.020
03-S-1FRP-S&P	34.34	-	-	33.86	0.480
04-S-1FRP-S&P	34.54	-	-	34.20	0.340
05-S-1FRP-NM	33.84	-	-	33.44	0.400
06-S-1FRP-NM	34.66	-	-	34.42	0.240
07-IS-3m-0FRP	34.28	34.22	60	34.16	0.120
08-IS-3m-1FRP-S&P	34.10	34.08	20	33.76	0.340
10-IS-3m-1FRP-NM	34.28	34.28	0	33.94	0.340
12-IS-4m-0FRP	34.04	33.96	80	33.86	0.180
13-IS-4m-1FRP-S&P	34.18	34.06	120	33.62	0.560
14-IS-4m-1FRP-S&P	34.16	34.14	20	33.68	0.480

Test beam	Weight before testing [kg]	Weight after dynamic testing [kg]	Weight loss after dynamic testing [g]	Weight after static testing [kg]	Total weight loss [kg]
15-IS-4m-1FRP-NM	34.16	34.14	20	33.58	0.580
16-IS-4m-1FRP-NM	34.30	34.30	0	32.96	1.340
17-IS-5m-0FRP	34.06	33.72	340	33.44	0.620
19-IS-5m-1FRP-S&P	34.36	33.88	480	33.56	0.800
20-IS-5m-1FRP-S&P	34.14	34.12	20	33.48	0.660
21-IS-5m-1FRP-NM	34.70	33.94	760	33.38	1.320
22-IS-5m-1FRP-NM	34.66	34.52	140	34.16	0.500
18-IS-5.7m-0FRP	33.92	31.88	2040	31.4	2.520
09-IS-5.7m-1FRP-S&P	34.38	33.52	860	33.28	1.100
11-IS-5.7m-1FRP-NM	34.70	33.64	1060	32.50	2.200
Mean 0FRP	**34.11**	**33.45**	**630**	**33.52**	**0.587**
Mean 1FRP	**34.34**	**34.05**	**292**	**33.61**	**0.730**
Mean	**34.28**	**33.90**	**376**	**33.59**	**0.691**
Mean 3m 0FRP	**34.28**	**34.22**	**60**	**34.16**	**0.120**

Test beam	Weight before testing [kg]	Weight after dynamic testing [kg]	Weight loss after dynamic testing [g]	Weight after static testing [kg]	Total weight loss [kg]
Mean 3m 1FRP	**34.19**	**34.18**	**10**	**33.85**	**0.340**
Mean 4m 0FRP	**34.04**	**33.96**	**80**	**33.86**	**0.180**
Mean 4m 1FRP	**34.20**	**34.16**	**40**	**33.46**	**0.740**
Mean 5m 0FRP	**34.06**	**33.72**	**340**	**33.44**	**0.620**
Mean 5m 1FRP	**34.47**	**34.12**	**350**	**33.65**	**0.820**
Mean 5.7m 0FRP	**33.92**	**31.88**	**2040**	**31.40**	**2.520**
Mean 5.7m 1FRP	**34.54**	**33.58**	**960**	**32.89**	**1.650**

As can be seen in Table F.1, the total weight loss increased with increasing height. For 3 and 4 m, the difference between unstrengthened and FRP strengthened was large, where the FRP strengthened beam lost less more material at the drop weight impact. The total weight loss on the other hand was larger for the FRP strengthened beams. At 5 m was the weight loss due to drop weight impact similar for the unstrengthened beam and the FRP strengthened beams. The total weight loss at 5 m was larger for the FRP strengthened beams than the unstrengthened one though. At 5.7 m did the drop weight impact cause so large damages though so that the unstrengthened beam lost more than twice as much as the FRP strengthened beams. The total weight loss at 5.7 m was also different compared to the other heights where the unstrengthened beam lost more than the FRP strengthened beams due to the large weight loss at the drop weight impact. If the weight loss during the static test is studied the FRP strengthened beams lost more material than the unstrengthened.

Appendix G Results from Material Tests of Reinforcement

The stress versus strain relationships for the material tests of reinforcement bars are presented in Figure G.1.

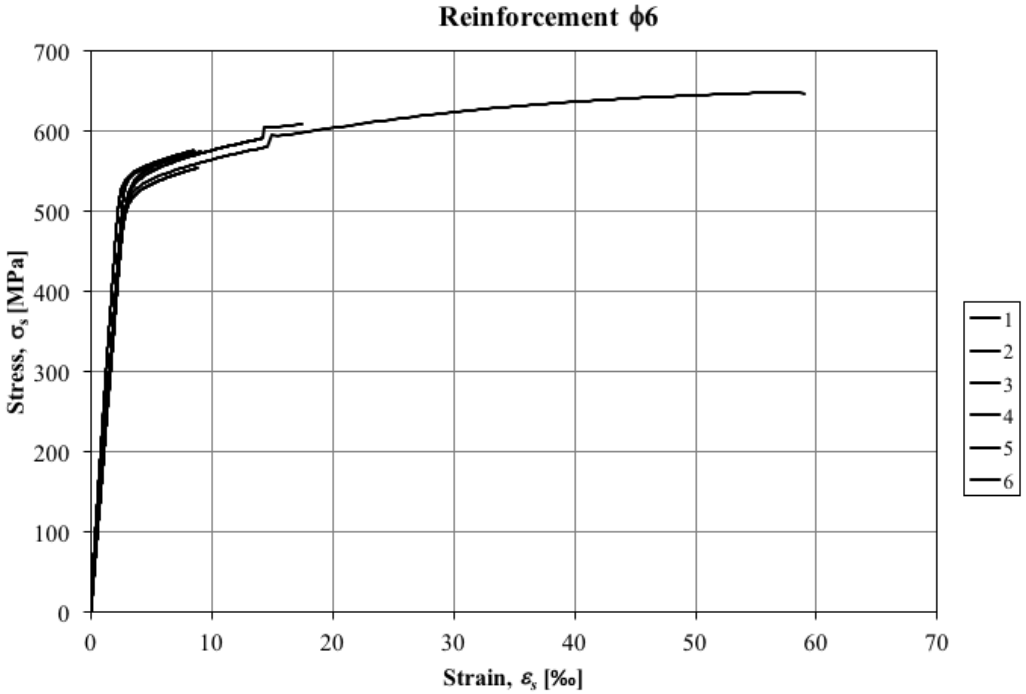

Figure G.1 Stress versus strain relationship for tested reinforcement bars.

Appendix H Strain Fields Static

In this appendix are the strain fields for all beams either only statically loaded or both subjected to a drop weight impact followed by static loading presented. Strain fields at maximum load and deformation is presented in Table H.1 and Table H.2 followed by strain fields before and after debonding for the beams where debonding did not occur at the dynamic tests but at the static tests in Table H.3. In some exceptional cases did debonding of the FRP never take place so they are not presented here. When debonding of FRP occurred in several sequences strain fields before and after each partial debonding is presented.

Table H.1 Strain fields at maximum load and maximum deformation for beams only statically loaded.

0.2 % — 3.0 %	
01-S-0FRP F_{max}= 10.2 kN u_{max}= 58 mm	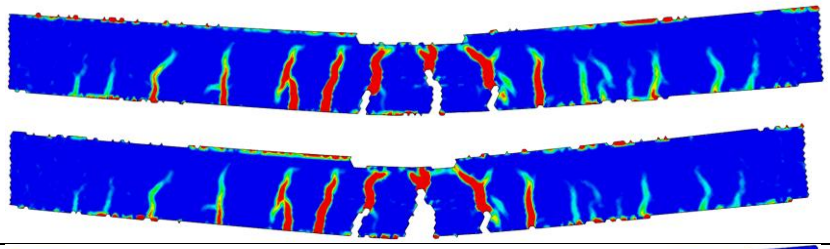
02-S-0FRP F_{max}= 10.5 kN u_{max}= 58 mm	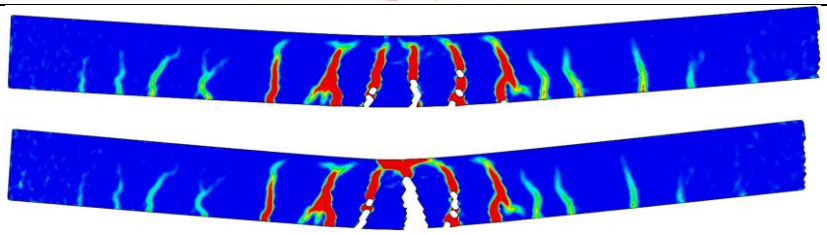
03-S-1FRP-S&P F_{max}= 20.1 kN u_{max}= 99 mm	This image, sought to illustrate the strain field at maximum force, was not able to be captured in GOM Correlate due to intense sunlight. 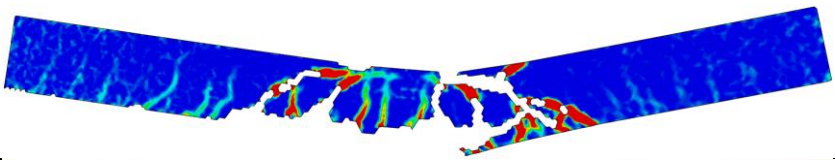
04-S-1FRP-S&P F_{max}= 20.3 kN u_{max}= 99 mm	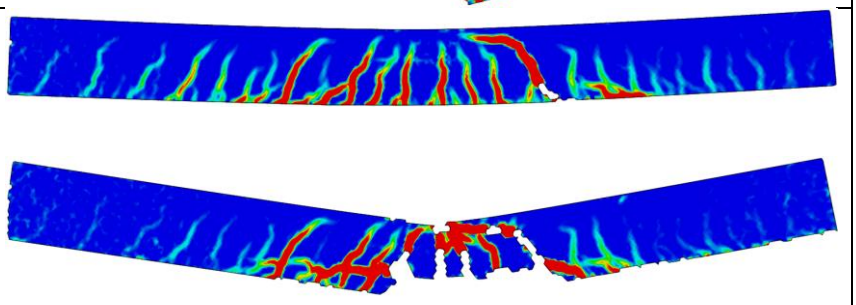
05-S-1FRP-NM F_{max}= 18.6 kN	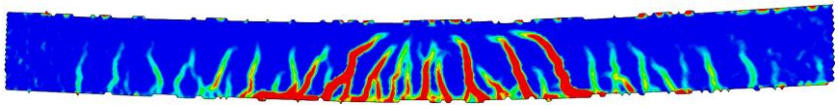

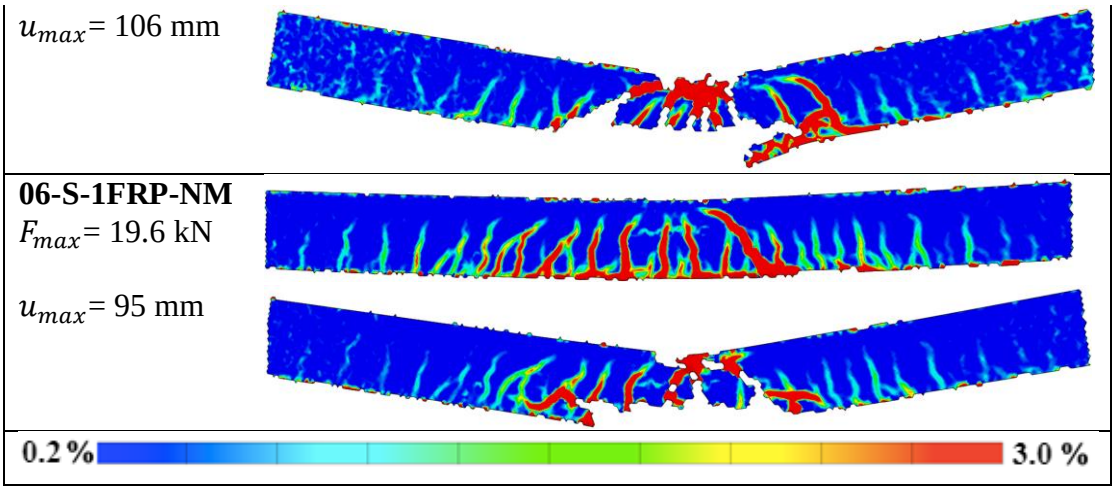

Table H.2 *Strain fields at maximum load and maximum deformation for beams subjected to a drop weight followed by static loading.*

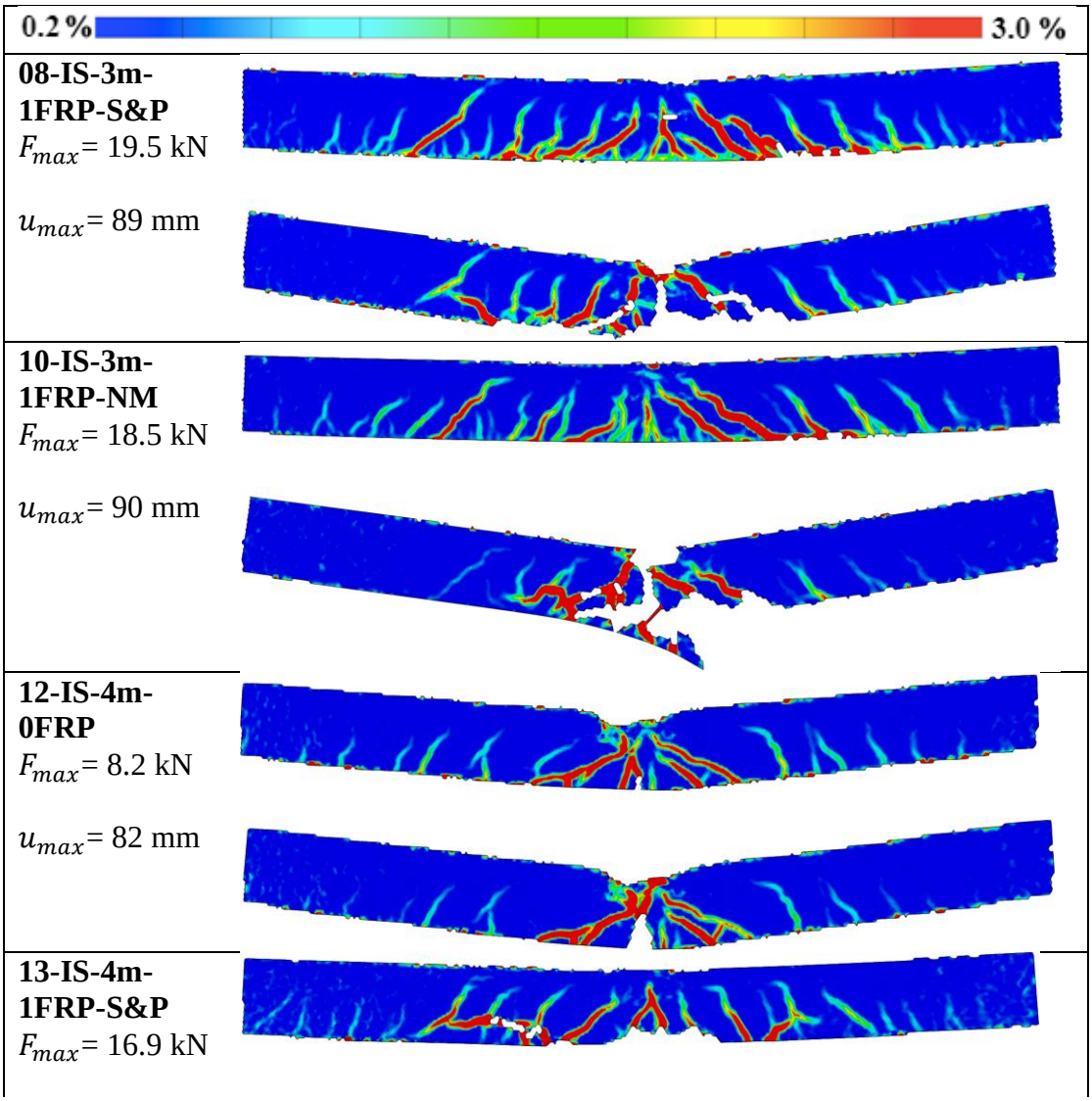

u_{max}= 87 mm	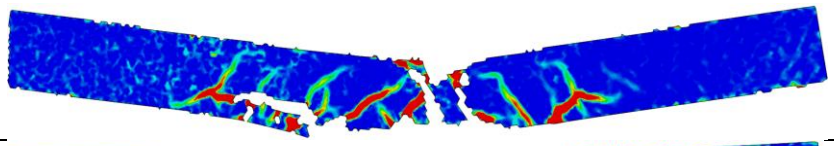
14-IS-4m-1FRP-S&P F_{max}= 17.2 kN u_{max}= 99 mm	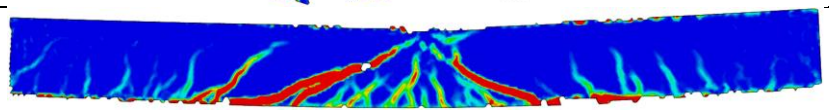 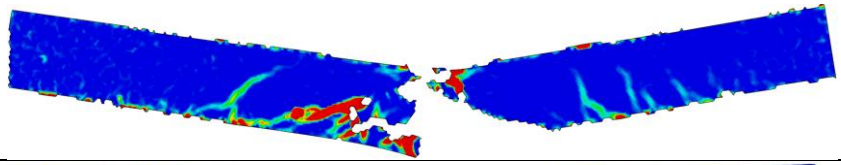
15-IS-4m-1FRP-NM F_{max}= 17.4 kN u_{max}= 90 mm	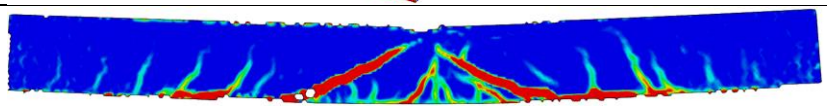 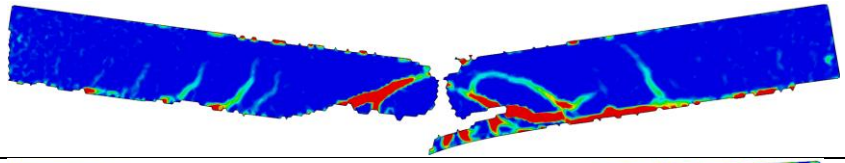
16-IS-4m-1FRP-NM F_{max}= 18.8 kN Between max. force and max. deformation. u_{max}= 95 mm	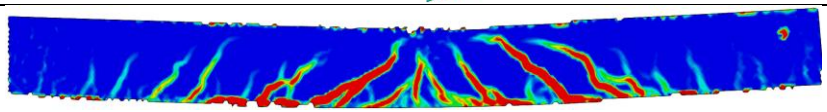 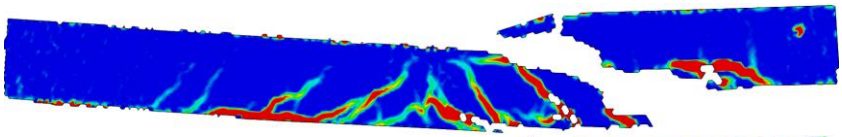 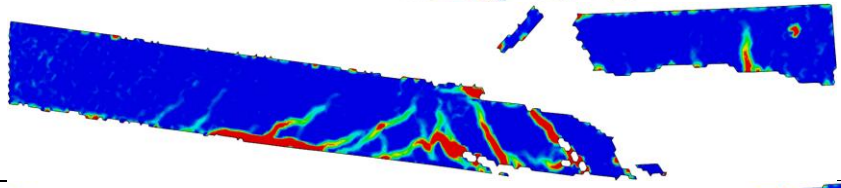
17-IS-5m-0FRP F_{max}= 7.9 kN u_{max}= 93 mm	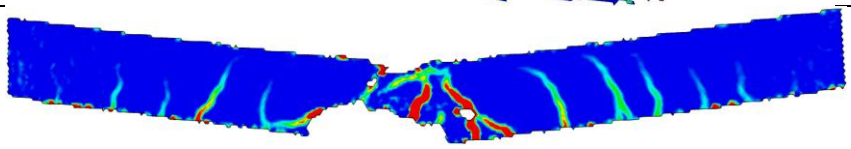 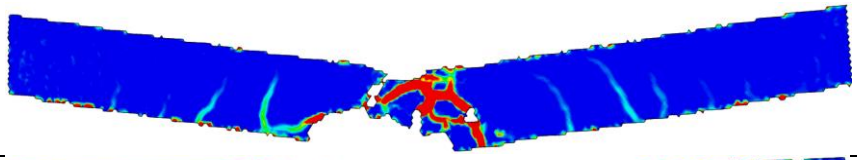
19-IS-5m-1FRP-S&P F_{max}= 5.1 kN u_{max}= 53 mm	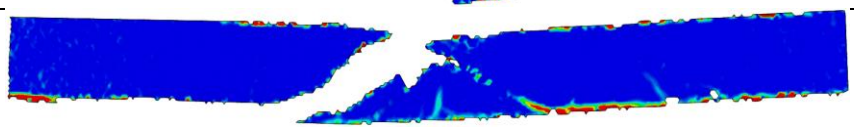 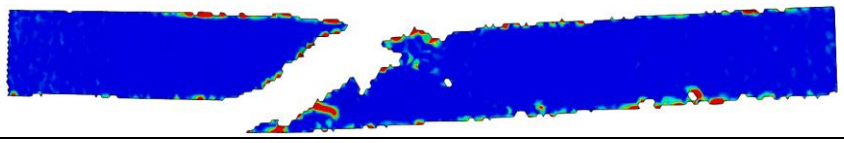

20-IS-5m-1FRP-S&P F_{max}= 18.1 kN u_{max}= 97 mm	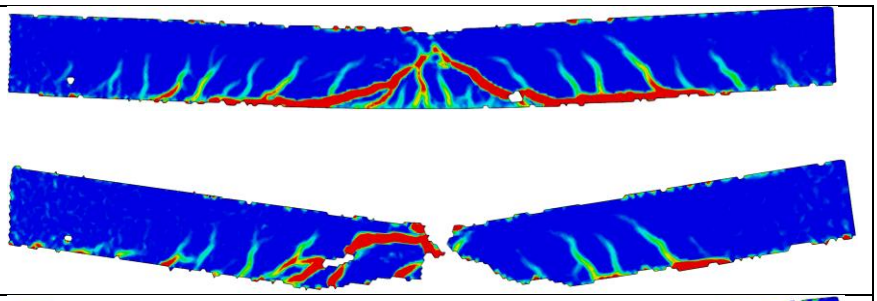
21-IS-5m-1FRP-NM F_{max}= 8.0 kN u_{max}= 100 mm	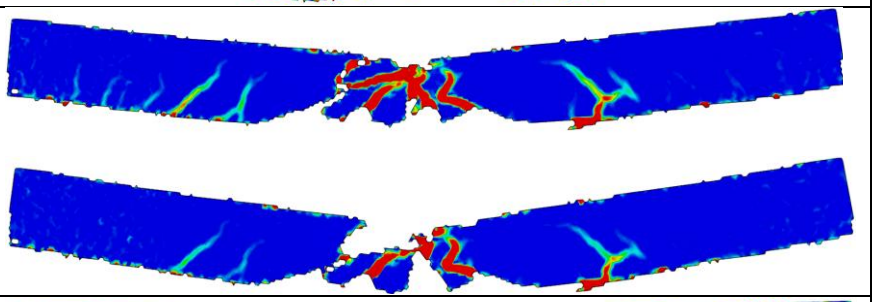
22-IS-5m-1FRP-NM F_{max}= 10 kN u_{max}= 95 mm	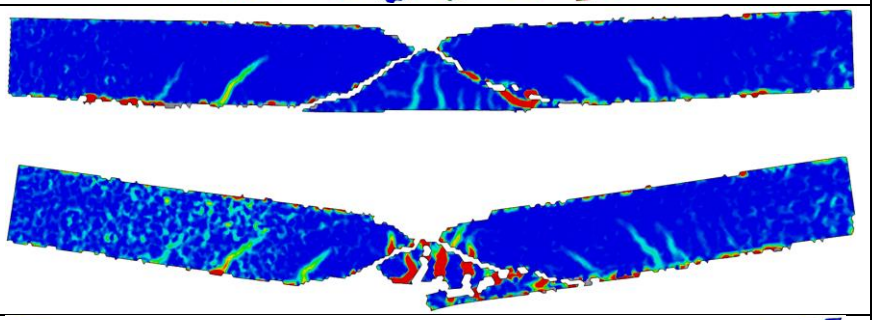
18-IS-5.7m-0FRP F_{max}= 4.7 kN u_{max}= 120 mm	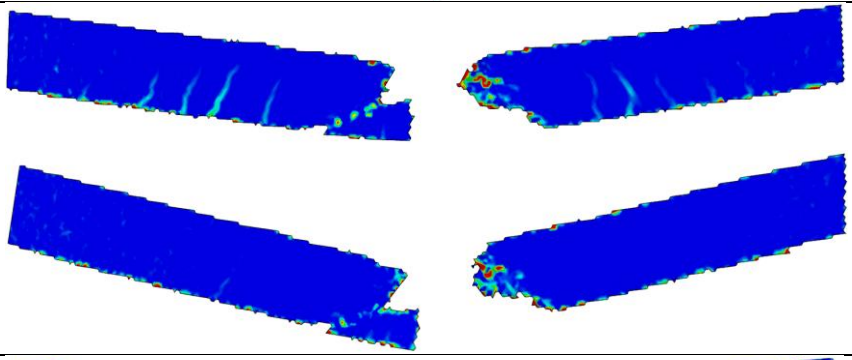
09-IS-5.7m-1FRP-S&P F_{max}= 8.2 kN u_{max}= 89 mm	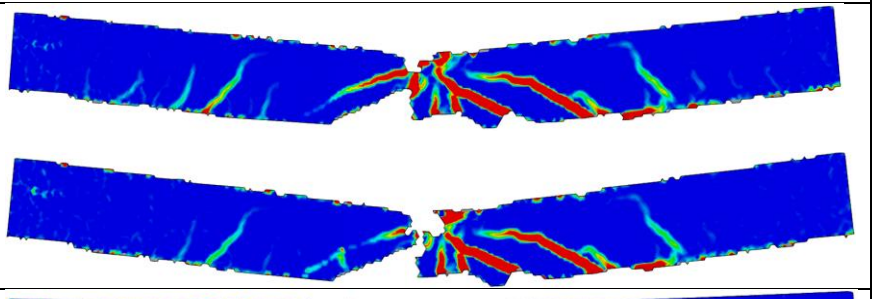
11-IS-5.7m-1FRP-NM F_{max}= 4.9 kN u_{max}= 106 mm	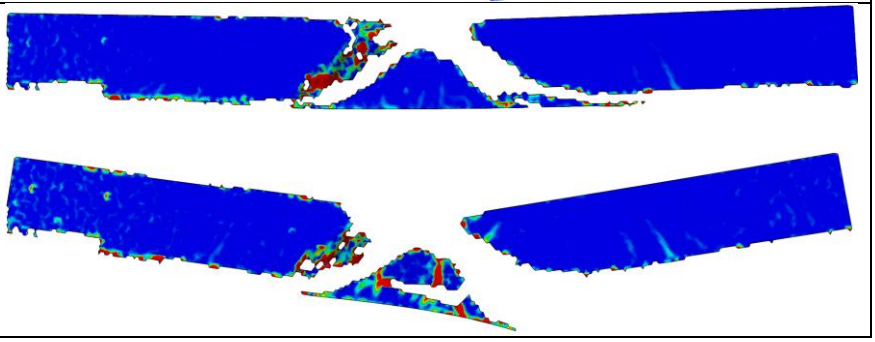

Table H.3 Strain fields before and after debonding of FRP.

0.2 % 3.0 %	
08-IS-3m-1FRP-S&P Before debonding	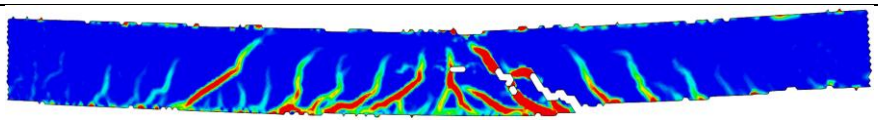
After debonding	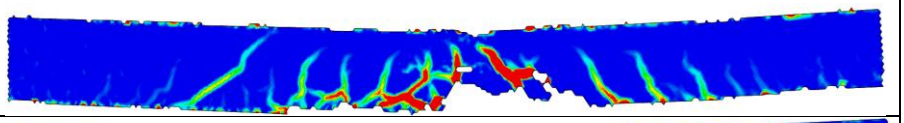
10-IS-3m-1FRP-NM Before first debonding	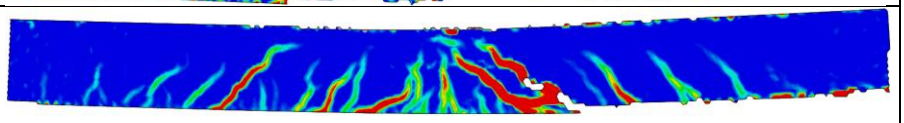
After first debonding	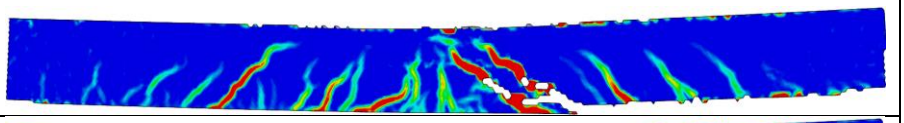
Before second debonding	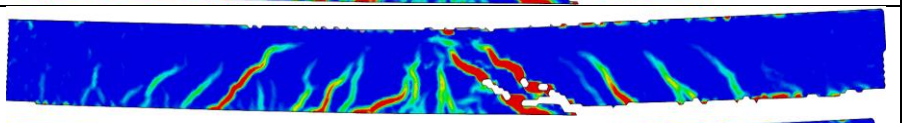
After second debonding	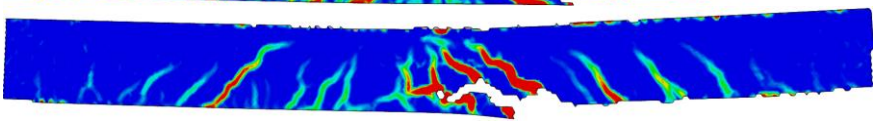
Before third debonding	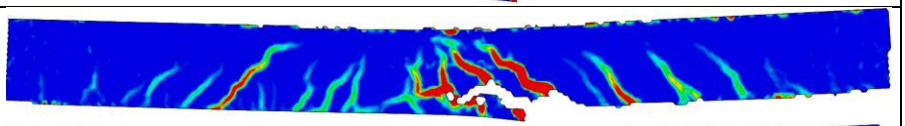
After third debonding	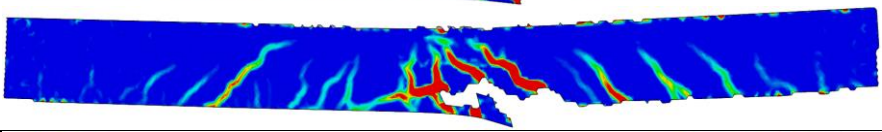
20-IS-5m-1FRP-S&P Before debonding	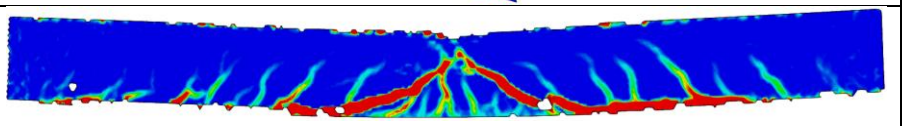
After debonding	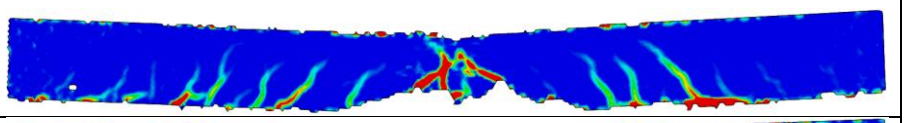
22-IS-5m-1FRP-NM Before debonding	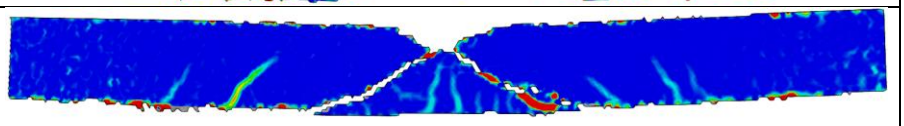
After debonding	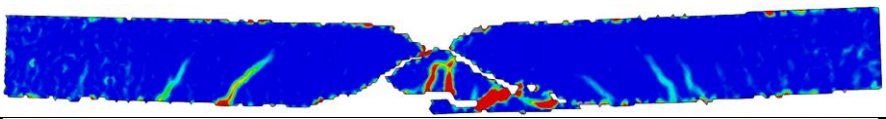
11-IS-5.7m-1FRP-NM Before first debonding	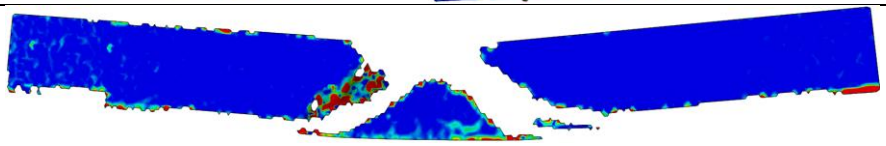

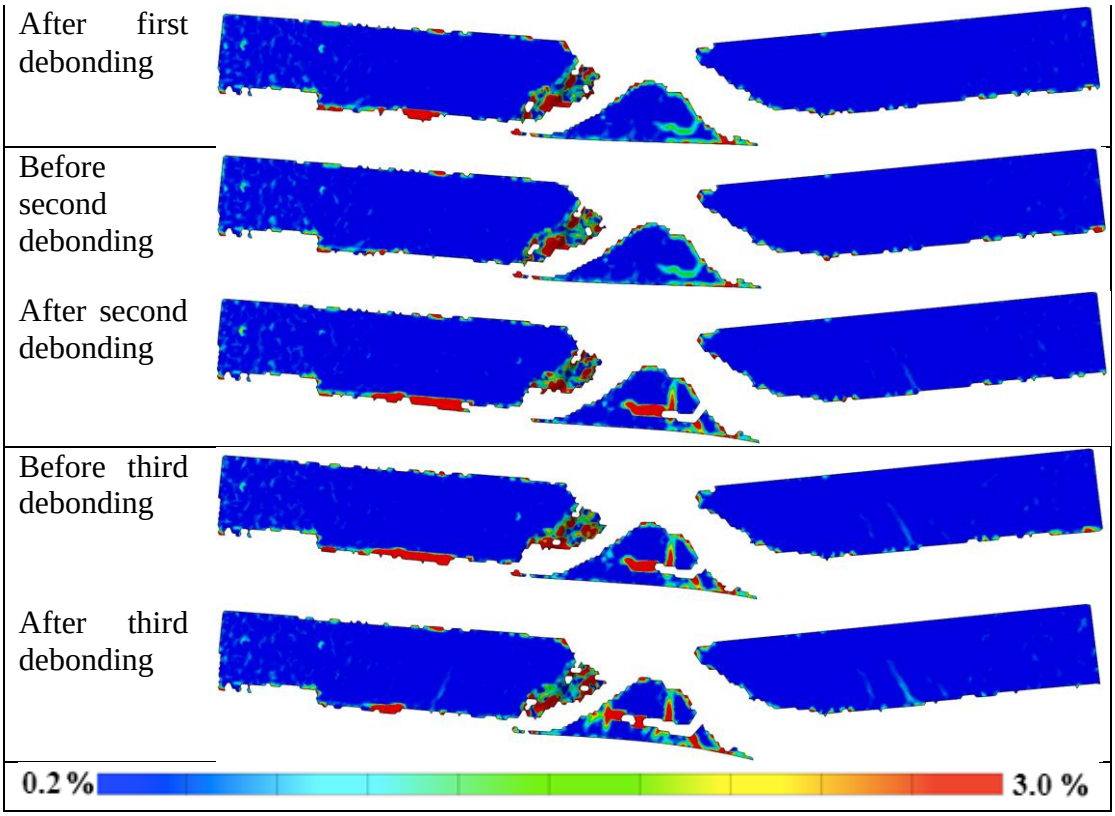
After first debonding
Before second debonding
After second debonding
Before third debonding
After third debonding
0.2 %
3.0 %

Appendix I Internal Work for Statically Only Loaded Beams

In this appendix the procedure of calculating the internal work for the statically only loaded beams is presented. The procedure used in accordance with Figure 4.6 combined with Section 5.4. Figure I.1 illustrates how the energy was calculated for an unstrengthened beam subjected to static loading only. In the load-deflection relationship the state II stiffness of a beam was found. Thereafter, the different load levels were marked in the graph and the two points between from which the area under the graph was calculated were found. The first point, in Figure 4.6 denoted as u_a, were the point where the state II stiffness intersected the load level of interest. The second point, in Figure 4.6 denoted as u_b, were the point where the descending branch of the curve intersected the load level of interest. The different areas in Figure I.1 are plastic internal energy at 100 % load level marked with green, plastic internal energy at 75 % load level marked in blue and the elastic internal work for 75 % load level is marked in red. The elastic internal work is illustrated for 75% load level just as an example. The elastic internal work is calculated as the area from origin to the point where the plastic internal work at a specific load level begins, i.e. the area under the curve left of the intersection between state II stiffness and corresponding load level.

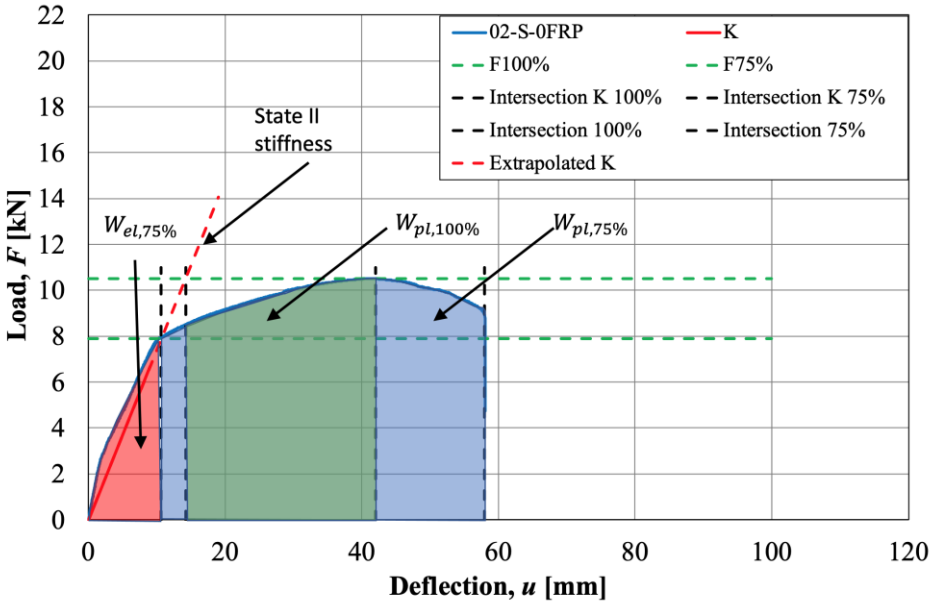

Figure I.1 Illustration of internal work at different load levels for an unstrengthened beam subjected to static loading only.

The internal work for the FRP strengthened beams was calculated using a similar approach. This is illustrated in Figure I.2 where the areas are found in the same way. The first point was chosen in the same way where the state II intersected the load level of interest. The second point were where the descending branch after debonding of FRP intersected the load level of interest. The ascending branch after debonding of FRP, though, never reached the load level 100 % of the reference beam and therefore several of the intervals were not reached for the FRP strengthened beams.

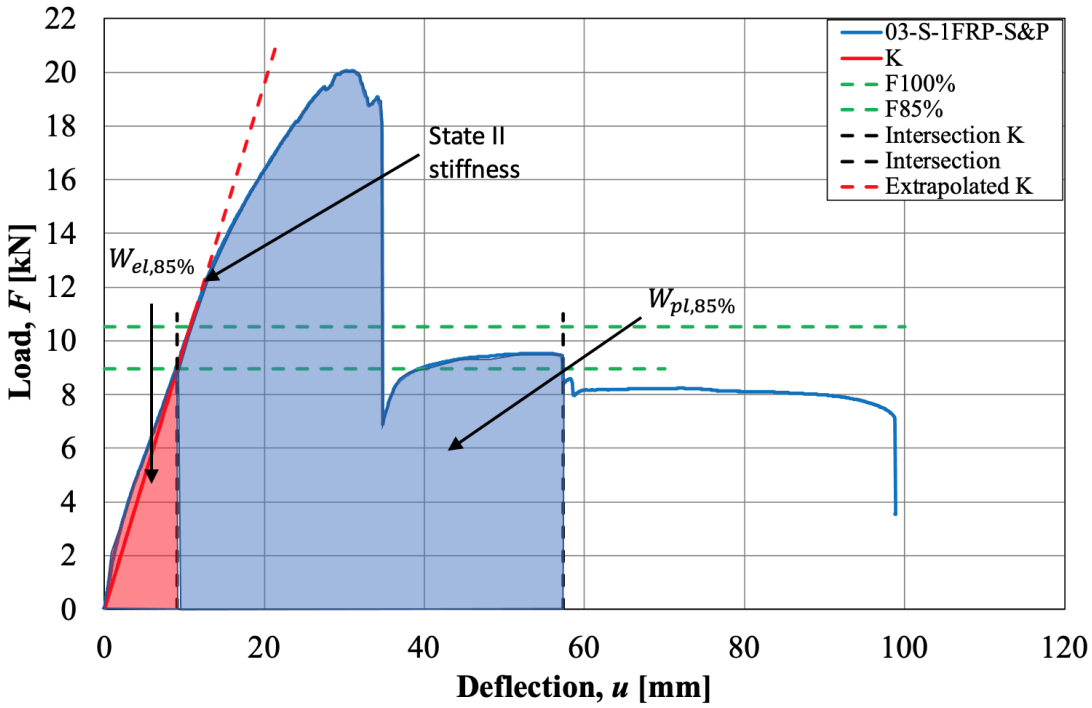

Figure I.2 *Illustration of internal work at load levels 85 % for a FRP strengthened beam subjected to static loading only.*

Appendix J Internal Work from Drop Weight Impact and for the Residual Internal Energy

In order to calculate the internal work consumed in the drop weight impact a method to estimate this energy were needed to be defined. This concept used for this estimation, together with the plastic internal work of the residual strength, is presented in this appendix.

In order to estimate the internal work consumed in the impact the load-deflection relationship of the residual strength for a beam subjected to a drop weight were related to the corresponding type of beam subjected to static loading only. Hence, the unstrengthened beams that had been subjected to a drop weight were related to the load-deflection curve of beam 02-S-0FRP. The load-deflection curves of both beams were very similar overall. The difference between maximum load level for beam 2 and the mean value between the two unstrengthened beams were just 0.14 kN and the same comparison for ultimate deflection was 0.25 mm. More accurately would have been to have used the mean value of the curves. However, since the curves were so similar beam 2 were simply chosen which is deemed to be acceptable since it is merely an approximation. In the same way, FRP strengthened beams with S&P and NM adhesive were related to the reference beam 04-S-1FRP-S&P and 06-S-1FRP-NM respectively. Figure J.1 illustrates how the internal work consumed in the impact was estimated and calculated. The beam that had been subjected to a drop weight impact were plotted in the same graph as the reference beam for that type of beam. After that the stiffness of the ascending branch for the residual strength was found. In the figures in this appendix this stiffness is referred to as state II stiffness and could also have been referred to as residual stiffness. This terminology of residual stiffness is probably more correct for the case where the damages from the drop weight resulted in severe damages of the compressive zone and in a very low stiffness. So, for this case residual stiffness is a suitable term but if state II for the residual strength curve is used it is the same. If needed this stiffness was extrapolated until the line intersected the curve of the reference beam. The area under the reference curve from the origin to this point of intersection was the energy that was estimated to have been consumed in the impact. The energy that was to the right of this point under the residual strength curve were the remaining plastic internal work for that beam. This is illustrated throughout this appendix for different cases.

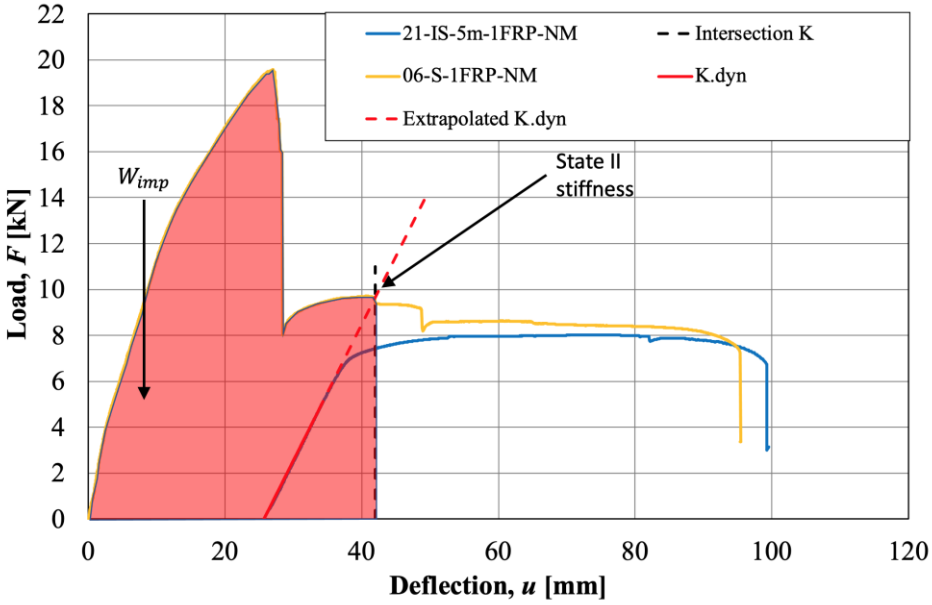

Figure J.1 *Illustration of how the internal work consumed in the drop weight impact was estimated using the load-deflection relation from a corresponding type of beam subjected to static loading only.*

The plastic internal work of the residual strength was also calculated for different load levels. The first point was the point dividing the internal work from the drop weight impact and the second point was where the descending branch intersected the load level of interest. This is illustrated for the same beam as in Figure J.1 for load level 75 % in Figure J.2.

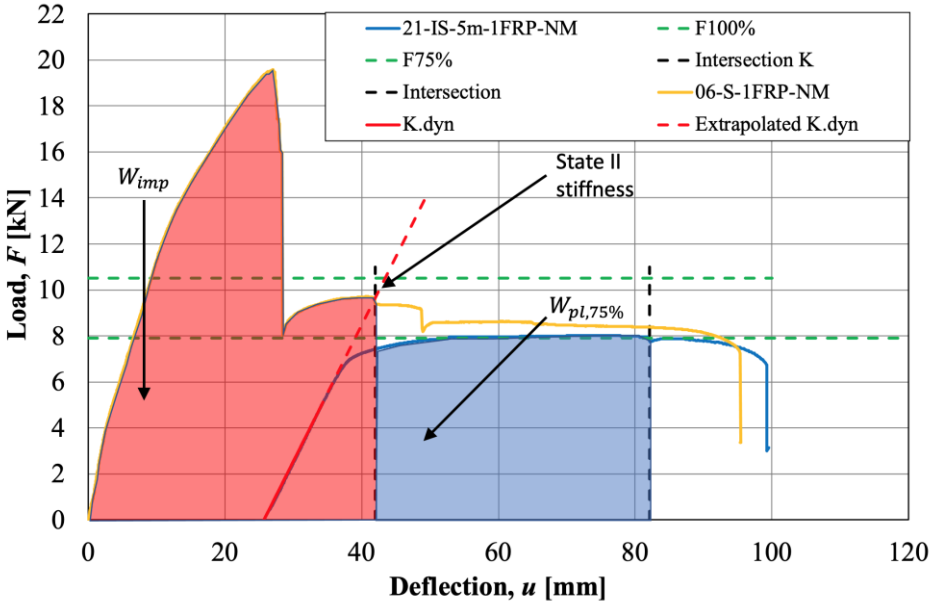

Figure J.2 *Illustration of internal work consumed in the drop weight impact together with the remaining plastic internal work.*

Figure J.3 illustrates the same procedure but for another beam where the stiffness of the residual strength of beam 08-IS-3m-1FRP-S&P was extrapolated to the intersection

point of the reference curve. As stated earlier the internal work consumed in the impact is the area under the reference curve from the origin to this point. The residual energy was then the area under the residual strength curve from point the stiffness intersected the reference curve to the point where the descending branch of the residual strength curve intersected the load level of interest.

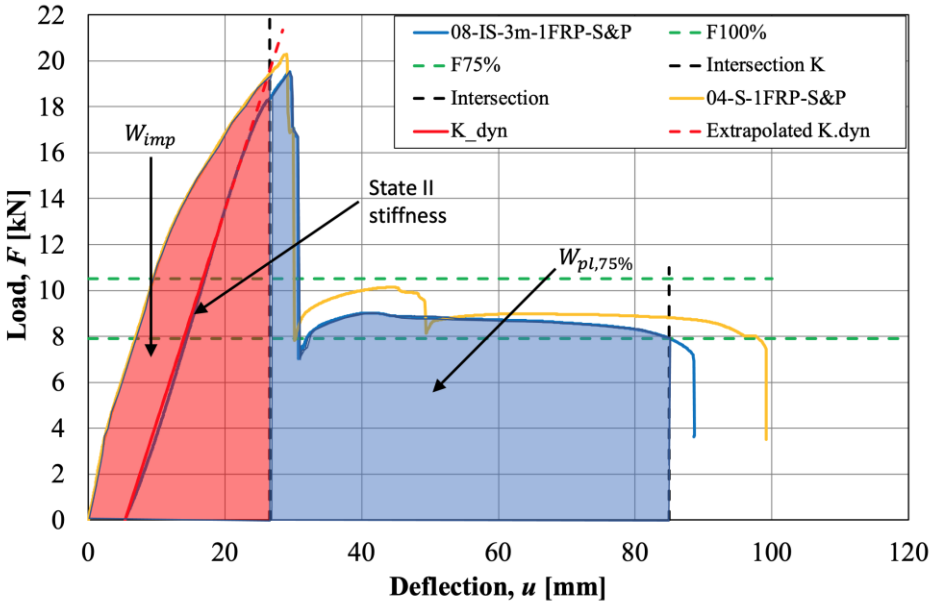

Figure J.3 *Illustration of internal work consumed in the drop weight impact together with the remaining plastic internal work.*

This method could be used for all but a few beams. The beams for when the method could not be used had all experienced large plastic deformations due to the drop weight impact and the stiffness of the ascending branch of the residual load-deflection curve never intersected the load-deflection curve of the reference beam. This was e.g. the case for the unstrengthened beams (beam 17 and 18) subjected to drop weight from the higher drop heights where the plastic deformation of these beams was larger than the ultimate deflection of the unstrengthened reference beam. For this case the load-deflection relationship for the reference was extrapolated horizontally at the load level just before rupture of the reinforcement bar. When the stiffness of the ascending branch for the residual load-deflection curve intersected the horizontally extrapolated reference curve this area was the estimated internal work consumed in the drop weight impact. This case is illustrated in Figure J.4.

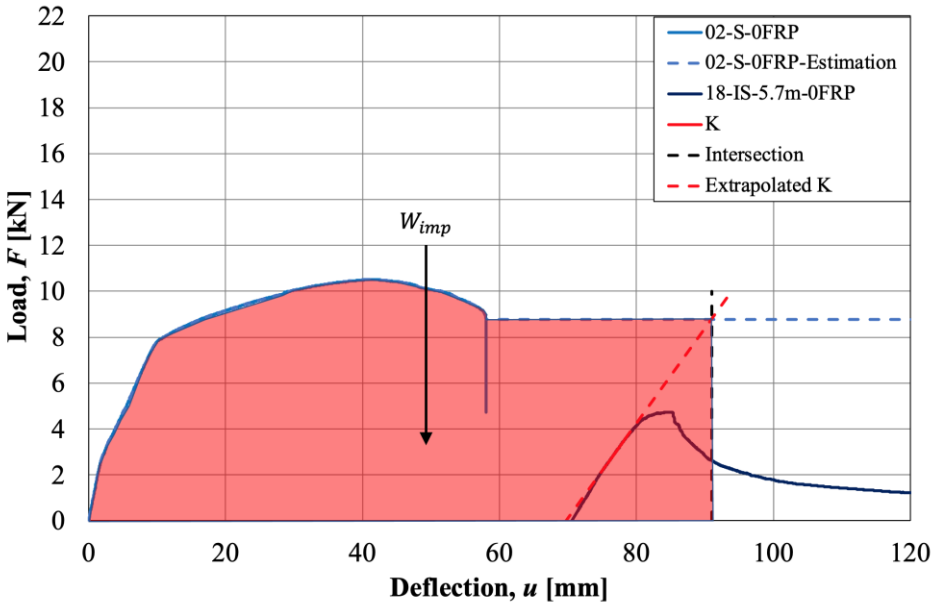

Figure J.4 *Illustration of internal work consumed in the drop weight impact when the plastic deformation exceeded the ultimate deflection of the reference curve.*

Appendix K Plastic Rotation Capacity for Beams Subjected to Dynamic Loading

This appendix treats how the plastic rotation capacity for beams subjected to dynamic loading was calculated. For statically only loaded beams the rotation capacity was calculated according to Figure 4.6 and Section 4.2.4 and for the beams that had been subjected to a drop weight impact the plastic rotation capacity was calculated as illustrated in Figure K.1. The state II stiffness of the undamaged reference beam was found, and just as for the undamaged case, the intersection point between the stiffness and the load level of interest, denoted u_a, was found. The second point, denoted u_b, was found where the descending branch of the residual strength curve of the beam that had been subjected to a drop weight impact intersected the load level of interest. These deflections were then used in Equation (4.25).

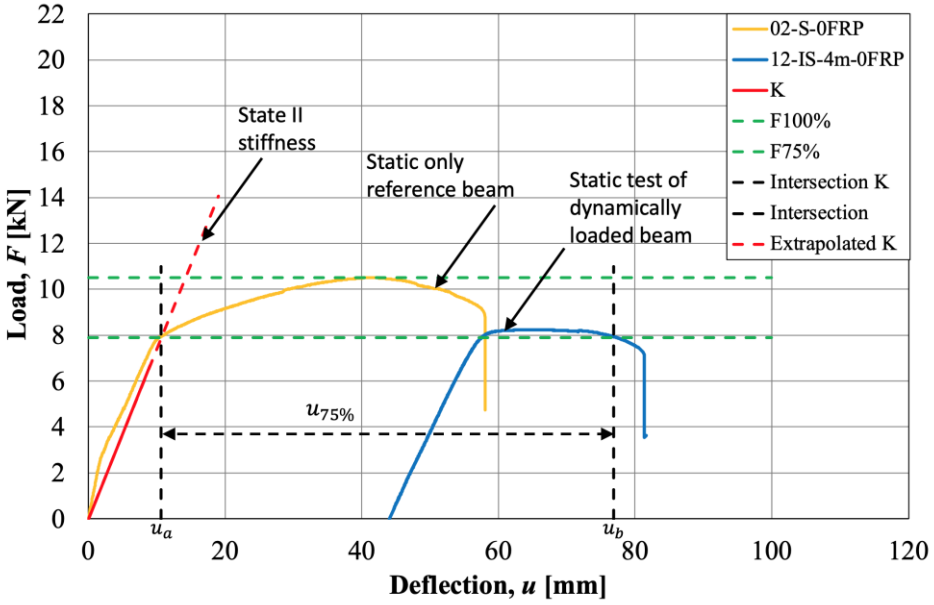

Figure K.1 *Illustration of plastic rotation capacity for a beam subjected to dynamic loading at load level of 75%.*

Appendix L MATLAB 2DOF Model

```
%%%%%%%%%%%%%%%%%%%%%%%%%%%%%%%%%%%%%%%%%%%%%%%%%%%%%%%%%%%%%%%%%%%%%%%%%%%%%%%%
%%%%%%%%%%%% %%%%%%%%%%%%%%%%%%%%%%%%%%%%%%%%%%%%%%%%%%%%%%%%%%%% %%%%%%%%%%%%%%
%%%%%%%%%%%% Simplified 2DOF system %%%%%%%%%%%%%%%%%%%%%%%%%%%%%%% %%%%%%%%%%%%%%
%%%%%%%%%%%% %%%%%%%%%%%%%%%%%%%%%%%%%%%%%%%%%%%%%%%%%%%%%%%%%%%%%%% %%%%%%%%%%%%%%
%%%%%%%%%%%% Edvard Eriksson   %%%%%%%%%%%%%%%%%%%%%%%%%%%%%%%%%%%% %%%%%%%%%%%%%%
%%%%%%%%%%%% Viktor Gustafsson %%%%%%%%%%%%%%%%%%%%%%%%%%%%%%%%%%%% %%%%%%%%%%%%%%
%%%%%%%%%%%% %%%%%%%%%%%%%%%%%%%%%%%%%%%%%%%%%%%%%%%%%%%%%%%%%%%%%%% %%%%%%%%%%%%%%
%%%%%%%%%%%% Modified from the version made by %%%%%%%%%%%% %%%%%%%%%%%%%%%%%%
%%%%%%%%%%%% Fabio Lozano Mendoza and Josef Makdesi Aphram  %%%%%%%%%%%%%%%%%%
%%%%%%%%%%%% %%%%%%%%%%%%%%%%%%%%%%%%%%%%%%%%%%%%%%%%%%%%%%%%%%%%%%% %%%%%%%%%%%%%%
%%%%%%%%%%%% Chalmers University of Technology %%%%%%%%%%%% %%%%%%%%%%%%%%%%%%
%%%%%%%%%%%% %%%%%%%%%%%%%%%%%%%%%%%%%%%%%%%%%%%%%%%%%%%%%%%%%%%%%%% %%%%%%%%%%%%%%
%%%%%%%%%%%% 21/4-2021 %%%%%%%%%%%%%%%%%%%%%%%%%%%%%%%%%%%%%%%%%%%% %%%%%%%%%%%%%%
%%%%%%%%%%%% %%%%%%%%%%%%%%%%%%%%%%%%%%%%%%%%%%%%%%%%%%%%%%%%%%%%%%% %%%%%%%%%%%%%%
%%%%%%%%%%%% %%%%%%%%%%%%%%%%%%%%%%%%%%%%%%%%%%%%%%%%%%%%%%%%%%%%%%% %%%%%%%%%%%%%%
%%%%%%%%%%%%%%%%%%%%%%%%%%%%%%%%%%%%%%%%%%%%%%%%%%%%%%%%%%%%%%%%%%%%%%%%%%%%%%%%
clear all
close all
clc
conditions=1; %Indata for different impact conditions
 % 1 - 3 m drop height
 % 2 - 4 m drop height
 % 3 - 5 m drop height
 % 4 - 5.7 m drop height
resistance=1; %Indata for resistance
 % 1 - calculated resistance, no FRP
 % 2 - measured resistance, no FRP
%%%%%%%%%%%%%%%%%%%%%%%%%%%%%%%%%%%%%%%%%%%%%%%%%%%%%%%%%%%%%%%%%%%%%%%%%%%%%%%%

if conditions==1
 height=3; %Drop height [m]
 v_d=sqrt(2*9.81*height); % drop weight velocity [m/s]
elseif conditions==2
 height=4; %Drop height [m]
 v_d=sqrt(2*9.81*height); % drop weight velocity [m/s]
elseif conditions==3
 height=5; %Drop height [m]
 v_d=sqrt(2*9.81*height); % drop weight velocity [m/s]
elseif conditions==4
    height=5.7; %Drop height [m]
    v_d=sqrt(2*9.81*height);    % drop weight velocty [m/s]
end
if resistance==1
 R_u=8.47e3; %Calculated resistance [N]
elseif resistance==2
 % beam resistance to get the same umax as from dynamic tests
 % data insted of theoretical velocity [m/s]
 if conditions==1
     v_d=mean([7.6 7.6 7.59]);  % drop weight velocity [m/s]
     R_u=10.8e3;  % beam resistance for 3m [N]
 elseif conditions==2
     v_d=mean([8.73 8.73 8.75 8.71 8.73]);  % drop weight velocity [m/s]
     R_u=9.625e3;  % beam resistance for 4m [N]
```

```
 elseif conditions==3
     v_d=mean([9.77 9.78 9.74 9.79 9.80]);  % drop weight velocity [m/s]
     R_u=9.752e3;  % beam resistance for 5m [N]
 elseif conditions==4
     v_d=mean([10.38 10.43 10.39]);         % drop weight velocity [m/s]
     R_u=8.9895e3;  % beam resistance for 5.7m [N]
 end
end

%MATERIAL PROPERTIES
%Concrete
rho_c=2445;     %Mass density [kg/m3]
E_c=36.817e9;   %Modulus of elasticity [Pa]
%Reinforcement
rho_s=7800;     %Mass density [kg/m3]
E_s=198e9;      %Modulus of elasticity [Pa]

%GEOMETRY
%Drop weight
r_d=0.04;       %Radius of drop weight [m]
A_1=pi*0.04^2;  %Area of drop weight [m2]
L_d=0.505;      %Height of drop weight [m]
%Beam
h_b=0.1;     %Height of beam [m]
w_b=0.1;     %Width of beam [m]
A_2=h_b*w_b; %Area of beam [m2]
L_b=1.3;     %Length of span of beam [m]

%TRANSFORMATION FACTORS
%Transformation factors for the drop weight
k_d_m=1; %Plastic mass transformation factor [-]
k_d_F=1; %Plastic load transformation factor [-]
k_d_K=1; %Plastic stiffness transformation factor [-]
%Transformation factors for the beam
k_b_m_el=0.486; %Elastic mass transformation factor [-]
k_b_m_pl=0.333; %Plastic mass transformation factor [-]
k_b_F_el=1; %Elastic load transformation factor [-]
k_b_F_pl=1; %Plastic load transformation factor [-]
k_b_K_el=1; %Elastic stiffness transformation factor [-]
k_b_K_pl=1; %Plastic stiffness transformation factor [-]

%MASS PROPERTIES
m_1=20; %Mass of drop weight [kg]
m_2=rho_c*A_2*L_b; %Mass of beam [kg]
%Mass matrix
M=[m_1*k_d_m 0; 0 m_2*k_b_m_pl];

%STIFFNESS PROPERTIES
I_b_ii=1.36e-6; %Second moment of inertia of beam, state II [m4]
                %calculated in mathcad

K_el_1=min(E_s*A_1/L_d,E_c*A_1/h_b);
K_el_2=48*E_c*I_b_ii/L_b^3;
%Initial stiffness matrix
K_el=[K_el_1 -K_el_1
 -K_el_1 K_el_1+K_el_2];

%MATERIAL RESPONSE
```

```
%Drop weight
R_1=70e+3; %Plastic resistance [N]
u_el_1=R_1/K_el_1; %Limit of elastic deformation [m]
u_rd_1=50; %Limit of plastic deformation [m]
%Beam
R_2_sw=rho_c*9.81*A_2*L_b/2; %Reduction of plastic resistance due to
%self-weight [N]
R_2=R_u-R_2_sw; %Plastic resistance [N]
u_el_2=R_2/K_el_2; %Limit of elastic deformation [m]
u_rd_2=50; %Limit of plastic deformation [m]
%DETERMINATION OF EIGENFREQUENCIES
[L,X]=eig(K_el, M); %L is a matrix containing the eigenvectors
 %X is a matrix containing the eigenvalues
%Maximum eigenfrequency
w_max=sqrt(max(max(X)));
%CRITICAL TIME-STEP
h_crit=2/w_max; %Maximum admissible value [s]
h=0.1e-4; %Chosen time step [s]
t_end=80e-3; %End of sequence [s]
t=linspace(0,t_end,t_end/h); %Time vector
if h>=h_crit
 disp('ERROR, chosen time step too large')
end

%INITIAL CONDITIONS
%Empty matrices
dofs=2; %Number of degree of freedom
u=zeros(dofs, length(t)); %Empty matriX storing displacement vectors
v=zeros(dofs, length(t)-1); %Velocity vectors
a=zeros(dofs, length(t)-1); %Acceleration vecors
%Assigning initial values
u(:,1)=[0;0]; %Initial displacement
% v_d=sqrt(2*9.81*height); %Initial velocity of drop weight [m/s]
v(:,1)=[v_d; 0]; %Velocities at time t=0
a_0=inv(M)*(-K_el*u(:,1)); %Initial acceleration vector
a(:,1)=a_0; %Initial acceleration as calculated before
u_b0=u(:,1)-h*v(:,1)+h^2/2*a(:,1); %Displacement at time step n-1
%Initial plastic deformation
u_pl_1=0; %Plastic deformation of rod
u_pl_2_pos=0; %Plastic deformation of beam in compression
u_pl_2_neg=0; %Plastic deformation of beam in tension
%CENTRAL DIFFERENTIAL METHOD
for i=2:length(t)
 du=u(1,i-1)-u(2,i-1); %Relative displacement between beam and
 %drop weight [m]
 u2=u(2,i-1); %Downward displacement for beam [m]
 %Determining resistance and stiffness of fictitious spring between
 %drop weight and beam
 %if du=0, set stiffness equal to elastic stiffness
 if du==0
 K_1=K_el_1;
 %If spring is in tension set stiffness to 0
 elseif du < u_pl_1
 K_1=0;
 %If spring is in elastic range
 elseif du > u_pl_1 && du <= u_pl_1+u_el_1
 R=K_el_1*(du-u_pl_1);
 K_1=R/du;
```

```
 %If spring is in plastic range
 elseif du > u_pl_1+u_el_1
 K_1=R_1/du;
 u_pl_1=du-u_el_1;
 end
 %Determining resistance and stiffness of beam spring
 %If u2=0, set stiffness equal to elastic stiffness
 if u2==0
 K_2=K_el_2;
 %If spring is in elastic tension/compression
 elseif u2 > u_pl_2_pos-u_el_2 && u2 <= u_pl_2_pos+u_el_2
 R=K_el_2*(u2-u_pl_2_pos);
 K_2=R/u2;
 %If spring is in plastic compression
 elseif u2 > u_pl_2_pos+u_el_2
 K_2=R_2/u2;
 u_pl_2_pos=u2-u_el_2;
 %If spring is in plastic tension
 elseif u2 <= u_pl_2_pos-u_el_2
 K_2=-R_2/u2;
 u_pl_2_neg=abs(u2+u_el_2-u_pl_2_pos);
 u_pl_2_pos=u_pl_2_pos-u_pl_2_neg;
 end
 %Storing values of resistance for all time steps
 RES(1,i-1)=K_1*du;
 RES(2,i-1)=K_2*u2;
 %Computing stiffness matrix
 K=[(K_1) (-K_1); (-K_1) (K_1)+(K_2)];
 %Calculation of displacement, velocity and acceleration
 if i==2
 u(:,i)=inv(M/h^2)*(-(K-2*M/h^2)*u(:,i-1)-(M/h^2)*u_b0);
 else
 u(:,i)=inv(M/h^2)*(-(K-2*M/h^2)*u(:,i-1)-(M/h^2)*u(:,i-2));
 v(:,i-1)=(u(:,i)-u(:,i-2))/(2*h);
 a(:,i-1)=(u(:,i)-2*u(:,i-1)+u(:,i-2))/h^2;
 end
end

%CALCULATION OF ENERGY
%External work of beam
DeltaWe(1)=0;
We(1)=0;
for i=2:(length(t)-1)
 DeltaWe(i)=0.5*(RES(1,i-1)+RES(1,i))*(u(2,i)-u(2,i-1));
 We(i)=We(i-1)+DeltaWe(i);
end
%Internal work of beam
DeltaWi(1)=0;
Wi(1)=0;
for i=2:(length(t)-1)
 DeltaWi(i)=0.5*(RES(2,i-1)+RES(2,i))*(u(2,i)-u(2,i-1));
 Wi(i)=Wi(i-1)+DeltaWi(i);
end
%Kinetic energy
Wk(1)=0;

for i=2:(length(t)-1)
 Wk(i)=m_2*k_b_m_pl*0.5*v(2,i-1)^2;
```

```
end
%Total energy
Wt(1)=0;
for i=2:(length(t)-1)
 Wt(i)=Wi(i)+Wk(i);
end

%CREATING PLOTS
%Displacement-time
figure(1)
plot(t*1000,u(1,:)*1000,'LineWidth',3)
set(gca,'fontsize',16)
title('Displacement of mass 1','FontSize',30)
xlabel('Time [ms]');
ylabel('Displacement [mm]');
% figure(2)
plot(t*1000,u(2,:)*1000,'LineWidth',3)
grid on
set(gca,'fontsize',16)
title('Displacement of mass 2','FontSize',30)
xlabel('Time [ms]');
ylabel('Displacement [mm]');
hold on
%Resistance-displacement
figure(3)
plot(u(2,1:length(u)-1)*1000,RES(2,:)/1000,'LineWidth',3)
set(gca,'fontsize',16)
title('Internal resistance vs displacement - body 2','FontSize',30)
xlabel('Displacement [mm]');
ylabel('Resistance [kN]');
figure(4)
plot(u(1,1:1500)*1000-u(2,1:1500)*1000,RES(1,1:1500)/1000,'LineWidth',3)
set(gca,'fontsize',16)
title('Internal resistance vs displacement - body 1','FontSize',30)
xlabel('Displacement [mm]');
ylabel('Resistance [kN]');
%Resistance-time
figure(5)
plot(t(1:length(t)-1)*1000,RES(2,:)/1000,'LineWidth',3)
set(gca,'fontsize',16)
title('Internal resistance vs time - body 2','FontSize',30)
xlabel('Time [ms]');
ylabel('Resistance [kN]');
figure(6)
plot(t(1:1500)*1000,RES(1,1:1500)/1000,'LineWidth',3)

set(gca,'fontsize',16)
title('Internal resistance vs time - body 1','FontSize',30)
xlabel('Time [ms]');
ylabel('Resistance [kN]');
% Velocity-time
figure(7)
plot(t(1:(length(t)-1))*1000,v(1,:),'LineWidth',3)
set(gca,'fontsize',16)
title('Velocity of body 1','FontSize',30)
xlabel('Time [ms]');
ylabel('Velocity [m/s]');
hold on
```

```
figure(8)
plot(t(1:(length(t)-1))*1000,v(2,:),'LineWidth',3)
set(gca,'fontsize',16)
title('Velocity of body 2','FontSize',30)
xlabel('Time [ms]');
ylabel('Velocity [m/s]');
hold on
%Work-time
figure(9)
plot(t(1:(length(t)-1))*1000,We(:),'LineWidth',3)
hold on
plot(t(1:(length(t)-1))*1000,Wi(:),'LineWidth',3)
hold on
plot(t(1:(length(t)-1))*1000,Wk(:),'LineWidth',3)
hold on
plot(t(1:(length(t)-1))*1000,Wt(:),'LineWidth',3)
set(gca,'fontsize',16)
title('External work of body 2','FontSize',30)
xlabel('Time [ms]');
ylabel('work [J]');
height;
v_init=v(1,2);
maxdisp=max(max(u(2,:)));
u_pl=maxdisp-u_el_2;
[height v_init maxdisp u_pl];
%1 - Drop weight
%2 - Beam
%CREATE TXT-FILE WITH DATA
% Create a table with the data for beam deflection-time curve

a=t*1000;
b=u(2,:)*1000;
A = a.';
B = b.';
AB = table(A, B, 'VariableNames', { 'A', 'B'} );
% Write data to text file
writetable(AB, 'PredictionDeflectionVersusTime.txt');
% Create a table with the data for drop weight velocity-time curve
c=t(1:(length(t)-1))*1000;
d=v(1,:);
C = c.';
D = d.';
CD = table(C, D, 'VariableNames', { 'C', 'D'} );
% Write data to text file
writetable(CD, 'PredictionVelocityVersusTime.txt')
```

Appendix M Hand Calculations for Static Predictions

Mathcad calculations

Early predictions of cross sectional capacities - hand calculations

Indata for the beam:

$b_{beam} := 0.1m$ width of cross section

$h_{beam} := 0.1m$ height of cross section

$L_{beam} := 1.3m$ length of beam

$\phi := 6mm$ diameter of reinforcement bar

$n'_{bar} := 2$ number of reinforcement bars in the top

$n_{bar} := 2$ number of renforcement bars in the bottom

$A_{si} := \frac{\phi^2 \cdot \pi}{4} = 28.274 \cdot mm^2$ area of one reinforcement bar

$A_s := n_{bar} \cdot A_{si} = 56.549 \cdot mm^2$

$A'_s := n'_{bar} \cdot A_{si} = 56.549 \cdot mm^2$

$d := 100mm - 20mm = 80 \cdot mm$ effective height for top reinforcement

$d' := 20mm$ effective height for bootom reinforcment

Material indata:

$f_{cm.cube} := 66.77MPa$ mean cube compressive strength of concrete @ 28 days

$f_{cm} := \frac{f_{cm.cube}}{1.2} = 55.642 \cdot MPa$ mean cylinder compressive strength of concrete @ 28 days

$f_{ck} := f_{cm} - 8MPa = 47.642 \cdot MPa$ characteristic compressive strength

$E_{cm} := 22GPa \cdot \left(\frac{\frac{f_{cm}}{1MPa}}{10} \right)^{0.3} = 36.817 \cdot GPa$ mean modlus of elasticity

$f_{ym} := 543MPa$ mean yield limit of reinforcement steel, 0.2% limit for cold treated steel

$\gamma_c := 1.0$ partial safety factor for concrete and steel. Set to 1.0 due to prediction and not design.

$\gamma_s := 1.0$

$f_{cd} := \frac{f_{cm}}{\gamma_c} = 55.642 \cdot MPa$

$f_{yd} := \frac{f_{ym}}{\gamma_s} = 543 \cdot MPa$

$E_{sm} := 198GPa$

$f_t := 661MPa$ ultimate capacity of reinforcement bar

Stress-strain relationship for concrete and reinforcement

Parameters needed to describe the stress-strain relationship for concrete in compression

$\varepsilon_{c2} := 2 \cdot 10^{-3}$ the strain where the stress starts being constant with increasing strain

$\varepsilon_{cu2} := 3.5 \cdot 10^{-3}$ the failure strain for concrete

$n := 2$ coefficent to describe the parabolic shape for the concrete class

$$\sigma_c(\varepsilon_c) := \begin{cases} \left[1 - \left(1 - \frac{\varepsilon_c}{\varepsilon_{c2}}\right)^n\right] \cdot f_{cm} & \text{if } 0 \le \varepsilon_c \le \varepsilon_{c2} \\ f_{cm} & \text{if } \varepsilon_{c2} \le \varepsilon_c \le \varepsilon_{cu2} \end{cases}$$

$\varepsilon_c := 0, 1 \cdot 10^{-4} .. \varepsilon_{cu2}$

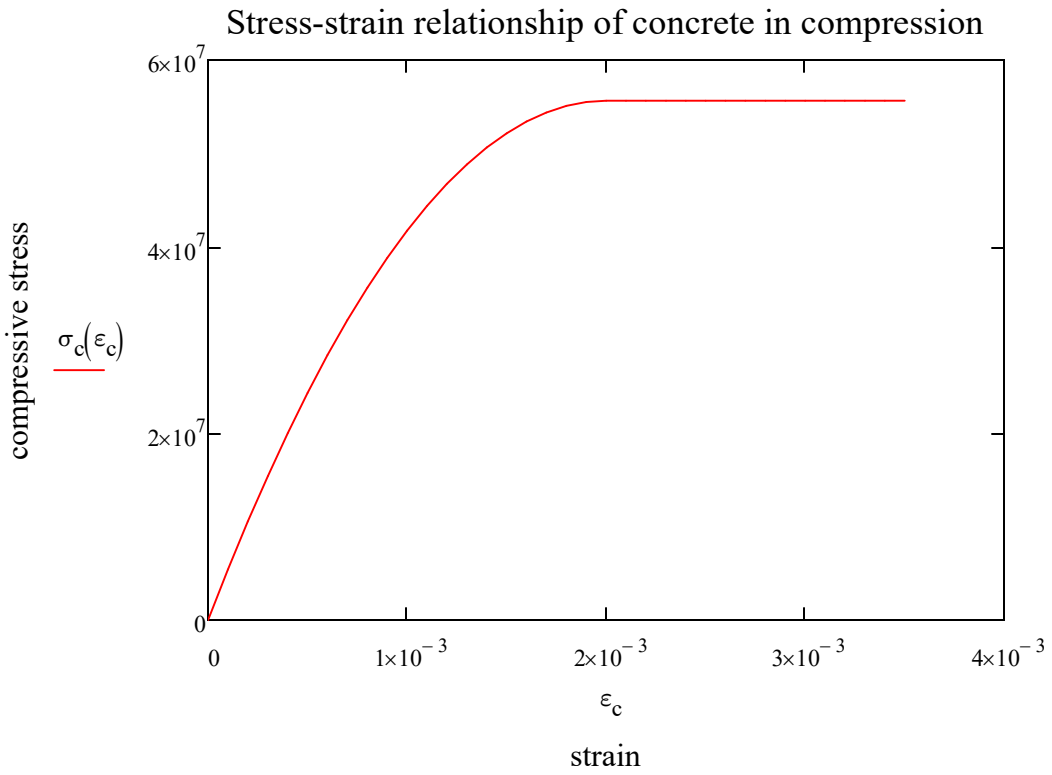

$$\text{Area}(\varepsilon_c) := \int_0^{\varepsilon_c} \sigma_c(\varepsilon_c)\, d\varepsilon_c$$

$$A_{\text{levelarm\_from\_origin}}(\varepsilon_c) := \int_0^{\varepsilon_c} \sigma_c(\varepsilon_c)\cdot\varepsilon_c\, d\varepsilon_c$$

$$\alpha_R(\varepsilon_c) := \frac{\text{Area}(\varepsilon_c)}{f_{cm}\cdot\varepsilon_c}$$

$$\beta_R(\varepsilon_c) := 1 - \frac{A_{\text{levelarm\_from\_origin}}(\varepsilon_c)}{\text{Area}(\varepsilon_c)\cdot\varepsilon_c}$$

$\alpha_R(\varepsilon_{cu2}) = 0.81$ stress block factors at ultimate concete strain

$\beta_R(\varepsilon_{cu2}) = 0.416$

$\varepsilon_{su} := 8.3 \cdot 10^{-2} = 0.083$

$\varepsilon_{sy} := \frac{f_{yd}}{E_{sm}} = 2.742 \times 10^{-3}$

$k := \frac{f_t}{f_{yd}}$

$$\sigma_s(\varepsilon_s) := \begin{cases} E_{sm} \cdot \varepsilon_s & \text{if } \varepsilon_s \le \varepsilon_{sy} \\ f_{ym} + \frac{\varepsilon_s - \varepsilon_{sy}}{\varepsilon_{su} - \varepsilon_{sy}} \cdot (k \cdot f_{ym} - f_{ym}) & \text{if } \varepsilon_{sy} \le \varepsilon_s \le \varepsilon_{su} \end{cases}$$

$\varepsilon_s := 0, 1 \cdot 10^{-4} .. \varepsilon_{su}$

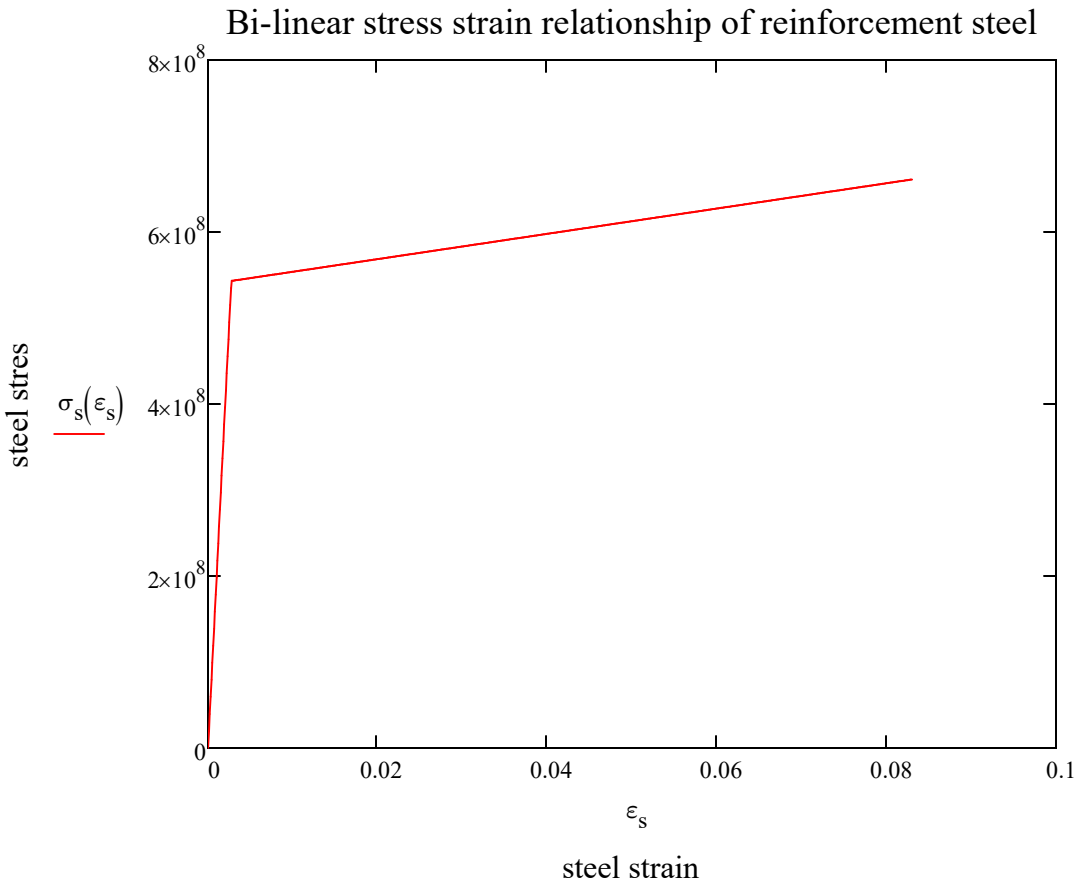

Moment capacity in ULS

Just considering the bottom reinforcement

$x_1 := 25mm$

$$x_1 := root\left(\alpha_R\left(\varepsilon_{cu2}\right)\cdot f_{cd}\cdot b_{beam}\cdot x_1 - \sigma_s\left(\frac{d - x_1}{x_1}\cdot\varepsilon_{cu2}\right)\cdot A_s, x_1\right)$$

$x_1 = 7.4\cdot mm$

control of yielding assumption

$$\varepsilon_{s1} := \frac{d - x_1}{x_1}\cdot\varepsilon_{cu2} = 0.034$$

$$\begin{cases} \text{"Bottom reinforcement yields "} & \text{if } \varepsilon_{s1} > \varepsilon_{sy} \\ \text{"Bottom reinforcement does not yield"} & \text{otherwise} \end{cases} = \text{"Bottom reinforcement yields "}$$

Ultimate moment capacity of cross section

$$M_{Rd1} := \alpha_R\left(\varepsilon_{cu2}\right)\cdot f_{cd}\cdot b_{beam}\cdot x_1\cdot\left(d - \beta_R\left(\varepsilon_{cu2}\right)\cdot x_1\right) = 2.564\cdot kN\cdot m$$

$$F_{u1} := \frac{4\cdot M_{Rd1}}{L_{beam}} = 7.889\cdot kN$$

Considering top and bottom reinforcement

$x_2 := 25mm$

$$x_2 := root\left(\alpha_R\left(\varepsilon_{cu2}\right)\cdot f_{cd}\cdot b_{beam}\cdot x_2 + \sigma_s\left(\frac{x_2 - d'}{x_2}\cdot\varepsilon_{cu2}\right)\cdot A'_s - \sigma_s\left(\frac{d - x_2}{x_2}\cdot\varepsilon_{cu2}\right)\cdot A_s, x_2\right)$$

$x_2 = 12.424\cdot mm$

Top reinforcment also in tension:

$x_2 := 15mm$

$$x_2 := root\left(\alpha_R\left(\varepsilon_{cu2}\right)\cdot f_{cd}\cdot b_{beam}\cdot x_2 - \sigma_s\left(\frac{d' - x_2}{x_2}\cdot\varepsilon_{cu2}\right)\cdot A'_s - \sigma_s\left(\frac{d - x_2}{x_2}\cdot\varepsilon_{cu2}\right)\cdot A_s, x_2\right)$$

$x_2 = 12.424 \cdot mm$

$$\varepsilon_{s2} := \frac{d - x_2}{x_2} \cdot \varepsilon_{cu2} = 0.019$$

$$\begin{cases} \text{"Bottom reinforcement yields "} & \text{if } \varepsilon_{s1} > \varepsilon_{sy} \\ \text{"Bottom reinforcement does not yield"} & \text{otherwise} \end{cases} = \text{"Bottom reinforcement yields "}$$

$$\varepsilon'_{s2} := \frac{d' - x_2}{x_2} \cdot \varepsilon_{cu2} = 2.134 \times 10^{-3}$$

$$\begin{cases} \text{"Top reinforcement yields "} & \text{if } \varepsilon'_{s2} > \varepsilon_{sy} \\ \text{"Top reinforcement does not yield"} & \text{otherwise} \end{cases} = \text{"Top reinforcement does not yield"}$$

Ultimate moment capacity of cross section with top and bottom reinforcement considered

$$M_{Rd2} := \alpha_R(\varepsilon_{cu2}) \cdot f_{cd} \cdot b_{beam} \cdot x_2 \cdot \left(d - \beta_R(\varepsilon_{cu2}) \cdot x_2\right) - \sigma_s\left(\frac{d' - x_2}{x_2} \cdot \varepsilon_{cu2}\right) \cdot A'_s \cdot (d - d') = 2.754 \cdot kN \cdot m$$

$$F_{u2} := \frac{4 \cdot M_{Rd2}}{L_{beam}} = 8.473 \cdot kN$$

Moment capacity in ULS - FRP strenghtened cross section

$$E_f := 120GPa \qquad t_{FRP} := 0.2mm \qquad A_f := b_{beam} \cdot t_{FRP} = 20 \cdot mm^2 \qquad d_f := h_{beam} + \frac{t_{FRP}}{2} = 100.1 \cdot mm$$

Top and bottom reinforcment considered with FRP

$$x_{FRP2} := 25mm$$

$$x_{FRP2} := \text{root}\left[\begin{array}{l} \alpha_R(\varepsilon_{cu2}) \cdot f_{cd} \cdot b_{beam} \cdot x_{FRP2} + \sigma_s\left(\frac{x_{FRP2} - d'}{x_{FRP2}} \cdot \varepsilon_{cu2}\right) \cdot A'_s \ldots \\ + (-1)\sigma_s\left(\frac{d - x_{FRP2}}{x_{FRP2}} \cdot \varepsilon_{cu2}\right) \cdot A_s - E_f \cdot \left(\frac{d_f - x_{FRP2}}{x_{FRP2}} \cdot \varepsilon_{cu2}\right) \cdot A_f \end{array}, x_{FRP2}\right]$$

$x_{FRP2} = 17.293 \cdot mm$

top reinforcement is in tension

$x_{FRP2} := 15mm$

$$x_{FRP2} := \text{root}\left[\begin{array}{l}\alpha_R\left(\varepsilon_{cu2}\right)\cdot f_{cd}\cdot b_{beam}\cdot x_{FRP2} - \sigma_s\left(\frac{d' - x_{FRP2}}{x_{FRP2}}\cdot\varepsilon_{cu2}\right)\cdot A'_s \ldots \\ +(-1)\sigma_s\left(\frac{d - x_{FRP2}}{x_{FRP2}}\cdot\varepsilon_{cu2}\right)\cdot A_s - E_f\cdot\left(\frac{d_f - x_{FRP2}}{x_{FRP2}}\cdot\varepsilon_{cu2}\right)\cdot A_f\end{array}, x_{FRP2}\right]$$

$x_{FRP2} = 17.293 \cdot mm$

control of yielding assumption

$$\varepsilon_{s2} := \frac{d - x_{FRP2}}{x_{FRP2}}\cdot\varepsilon_{cu2} = 0.013$$

$$\begin{cases}\text{"Bottom reinforcement yields "} & \text{if } \varepsilon_{s2} > \varepsilon_{sy} \\ \text{"Bottom reinforcement does not yield"} & \text{otherwise}\end{cases} = \text{"Bottom reinforcement yields "}$$

$$\varepsilon'_{s2} := \frac{d' - x_{FRP2}}{x_{FRP2}}\cdot\varepsilon_{cu2} = 5.479 \times 10^{-4}$$

$$\begin{cases}\text{"Top reinforcement yields "} & \text{if } \varepsilon'_{s2} > \varepsilon_{sy} \\ \text{"Top reinforcement does not yield"} & \text{otherwise}\end{cases} = \text{"Top reinforcement does not yield"}$$

control of strain in the FRP

$n_{FRP\_layers} := 1 \qquad \varepsilon_{fu} := 2.5\cdot 10^{-2} \qquad t_f := t_{FRP}$

$$\varepsilon_{fd.ic} := \min\left(0.41\cdot\sqrt{\frac{\frac{f_{cd}}{Pa}}{n_{FRP\_layers}\cdot\frac{E_f\cdot t_f}{1Pa\cdot m}}}, 0.9\varepsilon_{fu}\right) = 0.023$$

$$\varepsilon_{FRP2} := \frac{d_f - x_{FRP2}}{x_{FRP2}} \cdot \varepsilon_{cu2} = 0.017$$

"FRP strain okay" if $\varepsilon_{FRP2} < \varepsilon_{fd.ic}$ = "FRP strain okay"

"NOT okay" otherwise

Ultimate moment capacity of FRP strengthened cross section with top and bottom reinforcement considered

$$M_{Rd.FRP2} := \alpha_R(\varepsilon_{cu2}) \cdot f_{cd} \cdot b_{beam} \cdot x_{FRP2} \cdot \left(d - \beta_R(\varepsilon_{cu2}) \cdot x_{FRP2}\right) \ldots + \varepsilon_{FRP2} \cdot E_f \cdot A_f \cdot \left(d_f - d\right) - \sigma_s\left(\frac{d' - x_{FRP2}}{x_{FRP2}} \cdot \varepsilon_{cu2}\right) \cdot A'_s \cdot (d - d') = 6.111 \cdot kN \cdot m$$

$$F_{u.FRP2} := \frac{4 \cdot M_{Rd.FRP2}}{L_{beam}} = 18.804 \cdot kN$$

Moment capacity in ULS - FRP strenghtened cross section - according to *Kompositförstärkning av betong*

$\lambda := 0.8$ stress block factor for concrete with fck<50MPa

$\eta := 1.0$ stress block factor for concrete with fck<50MPa

$$x := \frac{A_s \cdot f_{yd} + \varepsilon_f \cdot E_f \cdot A_f}{\eta \cdot f_{cd} \cdot b_{beam}}$$

$x := 25mm$

$$x := \text{root}\left[\eta \cdot f_{cd} \cdot b_{beam} \cdot x - A_s \cdot f_{yd} - E_f \cdot \left(\frac{d_f - x}{x} \cdot \varepsilon_{cu2}\right) \cdot A_f, x\right]$$

$x = 14.46 \cdot mm$

control of yielding assumption

$$\varepsilon_s := \frac{d - x}{x} \cdot \varepsilon_{cu2} = 0.016$$

"Bottom reinforcement yields " if $\varepsilon_s > \varepsilon_{sy}$ = "Bottom reinforcement yields "

"Bottom reinforcement does not yield" otherwise

control of strain in the FRP

$$\varepsilon_{fd.ic} := \min\left(0.41\cdot\sqrt{\frac{\frac{f_{cd}}{Pa}}{n_{FRP\_layers}\cdot\frac{E_f\cdot t_f}{1Pa\cdot m}}}, 0.9\varepsilon_{fu}\right) = 0.023$$

$$\varepsilon_{Komp} := \frac{d_f - x}{x}\cdot\varepsilon_{cu2} = 0.021$$

$$\begin{cases} \text{"FRP strain okay"} & \text{if } \varepsilon_{Komp} < \varepsilon_{fd.ic} \\ \text{"NOT okay"} & \text{otherwise} \end{cases} = \text{"FRP strain okay"}$$

$$M_{Rd.Komp} := A_s\cdot f_{yd}\cdot\left(d - \frac{\lambda}{2}\cdot x\right) + E_f\cdot\left(\frac{d_f - x}{x}\cdot\varepsilon_{cu2}\right)\cdot A_f\cdot\left(d_f - \frac{\lambda}{2}\cdot x\right) = 6.971\cdot kN\cdot m$$

$$F_{u.Komp} := \frac{4\cdot M_{Rd.Komp}}{L_{beam}} = 21.45\cdot kN$$

Moment capacity in ULS - FRP strenghtened cross section - according to *fib*

Only considering top reinforcment

$$\psi(\varepsilon_c) := \begin{cases} 1000\cdot\varepsilon_c\cdot\left(0.5 - 1000\cdot\frac{\varepsilon_c}{12}\right) & \text{if } \varepsilon_c < \varepsilon_{c2} \\ 1 - \frac{2}{3000\cdot\varepsilon_c} & \text{if } \varepsilon_{c2} \le \varepsilon_c \le \varepsilon_{cu2} \end{cases}$$

$$\delta_G(\varepsilon_c) := \begin{cases} \frac{8 - 1000\cdot\varepsilon_c}{4\cdot(6 - 1000\cdot\varepsilon_c)} & \text{if } \varepsilon_c < \varepsilon_{c2} \\ \frac{1000\cdot\varepsilon_c\cdot(3000\cdot\varepsilon_c - 4) + 2}{2000\cdot\varepsilon_c\cdot(3000\cdot\varepsilon_c - 2)} & \text{if } \varepsilon_{c2} \le \varepsilon_c \le \varepsilon_{cu2} \end{cases}$$

Considering top and bottom reinforcement

$x := 25mm$

$$x := \text{root}\left[0.85\cdot\psi\left(\varepsilon_{cu2}\right)\cdot f_{cd}\cdot b_{beam}\cdot x - E_{sm}\cdot\left(\frac{d' - x}{x}\cdot\varepsilon_{cu2}\right)\cdot A'_s - A_s\cdot f_{yd} - E_f\cdot\left(\frac{d_f - x}{x}\cdot\varepsilon_{cu2}\right)\cdot A_f, x\right]$$

$x = 18.512\cdot mm$

control of yielding assumption

$$\varepsilon_s := \frac{d - x}{x}\cdot\varepsilon_{cu2} = 0.012$$

"Bottom reinforcement yields " if $\varepsilon_s > \varepsilon_{sy}$ = "Bottom reinforcement yields "

"Bottom reinforcement does not yield" otherwise

$$\varepsilon'_{s2} := \frac{d' - x}{x}\cdot\varepsilon_{cu2} = 2.813\times 10^{-4}$$

"Top reinforcement yields " if $\varepsilon'_{s2} > \varepsilon_{sy}$ = "Top reinforcement does not yield"

"Top reinforcement does not yield" otherwise

control of strain in the FRP

$$\varepsilon_{fd.ic} := \min\left(0.41\cdot\sqrt{\frac{\frac{f_{cd}}{Pa}}{n_{FRP\_layers}\cdot\frac{E_f\cdot t_f}{1Pa\cdot m}}}, 0.9\varepsilon_{fu}\right) = 0.023$$

$$\varepsilon_{fib2} := \frac{d_f - x}{x}\cdot\varepsilon_{cu2} = 0.015$$

"FRP strain okay" if $\varepsilon_{fib2} < \varepsilon_{fd.ic}$ = "FRP strain okay"

"NOT okay" otherwise

$$M_{Rd.fib2} := A_s\cdot f_{yd}\cdot\left(d - \delta_G\left(\varepsilon_{cu2}\right)\cdot x\right) + A_f\cdot E_f\cdot\left(\frac{d_f - x}{x}\cdot\varepsilon_{cu2}\right)\cdot\left(d_f - \delta_G\left(\varepsilon_{cu2}\right)\cdot x\right) \ldots = 5.68\cdot kN\cdot m$$
$$+ A'_s\cdot E_{sm}\cdot\left(\frac{d' - x}{x}\cdot\varepsilon_{cu2}\right)\cdot\left(d' - \delta_G\left(\varepsilon_{cu2}\right)\cdot x\right)$$

$$F_{u.fib2} := \frac{4 \cdot M_{Rd.fib2}}{L_{beam}} = 17.475 \cdot kN$$

Cracking moments and cracking loads

Unstrengthened cross section

$$k_{fl} := \max\left(1.6 - \frac{\frac{h_{beam}}{1mm}}{1000}, 1.0\right) = 1.5$$

$$f_{ctm} := 0.3 \cdot \left(\frac{f_{ck}}{MPa}\right)^{\frac{2}{3}} \cdot 1MPa = 3.943 \cdot MPa$$

$$f_{ct.fl} := k_{fl} \cdot f_{ctm} = 5.914 \cdot MPa$$

$$\alpha_s := \frac{E_{sm}}{E_{cm}} = 5.378$$

$$I_I := \frac{b_{beam} \cdot h_{beam}^{3}}{12} + (\alpha_s - 1) \cdot A_s \cdot \left(d - \frac{h_{beam}}{2}\right)^2 + (\alpha_s - 1) \cdot A'_s \cdot \left(d' - \frac{h_{beam}}{2}\right)^2 = 8.779 \times 10^{-6} m^4$$

$$M_{cr} := \frac{f_{ct.fl} \cdot I_I}{\frac{h_{beam}}{2}} = 1.038 \cdot kN \cdot m$$

$$F_{cr} := \frac{4 \cdot M_{cr}}{L_{beam}} = 3.195 \cdot kN$$

$$x_{II} := 25mm$$

$$x_{II} := root\left[b_{beam} \cdot \frac{x_{II}^{2}}{2} + (\alpha_s - 1) \cdot A'_s \cdot (x_{II} - d') - \alpha_s \cdot A_s \cdot (d - x_{II}), x_{II}\right]$$

$$x_{II} = 19.304 \cdot mm$$

$$I_{II} := \frac{b_{beam} \cdot x_{II}^{3}}{3} + \alpha_s \cdot A_s \cdot (d - x_{II})^2 + (\alpha_s - 1) \cdot A'_s \cdot (d' - x_{II})^2 = 1.36 \times 10^{-6} m^4$$

FRP strengthened cross section

$$\alpha_f := \frac{E_f}{E_{cm}} = 3.259$$

$$I_{I.FRP} := \frac{b_{beam} \cdot h_{beam}^{3}}{12} + \left(\alpha_s - 1\right) \cdot A_s \cdot \left(d - \frac{h_{beam}}{2}\right)^2 \ldots + \left(\alpha_s - 1\right) \cdot A'_s \cdot \left(d' - \frac{h_{beam}}{2}\right)^2 + \alpha_f \cdot A_f \cdot \left(d_f - \frac{h_{beam}}{2}\right)^2 = 8.943 \times 10^{-6}\, m^4$$

$$M_{cr.FRP} := \frac{f_{ct.fl} \cdot I_{I.FRP}}{\frac{h_{beam}}{2}} = 1.058 \cdot kN \cdot m$$

$$F_{cr.FRP} := \frac{4 \cdot M_{cr.FRP}}{L_{beam}} = 3.254 \cdot kN$$

$$x_{II.FRP} := 25mm$$

$$x_{II.FRP} := root\left[\begin{matrix} b_{beam} \cdot \frac{x_{II.FRP}^{2}}{2} + \left(\alpha_s - 1\right) \cdot A'_s \cdot \left(x_{II.FRP} - d'\right) \ldots \\ + (-1)\alpha_s \cdot A_s \cdot \left(d - x_{II.FRP}\right) - \alpha_f \cdot A_f \cdot \left(d_f - x_{II.FRP}\right) \end{matrix}, x_{II.FRP}\right]$$

$$x_{II.FRP} = 21.294 \cdot mm$$

$$I_{II.FRP} := \frac{b_{beam} \cdot x_{II.FRP}^{3}}{3} + \alpha_s \cdot A_s \cdot \left(d - x_{II.FRP}\right)^2 \ldots + \left(\alpha_s - 1\right) \cdot A'_s \cdot \left(d' - x_{II.FRP}\right)^2 + \alpha_f \cdot A_f \cdot \left(d_f - x_{II.FRP}\right)^2 = 1.775 \times 10^{-6}\, m^4$$

Appendix N Prediction of Plastic Rotation Capacity

Plastic rotation capacity

Eurocode 2 - section 5.6.3

Input data

$L := 1300\ mm$ — *Span length*

$h := 100\ mm$ — *Height*

$b := 100\ mm$ — *Width*

$c := 17\ mm$ — *Cover thickness*

$\phi_6 := 6\ mm$ — *Reinforcement diameter*

$d := h - c - \frac{\phi_6}{2} = 80\ mm$ — *Effective depth*

$L_0 := \frac{L}{2} = 650\ mm$

$x_u := 7.4\ mm$ — *Distance to neutral axis from top, only bottom reinforcement considered*

$\frac{x_u}{d} = 0.093$ — *Should be smaller than 0.45 for C50/60 and lower classes and smaller than 0.35 for C55/67 and higher classes*

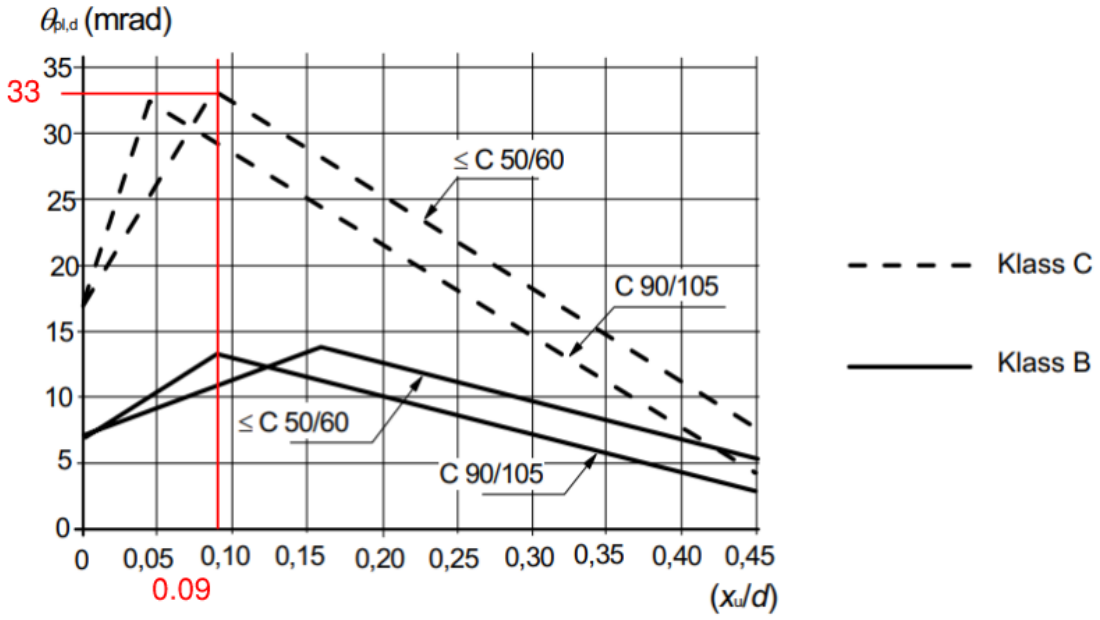

$\theta_{pl.d} := 33 \cdot 10^{-3}\ rad$ — *Class C, C40/50*

$\lambda := \frac{L_0}{d} = 8.125$ — *Need to multiply* $\theta_{pl.d}$ *with a factor since* λ *is not equal to 3*

$k_\lambda := \sqrt{\frac{\lambda}{3}} = 1.646$

$\theta_{tot.pl.d.EC2} := \theta_{pl.d} \cdot k_\lambda = 0.054\ rad$ *Rotation capacity corrected for slenderness not equal to 3*

$\theta_{pl.EC2} := \frac{\theta_{tot.pl.d.EC2}}{2} = 0.027$ *The angle in EC2 is twice the size of the angle considered in this thesis*

$u_{pl.EC2} := \theta_{pl.EC2} \cdot L_0 = 17.65\ mm$ *Plastic deformation*

ABC-method

Input data

$L := 1300\ mm$ *Span length*

$h := 100\ mm$ *Height*

$b := 100\ mm$ *Width*

$c := 17\ mm$ *Cover thickness*

$\phi_6 := 6\ mm$ *Reinforcement diameter*

$A_s := 2 \cdot \frac{\phi_6^{\,2} \cdot \pi}{4} = 56.549\ mm^2$

$d := h - c - \frac{\phi_6}{2} = 80\ mm$ *Effective depth*

$L_0 := \frac{L}{2} = 650\ mm$

Material properties

$f_{cc} := 55.642\ MPa$ *Mean compression strength of concrete*

$f_{st} := 543\ MPa$ *Mean proof strength of reinforcement,* $f_{0.2.m}$

$f_{su} := 661\ MPa$ *Ultimate steel strength*

$E_s := 198\ GPa$ *Young's modulus*

$\varepsilon_{cu} := 3.5 \cdot 10^{-3}$ *Ultimate concrete strain*

$\varepsilon_s := \frac{f_{st}}{E_s} = 0.003$ *Proof strain*

$\varepsilon_{su} := 0.083$ *Ultimate strain*

Calculation

$\omega_v := 0$ *Mechanical ratio for the shear reinforcement is 0 since no shear reinforcement is used*

$\omega_{s'} := 0$ *Mechanical ratio for the top reinforcement is 0 since the top reinforcement is subjected to tensile forces*

$\omega_s := \frac{A_s}{b \cdot d} \cdot \frac{f_{st}}{f_{cc}} = 0.069$ *Mechanical ratio for the bottom reinforcement in tension, top bars are neglected*

$\omega_{bal} := \frac{0.8 \cdot \varepsilon_{cu}}{\varepsilon_{cu} + \varepsilon_s}$

$A := 1 + 0.6 \cdot \omega_v + 1.7 \cdot \omega_{s'} - 1.4 \cdot \frac{\omega_s}{\omega_{bal}} = 0.785$

$0.05 \le A \le 2.30$ *OK!*

$B := 1.0$ *Our reinforcement was K500C, the value for B is corresponding to reinforcement type Ks 60 and Ks 40, which are closest to our reinforcement.*

$AB := min(A \cdot B, 1.7) = 0.785$ *Value corresponding to Ks 40 or Ks 60 reinforcement*

$C := 7 \cdot \frac{L_0}{d} = 56.875$ *Factor C calculated with assupmtion of plastic hinge in midsection*

$\theta_{pl.ABC} := A \cdot B \cdot C \cdot 10^{-3} = 0.045$ *Plastic rotation*

$u_{pl.ABC} := \theta_{pl.ABC} \cdot L_0 = 29.009\ mm$ *Plastic deformation*

BK25

Input data

$L := 1300\ mm$ *Span length*

$h := 100\ mm$ *Height*

$b := 100\ mm$ *Width*

$c := 17\ mm$ *Cover thickness*

$\phi_6 := 6\ mm$ *Reinforcement diameter*

$A_s := 2 \cdot \frac{\phi_6^{\,2} \cdot \pi}{4} = 56.549\ mm^2$

$d := h - c - \frac{\phi_6}{2} = 80\ mm$ *Effective depth*

$L_0 := \frac{L}{2} = 650\ mm$

Material properties

$f_{cc} := 55.642\ MPa$ *Mean compression strength of concrete*

$f_{st} := 543\ MPa$ *Mean proof strength of reinforcement,*

$f_{su} := 661\ MPa$ *Ultimate steel strength*

$E_s := 198\ GPa$ *Young's modulus*

$\varepsilon_{cu} := 3.5 \cdot 10^{-3}$ *Ultimate concrete strain*

$\varepsilon_s := \frac{f_{st}}{E_s} = 0.003$ *Proof strain*

$\varepsilon_{su} := 0.4 \cdot 0.083 = 0.033$ *Ultimate strain, factor 0.4 according to Morgan Johansson (2021).*

Calculation

$\omega_{s.crit} := \frac{0.8 \cdot \varepsilon_{cu}}{\varepsilon_{cu} + \varepsilon_{su}} = 0.076$ *Critical ratio, if mechanical ratio for reinforcement is smaller than the critical ratio the failure mode is in steel, otherwise in the concrete*

$\omega_s := \frac{A_s}{b \cdot d} \cdot \frac{f_{st}}{f_{cc}} = 0.069$ *Mechanical ratio for the bottom reinforcement in tension, top bars are neglected*

$\omega_s \le \omega_{s.crit}$ *Failure in reinforcement* ω_s *since is smaller than* $\omega_{s.crit}$

$\theta_{pl.BK25} := \frac{0.4 \cdot \varepsilon_{su}}{0.8 - \omega_s} \cdot \left(1 + 0.3 \cdot \frac{L}{d}\right) = 0.107$ *Plastic rotation*

$u_{pl.BK25} := \theta_{pl.BK25} \cdot L_0 = 69.373\ mm$ *Plastic deformation*

Summary

Plastic rotation

$\theta_{pl.EC2} = 0.027$ $u_{pl.EC2} = 17.65\ mm$

$\theta_{pl.ABC} = 0.045$ $u_{pl.ABC} = 29.009\ mm$

$\theta_{pl.BK25} = 0.107$ $u_{pl.BK25} = 69.373\ mm$

DEPARTMENT OF ARCHITECTURE AND CIVIL ENGINEERING
DIVISION OF STRUCTURAL ENGINEERING
CHALMERS UNIVERSITY OF TECHNOLOGY
Gothenburg, Sweden 2021
www.chalmers.se

CHALMERS
UNIVERSITY OF TECHNOLOGY